UNIVERSITÀ
DEGLI STUDI
DI TRIESTE

UNIVERSITÀ DEGLI STUDI DI TRIESTE

XXXVIII CICLO DEL DOTTORATO DI RICERCA IN BIOMEDICINA MOLECULARE

CHARACTERIZATION OF THE ROLES OF THE DISCS LARGE MAGUK SCAFFOLD PROTEIN 5 IN HEPATOCELLULAR CARCINOMA

Settore scientifico-disciplinare: **MED/12**

DOTTORANDA
THERRIZ MAE P. MAMERTO

COORDINATORE
PROF. ALESSANDRO TOSSI
Alessandro Tossi

SUPERVISORE DI TESI
PROF. CLAUDIO TIRIBELLI

SUPERVISORE DI TESI
DOTT. DEVIS PASCUT

ANNO ACCADEMICO 2024/2025

ABSTRACT

Hepatocellular carcinoma (HCC) remains a leading cause of cancer-related deaths worldwide, characterized by high recurrence, therapeutic resistance, and molecular heterogeneity. One hallmark of liver cancer is the progressive loss of hepatocyte polarity and tissue organization. This study investigated the polarity protein Discs Large Homolog 5 (DLG5), a membrane-associated guanylate kinase (MAGUK) scaffold involved in maintaining epithelial integrity. DLG5 expression and localization were analyzed in paired HCC and adjacent liver tissues using quantitative PCR, western blotting, immunohistochemistry, and immunofluorescence, complemented by *in silico* correlation and colocalization analyses with β-catenin. The results showed that while DLG5 mRNA was significantly elevated in HCC, its protein expression was reduced and mislocalized, shifting from the membrane to cytoplasmic and perinuclear regions. These findings indicate that DLG5 functions in a localization-dependent manner, where its submembranous positioning is essential for maintaining epithelial polarity, stabilizing β-catenin at adherens junctions, and preserving junctional integrity in hepatocytes.

RIASSUNTO

L’epatocarcinoma (HCC) rimane una delle principali cause di mortalità correlata al cancro a livello mondiale, caratterizzato da elevati tassi di recidiva, resistenza terapeutica e marcata eterogeneità molecolare. Una delle caratteristiche distintive del carcinoma epatico è la progressiva perdita della polarità degli epatociti e dell’organizzazione tissutale. Questo studio ha indagato la proteina di polarità Discs Large Homolog 5 (DLG5), una proteina scaffold appartenente alla famiglia delle chinasi guanilato–associate alla membrana (MAGUK), coinvolta nel mantenimento dell’integrità epiteliale. L’espressione e la localizzazione di DLG5 sono state analizzate in campioni appaiati di tessuto HCC e fegato adiacente mediante PCR quantitativa, western blot, immunoistochimica e immunofluorescenza, integrate con analisi *in silico* di correlazione e studi di colocalizzazione con β-catenina. I risultati hanno mostrato che, sebbene l’mRNA di DLG5 risulti significativamente aumentato nei campioni HCC, l’espressione proteica appare ridotta e mal localizzata, con uno spostamento dal dominio di membrana verso le regioni citoplasmatiche e perinucleari. Questi risultati indicano che DLG5 agisce in modo dipendente dalla localizzazione, e che il suo posizionamento submembranoso è essenziale per mantenere la polarità epiteliale, stabilizzare la β-catenina nelle giunzioni aderenti e preservare l’integrità giunzionale negli epatociti.

PREFACE

This thesis comprises solely my original work undertaken for the PhD in Molecular Biomedicine. Due acknowledgement has been made in the text to all sources used.

"A mio padre, Restituto — dedico a te la Figura 23. Il tuo ricordo ispira ogni dettaglio di questo lavoro."

Table of Contents

LIST OF ABBREVIATIONS

A	Adjacent
AD	Apical domain
AFP	Alpha-Fetoprotein
AJ	Adherens junction
AKT	Protein kinase B
ALT	Alanine Aminotransferase
aPKC	Atypical protein kinase C
APS	Ammonium persulfate
AST	Aspartate aminotransferase
ASUGI	Azienda Sanitaria Universitaria Giuliano Isontina
AXIN1	Axis Inhibition Protein 1
BC	Bile canaliculus
BCA	Bicinchoninic acid
BCLC	Barcelona Clinic Liver Cancer
BD	Basolateral domain
BSA	Bovine serum albumin
C	Cytoplasmic
CARD	Caspase recruitment domain
CC	Coiled coil
CDK1	Cyclin-dependent kinase 1
CDC42	Cell division cycle 42
CLDN2	Claudin-2
CRB	crumbs
CRB3	Crumbs3
CT	Computed Tomography
CTNNB1	Catenin Beta 1
DAB	3,3′-Diaminobenzidine
DAPI	4′,6-diamidino-2-phenylindole
DLG	Discs large

DLG5	Discs large homolog 5
DMEM	Dulbecco’s Modified Eagle Medium
DNA	Deoxyribonucleic acid
DTT	Dithiothreitol
EASL	European Association for the Study of the Liver
ECM	Extracellular matrix
EDTA	Ethylenediaminetetraacetic acid
EMT	Epithelial-mesenchymal transition
ENCORI	Encyclopedia of Noncoding CRNA Interactomes
ERK	Extracellular signal-regulated kinase
ESR1	Estrogen receptor alpha
ESR2	Estrogen receptor beta
FITC	Fluorescein Isothiocyanate
FZR1	Fizzy-Related Protein 1
GLOBOCAN	Global Cancer Observatory
GSK3B	Glycogen synthase kinase 3 beta
GUK	Guanylate kinase
HBV	Hepatitis B virus
HCV	Hepatitis C virus
HCC	Hepatocellular carcinoma
Hh	Hedgehog
HRP	Horseradish Peroxidase
HSC	Hepatic stellate cells
Huh7	Human Hepatoma 7
IF	Immunofluorescence
IHC	Immunohistochemistry
IL-6	Interleukin-6
IQR	Interquartile range
JHH6	Japanese Human Hepatoma 6
K_2HPO_4	Dipotassium hydrogen phosphate
KH_2PO_4	Potassium dihydrogen phosphate

KRAS	Kirsten Rat Sarcoma viral oncogene homolog
LGL	Lethal giant larvae
LI-RADS	Liver Imaging Reporting and Data System
LIHC	Liver Hepatocellular Carcinoma
LLGL1	Lethal giant larvae protein homolog 1
LLGL2	Lethal giant larvae protein homolog 2
LSEC	Liver sinusoidal endothelial cell
MAGUK	Membrane-associated guanylate kinase
MAPK	Mitogen-activated protein kinase
MASH	Metabolic dysfunction-associated steatohepatitis
MASLD	Metabolic dysfunction-associated steatotic liver disease
MELD	Model for End-Stage Liver Disease
MRI	Magnetic Resonance Imaging
MTOR	mammalian target of rapamycin
Na^+/K^+-ATPase	Sodium / Potassium - ATPase
NAFLD	Nonalcoholic fatty liver disease
NASH	Non-alcoholic steatohepatitis
NF-κB	Nuclear Factor Kappa-light-chain enhancer of activated B cells
NHS	Normal Horse Serum
NOS	Not otherwise stated
NR3C1	Nuclear Receptor Subfamily 3, Group C, Member 1
OCLN	Occludin
P	Perinuclear (ring)
PALS1	Protein associated with Lin-7-1
PAR3	Partitioning defective protein 3
PAR6	Partitioning defective protein 6
PATJ	PALS1-associated tight junction protein
PBS	Phosphate-buffered saline
PDZ	Post-synaptic density protein 95/disc large tumor suppressor/zona occludens
PFA	Paraformaldehyde
PGLYRP1	Peptidoglycan recognition protein 1

PI3K	phosphoinositide 3-kinase
PVDF	Polyvinylidene difluoride
RHOB	Ras Homolog Family Member B
RNA	Ribonucleic acid
SCRIB	Scribble
SD	Standard deviation
SH3	SRC homology 3
siRNA	Small interfering RNA
SLC22A4	Solute carrier family 22 member 4
SM	Submembranous
SNARE	Soluble N-ethylmaleimide-sensitive factor attachment protein receptors
SNTX4	Syntaxin-4
SORBS3	Sorbin and SH3 domain-containing protein 3
T	Tumoral
TACE	Transarterial chemoembolization
TARE	Transarterial radioembolization
TC	Total Cell
TCGA	The Cancer Genome Atlas
TERT	Telomerase reverse transcriptase
TGF-β	Transforming growth factor-beta
TJ	Tight junction
TNF-α	Tumor necrosis factor - alpha
TNM	Tumor, node, metastasis
TP53	Tumor Protein p53
TPM1	Tropomyosin alpha-1 chain
TRITC	Tetramethylrhodamine Isothiocyanate
WB	Western Blot
WNT	Wingless/integrated signaling molecules
YAP	Yes-associated protein
ZO1	Zonal occludens 1

LIST OF FIGURES

LIST OF TABLES

CHAPTER 1. INTRODUCTION

The liver is recognized as a structurally complex and versatile organ [13]. With hepatocyte polarity, its histological structure features a unique compartmentalized radial morphology that regulates physiological functions simultaneously [14]. This architecture of polarized hepatocytes enables the formation of a bile canaliculi network on the apical domain while maintaining sinusoidal interfaces at the basolateral domain [15]. The regulation of hepatic polarity is conserved by a set of cell polarity protein complexes, such as Crumbs (CRB), Partition defective protein (PAR), and Scribble (SCRIB) [16]. Dysregulation among the polarity protein complexes impairs hepatocellular polarity and is marked as one of the hallmarks of hepatocarcinogenesis [4].

Hepatocarcinogenesis arises as a consequence of progressive chronic liver damage, often driven by metabolic dysfunction-associated steatohepatitis (MASH), the inflammatory and fibrogenic form of metabolic dysfunction-associated steatotic liver disease (MASLD) [17-19].

Hepatocellular carcinoma (HCC) is the most prevalent primary liver malignancy [1]. It poses a substantial global health challenge due to rising incidence, mortality rates, and clinical complexity [20]. Although detection, surveillance, and treatment strategies of HCC have improved, most cases are detected at intermediate or advanced stages, restricting the feasibility of curative interventions such as resection or transplantation [21]. For instance, clinical staging systems such as Barcelona Clinic Liver Cancer (BCLC), Tumor-Node-Metastasis (TNM), and Cancer of the Liver Italian Program (CLIP) are used to assess tumor characteristics, liver function, and patient treatment planning, though each has limitations in addressing the complexity of HCC heterogeneity [22].

The BCLC, TNM, and CLIP staging systems are based on anatomical and clinical parameters [23-25]. However, these staging systems do not incorporate molecular alterations that may significantly influence tumor behavior and therapeutic response [1]. While phenotypic heterogeneity in HCC manifests variably in tumor size, histological grade, and morphology, this heterogeneity is paralleled and often driven by pronounced molecular heterogeneity [26]. At the molecular level, HCC is characterized by a diverse spectrum of genetic mutations, transcriptomic profiles, and epigenetic modifications, which influence the activation of key oncogenic signaling pathways such as Wingless/integrated signaling molecules/beta-catenin (Wnt/β-catenin), Transforming growth factor-beta (TGF-β), Hippo-yes associated protein/transcriptional coactivator with PDZ-binding motif (Hippo-YAP/TAZ) [27-29].

Wnt/β-catenin, TGF-β, and Hippo-YAP/TAZ are key oncogenic signaling pathways that exhibit crosstalk with cell polarity [30-32]. For instance, Discs large homolog 5 (DLG5) protein a scaffold protein and key cell polarity protein regulator, exhibits a stabilizing role by binding to β-catenin-cadherin complex at adherens junctions (AJ) [12].

This study aims to molecularly characterize DLG5 in HCC by evaluating its expression and localization in both HCC-derived cell lines and patient-derived tissue samples.

1.1 Epidemiology, etiology, and clinical challenges of HCC

Liver cancer ranks as the sixth most prevalent diagnosed malignancy and is the third-leading cause of cancer-related mortality worldwide [33-35]. Among all the primary liver cancers, HCC is the most predominant histological type, representing approximately 75–85% of global liver cancer cases [35]. The global burden of HCC is projected to increase in the coming years, reflecting both the continued prevalence of etiological factors and the persistent challenges in clinical detection, prognostic stratification, and therapeutic management [36-38]. According to the latest estimates from Global Cancer Observatory (GLOBOCAN) 2022, the age-standardized incidence rate (ASR) of HCC is highest in Southeast Asia, ranging between 10-14 cases per 100,000 population. Followed by sub-Saharan Africa (8-14 per 100,000). In contrast, HCC incidence is considerably lower in Europe and North America with 2-7 per 100,000 (Figure 1). The mortality patterns mirror incidence and highlight the clinical challenges inherent in HCC management. In Southeast Asia, the ASR mortality rate is estimated at 9-13 per 100,000, followed by sub-Saharan Africa with a mortality rate of 7-13 per 100,000. By comparison, Europe and North America have 2-8 per 100,000 report lower mortality rates (Figure 2).

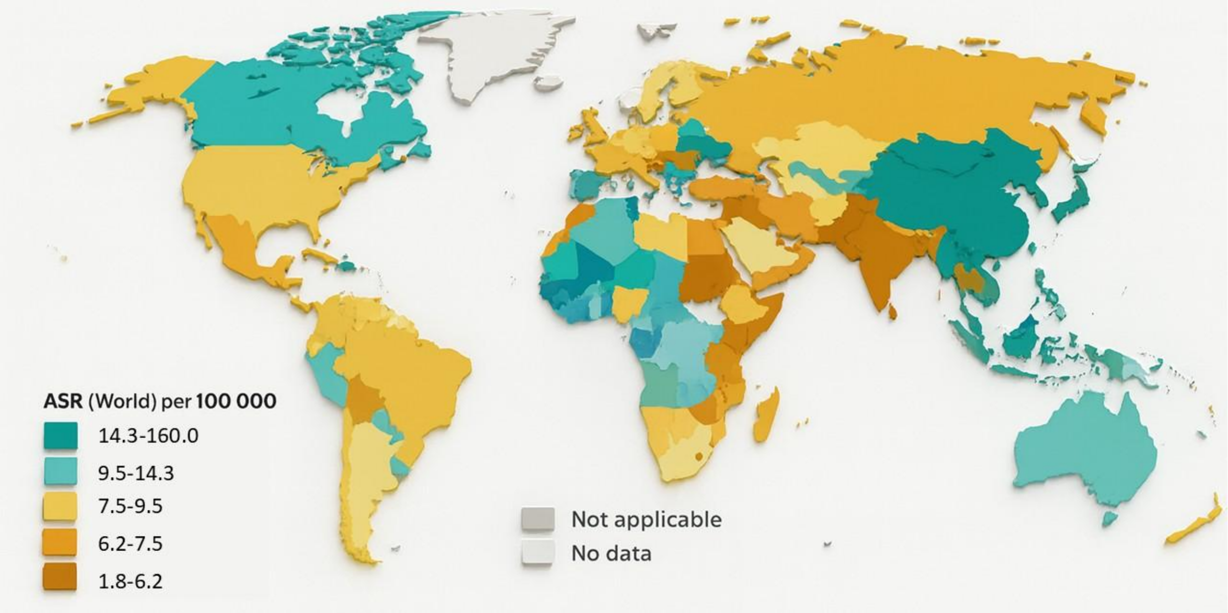

Figure 1. Global Age-Standardized Incidence Rates of Liver Cancer, 2022. This map illustrates the global incidence ASIR of liver and intrahepatic bile duct cancers of both genders with age 20-85+. The incidence demonstrates striking geographical disparities, with the highest rates observed in East Asia and parts of sub-Saharan Africa (ASR ≥14.3 per 100,000). Intermediate incidence rates (7.5–14.3 per 100,000) are reported in Southeast Asia, Central Africa, and regions of Latin America, while Europe and North America generally display lower incidence (<7.5 per 100,000). These patterns reflect differences in the prevalence of major etiological factors, including HBV, HCV, and MASLD. The data highlight the urgent need for region-specific prevention and surveillance strategies tailored to local risk factor burdens. Image generated and enhanced from [6, 10].

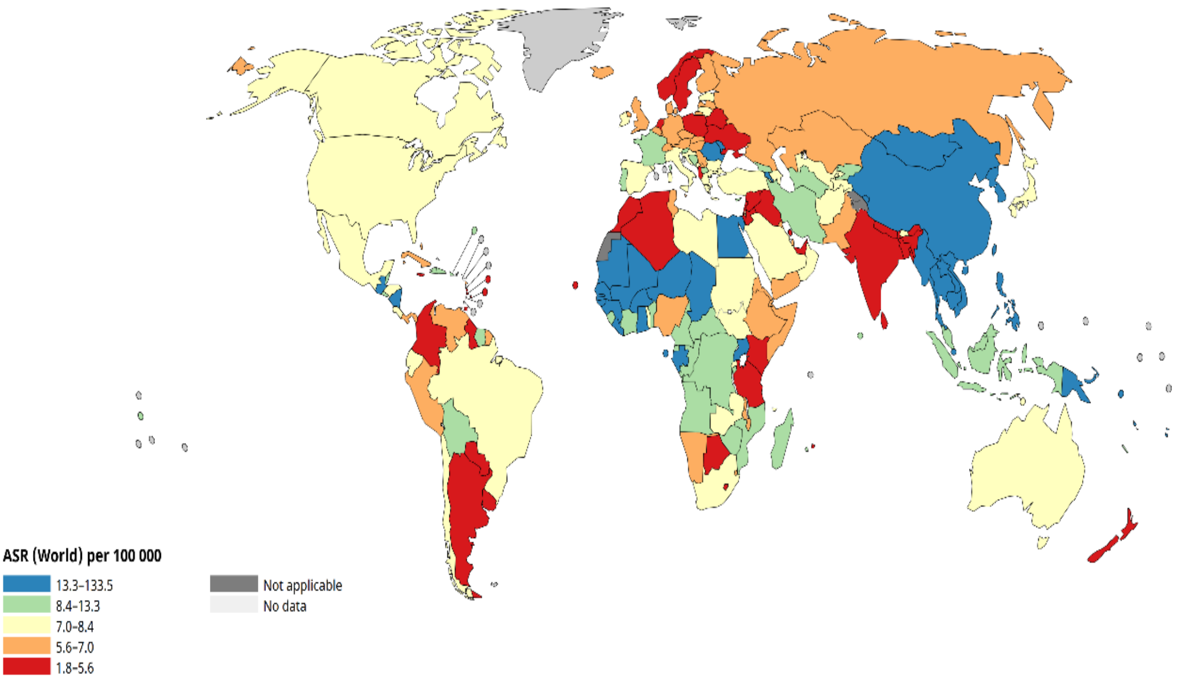

Figure 2. Global Age-Standardized Mortality Rates of Liver Cancer, 2022. This map presents the global ASMR for liver and intrahepatic bile duct cancers of both genders with age 20-85+. Mortality patterns closely parallel incidence rates, with the highest mortality observed in East Asia and sub-Saharan Africa (ASR ≥8.0 per 100,000). Intermediate mortality rates are reported in Southeast Asia and parts of Latin America, while Europe and North America show comparatively lower mortality burdens (<5.6 per 100,000). The strong overlap between incidence and mortality reflects the limited access to early detection and curative treatment in high-burden regions. Image generated and enhanced from [6].

As illustrated in Figure 3, the geographical distribution of HCC demonstrates a pronounced disparity that is attributable to various etiological factors [1, 33]. The high incidence rates in Asian and African regions are attributed to endemic hepatitis B virus (HBV) infection [39]. Indeed, chronic HBV infection is one of the most well-established HCC risk factors, accounting for more than half of global cases [1]. Another major etiological factor of HCC is Hepatitis C virus (HCV), which is particular in regions of Japan, the Mediterranean, and parts of North America [39-41]. Furthermore, the Western population has shifted to MASLD as the major cause of HCC due to increasing prevalence of obesity and type 2 diabetes mellitus (T2DM) cases [42]. Moreover, both obesity and T2DM accelerate MASLD progression and increase MASH development even in the absence of cirrhosis [43]. A well-recognized major risk factor of HCC is chronic alcohol consumption, it acts as a co-factor with HBV, HCV, or MASLD, amplifying hepatocarcinogenesis through acetaldehyde-mediated DNA damage, oxidative stress, and repeated cycles of hepatocyte turnover [44, 45]. Minor etiologies of HCC include: a. genetic disorders such as hemochromatosis, α-1 antitrypsin deficiency, and Wilson's disease [46]; b. lifestyle including diet and smoking [47, 48]; and c. carcinogenic substances such as aflatoxin B1 [49, 50].

Figure 3. Global distribution of HCC risk factors. HBV predominates in most of Asia (excluding Japan), South America, and Africa, while HCV is the leading cause in Western Europe, North America and Japan. Alcohol consumption serves as the primary etiological factor in Central and Eastern Europe. Meanwhile, non-alcoholic steatohepatitis (NASH) recently redefined as MASH under the broader category of MASLD is an increasingly important cause of HCC in high-income nations. MASH-related HCC is projected to surpass viral and alcohol-related cases in the coming decades, particularly in regions with rising obesity and metabolic syndrome prevalence. Caption and image modified from [1].

The clinical management of HCC is challenged by its asymptomatic onset, which frequently results in delayed diagnosis and eventually restricts available therapeutic interventions. According to the European Association for the Study of the Liver (EASL) 2018 guidelines, the gold standard for the diagnosis of HCC is the histopathological confirmation, however, in clinical practice, non-invasive imaging is sufficient for diagnosis of HCC in the population at risk. A liver biopsy remains the definitive diagnostic method in cases where imaging is inconclusive [21, 51]. Concordance in at least two imaging techniques such as Computed Tomography (CT) scan, Magnetic Resonance Imaging (MRI), and Liver Imaging Reporting and Data System (LI-RADS), ensures standardized HCC detection however these techniques are costly thus being less accessible in low-resource settings [52, 53].

Prognostic assessment in HCC is particularly complex as it depends on both tumor characteristics and functional status of the liver. The BCLC, TNM and CLIP staging systems have been developed to address this complexity [54]. Currently, BCLC staging system is the most widely used framework for HCC. It integrates tumor stage, liver function (assessed by Child-Pugh), and patient performance status, thereby providing treatment allocation in a single model [55]. The main strength of BCLC lies in its comprehensive and clinically practical approach, yet its rigid stage-to-treatment recommendations often limit individualized therapeutic decisions, particularly among patients in intermediate stages [56]. In contrast, the TNM American Joint Committee on Cancer (AJCC) classification provides a detailed anatomical description of tumor extent and remains useful for pathological staging and surgical evaluation [1, 57]. However, it does not account for underlying liver function, rendering it less applicable in patients with cirrhosis or significant hepatic impairment [58]. Meanwhile, CLIP score was developed to overcome some of these limitations by incorporating both tumor morphology and liver function, including portal vein thrombosis, AFP levels, and Child–Pugh stage [25]. Although the CLIP score has demonstrated reliable prognostic value, particularly in advanced disease, its global adoption remains limited compared with the BCLC system [59, 60].

The clinical management of HCC encompasses curative, locoregional, and systemic approaches, each presenting distinct limitations. Curative therapies such as surgical resection, liver transplantation, and local ablation (radiofrequency or microwave) offer the greatest potential for long-term survival though eligibility is limited [21]. Liver transplantation simultaneously treats both tumor burden and underlying cirrhosis, yet organ scarcity and tumor progression beyond transplant criteria limit eligibility [1]. Surgical resection is feasible only in non-cirrhotic or well-compensated patients with preserved hepatic reserve, while local ablation remains effective primarily for tumors ≤3 cm in diameter [21]. Locoregional therapies, such as transarterial chemoembolization (TACE) and transarterial radioembolization (TARE), are recommended for intermediate-stage disease, offering palliative benefit through localized cytotoxic and ischemic effects [21]. Although these interventions can delay progression, they seldom achieve complete tumor eradication and are not curative. Systemic therapy has undergone substantial development in recent years. The introduction of multikinase inhibitors such as sorafenib, lenvatinib, regorafenib, and cabozantinib has modestly improved overall survival in advanced HCC, though resistance development and heterogeneous patient response remain major challenges [61]. More recently, immune checkpoint inhibitors such as atezolizumab, bevacizumab, nivolumab, and pembrolizumab have shown promising efficacy; however, their availability remains limited in many regions [62]. Despite these therapeutic combinations, high recurrence rates, restricted curative eligibility, and treatment-related adverse effects are still experienced by some patients [63]. These challenges underscore the urgent need for refined prognostic tools, personalized treatment algorithms, and novel molecular targets to improve the long-term management of HCC.

1.2 Chronic liver damage as a precursor to hepatocarcinogenesis

The liver is the largest glandular organ and is essential for major physiological functions such as metabolism, detoxification, and bile production. Its functional unit is called hepatic lobules, which contain plates of polarized hepatocytes arranged radially around the central veins and bordered by portal triads [16]. Hepatocytes exhibit a unique polarity characterized by apical domains and embedded within basolateral membranes, forming branches of bile canalicular network [14]. Another feature of hepatocyte polarity is the ability to facilitate directional segregation of bile secretion into canaliculi and nutrient exchange from blood [16].

A healthy liver subjected to chronic injury induced by hepatitis viruses, excessive alcohol consumption, or metabolic dysfunction, undergoes hepatocyte apoptosis, inflammation, and compensatory regeneration that can lead to hepatocarcinogenesis [64]. In conditions of prolonged liver injury, the hepatic stellate cells become activated and deposit excessive extracellular matrix (ECM), altering hepatic lobules and progress to fibrosis [65]. Eventually, as fibrosis advances to liver cirrhosis, it disrupts hepatocyte organization impairing cell polarity [66].

Chronic liver damage represents a spectrum of pathological conditions characterized by ongoing inflammation, hepatocellular injury, and progressive fibrotic remodeling of the hepatic parenchyma [66, 67]. It serves as a common pathological endpoint for diverse etiologies which initiate hepatocyte stress and apoptosis [68]. In response, the liver initiates a repair program involving Kupffer cells, hepatic stellate cells (HSCs), and infiltrating immune populations [69]. Early hepatocyte apoptosis triggers compensatory proliferation of surviving hepatocytes and activation of progenitor cells. However, this regenerative response often becomes maladaptive due to a hostile microenvironment dominated by oxidative stress, pro-inflammatory cytokines, and reactive oxygen species, ultimately laying the groundwork for tumorigenesis [70].

Upon activation, HSCs differentiate into myofibroblast-like cells and secrete ECM proteins, predominantly collagen types I and III [66, 67]. This excessive ECM accumulation gradually disrupts the normal sinusoidal architecture and alters hepatic morphology. As fibrosis advances, the accumulation of fibrous tissue leads to widespread scarring and mechanical disruption of ECM interactions [71]. Eventually, this process culminates in cirrhosis, a critical transitional stage characterized by the formation of fibrotic septa and regenerative nodules [68]. Within this altered environment, dysplastic nodules may emerge as pre-neoplastic lesions [68]. The cirrhotic liver becomes increasingly enriched with pro-oncogenic cytokines, notably Interleukin-6 (IL-6), Tumor Necrosis Factor-alpha (TNF-α), and TGF-β [72, 73].

HCC commonly develops as the end stage of cirrhosis, arising through the progressive accumulation of genetic, epigenetic, and signaling alterations within chronically regenerating hepatocytes [1, 33]. Over time, dysplastic hepatocytes within regenerative nodules accumulate key oncogenic alterations that drive malignant transformation. Mutations in *Telomerase Reverse Transcriptase* (*TERT*), *Tumor Protein p53* (*TP53*), and *Catenin Beta 1* (*CTNNB1*) act as pivotal events that promote uncontrolled proliferation, resistance to senescence, and evasion of growth suppression [74, 75]. Additionally, widespread reprogramming of chromatin structure and DNA methylation patterns further modifies gene expression, reinforcing abnormal growth and survival phenotypes [76]. Concurrently, persistent activation of pro-survival signaling pathways such as Janus Kinase/Signal Transducer and Activator of Transcription 3 (JAK/STAT3), Phosphatidylinositol 3-Kinase/Protein Kinase B (PI3K/AKT), and Wnt/β-catenin enhances cellular proliferation, metabolic adaptation, and resistance to apoptosis, collectively establishing a self-sustaining oncogenic network that culminates in HCC [77]. Collectively, these molecular alterations convert dysplastic nodules into malignant clones, defining the histological and functional transition from cirrhosis to HCC [78]. The sequential progression of chronic liver injury toward hepatocarcinogenesis is summarized in Figure 4.

1.3 Molecular pathogenesis of HCC

The molecular pathogenesis of HCC involves a multistep process driven by cumulative genetic, epigenetic, and microenvironmental alterations [1]. Among the most frequently altered genes are *TP53*, *CTNNB1*, *TERT*, and *Axis Inhibition Protein 1* (*AXIN1*). Mutations in *TP53* impair DNA repair and apoptosis, allowing defective hepatocytes to evade cell cycle checkpoints [79, 80]. Gain-of-function mutations in *CTNNB1* activate the Wnt/β-catenin pathway, promoting uncontrolled proliferation and the emergence of stem-like phenotypes [81, 82]. Early in hepatocarcinogenesis, *TERT* promoter mutations reactivate telomerase, conferring replicative immortality [83]. In contrast, *AXIN1* mutations, which disrupt β-catenin degradation, further potentiate Wnt-driven oncogenic transcription [74].

These genetic alterations converge on several intracellular signaling cascades that orchestrate malignant transformation. Activation of the PI3K/AKT//mammalian target of rapamycin (mTOR) pathway supports cell survival, metabolic adaptation, and resistance to oxidative stress [84]. The mitogen-activated protein kinase/extracellular signal-regulated kinase (MAPK/ERK) pathway promotes cellular proliferation, supports angiogenic processes, and increases sensitivity to growth factors [85]. The TGF-β pathway, initially tumor-suppressive, shifts to a pro-oncogenic role in advanced disease by promoting epithelial-mesenchymal transition (EMT), immune evasion, and metastasis [86]. Likewise, inactivation of the Hippo pathway results in nuclear accumulation of the transcriptional co-activators YAP and TAZ, promoting tumorigenesis [87]. EMT represents a pivotal event in HCC progression, enabling hepatocytes to lose epithelial characteristics and acquire migratory and invasive capacities [88]. This process is jointly regulated by TGF-β, Wnt/β-catenin, and YAP/TAZ signaling pathways that are frequently dysregulated in HCC and contribute to cytoskeletal remodeling, ECM reorganization, and loss of adhesion [73, 87, 89].

As molecular dysregulation continues, tumor cells interact dynamically with their surrounding microenvironment. The tumor microenvironment is invaded with tumor-associated macrophages, myeloid-derived suppressor cells, and regulatory T cells [90]. Inflammatory signaling mediated by nuclear factor kappa-light-chain enhancer of activated B cells (NF-κB) and signal transducer and activator of STAT3 reinforces pro-survival and angiogenic programs while dampening anti-tumor immunity [91, 92].

1.4 Hepatic polarity to maintain liver homeostasis

Hepatic polarity refers to the asymmetric organization of cellular components, that enables hepatocytes to perform coordinated metabolic, secretory, and detoxification functions [4, 14]. Hepatocytes exhibit a distinctive form of multi-axial polarity, allowing simultaneous interaction with both the vascular and biliary systems. This basolateral surface mediates the bidirectional exchange of metabolites, hormones, and plasma proteins, forming the principal interface between the hepatocyte and systemic circulation. In contrast, the apical membranes of adjacent hepatocytes connect through tight junctions, delineating the bile canaliculi, the smallest ducts of the biliary network responsible for bile formation and excretion (Figure 5) [16].

Hepatocytes are radially arranged around the central vein and portal triads, establishing a zonated metabolic landscape along the porto-central axis, known as liver zonation (Figure 6) [93]. This spatial organization reflects gradients of oxygen, nutrients, and hormones, resulting in regional metabolic specialization [94]. Periportal hepatocytes predominantly perform oxidative energy metabolism, ureagenesis, and gluconeogenesis, whereas pericentral hepatocytes specialize in glycolysis, lipogenesis, and xenobiotic metabolism to gluconeogenesis, urea cycle, and lipoprotein production (Figure 7) [95-97]. Such functional compartmentalization relies on the maintenance of hepatocyte polarity, ensuring directional transport and coordinated metabolic communication across the hepatic lobule.

At the molecular level, hepatocyte polarity is sustained by three conserved polarity complexes CRB, PAR, and SCRIB which collectively establish and preserve the distinct identities of apical and basolateral membrane domains [14, 16]. Among these, SCRIB plays a central role in defining basolateral identity and maintaining junctional integrity and preserving hepatic tissue architecture. Notably, mislocalization of the basolateral SCRIB has been shown to drive HCC initiation and progression through activation of AKT- Activator Protein-1 (AP-1)- Secreted Acidic and Rich in Cysteine (SPARC) signaling axis, thereby promoting EMT, invasion, and poor patient prognosis [98]. Indeed, hepatic polarity is highly sensitive to chronic injury, and its structural and molecular disintegration leads to impaired bile flow, altered transporter localization, and dysregulated intracellular signaling [16, 99]. These events collectively promote hepatocyte dedifferentiation and malignant transformation, representing hallmark processes in the early pathogenesis of HCC.

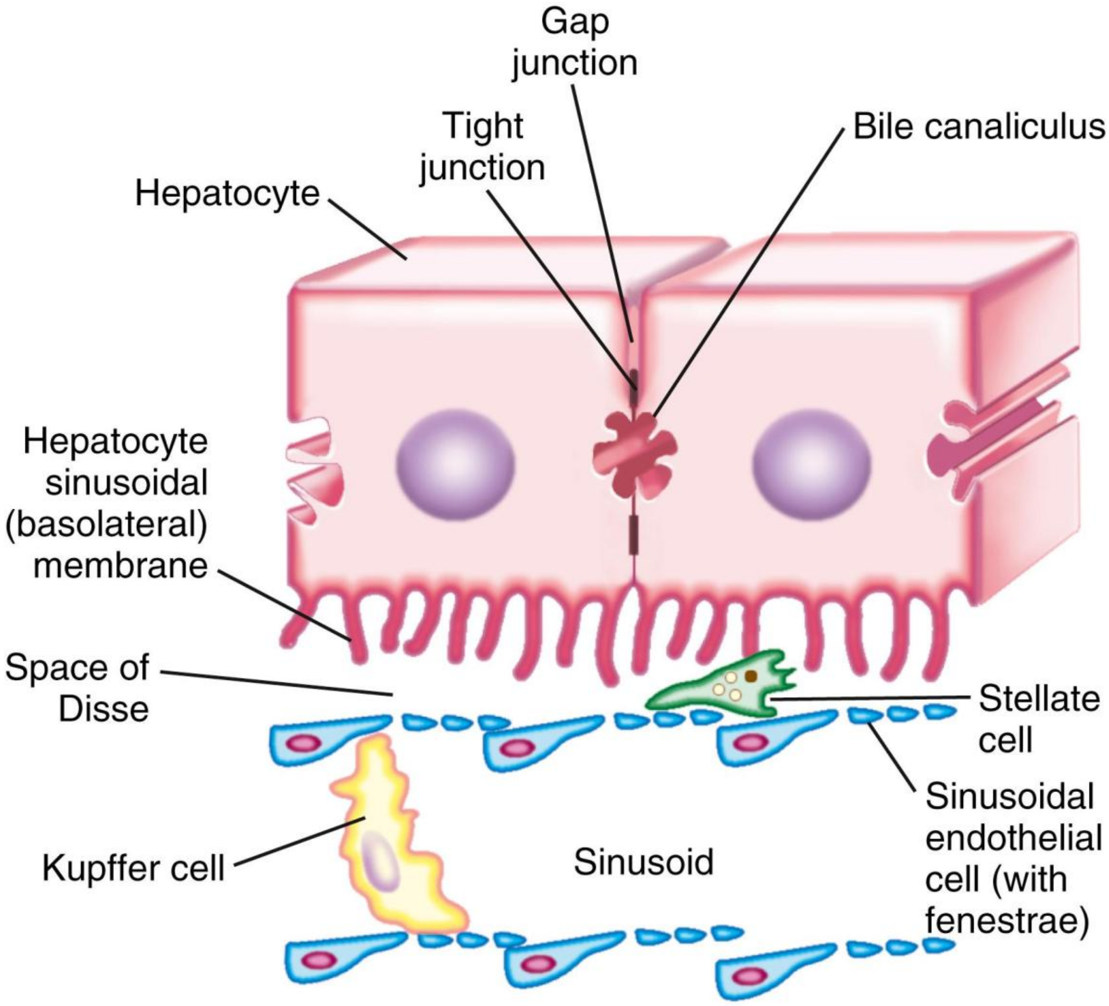

Figure 4. Structural organization of hepatocyte polarity. Hepatocytes are arranged in interconnected plates bordered by tight junctions (TJ) that delineate distinct apical (canalicular) and basolateral (sinusoidal) membrane domains. The apical domain forms the bile canaliculi (BC), which mediate bile secretion, while the basolateral domain faces the sinusoidal lumen and facilitates bidirectional exchange of metabolites, nutrients, and signaling molecules with the blood. Surrounding sinusoidal endothelial cells and Kupffer cells contribute to the specialized microenvironment that supports hepatic polarity and metabolic function. Caption and image modified from [7].

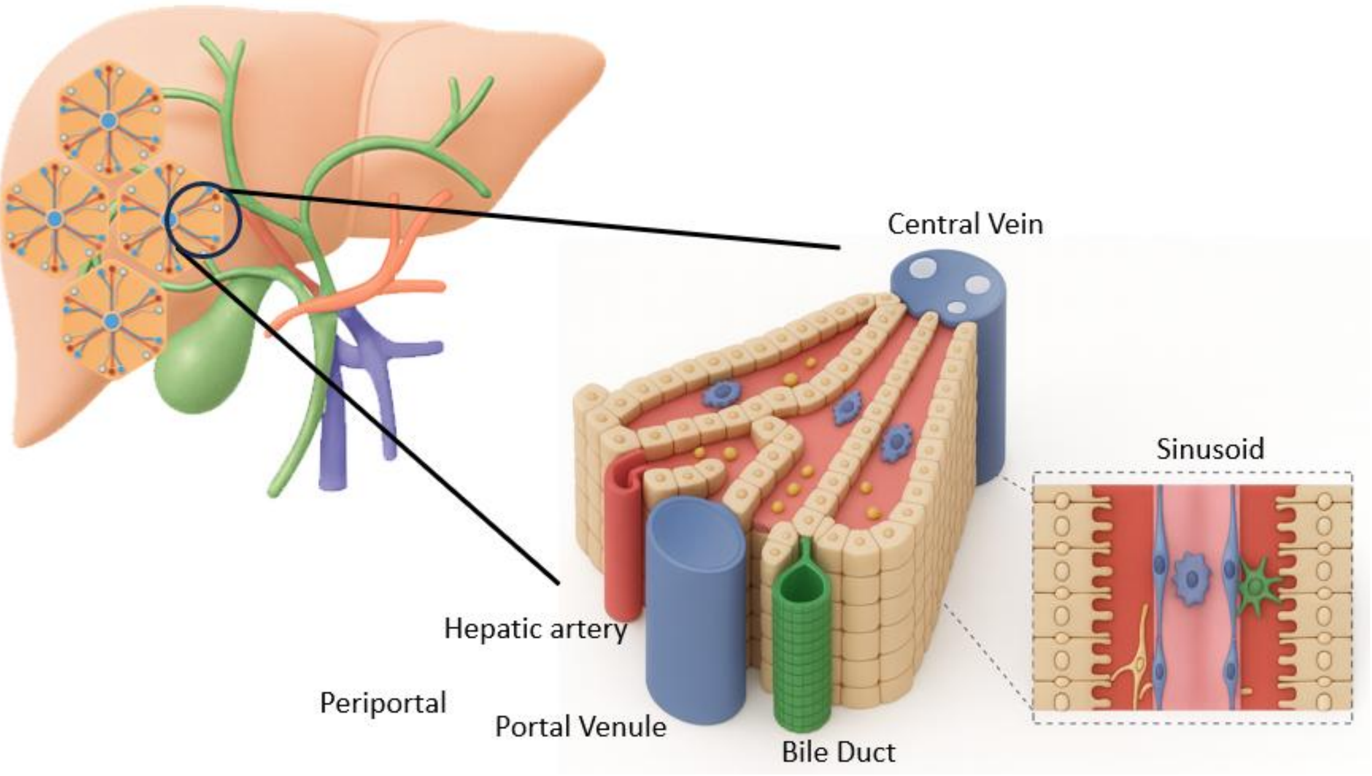

Figure 5. Hepatic lobule and sinusoidal microarchitecture. The liver consists of hexagonally organized hepatic lobules, each centered around a central vein and bordered by portal triads containing branches of the hepatic artery, portal vein, and bile duct. Blood from the portal vein and hepatic artery flows centripetally through the sinusoids toward the central vein, while bile produced by hepatocytes flows centrifugally through the bile canaliculi toward the bile ducts, illustrating the liver's characteristic dual-flow system. The inset highlights the sinusoidal interface, showing the close spatial relationship among hepatocytes, sinusoidal endothelial cells, and Kupffer cells, which collectively maintain metabolic exchange and immune surveillance. Caption and image modified from [8].

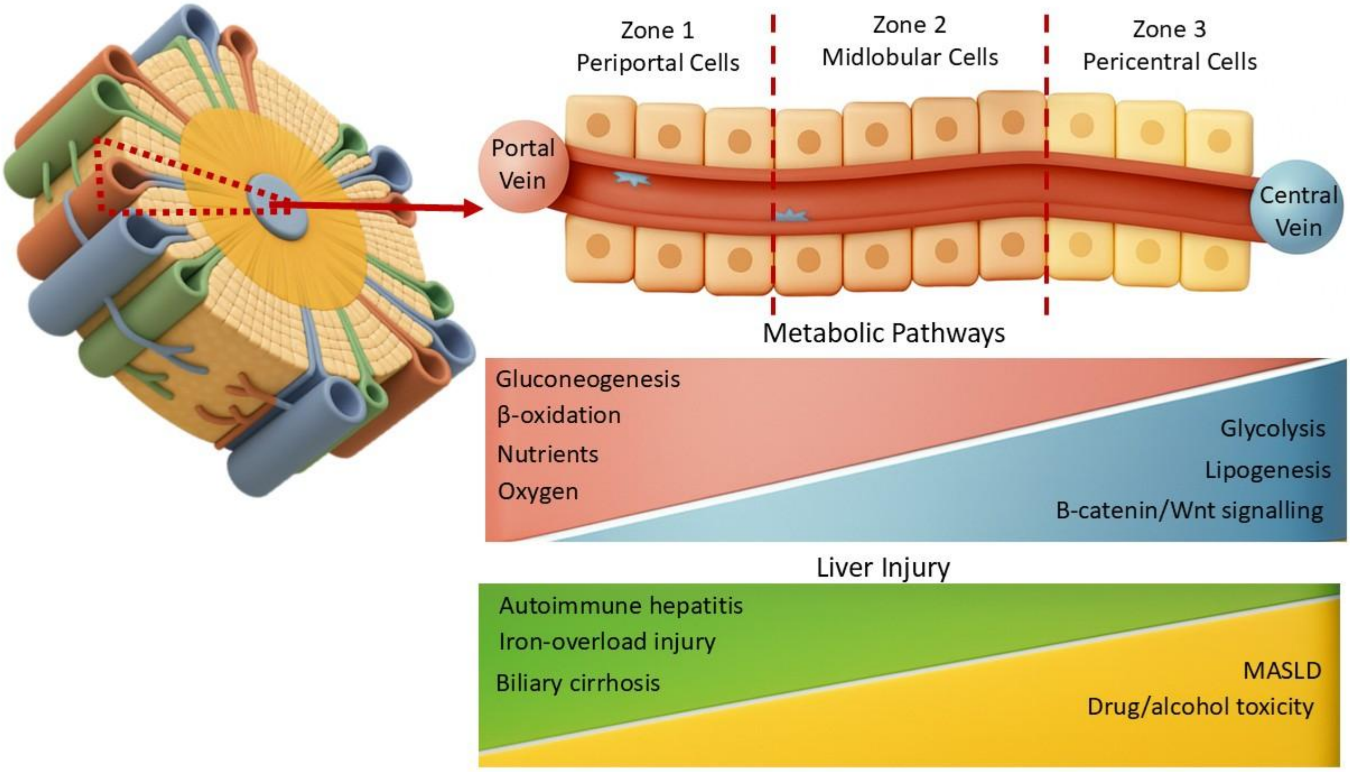

Figure 6. Liver zonation and metabolic compartmentalization. The hepatic lobule exhibits a zonated organization of hepatocytes along the portal–central (porto-central) axis, creating distinct metabolic areas. Zone 1 (periportal cells), located nearest to the portal triads, receives blood rich in oxygen and nutrients and primarily performs gluconeogenesis, β-oxidation, and ureagenesis. Zone 3 (pericentral cells), adjacent to the central vein, operates under lower oxygen tension and specializes in glycolysis, lipogenesis, and xenobiotic metabolism regulated by β-catenin/Wnt signaling. These gradients in oxygen, hormones, and substrates define functional heterogeneity essential for liver homeostasis. The lower panel depicts the zonal susceptibility to injury, showing that periportal regions are more prone to autoimmune and cholestatic damage, while pericentral areas are preferentially affected by MASLD and drug- or alcohol-induced toxicity. Caption and image modified from [11].

1.5 From order to chaos: Disruption of hepatic polarity as a hallmark of HCC

The loss of hepatocyte polarity is a defining hallmark in the initiation and progression of HCC. It is closely intertwined with EMT, wherein hepatic cells downregulated, or polarity regulators have mislocalized. The breakdown of these intercellular junctions facilitates detachment from neighboring cells, loss of epithelial cohesion, and enhanced migratory capacity which hallmarks hepatocarcinogenesis Figure 8 [100].

On the molecular level, the dysregulation of principal cell polarity protein complexes impacts signaling cascades such as Wnt/β-catenin, Hippo, and Notch, influencing cell fate, growth, and proliferation [101, 102] These phenomenon includes EMT, which enables hepatocytes to acquire migratory and invasive properties, followed by the suppression of E-cadherin and induction of mesenchymal markers like N-cadherin and vimentin [100]. Clinically, loss of cell polarity correlates with more aggressive HCC phenotypes, including poor differentiation, vascular invasion, and poor patient survival [103]. Experimental re-establishment of cell polarity complexes has demonstrated partial reversal of EMT and a reduction in tumorigenic potential, suggesting that polarity restoration holds therapeutic promise [104]. Notably, among the cell polarity regulators implicated in HCC, DLG5 emerged as relevant player in hepatocarcinogenesis [105]. DLG5 contributes to the integrity of epithelial polarity by stabilizing intercellular junctions and regulating signal transduction pathways [106]. Thus, DLG5 stands at the intersection of polarity maintenance and tumor suppression, offering a compelling target for further investigation in liver cancer.

At the tissue level, HCC exhibits profound architectural distortion. Tumor cells lose the typical apico–basal orientation and form irregular trabecular, pseudoglandular, or compact solid patterns (Figure 9) [107]. These dedifferentiated cells often display high plasticity and a progenitor-like phenotype, accompanied by disrupted bile canaliculi and distorted sinusoidal networks [108]. Within chronically diseased liver, hepatocytes and hepatic progenitor cells that have lost polarity may acquire self-renewal capacity and oncogenic potential, forming the cellular foundation for malignant clones. Such cells also exhibit increased resistance to apoptosis and immune evasion due to impaired cell–cell and cell–matrix interactions.

Polarity proteins, once regarded merely as structural scaffolds, are now recognized as active regulators of intracellular signaling and transcriptional control. Their loss not only compromises tissue cohesion but also rewires key signaling pathways governing proliferation, differentiation, and survival that ultimately drive hepatocytes toward a malignant phenotype [4, 101]. Thus, polarity loss in HCC represents both a morphologic manifestation of tissue disorganization and a molecular signature of oncogenic reprogramming. The maintenance of epithelial polarity depends on three evolutionarily conserved protein complexes: CRB, PAR, and SCRIB.

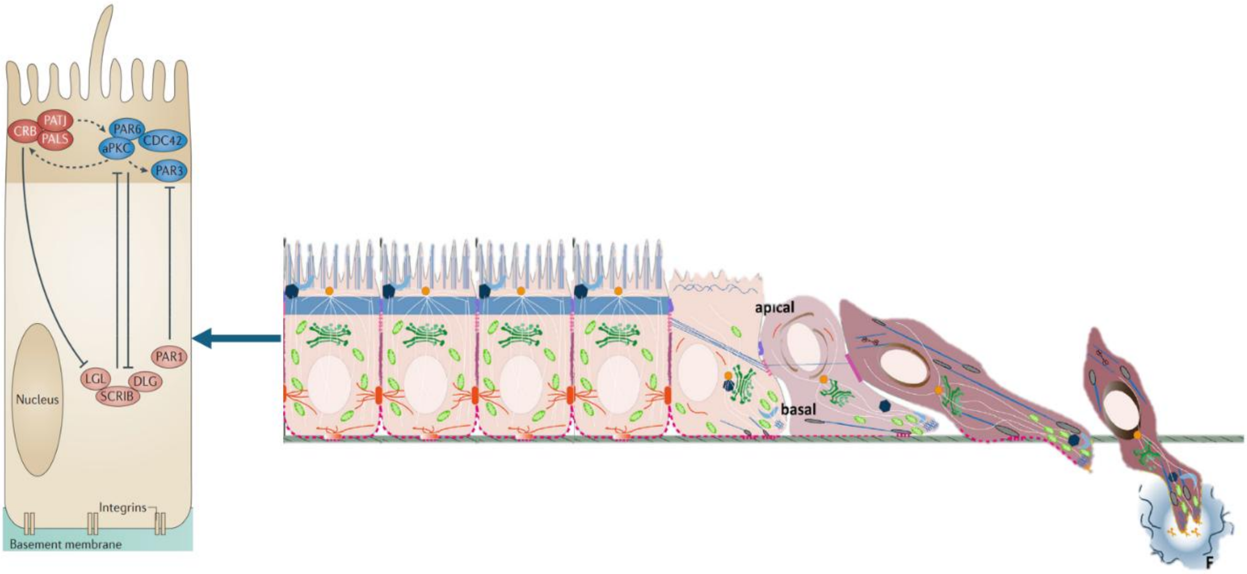

Figure 7. Progressive loss of hepatocyte polarity during the transition to hepatocellular carcinoma. The schematic depicts the morphological continuum from polarized hepatocytes to malignant HCC cells. Normal hepatocytes maintain apical–basal polarity regulated by Crumbs, Par, and Scribble complexes (left). With disease progression, dysplastic cells exhibit disrupted junctional integrity, irregular membranes, and loss of cytoskeletal organization (middle). Fully transformed hepatocytes show nuclear atypia, cytoplasmic disorganization, and invasive protrusions consistent with HCC phenotype. Malignant hepatocytes display nuclear pleomorphism, cytoplasmic abnormalities, and invasive protrusion hallmarks of HCC transformation. Caption and image modified from [2, 4].

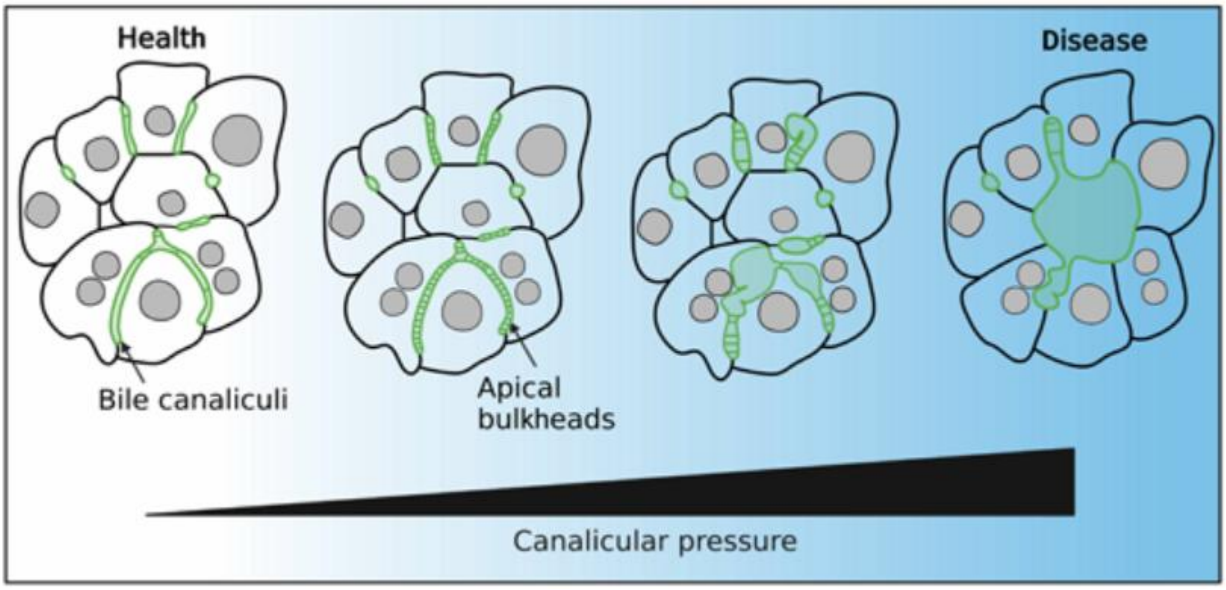

Figure 8. Tissue-level consequences of hepatic polarity loss illustrated through bile canaliculi organization. This schematic depicts the progressive disruption of bile canaliculi architecture as a tissue-level representation of hepatic polarity loss. In healthy liver tissue (left), hepatocytes display organized apico–basal polarity and form continuous, well-defined bile canaliculi that ensure directional bile flow. With increasing canalicular pressure and polarity disruption (middle), canalicular branching and apical bulkheads become irregular, leading to altered luminal continuity. In diseased states (right), the collapse of apical domains results in canalicular dilation, disorganized hepatocyte alignment, and loss of coordinated bile secretion are morphological hallmarks of polarity breakdown observed during chronic liver injury and hepatocarcinogenesis. Caption and image modified from [5].

1.6 Principal molecules in hepatic polarity regulation

Hepatocyte polarity is sustained by a network of specialized molecular complexes and junctional proteins (Figure 10). While the principal polarity complexes such as PAR, Crumbs, and Scribble establish and preserve epithelial architecture, additional scaffold proteins such as DLG5 have emerged as pivotal integrators linking these complexes to cytoskeletal and signaling regulation. Although traditionally less characterized than other polarity components, DLG5 has gained increasing attention for its potential role in maintaining hepatocellular integrity and mediating the crosstalk between polarity disruption and oncogenic transformation.

Par complex, composed of Partitioning-defective 3 (PAR3), Partitioning-defective 6 (PAR6), and atypical protein kinase C (aPKC), is indispensable for apico-basal domain segregation [109]. PAR6 interacts with Cell division cycle 42 (CDC42) to recruit aPKC to the apical cortex, promoting tight-junction formation and cytoskeletal polarization. PAR3 acts as a molecular scaffold linking polarity proteins to microtubules and actin filaments. In HCC, PAR6–aPKC dysregulation enhances TGF-β–Mothers against decapentaplegic homologs 2 and 3 (SMAD2/3) signaling, facilitating EMT and invasive behavior [110]. Loss of PAR3 expression correlates with vascular invasion and poor differentiation, linking junctional disassembly to tumor aggressiveness.

The Crumbs complex is composed of Crumbs homolog 3 (CRB3), Protein associated with Lin-7-1 (PALS1), and PALS1-associated tight junction protein (PATJ) that stabilizes apical identity and collaborates with PAR components during bile-canaliculi morphogenesis [111]. In normal hepatocytes, CRB3 anchors PALS1 and PATJ at tight junctions to restrict basolateral encroachment. CRB3 downregulation in HCC mislocalizes PAR6 and aPKC, leading to apical collapse and activation of PI3K–AKT and Hippo–YAP/TAZ signaling cascade [112]. These alterations reinforce uncontrolled proliferation, demonstrating how structural polarity loss converges with oncogenic signaling.

These complexes, the SCRIB complex comprising Scribble, Discs large homolog 1 (DLG1), and Lethal giant larvae (LGL) defines basolateral identity and functions as a tumor-suppressor module [106]. Scribble anchors E-cadherin and β-catenin at adherens junctions, preserving epithelial cohesion [113]. In HCC, SCRIB loss or cytoplasmic mislocalization leads to E-cadherin downregulation, nuclear β-catenin accumulation, and activation of Wnt-responsive oncogenes [98]. Additionally, SCRIB scaffolds Large tumor suppressor kinases 1 and 2 (LATS1/2) within the Hippo pathway to restrain YAP activity; thus, its depletion drives YAP nuclear localization and proliferative gene expression [114].

Tight junctions act as physical and signaling barriers reinforcing hepatocyte compartmentalization. Zonula Occludens (ZO) proteins particularly ZO-1, ZO-2, and ZO-3 form cytoplasmic scaffolds that connect transmembrane occludins and claudins to actin filaments [115-117]. ZO-1 links to the PAR3–PAR6–aPKC complex, integrating polarity cues with cytoskeletal anchorage [118]. In HCC, ZO-1 delocalization from the junctional belt to the cytoplasm weakens cell adhesion and correlates with enhanced proliferation and invasive potential through MAPK/ERK activation.

Occludins are integral membrane components of tight junctions that regulate paracellular ion flux and intracellular signaling [119-121]. Under normal conditions, occludin interacts with ZO-1 and aPKC to maintain apical junctional integrity [122, 123]. Occludin downregulation or hyperphosphorylation in HCC increases paracellular permeability and activates NF-κB driven inflammatory signaling, thereby a tumor-promoting microenvironment [121].

Claudins, particularly Claudin-1, Claudin-2, and Claudin-3, determine selective permeability of tight junctions [124]. While Claudin-1 generally strengthens epithelial barriers, Claudin-2 upregulation in HCC confers a “leaky” phenotype that facilitates nutrient exchange and tumor growth [125]. Elevated Claudin-2 expression also augments Epidermal growth factor receptor (EGFR)/ERK and β-catenin signaling, supporting proliferation and metabolic adaptation of malignant hepatocytes [125].

At the adherens junction, E-cadherin, α-catenin, and β-catenin, maintain intercellular adhesion and transduce polarity-dependent signals [126]. Under physiological conditions, E-cadherin sequesters β-catenin at the membrane, preventing its nuclear entry. In HCC, E-cadherin repression through promoter methylation or transcriptional inhibitors (Snail, Zinc Finger E-box Binding Homeobox 1 (ZEB1)) liberates β-catenin, enabling nuclear translocation and activation of Wnt/β-catenin target genes (*Axis Inhibitor 2* (*AXIN2), Cyclin D1 (CCND1), Myeloctomatosis Proto-Oncogene Protein (MYC)*) [127]. Mutations in CTNNB1 further stabilize β-catenin, converting it from a structural adaptor to a transcriptional driver of proliferation and dedifferentiation [81].

The transition of β-catenin from a membrane-bound adherens component to a nuclear transcriptional effector exemplifies the molecular intersection between polarity loss and oncogenic reprogramming [128]. This shift destabilizes junctional complexes and highlights the importance of scaffolding proteins particularly DLG5 that anchor β-catenin and E-cadherin at the basolateral membrane [12]. The downregulation or mislocalization of DLG5 disrupts these anchoring interactions, amplifying Hippo–YAP/TAZ, NF-κB, and TGF-β/SMAD signaling [129].

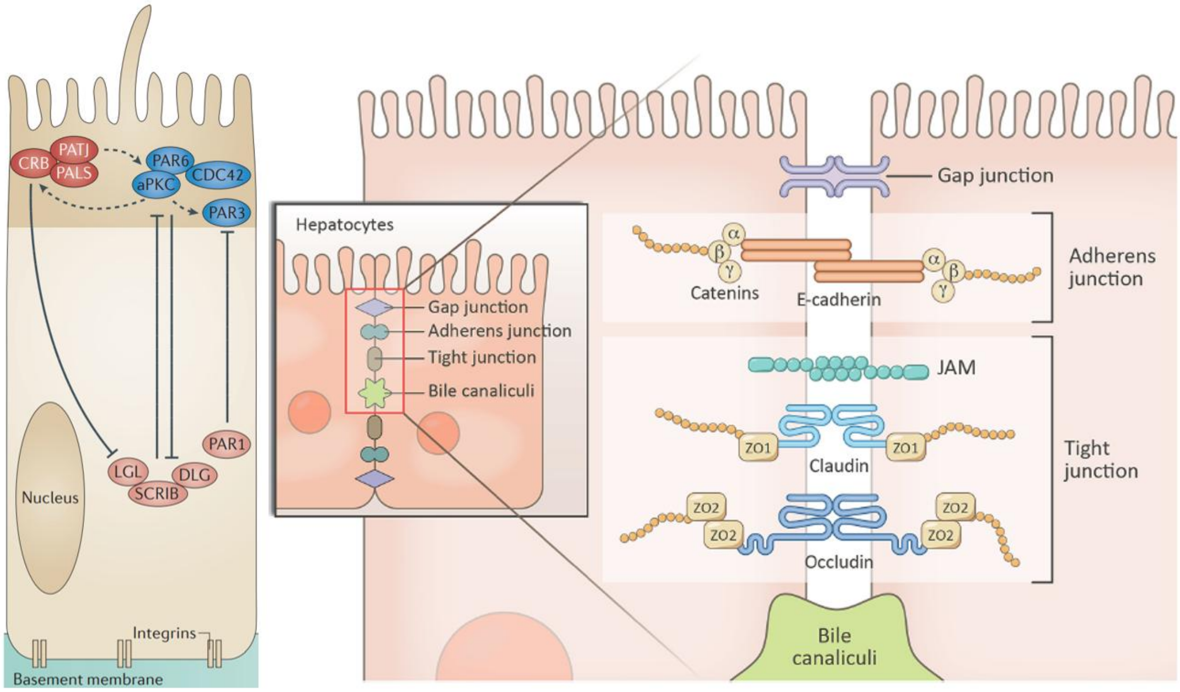

Figure 9. Polarity Protein Complexes. This schematic illustrates the molecular architecture of hepatocyte polarity at the apico–basal interface, emphasizing the bile canalicular region. Hepatocyte polarity is coordinated by three evolutionarily conserved multi-protein assemblies: the Crumbs complex (Crumbs, PALS1, PATJ) defining the apical domain; the PAR complex (PAR3, PAR6, aPKC) localized at the tight junction, linking apical and basolateral territories; and the Scribble complex (SCRIB, DLGs, LGL1/2) that anchors the basolateral membrane and maintains junctional integrity. Together, these complexes establish spatial domain identity and preserve hepatic epithelial organization essential for liver homeostasis. Caption and image modified from [2, 3]

Table 1. Hepatic polarity proteins and its biological function related to HCC

Protein	Complex / Category	UniProt ID (Human)	Principal Biological Function	Role / Alteration in HCC	Reference
PAR3	PAR complex	Q8TEW0	Scaffold protein linking tight junctions to microtubules and actin; defines apical–basal boundary.	Downregulated; loss correlates with poor differentiation and vascular invasion.	[109, 130, 131]
PAR6	PAR complex	Q9NPB6	Adaptor protein binding aPKC and CDC42; regulates tight junction assembly.	enhances TGF-β/SMAD2/3-mediated EMT and migration.	[109, 129, 132-134]
aPKC	PAR complex kinase	P41743	Phosphorylates polarity substrates such as PAR3, LGL; maintains apical identity.	Overactivation drives EMT and cell proliferation via TGF-β and CDC42 signaling.	[109, 132, 134, 135]
CRB3	Crumbs complex	Q5I7T1	Transmembrane apical determinant recruiting PALS1 and PATJ.	Downregulated in HCC; loss activates PI3K/AKT and YAP/TAZ signaling.	[111, 112, 136, 137]
ZO-1	Tight junction scaffold	Q07157	Links occludin/claudins to actin cytoskeleton; maintains barrier integrity.	Mislocalized in HCC; loss enhances ERK/MAPK and proliferation.	[115, 116, 122, 138]
Occludin	Tight junction	Q16625	Transmembrane barrier protein controlling paracellular permeability.	Downregulated; loss activates NF-κB and inflammatory tumor microenvironment.	[119-122]
Claudin-2	Tight junction	O95471	Forms paracellular cation-selective channels; regulates epithelial permeability.	Upregulated in HCC; promotes MAPK and β-catenin activation, metabolic adaptation.	[124, 125, 139, 140]
SCRIB	Scribble complex	Q14160	Basolateral scaffold linking E-cadherin and LATS1/2; tumor suppressor.	Downregulated or cytoplasmic; leads to YAP nuclear activation and EMT.	[98, 141]
DLG1	Scribble complex	Q12959	PDZ scaffold stabilizing adherens junctions and receptor localization.	Loss disrupts basolateral polarity and enhances Wnt/β-catenin signaling.	[98] [98, 106, 142] [106, 142]
CTNNB1	Adherens junction / Wnt pathway	P35222	Links E-cadherin to actin cytoskeleton; transcriptional co-activator when nuclear.	Mutated/stabilized in ~30% of HCCs; drives proliferation via Wnt target gene expression.	[26, 81, 128]
DLG5	Scribble-related scaffold	Q8TDM6	Multi-domain scaffold (PDZ, SH3, GUK) linking E-cadherin/β-catenin to cytoskeleton.	Downregulated or perinuclear in HCC; loss destabilizes junctions and activates YAP, NF-κB, and TGF-β/SMAD signaling.	[12, 105]

1.7 DLG5 as a polarity scaffold at the interface of hepatic homeostasis and carcinogenesis

DLG5 is a multi-domain scaffolding protein encoded by the *DLG5* gene located on chromosome 10q23.1 in humans. It belongs to the MAGUK family, whose members organize spatial signaling by anchoring transmembrane proteins to the cytoskeleton and intracellular signaling networks (Figure 11) [12]. In hepatocytes, DLG5 is predominantly localized to basolateral membranes and pericanalicular regions, where it stabilizes adherens junctions and supports bile canalicular organization. Expression of DLG5 is developmentally regulated and tissue-specific, and its activity is modulated by multiple post-transcriptional mechanisms including phosphorylation, ubiquitination, and microRibonucleic Acid (microRNA) repression [143]. These regulatory layers fine-tune DLG5 abundance and distribution in response to mechanical and biochemical stimuli, rendering it a dynamic polarity sensor.

the *DLG5* gene encodes multiple protein isoforms generated through alternative splicing, each differing in domain composition and potentially in subcellular distribution. Among these, isoform 1 (1919 amino acids; ~214 kDa) represents the predominant, full-length, and most functionally characterized variant. It contains full complement of structural modules: an N-terminal coiled-coil region, four PDZ domains, one SH3 domain, and a C-terminal catalytically inactive GUK domain that collectively confer its scaffolding and polarity-regulating functions. In contrast, isoform 2 (1730 aa) and isoform 3 (1500 aa) lack portions of the N-terminal coiled-coil or C-terminal GUK-like domains, features that may reduce their membrane anchoring capacity or modify interaction specificity with polarity complexes such as SCRIB or PAR3-PAR6-aPKC. These shorter variants have been detected in certain epithelial and neural tissues, where they might fine-tune junctional signaling or adapt MAGUK functions to tissue-specific requirements [12]. In hepatic tissue, however, transcriptomic and proteomic datasets indicate that the full-length canonical isoform predominates, consistent with the high polarity demands of hepatocytes and their complex canalicular architecture. The truncated variants appear either minimally expressed or induced under stress conditions such as inflammation or hypoxia, suggesting that they may arise secondarily during dedifferentiation or malignant transformation. Because isoform 1 uniquely retains all four PDZ domains required for assembling E-cadherin/β-catenin and aPKC polarity complexes, it is most relevant to liver homeostasis and HCC.

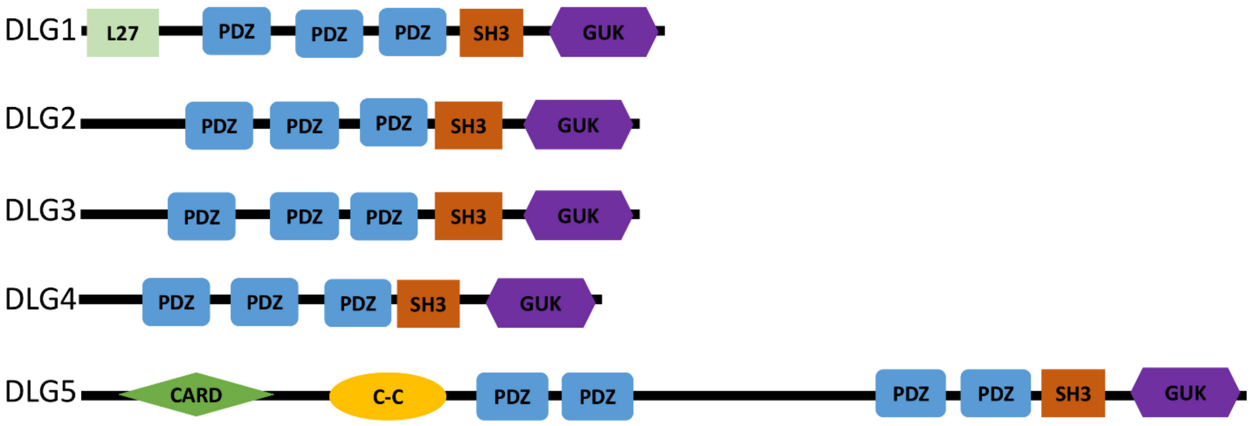

Figure 10. Comparison of domain structure in human DLG family protein. All members of the DLG protein family share a conserved structural architecture comprising multiple PDZ domains, an SH3 domain, and a GUK domain. Among them, DLG5 is uniquely distinguished by an extended N-terminal region that includes a CARD (caspase recruitment domain) and a coiled-coil (C-C) domain, as well as an additional PDZ domain compared to other DLG paralogs. Notably, DLG5 possesses the longest amino acid sequence (1,919 residues), highlighting its distinct structural complexity. Abbreviations: PDZ, post-synaptic density protein 95/discs large/zona occludens; SH3, Src homology 3; GUK, guanylate kinase; C-C, coiled-coil domain Caption and image modified from (5).

Under physiological conditions, DLG5 supports hepatocyte differentiation, suppresses unscheduled proliferation, and facilitates orderly regeneration after injury by maintaining adherens junction integrity and coordinating actin-based vesicular trafficking [144]. Its phosphorylation-dependent mobility ensures compartmentalized signaling and spatial fidelity of hepatic functions such as bile secretion and metabolic zonation [144]. In chronic liver disease, repeated injury and inflammatory stress downregulate or mislocalized DLG5, resulting in junctional disassembly, cytoskeletal disruption, and loss of canalicular polarity. Expression declines progressively from cirrhosis to dysplastic nodules and HCC, with multiple converging mechanisms including aberrant phosphorylation, ubiquitin-mediated degradation, and microRNA-driven silencing contributing to its depletion [12, 143]. Functionally, DLG5 acts as a tumor suppressor by stabilizing polarity complexes and restraining oncogenic signaling [120]. Indeed, its loss promotes EMT, enhances β-catenin nuclear activity, and activates TGF-β, MAPK, and Wnt/β-catenin pathways core mediators of hepatocarcinogenesis [145].

Despite consistent evidence of tumor-suppressive functions, DLG5's role in cancer remains evidence contradictory. In breast and colorectal cancers, its loss correlates with metastasis [12, 105], whereas in pancreatic and glioblastoma models, DLG5 can scaffold β-catenin or Hedgehog effectors to sustain oncogenic signaling. In HCC, expression patterns vary with tumor stage retained in early lesions but cytoplasmic or heterogeneous in advanced tumors suggesting that isoform-specific phosphorylation states or adaptive responses to oxidative stress modulate its function. Previous study showed that DLG5 loss contributes to architectural disarray, canalicular disruption, and aggressive tumor behavior [146].

Beyond structural polarity, DLG5 integrates mechanical and biochemical signals governing mitotic spindle orientation, centrosome stability, and vesicular delivery, all crucial for maintaining genomic integrity [146]. Under oxidative or fibrotic stress, aPKC-mediated hyperphosphorylation and extracellular-matrix–dependent signaling further suppress DLG5, compounding polarity breakdown [12]. In fibrotic liver, increased matrix stiffness and integrin engagement activate aPKC and perpetuate DLG5 repression. In parallel, oncogenic microRNAs such as miR-21 and miR-27, upregulated in HCC, directly target DLG5 transcripts, providing an additional regulatory layer. Collectively, these findings depict DLG5 as a critical polarity regulator vulnerable to both extracellular and intracellular perturbations. Its phosphorylation by aPKC defines a finely tuned equilibrium between epithelial stability and malignant plasticity.

Phosphorylation of DLG5 by aPKC plays a pivotal role in modulating its membrane affinity and spatial recruitment (Figure 12) [12]. The aPKC–PAR3–PAR6 complex acts as a polarity determinant in hepatocytes by establishing the boundary between apical and basolateral domains [147]. DLG5 interacts with aPKC via its coiled-coil and PDZ regions, forming a signaling axis that couples polarity cues with cytoskeletal remodeling [146]. Phosphorylation introduces negatively charged residues within the linker and C-terminal segments of DLG5, altering its electrostatic surface and thereby influencing its association with phospholipids and membrane-anchored complexes [148]. In its unphosphorylated state, DLG5 binds strongly to basolateral E-cadherin–β-catenin assemblies, reinforcing junctional stability. Upon aPKC-mediated phosphorylation, DLG5 undergoes partial detachment from the membrane and transient redistribution into the cytoplasm, enabling cyclical assembly and turnover of junctional complexes during regeneration, growth, and bile canalicular remodeling [12, 149]. Under pathological hyperactivation of aPKC, such as during inflammation or TGF-β stimulation, excessive phosphorylation impairs DLG5 recycling to the membrane, leading to polarity collapse, cytoplasmic sequestration, and β-catenin nuclear translocation. This mechanism mirrors findings in other epithelia where aPKC-driven phosphorylation of MAGUK proteins disrupts tight-junction stability and promotes EMT, underscoring aPKC–DLG5 interplay as a key molecular switch linking reversible polarity modulation to irreversible malignant conversion [12].

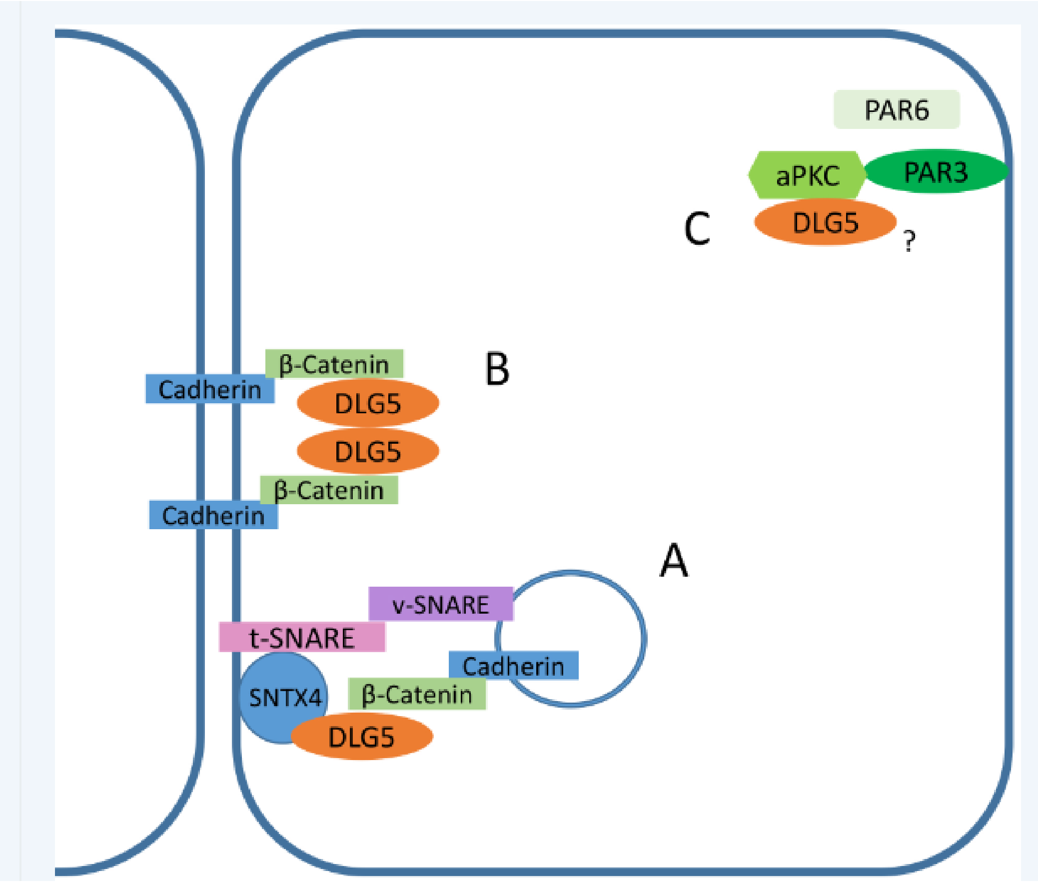

Figure 11. Model of DLG5 interactions with polarity and adhesion complexes. This schematic illustrates the proposed molecular organization and phosphorylation-dependent redistribution of DLG5 in hepatocytes. (A) At the basolateral domain, DLG5 forms a tripartite complex with β-catenin and E-cadherin, promoting adherens junction stability and vesicular trafficking via SNARE proteins. (B) DLG5 anchors β-catenin–cadherin assemblies to maintain basolateral identity. (C) DLG5 interacts with the aPKC–PAR3–PAR6 complex through its coiled-coil and PDZ domains, where aPKC-mediated phosphorylation modulates its membrane association and spatial localization. Excessive phosphorylation under pathological signaling may cause cytoplasmic retention and polarity loss. Caption and image modified from [12].

CHAPTER 2 AIMS OF THE STUDY

Maintenance of hepatocyte polarity is essential for preserving epithelial organization and liver-specific functions such as bile secretion, metabolic regulation, and detoxification. Disruption of this polarity results in loss of tissue architecture and is increasingly recognized as a hallmark in hepatocarcinogenesis. Among polarity-regulating molecules, the scaffolding protein DLG5 has emerged for its role in maintaining epithelial cohesion and junctional signaling. However, its functional role to HCC progression and polarity loss remains poorly defined [12].

2.1 Hypothesis

DLG5 contributes to HCC progression through altered subcellular localization, leading to loss of polarity.

2.3 Objectives

1. Identification of DLG5-interacting proteins involved in polarity regulation and HCC progression.

2. Quantitative determination of DLG5 expression at both mRNA and protein levels in paired HCC and adjacent tissues

3. Evaluate DLG5 localization patterns in paired HCC and adjacent tissues

CHAPTER 3. MATERIAL AND METHODS

3.1 Identification and Ranking of DLG5 Interactors

To construct the protein–protein interaction (PIP) network of DLG5, an integrative approach was applied across four major PIP databases: BioGRID [150], IntAct [151], STRING [9], and Pathway Commons [152]. To ensure data reliability and biological relevance, a manual ranking approach was implemented. The inclusion criteria required that each interactor possess both (i) published evidence supporting the interaction and (ii) experimental validation in prior studies. Entries supported solely by predictive, or text-mining evidence were excluded. Following this manual curation process, DLG5 interactors were selected for analysis. Network visualization was generated using STRING-db.org.

PIP network visualization was generated using STRING (Search Tool for the Retrieval of Interacting Genes/Proteins; https://string-db.org/) under default parameters. The database version 12.0 was used, with Homo sapiens as the selected organism, medium confidence ($score \geq 0.4$), and evidence-based interaction sources including experimental data, curated databases, co-expression, and neighborhood associations. Network edges represent interaction confidence, and unconnected nodes were omitted from visualization.

3.2 *In Silico* Expression, Correlation, and Functional Enrichment Analyses of the DLG5 Network

The *in silico* component of this study integrated three bioinformatics platforms: Genevestigator®, OncoDB, and ENCORI to characterize the transcriptional behavior and functional context of DLG5 and its interactors in HCC. Genevestigator® (Nebion AG, Zürich, Switzerland) was employed to examine differential mRNA expression between HCC and matched adjacent liver tissues. The analysis was performed under the mRNA-Seq Gene Level platform (Homo sapiens, Ensembl 97, GRCh38.p12) using The Cancer Genome Atlas – Liver Hepatocellular Carcinoma (TCGA-LIHC) dataset (study ID HS-01630). The 17-gene panel: *DLG5, SCRIB, LLGL1, CTNNB1, KRAS, CDK1, FZR1, TGFBR1, GSK3B, ESR1, ESR2, NR3C1, RHOB, SORBS3, TPM1, SLC22A4,* and *PGLYRP1* was identified from previous PIP mapping. Filtering was restricted to primary HCC not otherwise stated (NOS) and paired adjacent liver tissues. Expression visualization was performed through the Cancers and Perturbations modules, producing heatmaps that summarized relative gene up- or down-regulation ($\log_2$ intensity).

To evaluate transcriptional relationships among these genes, OncoDB (https://oncodb.org/) was used to calculate pairwise gene-expression correlations within the same TCGA-LIHC cohort. The Correlation module provided Pearson (r) values and p-values. Correlation analyses in OncoDB were performed using the platform's default settings. Pearson correlation coefficients (r) were calculated based on normalized RNA-Seq expression data ($\log_2(TPM+1)$) from the TCGA-LIHC cohort. Statistical significance was determined automatically by the platform ($p < 0.05$). The strength of correlation was interpreted according to standard criteria: strong ($|r| \geq 0.5$), moderate ($|r| = 0.3–0.5$), and weak ($|r| < 0.3$).

ENCORI (The Encyclopedia of RNA Interactomes; https://rnasysu.com/encori/) was employed to validate and expand co-expression relationships observed in OncoDB. The Pan-Cancer Co-expression module was used under default parameters, selecting LIHC as the cancer type. Correlation coefficients between DLG5 and its candidate polarity interactors were obtained from normalized RNA-sequencing datasets. The analysis generated correlation strength, direction (positive or negative), and statistical significance ($p<0.05$).

3.3 Ethics Approval

The study was approved by the Comitato Etico Regionale Unico of Friuli Venezia Giulia, Prot. No. 18854. Informed consent was diligently obtained from each patient or their legal representative, and sensitive data were meticulously protected through anonymization.

3.4 HCC patients used in the study

HCC-patients were predominantly male (n=35), with a mean age of 68.16±10.26 years and a median of 70.90years (interquartile range (IQR): 62.50–75.10). Hemoglobin levels were within the normal range, with a mean of 14.06±1.54 g/dL and a median of 14.10g/dL (IQR: 13.50–15.00) (Table 2). Platelet counts were also within normal limits, averaging $183.8 \pm 94.77 \times 10^3/\mu L$ with a median of $176.0 \times 10^3/\mu L$ (IQR: 115.5–222.5). Liver transaminases showed mild elevation, with

AST 39.58±25.89 U/L and ALT 39.00±30.67 U/L. The corresponding medians were 28.00U/L (IQR: 23.50–44.50) and 26.00U/L (IQR: 18.00–51.00), respectively. Total bilirubin was within limits with a mean of 0.86±0.42 mg/dL and a median of 0.78mg/dL (IQR: 0.56–0.99). Direct bilirubin levels averaged 0.23±0.16mg/dL, with a median of 0.19mg/dL (IQR: 0.14–0.23). Serum albumin was preserved, showing a mean of 4.13±0.50g/dL and a median of 4.15g/dL (IQR: 3.89–4.43). Creatinine levels remained within normal physiological range, with a mean of 0.88±0.22 mg/dL and a median of 0.84mg/dL (IQR: 0.73–0.96) (Table 2).

Histopathological evaluation revealed cirrhosis in 71% (32/45) of patients, while 29% (13/45) showed no cirrhotic changes. The major underlying etiologies included HCV infection 27% (12/45), HBV infection 8% (4/45), alcohol-related liver disease 38% (17/45), and MASH 4% (4/45); mixed etiologies were observed in a subset of cases. Based on Child–Pugh classification, 95.6% (43/45) of patients were categorized as Class A, indicating well-compensated hepatic function, and 4.4% (2/45) were Class B. The BCLC staging system showed, 62.2% (28/45) of the cohort were early stage (A), 22.2% (10/45) intermediate stage (B), and 11.1% (5/45) advanced stage (C). Vascular invasion was absent in 71.1% (32/45), and microscopic invasion in 22.2% (10/45). Fibrosis grading indicated moderate fibrosis in 35.6% (16/45) and severe fibrosis in 60.0% (27/45). According to the AJCC 8th edition TNM classification, 24.4% (11/45) of patients were staged as IB, 13.3% (6/45) as II, 4.4% (2/45) as IIIB, and 2.2% (1/45) as IA, whereas 55.6% (25/45) could not be assessed due to incomplete data or unavailable nodal evaluation (Table 2).

Table 2. Patient Demographics, Liver Function Tests, and Tumor Parameters

Clinical Variables	Male (Mean ± SD)	Female (Mean ± SD)	Combined (Mean ± SD)	Criteria
HCC-Patients (n)	35	10	45	-
Age (years)	69.37 ± 8.5	63.92 ± 14.8	68.16 ± 10.3	≥ 18
Biochemistry (n)				
Hemoglobin (g/dL)	14.10 ± 1.7	13.90 ± 0.9	14.06 ± 1.5	14.0 – 18.0 (M) 12.0 - 16.0 (F)
Platelet Count (10^3/µL)	184.3 ± 99.6	182.0 ± 79.1	183.8 ± 94.77	150 – 350
Aspartate aminotransferase (AST) (U/L)	40.63 ± 26.5	35.90 ± 24.6	39.58 ± 25.9	10 – 30
Alanine Aminotransferase (ALT) (U/L)	40.71 ± 32.6	33.0 ± 22.9	39.0 ± 30.7	10 – 40
Total Bilirubin (mg/dL)	0.88 ± 0.4	0.80 ± 0.5	0.86 ± 0.4	0.3 – 1.2
Direct Bilirubin (mg/dL)	0.24 ± 0.2	0.18 ± 0.2	0.23 ± 0.2	0.1 – 0.3
Albumin (g/dL)	4.16 ± 0.5	4.06 ± 0.5	4.13 ± 0.5	3.5 – 5.0
Creatinine (mg/dL)	0.94 ± 0.2	0.66 ± 0.1	0.88 ± 0.2	0.6 – 1.2
Pathology				
Cirrhosis (n)				
With	25	7	32	-
Without	10	3	13	-
Underlying Liver Disease (n)				
None	4	1	5	-
Hepatitis C Virus (HCV)	7	5	12	-
Hepatitis B Virus (HBV)	3	1	4	-
Alcohol	14	3	17	-
Metabolic dysfunction-associated steatohepatitis (MASH)	2	0	2	-
HCV + Alcohol	2	0	2	-
HBV + Alcohol	1	0	1	-
MASH + Alcohol	1	0	1	-
No data	1	0	1	-
Child-Pugh Classification (n)				
A	35	8	43	Well compensated disease
B	0	2	2	Significant functional compromise
C	0	0	0	Decompensated disease
Barcelona Clinic Liver Cancer (BCLC) Staging System (n)				
A	22	6	28	Early Stage
B	9	1	10	Intermediate Stage
C	4	1	5	Advanced Stage
No data	0	2	2	-
Histology				
Vascular Invasion (n)				
None	23	9	32	-
Micro	10	0	10	-
Macro	0	0	0	-
No Data	2	1	3	-
Fibrosis (n)				
Moderate	12	3	16	-
Severe	22	5	27	-
No Data	1	2	3	-
Tumor Node Metastasis (TNM) Staging of American Joint Committee on Cancer (AJCC 8th) (n)				
IA	1	0	1	-
IB	9	2	11	-
II	5	1	6	-
IIIB	2	0	2	-
Cannot be assessed	18	7	25	-

Forty paired samples were used for mRNA expression profiling, and 13 for immunohistochemistry (IHC). Among the 42 paired samples selected for western blot analysis, 12 pairs provided reliable results. Table 3 summarizes the biochemical and histological characteristics of these subgroups. Age, liver function indices (AST, ALT, bilirubin, albumin, creatinine), and tumor parameters (BCLC stage, vascular invasion, fibrosis) were comparable across groups.

For each patient, regions of the affected liver were collected, including the tumoral and the paired adjacent (non-tumoral) tissue. In the hospital, a uniform protocol was followed for sample collection with specified tissue dimensions, types, and storage conditions. Fresh liver specimens were carefully harvested and preserved either in RNAlater™ stabilization reagent (M7021, Invitrogen™, Waltham, MA, USA) or rapidly frozen in liquid nitrogen, then maintained at −80°C until further analysis. Parallel tissue portions were fixed in formalin, embedded in paraffin blocks, sectioned at 5μm in thickness, and subjected to routine histopathological evaluation. Hematoxylin and eosin (H&E) staining was performed by the diagnostic pathology unit of Azienda Sanitaria Universitaria Giuliano Isontina (ASUGI), Trieste, Italy.

Table 3. Patient Demographics, Liver Disease Profiles Across Experimental Subsets

Clinical Variables	mRNA (Mean ± SD)	WB (Mean ± SD)	IHC (Mean ± SD)	Criteria
HCC-Patients (n)	40/45	42/45	13/45	-
Age (years)	67.85 ± 10.5	67.75 ± 10.5	70.11 ± 5.5	≥ 18
Biochemistry (n)				
Hemoglobin (g/dL)	14.0 ± 1.6	14.03 ± 1.6	13.5 ± 2.1	14.0 – 18.0 (M) 12.0 - 16.0 (F)
Platelet Count (10^3/μL)	185.6 ± 100.3	180.9- ± 97.5	235.0 ± 130.5	150 – 350
Aspartate aminotransferase (AST) (U/L)	41.28 ± 26.8	38.69 ± 25.1	32.62 ± 20.3	10 – 30
Alanine Aminotransferase (ALT) (U/L)	40.65 ± 31.8	38.6 ± 31.0	24.23 ± 12.6	10 – 40
Total Bilirubin (mg/dL)	0.87 ± 0.4	0.87 ± 0.4	0.87 ± 0.6	0.3 – 1.2
Direct Bilirubin (mg/dL)	0.23 ± 0.2	0.23 ± 0.2	0.25 ± 0.2	0.1 – 0.3
Albumin (g/dL)	4.16 ± 0.5	4.14 ± 0.5	4.08 ± 0.3	3.5 – 5.0
Creatinine (mg/dL)	0.87 ± 0.2	0.89 ± 0.2	0.89 ± 0.3	0.6 – 1.2
Pathology				
Cirrhosis (n)				
With	29	29	9	-
Without	11	13	4	-
Underlying Liver Disease (n)				
None	3	5	1	-
Hepatitis C Virus (HCV)	11	11	5	-
Hepatitis B Virus (HBV)	4	3	1	-
Alcohol	15	16	4	-
Metabolic dysfunction-associated steatohepatitis (MASH)	2	2	1	-
HCV + Alcohol	2	2	0	-
HBV + Alcohol	1	1	1	-
MASH + Alcohol	1	1	0	-
No data	1	1	0	-
Child-Pugh Classification (n)				
A	39	40	13	Well compensated disease
B	1	2	0	Significant functional compromise
C	0	0	0	Decompensated disease
Barcelona Clinic Liver Cancer (BCLC) Staging System (n)				
A	28	28	8	Early Stage
B	7	9	2	Intermediate Stage
C	5	3	2	Advanced Stage
No data	-	-	1	-
Histology				
Vascular Invasion (n)				
None	28	32	10	-
Micro	9	8	2	-
Macro	0	0	0	-
No Data	3	2	1	-
Fibrosis (n)				
Moderate	12	14	4	-
Severe	26	25	9	-
No Data	2	3	0	-
Tumor Node Metastasis (TNM) Staging of American Joint Committee on Cancer (AJCC 8th) (n)				
IA	1	1	0	-
IB	9	11	3	-
II	6	4	1	-
IIIB	2	1	0	-
Cannot be assessed	22	25	9	-

3.5 Cell Culture

Two biologically distinct HCC cell lines were used in this study: Japanese Hospital for Hepatology 6 (JHH6) (JCRB1030) and Human hepatoma 7 (Huh7) (JCRB0403), both obtained from the Japan Health Science Research Resources Bank (HSRRB, Tokyo, Japan). These cell lines were selected based on their different morphological and molecular characteristics. JHH6 cells, derived from a 58-year-old Asian female patient, exhibit an undifferentiated, mesenchymal-like morphology and belong to Subtype 1 (S1). They are, characterized by activation of the TGF-β and Wnt signaling pathways [153]. In contrast, Huh7 cells, established from a 57-year-old Asian male, display an epithelial-like/hepatoblast-like phenotype. Huh7 cells are classified as Subtype 2 (S2) and are associated with a progenitor-like transcriptional signature [153].

JHH6 cells were maintained in Williams' E medium, while Huh7 cells were cultured in high-glucose Dulbecco's Modified Eagle Medium (DMEM). Both media were supplemented with 10% (v/v) fetal bovine serum (FBS), 1% L-glutamine (100X), and 1% penicillin-streptomycin (10,000 U/mL penicillin and 10 mg/mL streptomycin). Cell cultures were incubated at 37°C in a humidified atmosphere of 95% air with 5% CO_2. Both cell lines were grown in stock monolayer in a Nunc™ cell culture plastic flask (Thermo Fisher Scientific, Waltham, MA, USA). Cell line identity, morphology, and passage number were regularly monitored to ensure experimental consistency and reproducibility.

3.6 Total RNA extraction from solid tissue samples and cell lines

Total RNA was isolated from human tissues using Tri Reagent® (Sigma–Aldrich, St. Louis, MO, USA), whereas RNA from cultured cell lines was extracted using TriFast™ (EMR517100, Euroclone S.p.A, Milan, Italy), following the protocols provided by each manufacturer. Tissue homogenization was carried out using either a potter–Elvehjem glass homogenizer or ceramic homogenizing beads (1.4 mm, 651 mg/tube, (Omni International, Kennesaw, GA, USA) processed on the Bead Ruptor 4 at maximum speed for 60 seconds. Adherent cell lines were collected using sterile cell scrapers prior to lysis. For all sample types, the standard phenol–chloroform extraction procedure was followed: Chloroform was added to the lysates, followed by isopropanol-mediated RNA precipitation and washing in 75% ethanol. The RNA pellet was air-dried, resuspended in nuclease-free water, and stored at −80°C until use.

The concentration and purity of total RNA were assessed spectrophotometrically using a NanoDrop 2000c micro-volume spectrophotometer (Thermo Fisher Scientific, Waltham, MA, USA). For each measurement, 1μL of RNA eluate was loaded directly onto the measurement pedestal.

Absorbance values were recorded at 260 nm for nucleic acid quantification, and at 280 nm and 230 nm for purity assessment. The instrument automatically calculated RNA concentration (ng/μL) based on the A_{260} reading and the specific RNA extinction coefficient. Purity was evaluated using the A_{260}/A_{280} and A_{260}/A_{230} ratios, with acceptable values ranging between 1.8–2.1 and>1.8, respectively, as indicators of high-quality RNA free from protein or solvent contamination. All RNA samples meeting purity criteria were subsequently stored at –80°C until use.

3.7 Reverse transcription and quantitative real-time PCR

Complementary DNA (cDNA) was synthesized from 1μg of total RNA using the High-Capacity cDNA Reverse Transcription Kit (Applied Biosystems, Waltham, MA, USA), according to the manufacturer's guidelines. The reaction mixture consisted of 10×RT buffer, 25×dNTP mix (100 mM), 10×RT random primers, reverse transcriptase, and nuclease-free water. Reverse transcription was performed in a T100 Thermal Cycler (Bio-Rad, Hercules, CA, USA), using the following thermal profile: 25°C for 25 minutes (primer annealing), 37°C for 120 minutes (cDNA synthesis), and 85°C for 5 minutes (enzyme inactivation). The resulting cDNA was stored at −20°C for downstream applications.

Quantitative Real-Time PCR (RT-qPCR) was performed to determine gene expression levels. Each reaction was prepared in a final volume of 25μL, containing 25ng of SsoAdvanced™ Universal SYBR® Green Supermix (Bio-Rad Laboratories, Hercules, CA, USA), and 250nM of both forward and reverse primers (100nM for the 18S rRNA reference gene). Reactions were assembled in 96-well PCR plates (HSP-9601, Bio-Rad Laboratories, Hercules, CA, USA) and run in technical duplicates to ensure reproducibility.

Amplification was carried out on a CFX Connect™ Real-Time PCR Detection System (Bio-Rad Laboratories, Hercules, CA, USA) using the following cycling conditions: an initial denaturation and polymerase activation step at 95°C for 30 seconds, followed by 50 cycles of denaturation at 95°C for 5 seconds and annealing/extension at 60°C for 20 seconds.

Melting curve analysis was conducted immediately after amplification to verify the specificity of each primer pair and to exclude primer-dimer formation or non-specific amplification. Primer efficiencies were validated by generating standard curves for each target gene. Gene expression levels were quantified using Bio-Rad CFX Maestro v2.2 software (Bio-Rad Laboratories, Hercules, CA, USA), and cycle threshold (Ct) values were averaged from the technical duplicates for each sample. Relative expression values were calculated using the Pfaffl method, a modified ΔΔCt approach that incorporates individual primer efficiencies for more accurate normalization [154]. For normalization, 18S rRNA was used as the reference gene. Expression levels were presented as fold-change values relative to a designated reference sample. (Table 3.4.1) Primer sequences used for qPCR were synthesized by Metabion (Metabion, Planegg, Germany) and were designed using the software Beacon Designer 7.91 (PREMIER Biosoft International, Palo alto, CA USA).

Table 4. Primers

Gene	Accession Number	Forward Primer	Reverse Primer
18S	NR_003286.2	CGTCTGCCCTATCAACTTTCG	GCCTGCTGCCTTCCTTGG
DLG5	NM_004747.2	TACAGCAGGTACTTCACA	TTGTTCTTGATTGACCATTG

3.8 Tissue homogenization and protein extraction

Protein extraction was performed using different homogenization and lysis protocols based on the sample type. Frozen liver tissues from human HCC were homogenized in Tissue Homogenization Buffer (0.25 M sucrose, 9.8 mM K_2HPO_4, 40.2mM KH_2PO_4, 1mM EDTA, and 0.1mM dithiothreitol (DTT); pH 7.4) using 1.4mm ceramic beads in a Bead Ruptor 4 (Omni International, Kennesaw, GA, USA) at full speed for 1 minute.

For cell lines, adherent cultures were detached using trypsin-EDTA, washed twice with ice-cold PBS, and lysed directly in 1×Cell Lysis Buffer (#9803, Cell Signaling Technology, Danvers, MA, USA) while kept on ice for 5 minutes. The lysates were subjected to brief sonication (1 pulse, 15 seconds at 10W) using a UW3100 sonicator (Bandelin Electronics, Berlin, Germany). The homogenates were centrifuged at 14,000×g for 10minutes at 4°C, and supernatants were collected for protein concentration analysis, then stored at −80°C. Protein concentrations were determined using the Bicinchoninic Acid (BCA) Protein Assay Kit (B9643, Sigma-Aldrich, Merck KGaA, Darmstadt, Germany). Absorbance was measured at 562 nm using a PerkinElmer EnSpire® Multimode Plate Reader (PerkinElmer, Waltham, MA, USA).

3.9 Western Blot Analysis

A total of forty-two paired HCC and corresponding adjacent liver tissues were analyzed to assess DLG5 protein expression. Among all processed samples, four pairs exhibited no detectable DLG5 signal, and three pairs showed expression only in the distal tissue. The remaining thirty-five pairs demonstrated variable band clarity and intensity. After applying validation criteria, only twelve tissue pairs were suitable for analysis. Validation required the presence of clear and specific DLG5 bands in both distal and nodular tissues, with consistent vinculin loading controls. Exclusion of other samples was due to weak or ambiguous bands, technical inconsistencies that could affect analytical reliability. Restricting the analysis to twelve validated pairs ensured comparability of DLG5 expression between paired regions. Vinculin (~118 kDa) was used as the loading control.

Cellular and tissue lysates containing 50–80μg of protein were mixed with Laemmli buffer (5×) supplemented with 10% β-mercaptoethanol, then denatured by heating at 95°C for 5 minutes. Prepared samples were electrophoresed on 8% SDS-polyacrylamide gels using a two-phase protocol: an initial 30-minute run at 80V for stacking, followed by 90 minutes at 180V for separation. Proteins were transferred onto polyvinylidene difluoride (PVDF) membranes using a wet-transfer system operated at 100V. The transfer was carried out for 3 hours for DLG5 and 1 hour 30 minutes for Vinculin, in a transfer buffer containing 25mM Tris base, 190mM glycine, and 20% methanol. After transfer, the PVDF membrane was briefly stained with Ponceau S solution to verify protein transfer, while the gel was stained with Coomassie Brilliant Blue to confirm complete protein migration.

To block non-specific binding, PVDF membranes were incubated for 1 hour in either 4% non-fat milk or 4% Bovine Serum Albumin (BSA, Fraction V, PanReac

AppliChem, Monza, Italy), prepared in TBS with 0.1% Tween-20 (TBS-T) (Table 5). Membranes were incubated overnight at 4°C with the respective primary antibodies. Secondary antibody incubation was performed for 2 hours for DLG5 and 1 hour for Vinculin at room temperature (Table 5).

Chemiluminescent signal development was performed using the SuperSignal™ West Pico Plus Chemiluminescent Substrate (Thermo Fisher Scientific, Waltham, MA, USA) for DLG5, and the Immobilon® Classico HRP substrate (WBLUC, Merck Millipore, Darmstadt, Germany) for Vinculin. Membranes were incubated with the substrate for 5 minutes at room temperature. Signals were acquired at high sensitivity using the LI-COR C-Digit® Chemiluminescent Western Blot Scanner (LI-COR Biosciences, Lincoln, NE, USA) with a total exposure time of 12 minutes. Densitometric analysis of protein band intensity was performed using ImageJ software (National Institutes of Health, Bethesda, MD, USA) following standard procedures. Band densities were quantified using the Gel Analysis module, and the integrated density values were normalized to the corresponding Vinculin loading control for each sample.

Table 5. Antibodies used in the study

	Target (kDA)	Antibody ID	Species raised in / Clonality	Source	Methods/ Dilution	Diluent (WB only)
PRIMARY ANTIBODIES	DLG5 (~214)	WH0009231M1	Mouse / monoclonal	Sigma-Aldrich, Merck KGaA, Darmstadt, Germany	WB / IHC: 1:500	4% BSA TBS-0.1%T-20
	DLG5 (~214)	ab86783	Rabbit / polyclonal	Abcam, Cambridge, UK	IF: 1:500	-
	Vinculin (~124)	CSB-PA13779A0Rb	Rabbit / polyclonal	CUSABIO, Houston, TX, USA	WB: 1:1000;	4% BSA TBS-0.1%T-20
	ZO-1 (~220)	61-7300	Rabbit / polyclonal	Invitrogen, Thermo Fisher Scientific, Waltham, MA, USA	IF: 1:500	-
	Claudin-2 (~22)	51-600	Rabbit / polyclonal	Invitrogen, Thermo Fisher Scientific, Waltham, MA, USA	IF: 1:500	-
	Occludin (~59)	71-1500	Rabbit / polyclonal	Invitrogen, Thermo Fisher Scientific, Waltham, MA, USA	IF: 1:500	-
	Na^+/K^+-ATPase (ATP1A1) (~113)	ab7671	Mouse / monoclonal	Abcam, Cambridge, UK	IF: 1:500	-
	CTNNB1 (~88)	CAT-5H10	Mouse / monoclonal	Invitrogen, Thermo Fisher Scientific, Waltham, MA, USA	IF: 1:500	-
SECONDARY ANTIBODIES	-	Anti-Mouse IgG (HRP) P0260	-	Dako, Glostrup, Denmark	WB: 1:2000; IHC: 1:200	-
	-	Anti-Rabbit IgG (HRP) P0448	-	Dako, Glostrup, Denmark	WB: 1:2000; IHC: 1:200	-

3.10 Immunohistochemical Assay

Formalin-fixed, paraffin-embedded liver sections from thirteen individuals were examined for DLG5 expression and localization. Of these, nine paired samples were included in the analysis, while four were excluded due to poor slide quality, uneven coloration, or tissue loss.

For DLG5 immunostaining, tissue sections were first deparaffinized in xylene and rehydrated through a graded ethanol series. Antigen retrieval was carried out in 10mM Tris base buffer, (pH 9.0) containing 1mM EDTA and 0.05% Tween-20 at 98°C for 30 minutes. Following retrieval, sections were cooled to room temperature and treated with 3% hydrogen peroxide for 10 minutes to quench endogenous peroxidase activity prior to blocking and antibody incubation. The VECTASTAIN® Universal Quick HRP Kit (PK-8800, Vector Laboratories, Newark, CA, USA) in combination with the ImmPACT® 3,3′-diaminobenzidine (DAB) Substrate Kit (SK-4105, Vector Laboratories) DAB chromogen (SK-4105) was used for chromogenic detection, following the supplier's instructions. To reduce non-specific binding, slides were blocked with 5% Normal Horse Serum (included in VECTASTAIN® kit) in in PBS for 1 hour in humid chamber. Then, sections were incubated overnight at 4°C with primary antibody (Table 5). Detection was performed using the biotin–streptavidin peroxidase system provided in the VECTASTAIN® kit, sections were incubated in the biotinylated pan-specific universal secondary antibody for 2 hours at room temperature in a humidified chamber, followed by incubation with streptavidin–peroxidase complex for 30 minutes. Chromogenic visualization was achieved using the ImmPACT® DAB substrate for 10 minutes. Sections were then counterstained with hematoxylin, dehydrated through graded ethanol series, and cleared in xylene before mounting with EUKITT® Mounting Medium (Sigma-Aldrich, Merck KGaA, Darmstadt, Germany).

Microscopy images were captured using a Leica DM2000 brightfield microscope equipped with LAS X v3.10.0 Office software (Leica Microsystems GmbH, Wetzlar, Germany), fitted with an N Plan 40×/0.65 dry numerical aperture objective and a Leica DFC490 digital camera. Image acquisition parameters were standardized across all samples, with an exposure time of 6 ms, gain of 1.8, and saturation level of 50. Additional high-definition images were obtained using D-Sight FLUO Combo automated slide scanner (A. Menarini Diagnostics, Firenze, Italy). For quantitative analysis, 10 fields from both tumoral and adjacent regions were taken from paired 10 samples of 9 HCC-patients. All images used and presented are as acquired and were subsequently evaluated by a board-certified anatomical pathologist affiliated with Azienda Sanitaria Universitaria Giuliano Isontina (ASUGI).

3.11 Manual classification of DLG5 Immunostaining patterns

For quantitative analysis, ten representative fields from both 10 paired HCC and adjacent regions were captured. All images were used for manual counting and evaluation of DLG5 immunostaining. DLG5 immunohistochemical staining patterns were evaluated by using a hybrid approach of nuclei detection via QuPath (version

0.6.0) (University of Edinburgh, Edinburgh, UK) with manual classification of DAB staining patterns [155]. Microscopy images in Tagged Image File Format (TIF) were imported in the software, and tissue regions were annotated for subsequent analysis. The Positive Cell Detection module automatically identified cell nuclei based on hematoxylin staining and applied an optical density threshold to segment individual cells, classifying them as DAB-positive or DAB-negative according to their staining pattern.

The DLG5 localization patterns were classified by manual visual assessment based on the distribution of brown chromogen (DAB). Three distinct DAB staining patterns were defined: Submembranous (Pattern 1): dotted staining localized along the inner plasma membrane. Cytoplasmic (Pattern 2): Dotted or punctate staining distributed within the cytoplasm without clear compartmental enrichment. Cytoplasmic/Perinuclear (Pattern 3): Diffused or dotted signal encircling the nucleus, forming a ring-like or clustered pattern in the perinuclear region. Unclassifiable patterns: Indeterminate staining, artifacts, or ambiguous localization. These events were recorded but excluded from quantitative graphical analyses due to unreliable designation to a specific subcellular compartment. This classification system was applied uniformly to both HCC (tumoral) and adjacent (non-tumoral) tissues across the IHC patient cohort (Figure 12).

Each field was subdivided into a 3×3 grid, yielding nine regions per field (Figure 13). Subcellular compartment counts were summed across all grid regions within each field, and the resulting field-level values were averaged across the ten fields to generate a mean value per sample.

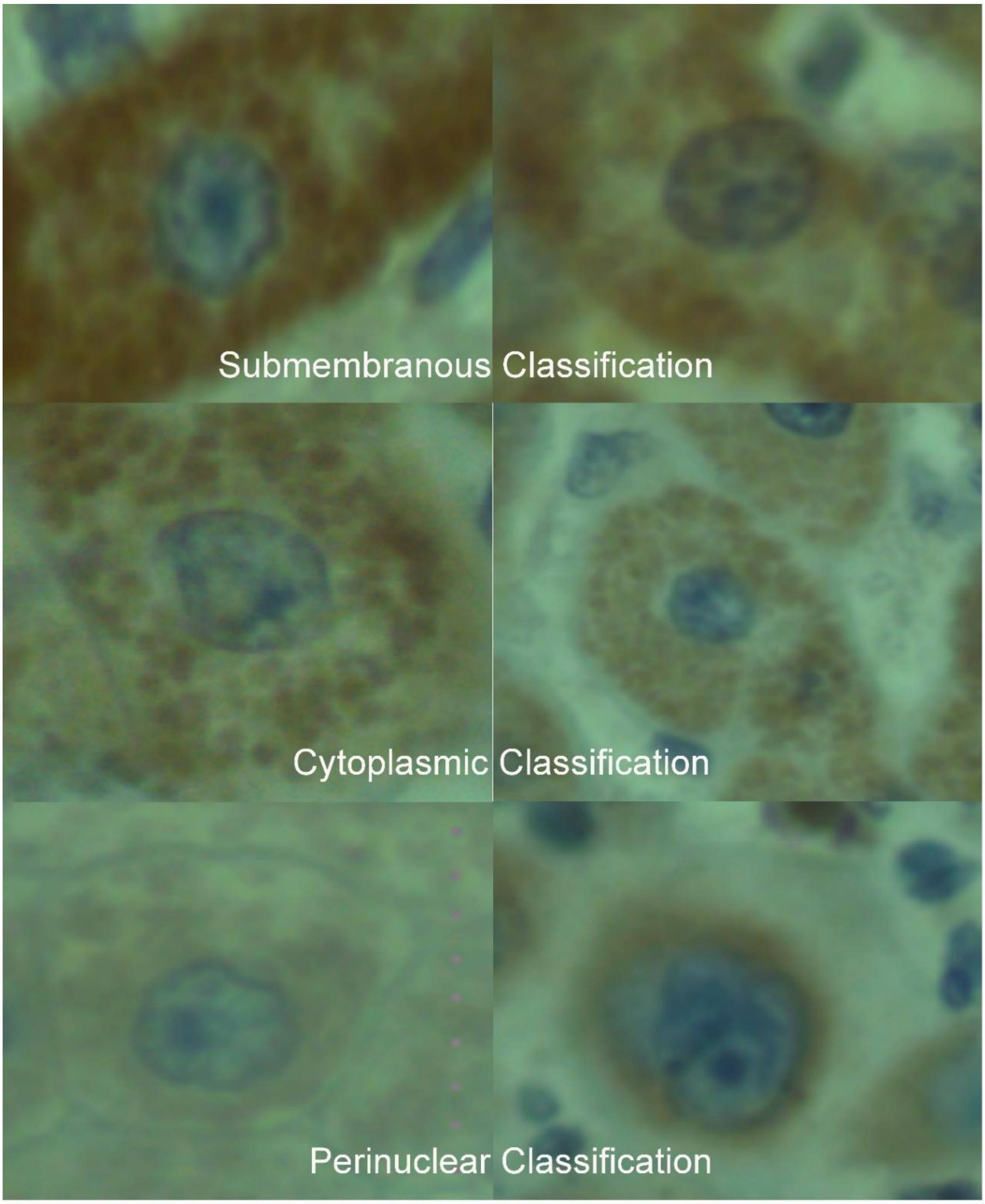

Figure 12. Representative DLG5 localization patterns used for manual visual classification. Representative images showing the three major DLG5 staining patterns identified through manual visual assessment: submembranous, cytoplasmic, and perinuclear classifications. These reference categories were used as visual standards for manual counting.

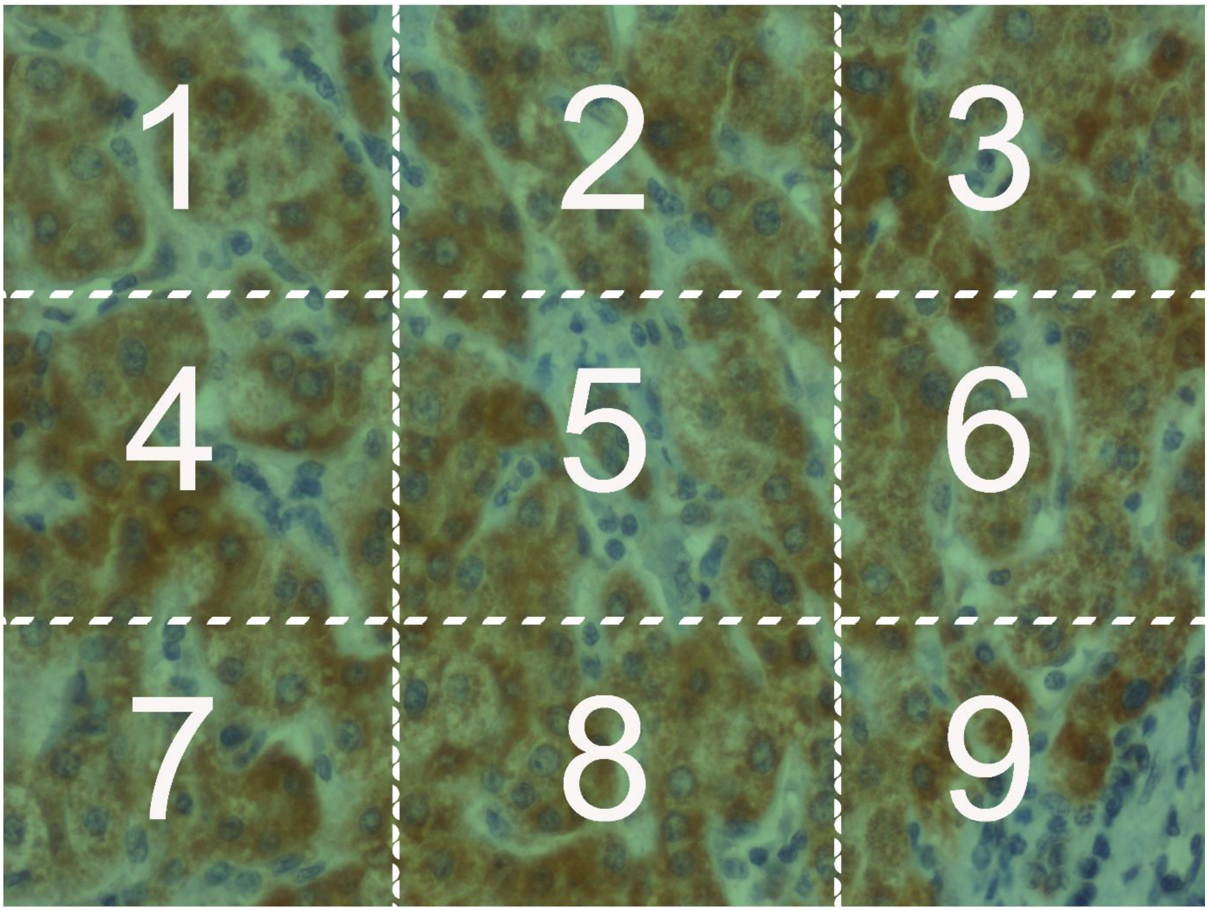

Figure 13. Representative IHC image illustrating the 3×3 grid subdivision approach. Each representative images (field) were partitioned into nine equal grid regions, to facilitate manual quantification of DLG5 subcellular localization patterns. Grid-level counts were integrated at the field level, and field-level measurements were combined across ten independent fields to derive mean values per sample.

3.12 Mean intensity and binary measurement of DLG5 in ImageJ

To minimize observer bias in the assessment of DLG5 expression, staining intensity was objectively quantified using ImageJ software (NIH, Bethesda, MD, USA) [156]. High-resolution brightfield images, similarly, obtained from IHC analysis, were used for quantitative assessment. A total of 10 representative fields were selected from 3 paired tumoral and adjacent tissue samples. Both channels were then converted into 8-bit grayscale format to ensure consistent processing. The grayscale DAB image underwent a thresholding process to distinguish positively stained regions from the background, resulting in a binary mask where DAB-positive areas were represented by white pixels (value = 255) and unstained regions by black pixels (value = 0).

To improve quantification accuracy, the binary mask was multiplied by the original grayscale DAB image using the Image Calculator function. This generated a masked grayscale image that retained intensity values only within DAB-positive regions while removing background noise. Quantitative parameters were extracted from this image using the Analyze Particles and Measure tools, including Integrated Density (sum of pixel intensities within the positive area), Mean Gray Value (average pixel intensity), and Area (total count of positive pixels). To standardize DLG5 expression levels across samples, a DAB Intensity from binary measurement was computed using the following formula:

$$DAB\ Intensity\ from\ binary = \frac{Integrated\ intensity}{Positive\ Area\ (in\ pixels)}$$

3.13 Mean intensity and binary measurement of DLG5 subcellular localization in CellProfiler

Two independent image analysis pipeline were developed in CellProfiler (version 4.2.8) (Broad Institute of Massachusetts Institute of Technology and Harvard, Cambridge, MA, USA) to objectively quantify DLG5 expression across defined subcellular compartments [157]. The first pipeline was designed to quantify the mean DLG5 intensity and to classify submembranous, cytoplasmic, and perinuclear compartments into low, medium, and high intensity categories. The second pipeline quantified binary values, from which localization indices were calculated to assess DLG5 redistribution across cellular compartments.

In both workflows, brightfield IHC images were subjected to color deconvolution to isolate DAB (DLG5) and hematoxylin (nuclear) channels, followed by automated object segmentation into nuclei, cytoplasm, perinuclear zones and membrane. Masks for submembranous, cytoplasmic, and perinuclear compartments were defined algorithmically in defined in CellProfiler, allowing for minimal boundary overlap between adjacent regions. For standardized comparison of DLG5 staining strength, DAB intensity values were categorized into low (0.00–0.55), medium (0.56–0.79), and high (0.80–1.00) categories (Table 6). Mean intensity and integrated DAB measurements were extracted for each compartment, and mathematical ratios were computed to generate localization indices. Each pipeline run required approximately five minutes per field, depending on image resolution and segmentation complexity. Measurements of nuclei were performed per field, ensuring consistent sampling across tissue regions. Final outputs from both pipelines were manually verified by visual inspection to ensure accurate segmentation and measurement consistency. The detailed CellProfiler pipelines, modules, and outputs are provided in Appendix A (Mean Intensity Pipeline) and Appendix B (Binary Analysis Pipeline).

Table 6. Classification of DLG5 in DAB staining intensity across subcellular compartments

Intensity Category	[1]Cut-off Value	Interpretation
Low	0.0 – 0.55	DAB background to weak DLG5 staining, corresponding to minimal or diffused signal
Medium	0.56 – 0.79	Intermediate to strong DLG5 staining, corresponding to moderate signal abundance
High	0.80 – 1.0	Very strong DLG5 staining, corresponding to pronounced accumulation of signal

NOTE:
1 Cut-off values were determined based on visual comparison of staining intensities across representative images and were applied uniformly across all samples and subcellular compartments. Normalized intensity values ranging from 0 to 1 were generated by the CellProfiler algorithm, which rescales raw DAB intensity measurements to a standardized unitless range for comparative analysis.

3.14 Immunofluorescence Assay

JHH6 and Huh7 cells were seeded at densities of 25,000 cells/cm² and 55,000 cells/cm², respectively, on sterile square glass coverslips placed in 6-well Nunc™ culture plates (Thermo Fisher Scientific, Waltham, MA, USA) and allowed to reach 100% confluence prior to fixation. The cells were fixed with 3% paraformaldehyde

(PFA) in PBS for 30 minutes at room temperature, followed by permeabilization with 0.1% Triton X-100 (v/v in PBS) for 5 minutes. To reduce nonspecific binding, cells were then incubated for 1 hour in a blocking solution containing 1% BSA and 5% normal goat serum (NGS; G9023, Sigma-Aldrich, Merck KGaA, Darmstadt, Germany) prepared in PBS.

Primary antibody incubation was carried out in a humidified chamber overnight at 4 °C (Table 5). After incubation, the coverslips were transferred back to their wells and incubated with the secondary antibody for 1 hour at room temperature in the dark. A negative control was prepared in parallel using the same procedure without primary antibody to evaluate background fluorescence. Following secondary antibody incubation, the cells were counterstained with Hoechst 33258 (1:5000 in PBS) for 10 minutes at room temperature, protected from light (Table 7). The coverslips were rinsed with PBS and distilled water, then air-dried, mounted and sealed with nail polish.

Fluorescence microscopy images were captured using a manual Leica DM2000 microscope equipped with LAS X v3.10.0 Office software (Leica Microsystems GmbH, Wetzlar, Germany), fitted with an N Plan 40×/0.65 dry numerical aperture objective and a Leica DFC490 digital camera. Image acquisition parameters were manually optimized and standardized across all samples. The 4′,6-diamidino-2-phenylindole (DAPI) filter was set to an exposure of 50 ms, gain of 7.1, and saturation level of 23; the Fluorescein Isothiocyanate (FITC) filter was set to an exposure of 747.77 ms, gain of 7.1, and saturation level of 23; and the Tetramethylrhodamine Isothiocyanate (TRITC) filter was set to an exposure of 899.93 ms, gain of 7.1, and saturation level of 23. Immunofluorescence images were used for qualitative analysis only. Brightness and contrast were adjusted uniformly across all channels and merged.

Table 7. Fluorescent Conjugates used in the study

Conjugate	ID	Species	Fluorophore	Excitation (nm)	Emission (nm)	Dilution
[1]Hoechst	33258	-	-	350	461	1:5000
[2]Anti-Mouse IgG	A21202	Donkey	Alexa Fluor 488	495	519	1:1000
[2]Anti-Rabbit IgG	A11008	Goat	Alexa Fluor 488	495	519	1:1000
[2]Anti-Mouse IgG	A10036	Donkey	Alexa Fluor 546	590	617	1:1000
[2]Anti-Rabbit IgG	A10040	Donkey	Alexa Fluor 546	590	617	1:1000

NOTE:
1 Merck KGaA, Darmstadt, Germany
2 Invitrogen, Thermo Fisher Scientific, Waltham, MA, USA

3.15 *DLG5* Gene Silencing

To downregulate DLG5 gene expression, small interfering RNA (siRNA)–mediated gene-silencing experiments were performed. A pre-designed siRNA specific to DLG5 (Silencer® Pre-designed siRNA, ID: s17650, Cat. No. 4392420; Ambion™, Thermo Fisher Scientific, Waltham, MA, USA) was used. A non-targeting control siRNA (Silencer® Select Negative Control No.2 siRNA, AM4613; Invitrogen™, Thermo Fisher Scientific, Waltham, MA, USA) served as the negative control. All siRNA oligonucleotides were reconstituted in nuclease-free water and applied at a final concentration of 5nM for siDLG5 transfection.

Transfections were performed using siLentFect™ Lipid Reagent (170-3362, Bio-Rad Laboratories, Hercules, CA, USA) according to the manufacturer's instructions, at a final dilution of 0.1% in culture medium. JHH6 and Huh7 cells were seeded at a density of 6,000 cells/cm² in 6-well Nunc™ culture plates (Thermo Fisher Scientific, Waltham, MA, USA) for treatment experiments, and at 4,000 cells/cm² for untreated control conditions. After 24 hours, the medium was replaced with freshly prepared antibiotic-free medium, and cells were pre-incubated for 1 hour. Transfection complexes were prepared by incubating the respective siRNA with siLentFect in serum- and antibiotic-free medium for 30 minutes at room temperature. The complexes were then added dropwise to the culture wells. After 24-hour incubation period, the medium was replaced with fresh complete culture medium. The impact of gene knockdown was assessed at 48 hours post-transfection.

3.16 Statistical Analysis

All statistical analyses and graph generation were performed using GraphPad Prism software, version 8.0 (GraphPad Software, San Diego, CA, USA). Statistical significance was defined as *P*<0.05, with significance levels denoted as **P*<0.05, ***P*<0.01, and ****P*<0.001.

Descriptive statistics were used to summarize clinical and experimental data and are reported as mean ± standard deviation (SD) for normally distributed variables, or as median with interquartile range (IQR) for non-normally distributed variables. Where appropriate, data are additionally presented as mean with 95% confidence intervals (CI). Graphical representations display values as mean ± SD, unless otherwise stated.

Data normality was assessed using the Shapiro–Wilk test. As several parameters deviated from a normal distribution, non-parametric statistical tests were applied. Paired comparisons between HCC and adjacent tissues were analyzed using the Wilcoxon signed-rank test. For comparisons involving more than two groups, the Kruskal–Wallis test was employed, followed by appropriate post hoc analyses when required.

CHAPTER 4. RESULTS

4.1 Identification of DLG5-associated protein networks in HCC

This section aimed to identify DLG5-associated protein interactors in HCC using *in silico* network analysis. Table 8 lists DLG5 interactors, while Table 9 presents the essential STRING confidence values supporting DLG5 protein network, Figure 14 strong associations with polarity proteins such as SCRIB, LLGL1, and CTNNB1. Enrichment maps showed overrepresented categories related to cell polarity, cytoskeletal organization, and Wnt/β-catenin signaling (Figure 15).

Figure 16 shows the Genevestigator transcriptomic profile of *DLG5* and its interactors in HCC and adjacent tissues to validate the STRING network at the expression level. The analysis revealed an upregulation of DLG5 and several polarity-associated genes, including CTNNB1 and SCRIB, in HCC samples. The complete heatmap output is provided in Appendix C.

Table 10 derived from OncoDB, was performed to validate the transcriptional relationships among *DLG5* and its interactors using TCGA-LIHC data. This correlation analysis confirmed moderate to strong positive associations, particularly with *CTNNB1, SCRIB,* and *LLGL1*. Table 11 and Figure 17 from ENCORI were employed to examine co-expression patterns based on independent experimental datasets, all consistently indicate that DLG5 is functionally linked with polarity and signaling regulators in HCC.

Table 8. DLG5 and its protein interactors

Name	UniProt ID	Full Protein Name	Node Color
DLG5	Q8TDM6	Discs large homolog 5	● Red
CTNNB1	P35222	Catenin beta-1	● Emerald
SCRIB	Q14160	Protein scribble homolog	● Yellow
LLGL1	Q15334	Lethal(2) giant larvae protein homolog 1	◍ Brown
SORBS3	O60504	Sorbin and SH3 domain-containing protein 1	◍ Light Green
TPM1	P09493	Tropomyosin alpha-1 chain	◍ Mint Green
PGLYRP1	Q96PD5	Peptidoglycan recognition protein 1	◍ Aqua Blue
SLC22A4	Q9H015	Solute carrier family 22 member 4	◍ Sky Blue
GSK3B	P49841	Glycogen synthase kinase 3 beta	◍ Navy Blue
CDK1	P06493	Cyclin-dependent kinase 1	▨ Violet
ESR1	P03372	Estrogen receptor alpha	◍ Old Rose
ESR2	Q92731	Estrogen receptor beta	◍ Tan
TGFBR1	P36897	Transforming growth factor-beta receptor type-1	◍ Light Brown
KRAS	P01116	Kirsten Rat Sarcoma Viral Oncogene Homolog	▨ Gold
NR3C1	P04150	Glucocorticoid receptor	◍ Yellow Green
RHOB	P62745	Rho-related GTP-binding protein	● Apple Green
FZR1	Q9UM11	Fizzy-related protein homolog 1	◍ Jade Green

Each node represents a protein and node colors are automatically assigned by STRING for visualization purposes; it does not correspond to expression levels. The red node indicates the query protein DLG5; while light blue, yellow green, emerald, light brown, tan, orange, apple green nodes represent direct interactors (first shell). other colors represent second to third shell.

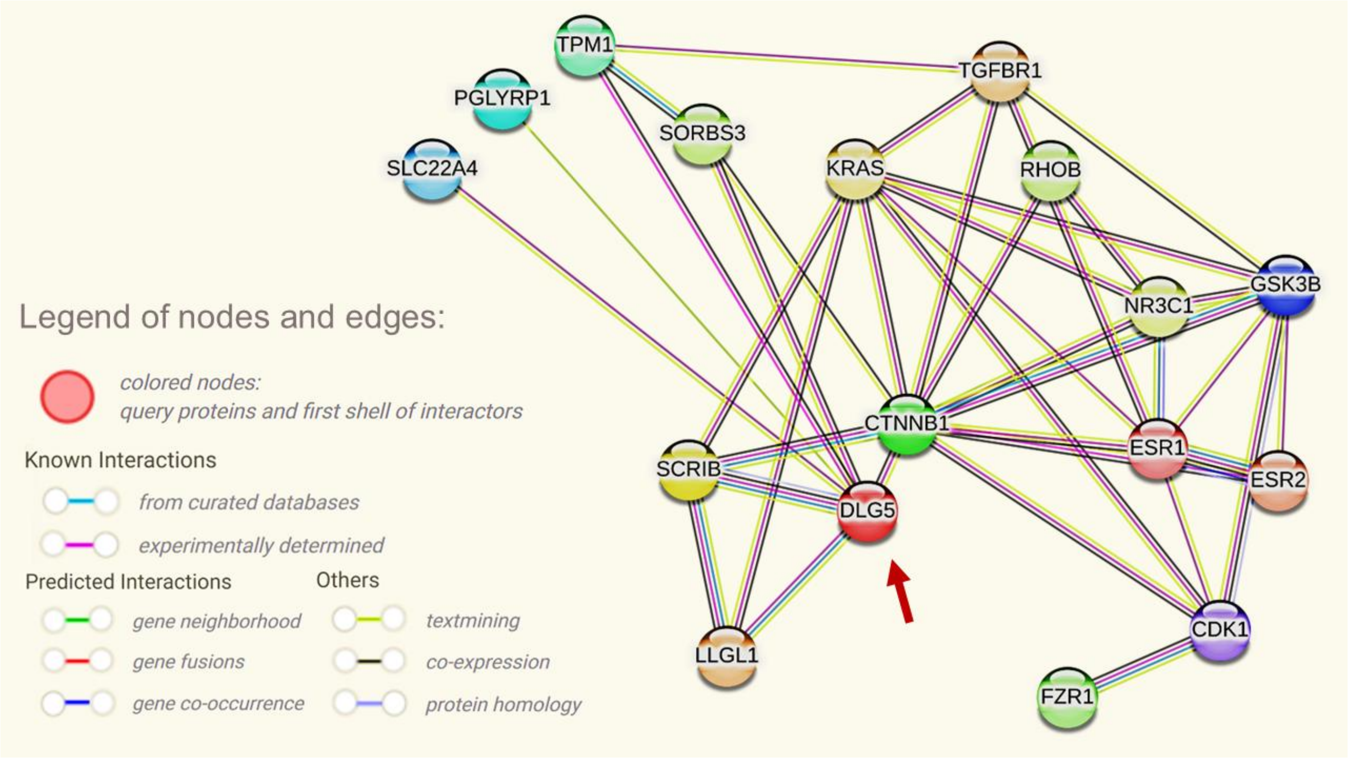

Figure 14. Protein-protein interaction network of DLG5 and its associated interactors. The network illustrates DLG5 (red arrow) and its 16 identified interactors from a combination of experimentally validated, database-curated, and data-mining evidence. These mixed-evidence connections show that DLG5 is linked to polarity-related scaffolds (SCRIB, LLGL1), cytoskeletal components (SORBS3, TPM1), and signaling regulators (CTNNB1, GSK3B, KRAS, TGFBR1, ESR1/2). Notably, DLG5 is directly linked to CTNNB1 and to the core polarity scaffolds SCRIB and LLGL1, placing DLG5 within a network associated with junctional organization and epithelial polarity. The colored edges represent the type of supporting interaction evidence: curated databases (light blue), experimental data (pink), predicted associations based on gene neighborhood (green), gene fusion (red), and gene co-occurrence (dark blue) analyses. Additional evidence is provided by text mining (yellow), co-expression (black), and protein homology (lavender). Image adapted from STRING database [9].

Table 9. Function and confidence levels of DLG5 protein interactors from STRING analysis

Node 1	Node 2 (Interactor)	Description of Interactor (Node 2)	Combined Score	Confidence Level
DLG5	CTNNB1	Catenin beta-1; key downstream component of Wnt signaling and cell adhesion.	0.746	High
DLG5	LLGL1	Lethal(2) giant larvae protein homolog 1; involved in cell polarity and asymmetric cell division.	0.841	Very High
DLG5	SCRIB	Protein scribble homolog; scaffold protein in basolateral polarity complex.	0.907	Very High
DLG5	PGLYRP1	Peptidoglycan recognition protein 1; pattern recognition receptor involved in innate immunity.	0.656	Moderate
DLG5	SLC22A4	Solute carrier family 22 member 4; sodium-dependent organic cation transporter.	0.656	Moderate
DLG5	SORBS3	Vinexin alpha; adaptor protein promoting actin cytoskeleton organization.	0.934	Very High
DLG5	TPM1	Tropomyosin alpha-1 chain; binds actin filaments and regulates cytoskeletal stability.	0.472	Low

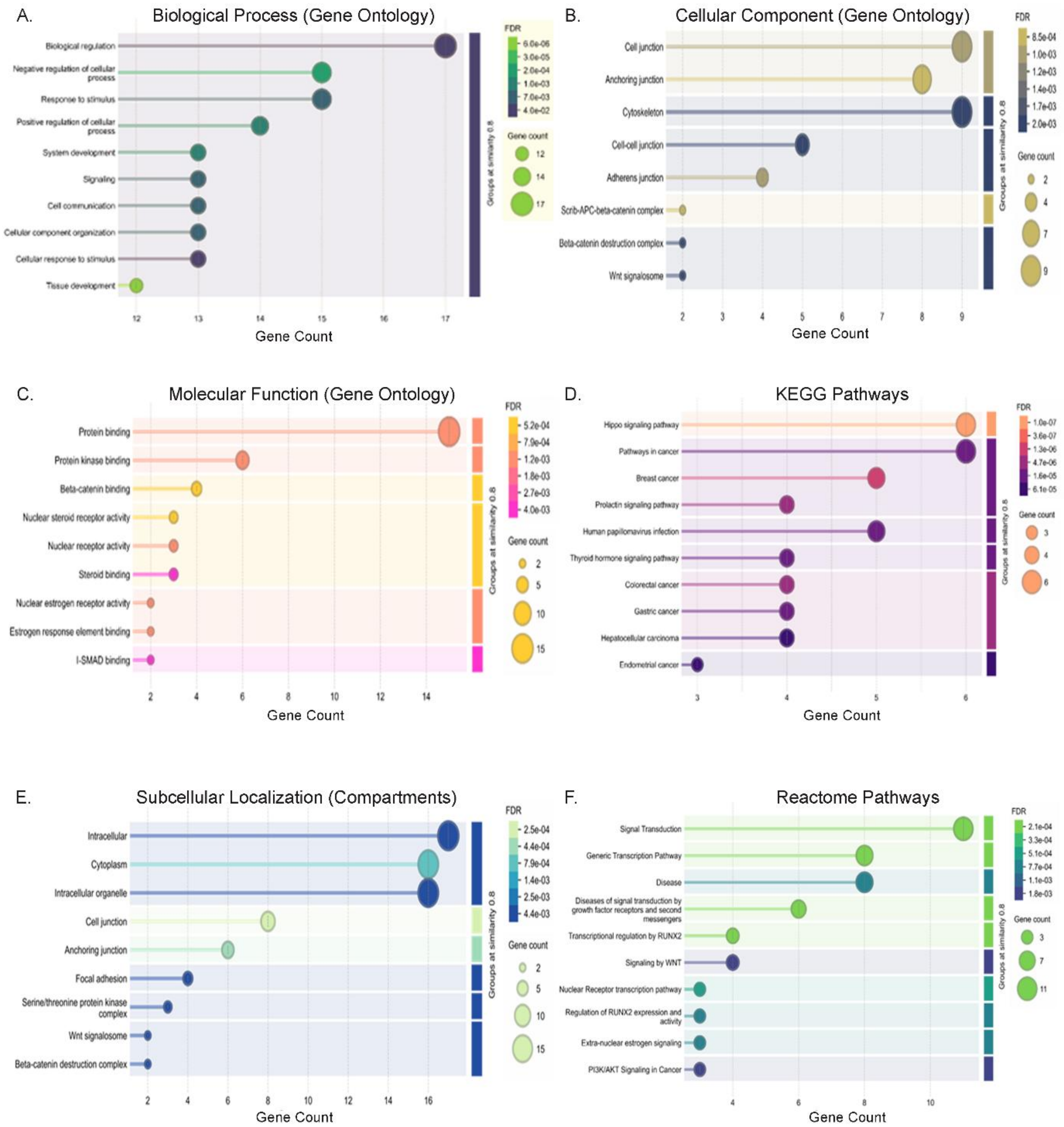

Figure 15. Functional Enrichment Analysis of DLG5 protein interactors by STRING. The network-derived protein set was analyzed for overrepresented categories. (A–C) Gene Ontology (GO) enrichment revealed terms under Biological Process, Cellular Component, and Molecular Function, highlighting DLG5 involvement in cell junction organization, cytoskeletal regulation, and β-catenin/Wnt signaling. (D) KEGG pathway enrichment demonstrated associations with hepatocellular carcinoma, Hippo, and PI3K–Akt signaling pathways. (E) Subcellular localization mapping indicated enrichment within intracellular and junctional compartments, consistent with DLG5's scaffold function. (F) Reactome pathway analysis further confirmed enrichment in signaling by Wnt and transcriptional regulation. STRING operates using

protein identifiers (UniProt accessions), however the software conventionally labels enriched term frequency as “gene count”, referring to the number of proteins annotated to each category. Circle size corresponds to the number of enriched terms, and the color gradient represents the adjusted significance level (FDR). Image by [9].

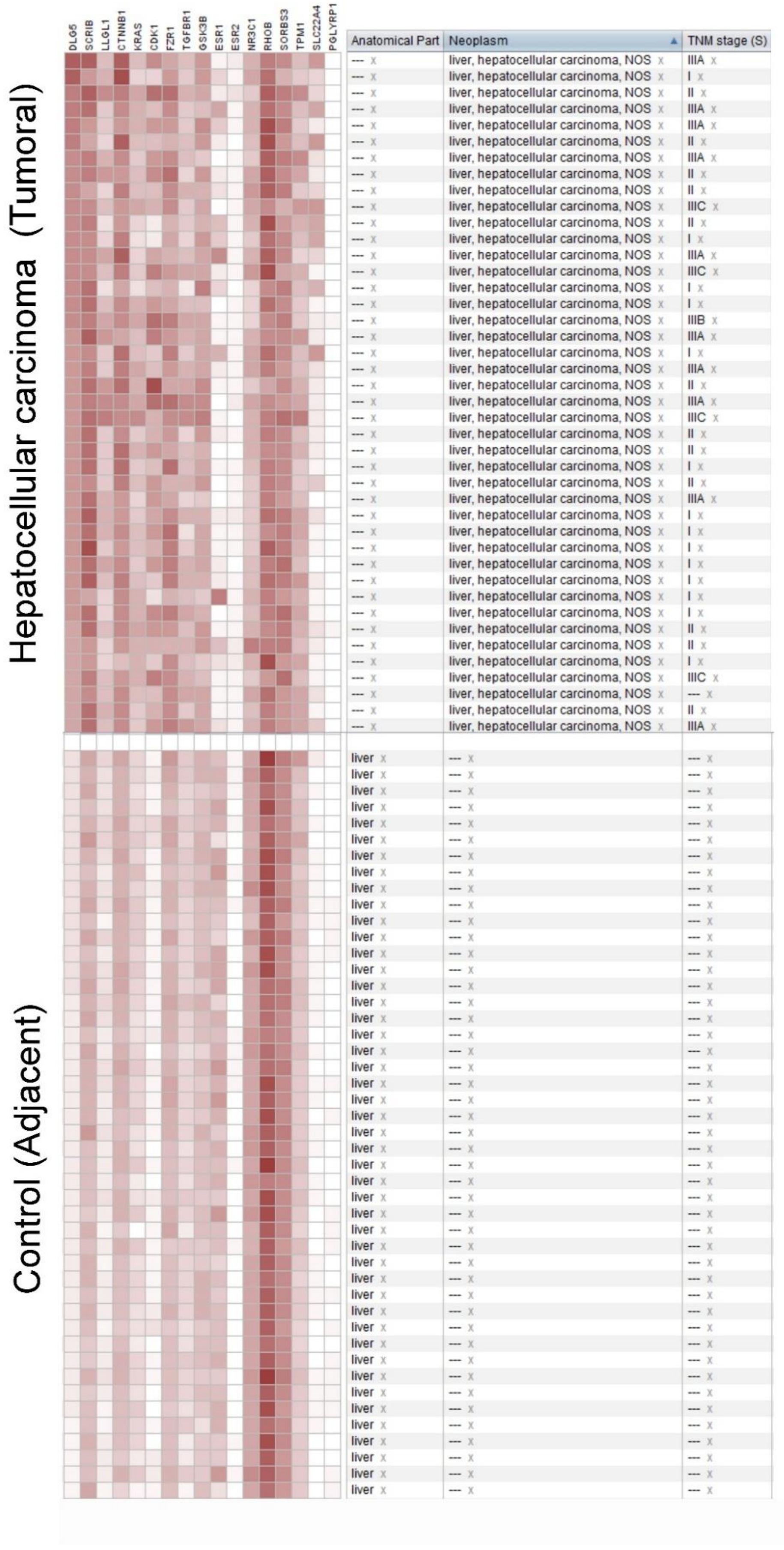

Anatomical Part	Neoplasm	TNM stage (S)
---	liver, hepatocellular carcinoma, NOS	IIIA
---	liver, hepatocellular carcinoma, NOS	I
---	liver, hepatocellular carcinoma, NOS	II
---	liver, hepatocellular carcinoma, NOS	IIIA
---	liver, hepatocellular carcinoma, NOS	IIIA
---	liver, hepatocellular carcinoma, NOS	II
---	liver, hepatocellular carcinoma, NOS	IIIA
---	liver, hepatocellular carcinoma, NOS	II
---	liver, hepatocellular carcinoma, NOS	II
---	liver, hepatocellular carcinoma, NOS	IIIC
---	liver, hepatocellular carcinoma, NOS	II
---	liver, hepatocellular carcinoma, NOS	I
---	liver, hepatocellular carcinoma, NOS	IIIA
---	liver, hepatocellular carcinoma, NOS	IIIC
---	liver, hepatocellular carcinoma, NOS	I
---	liver, hepatocellular carcinoma, NOS	I
---	liver, hepatocellular carcinoma, NOS	IIIB
---	liver, hepatocellular carcinoma, NOS	IIIA
---	liver, hepatocellular carcinoma, NOS	I
---	liver, hepatocellular carcinoma, NOS	IIIA
---	liver, hepatocellular carcinoma, NOS	II
---	liver, hepatocellular carcinoma, NOS	IIIA
---	liver, hepatocellular carcinoma, NOS	IIIC
---	liver, hepatocellular carcinoma, NOS	II
---	liver, hepatocellular carcinoma, NOS	II
---	liver, hepatocellular carcinoma, NOS	I
---	liver, hepatocellular carcinoma, NOS	II
---	liver, hepatocellular carcinoma, NOS	IIIA
---	liver, hepatocellular carcinoma, NOS	I
---	liver, hepatocellular carcinoma, NOS	I
---	liver, hepatocellular carcinoma, NOS	I
---	liver, hepatocellular carcinoma, NOS	I
---	liver, hepatocellular carcinoma, NOS	I
---	liver, hepatocellular carcinoma, NOS	I
---	liver, hepatocellular carcinoma, NOS	I
---	liver, hepatocellular carcinoma, NOS	II
---	liver, hepatocellular carcinoma, NOS	II
---	liver, hepatocellular carcinoma, NOS	I
---	liver, hepatocellular carcinoma, NOS	IIIC
---	liver, hepatocellular carcinoma, NOS	---
---	liver, hepatocellular carcinoma, NOS	II
---	liver, hepatocellular carcinoma, NOS	IIIA
liver	---	---
liver	---	---
liver	---	---
liver	---	---
liver	---	---
liver	---	---
liver	---	---
liver	---	---
liver	---	---
liver	---	---
liver	---	---
liver	---	---
liver	---	---
liver	---	---
liver	---	---
liver	---	---
liver	---	---
liver	---	---
liver	---	---
liver	---	---
liver	---	---
liver	---	---
liver	---	---
liver	---	---
liver	---	---
liver	---	---
liver	---	---
liver	---	---
liver	---	---
liver	---	---
liver	---	---
liver	---	---
liver	---	---
liver	---	---
liver	---	---
liver	---	---
liver	---	---
liver	---	---
liver	---	---
liver	---	---
liver	---	---
liver	---	---
liver	---	---
liver	---	---
liver	---	---
liver	---	---

Figure 16. Transcriptomic Expression Profile of DLG5 and its interactor genes in HCC vs adjacent tissues. The heatmap displays the relative transcript levels of each gene across multiple HCC and adjacent samples, with darker red shading indicating higher expression. Overall, DLG5 showed upregulation in HCC compared with adjacent portion, accompanied by parallel upregulation in SCRIB, and CTNNB1. Other interactors such as KRAS, GSK3B, and ESR1/2 exhibited variable but generally higher expression in tumor tissues. Adjacent liver samples displayed uniformly lower and more homogeneous expression levels across all genes. Image by [158].

Table 10. Correlation Analysis of DLG5 and Associated Genes in TCGA-LIHC Dataset Retrieved from OncoDB

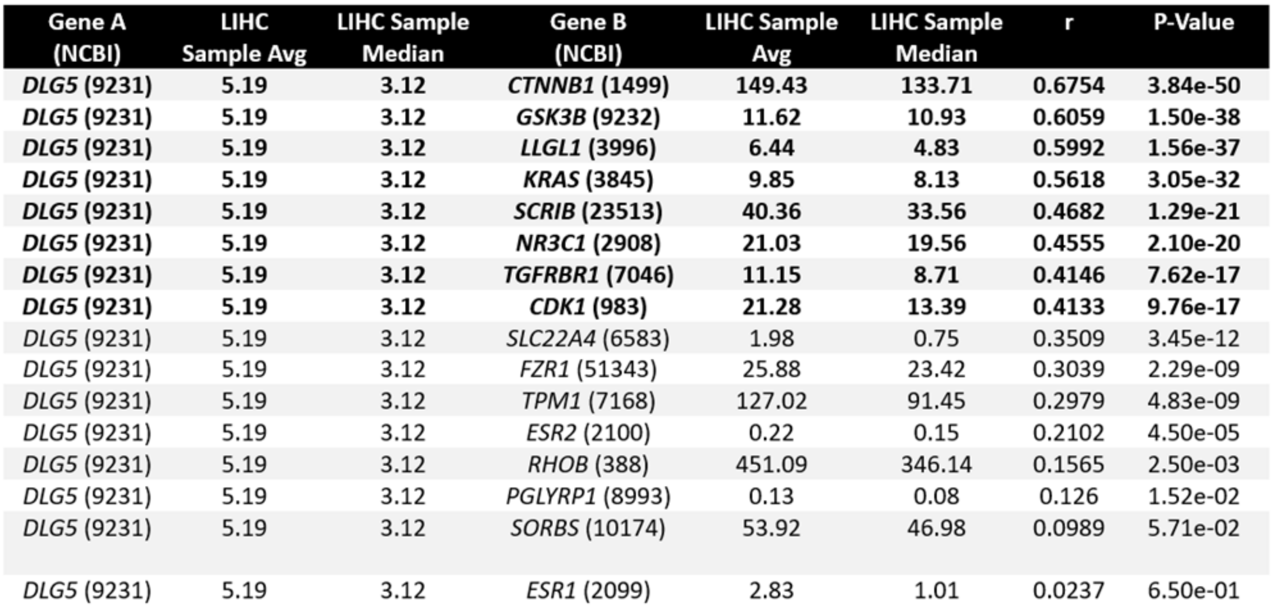

Gene A (NCBI)	LIHC Sample Avg	LIHC Sample Median	Gene B (NCBI)	LIHC Sample Avg	LIHC Sample Median	r	P-Value
***DLG5* (9231)**	**5.19**	**3.12**	***CTNNB1* (1499)**	**149.43**	**133.71**	**0.6754**	**3.84e-50**
***DLG5* (9231)**	**5.19**	**3.12**	***GSK3B* (9232)**	**11.62**	**10.93**	**0.6059**	**1.50e-38**
***DLG5* (9231)**	**5.19**	**3.12**	***LLGL1* (3996)**	**6.44**	**4.83**	**0.5992**	**1.56e-37**
***DLG5* (9231)**	**5.19**	**3.12**	***KRAS* (3845)**	**9.85**	**8.13**	**0.5618**	**3.05e-32**
***DLG5* (9231)**	**5.19**	**3.12**	***SCRIB* (23513)**	**40.36**	**33.56**	**0.4682**	**1.29e-21**
***DLG5* (9231)**	**5.19**	**3.12**	***NR3C1* (2908)**	**21.03**	**19.56**	**0.4555**	**2.10e-20**
***DLG5* (9231)**	**5.19**	**3.12**	***TGFRBR1* (7046)**	**11.15**	**8.71**	**0.4146**	**7.62e-17**
***DLG5* (9231)**	**5.19**	**3.12**	***CDK1* (983)**	**21.28**	**13.39**	**0.4133**	**9.76e-17**
DLG5 (9231)	5.19	3.12	*SLC22A4* (6583)	1.98	0.75	0.3509	3.45e-12
DLG5 (9231)	5.19	3.12	*FZR1* (51343)	25.88	23.42	0.3039	2.29e-09
DLG5 (9231)	5.19	3.12	*TPM1* (7168)	127.02	91.45	0.2979	4.83e-09
DLG5 (9231)	5.19	3.12	*ESR2* (2100)	0.22	0.15	0.2102	4.50e-05
DLG5 (9231)	5.19	3.12	*RHOB* (388)	451.09	346.14	0.1565	2.50e-03
DLG5 (9231)	5.19	3.12	*PGLYRP1* (8993)	0.13	0.08	0.126	1.52e-02
DLG5 (9231)	5.19	3.12	*SORBS* (10174)	53.92	46.98	0.0989	5.71e-02
DLG5 (9231)	5.19	3.12	*ESR1* (2099)	2.83	1.01	0.0237	6.50e-01

Bold characters: moderate to strong positive correlation in DLG5 and its interactors

Table 11. ENCORI-Based Correlation Matrix of DLG5 and its interactors

Gene / Ensembl ID	r (Pearson)	p-value	Correlation
CTNNB1 / ENSG00000168036	0.667	1.84×10^{-49}	Strongly Positive
SCRIB / ENSG00000180900	0.418	3.18×10^{-17}	Moderately Positive
LLGL1 / ENSG00000131899	0.593	7.59×10^{-37}	Moderately Positive
GSK3B / ENSG00000082701	0.583	2.27e-35	Moderately Positive
ESR1 / ENSG00000091831	0.030	5.62×10^{-1}	None
TPM1 / ENSG00000140416	0.195	1.52×10^{-4}	Weak
SORBS3 / ENSG00000120896	0.034	5.15×10^{-4}	None
PGLYRP1 / ENSG00000008438	0.098	5.74×10^{-2}	Very Weak
SLC22A4 / ENSG00000197208	0.391	4.18×10^{-15}	Weak
CDK1 / ENSG00000170312	0.366	2.75×10^{-13}	Weak
ESR2 / ENSG00000140009	0.186	2.88×10^{-4}	Weak
TGFBR1 / ENSG00000106799	0.371	1.28×10^{-13}	Weak
KRAS / ENSG00000133703	0.532	1.12×10^{-28}	Moderately Positive
NR3C1 / ENSG00000113580	0.399	9.74×10^{-16}	Weak
RHOB / ENSG00000143878	0.079	1.26×10^{-1}	Weak
FZR1 / ENSG00000105325	0.171	8.88×10^{-4}	Weak

Note: Correlation coefficients (r) and p-values were derived from ENCORI transcriptomic co-expression analysis using patient-derived primary HCC (TCGA-LIHC) RNA-seq datasets. The results show a strong positive correlation between DLG5 and CTNNB1 ($r=0.667$, $p=1.84\times10^{-49}$), and moderate positive correlations with LLGL1, GSK3B, SCRIB, and KRAS

Figure 17. Correlation of DLG5 with Selected Interactor Genes in HCC (ENCORI Dataset). Scatter plots show transcript-level correlations between DLG5 and selected interactors: (A) CTNNB1, (B) SCRIB, (C) LLGL1, and (D) ESR1. Each dot represents a single tumor sample, and red lines denote linear regression fits. DLG5 expression showed strong positive correlation with CTNNB1 (r=0.667, p=1.84×10^{-49}) and moderate correlations with SCRIB (r=0.418, p=3.18×10^{-17}) and LLGL1 (r=0.593, p=7.59×10^{-37}), whereas no significant association was observed with ESR1 (r=0.030, p=0.562*).

4.2 DLG5 Expression at gene and protein levels

The mean mRNA expression level of DLG5 was significantly higher in HCC (mean =0.7519, 95% CI 0.38-1.12) compared with adjacent tissue 0.0546, 95% CI 0.03-0.08 Figure 18A.

In Figure 18B The Log_2 fold change distribution ranged from –3.14 to 9.38, with a mean = 3.776 (95% CI: 3.03–4.53). Most samples demonstrated positive Log_2FC values.

The DLG5 protein expression level was 2.044, 95% CI 0.42–3.66 in HCC and 1.698, 95% CI 0.82–2.57 in adjacent tissue. Expression values ranged from 0.60 to 8.26 in HCC and 0.02 to 3.85 in adjacent tissue Figure 18C-D.

Figure 18E reflecting a heterogenous trend of DLG5 protein abundance in tumor samples compared with adjacent controls.

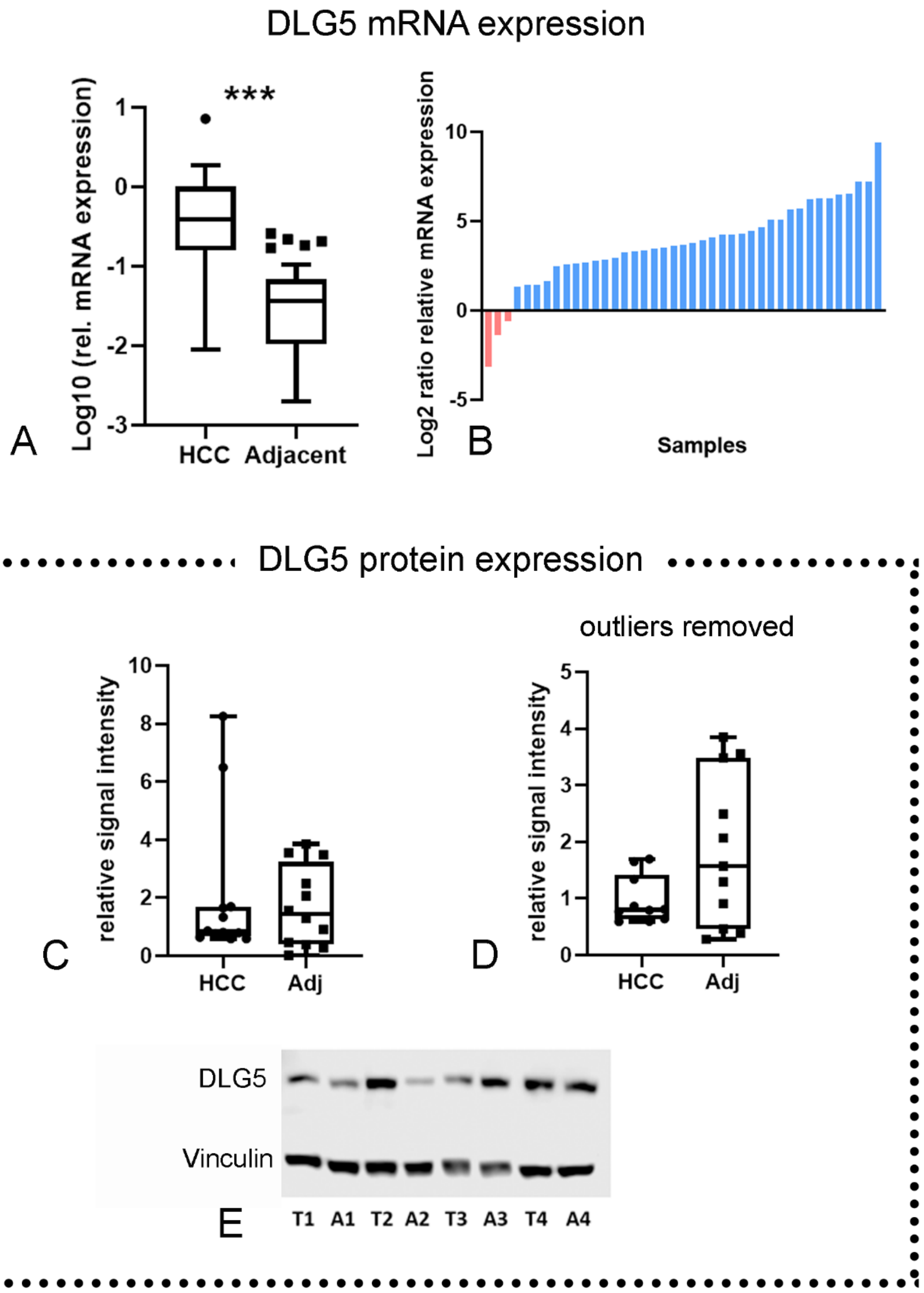

Figure 18. DLG5 expression at mRNA and protein levels in HCC. These results demonstrate a significant increased DLG5 mRNA expression but reduced DLG5 protein abundance in HCC compared with adjacent liver tissue. (A) Box plot showing relative DLG5 mRNA expression levels ($\log_{10}$ scale), indicating significantly higher transcript DLG5 abundance in HCC. (B) Log_2 fold-change distribution across paired

samples showing predominant upregulation of DLG5 in HCC. (C) Quantitative analysis of DLG5 protein expression from densitometric measurements of validated 12 paired tissue samples, showing reduced protein intensity in HCC relative to adjacent liver. (D) Same as (C), excluding statistical outliers for clearer visualization of central tendency. (E) Representative Western blot showing DLG5 protein bands (~214 kDa) and vinculin (~118 kDa) as the loading control in four paired samples (T=tumoral (HCC); A=adjacent). For DLG5 expression analyses, forty paired HCC and adjacent tissue samples were used for mRNA evaluation (n = 40), while twelve paired samples were analyzed for protein expression (n = 12). Data and error bars represent mean±SD. Corresponding mean values and 95% CI are reported in the text. Statistical significance was assessed using the paired Wilcoxon signed-rank test, with significance denoted by: ****P*<0.001.

4.3 Localization of DLG5 in hepatocellular carcinoma

DLG5 localization and staining intensity were quantitatively assessed in adjacent and HCC tissues using ImageJ and CellProfiler. Both analyses revealed significantly higher DLG5 abundance in adjacent liver compared with tumoral areas (Figure 19A–C), as demonstrated in paired tissues (Figure 19D–E). In Figures 20-22 (A–F), both manual classification counts and counts of mean intensity in high, medium, low revealed distinct distribution patterns across perinuclear, cytoplasmic, and submembranous compartments of paired HCC tissues. Localization indices derived from counts of cell compartment’s binary measurement and manual classification count are in appendix G and H, respectively.

Morphological evaluation (Figures 23) illustrated intact basolateral and apical domains in adjacent hepatocytes, and syncytial and disorganized architecture was observed in HCC tissues (Figures 24). Corresponding hematoxylin and DLG5 IHC counterparts for representative fields are provided in Appendix D Adjacent tissues, Appendix E HCC tissues and Appendix F illustrate representative features of steatosis.

To further verify the polarity-associated role of DLG5, immunofluorescence staining was performed in two HCC-derived cell lines, Huh7 and JHH6 (Figures 25-26). Both models demonstrated co-localization of DLG5 with CTNNB1 at the cell borders, particularly in Huh7 cells (Figure 27). Enlarged merge images of DLG5, Occludin, ZO-1 and colocalized DLG5 and CTNNB1 are in appendix I-L.

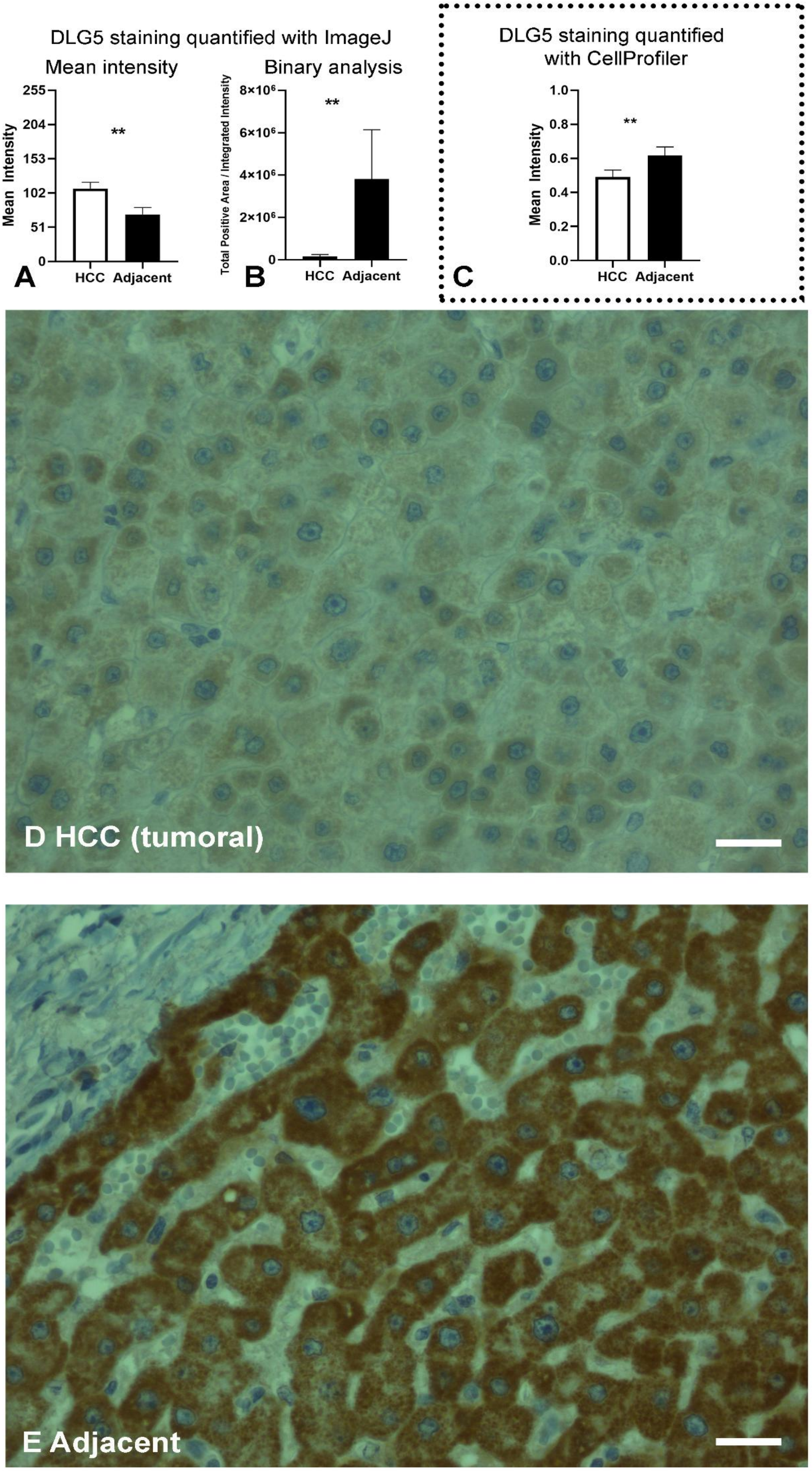
DLG5 staining quantified with ImageJ
Mean intensity
Binary analysis
DLG5 staining quantified with CellProfiler
255
204
153
102
51
0
Mean Intensity
**
A
HCC
Adjacent
8×10⁶
6×10⁶
4×10⁶
2×10⁶
0
Total Positive Area / Integrated Intensity
**
B
HCC
Adjacent
1.0
0.8
0.6
0.4
0.2
0.0
Mean Intensity
**
C
HCC
Adjacent
D HCC (tumoral)
E Adjacent

Figure 19. DLG5 staining on HCC and adjacent tissues. (A) Mean intensity of DLG5 IHC staining quantified in ImageJ. Analysis was performed without image inversion, where lower mean intensity corresponds to darker DAB staining or stronger signal. The mean intensity was 108.6, 95% CI 102.1-119.3 in HCC and 70.12, 95% CI 56.29-80.95 in adjacent liver tissue. (B) Binary measurement of DAB intensity ratio of DLG5 staining acquired from ImageJ quantification. This data represents the integrated density of DAB-positive regions normalized to positive area. Measurement revealed significant stronger DLG5 abundance in adjacent regions. The mean 161,537, 95% CI 83,471–277,236 in HCC and 3,811,314, 95% CI 510,496–5,650,522 in adjacent tissue. (C) Mean intensity of DLG5 staining quantified using CellProfiler automated image analysis. The DAB channel was extracted using the UnmixColors module, which inverts the DAB signal for measurement. DLG5 mean intensity demonstrated significantly higher DLG5 signal in adjacent liver compared with HCC. The mean was 0.4902, 95% CI 0.4386–0.5273 in HCC and 0.6178, 95% CI 0.5606–0.6836 in adjacent tissue. (D–E) Representative immunohistochemical images of DLG5 expression in paired HCC and adjacent liver tissues. For both ImageJ and CellProfiler analyses, ten paired HCC and adjacent tissue samples were analyzed (n = 10 pairs). Ten representative images were derived from these paired samples and used for quantitative analysis. Data and error bars represent mean±SD. Corresponding mean values and 95% CI are reported in the text. Statistical significance was assessed using the paired Wilcoxon signed-rank test, with significance denoted by: $^{**}P<0.01$. Scale bar: 25μm (panels D-E).

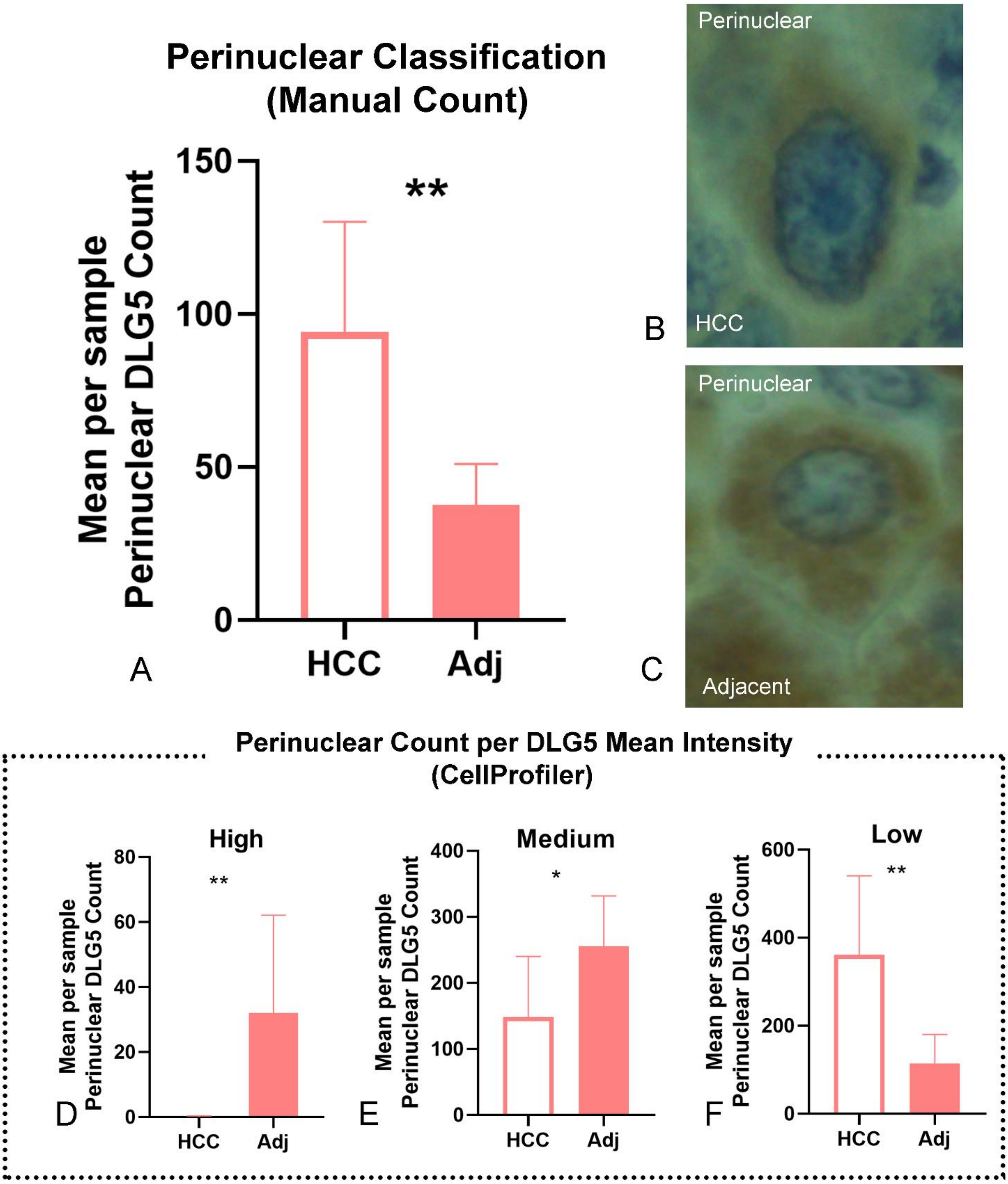
Perinuclear Classification (Manual Count)
Mean per sample Perinuclear DLG5 Count
150
100
50
0
**
HCC
Adj
A
Perinuclear
HCC
B
Perinuclear
Adjacent
C
Perinuclear Count per DLG5 Mean Intensity (CellProfiler)
High
Mean per sample Perinuclear DLG5 Count
80
60
40
20
0
**
HCC
Adj
D
Medium
Mean per sample Perinuclear DLG5 Count
400
300
200
100
0
*
HCC
Adj
E
Low
Mean per sample Perinuclear DLG5 Count
600
400
200
0
**
HCC
Adj
F

Figure 20. DLG5 abundance count in perinuclear of HCC and adjacent tissues. (A) Manual quantification of perinuclear DLG5-positive cells, showing significantly higher counts in HCC compared with adjacent tissue. The mean count was 94.21, 95% CI 68.45–120.0 in HCC and 37.55, 95% CI 27.91–47.19 in adjacent tissue. (B–C) Representative images of perinuclear DLG5 localization in HCC (B) and adjacent liver (C), illustrating DLG5 accumulation approximately in perinuclear region. Not to scale. (D-F) High, medium, low mean intensity classified perinuclear object counts from CellProfiler. (D) The perinuclear count of high mean intensity is significantly higher in adjacent (32.08, 95% CI 10.61-53.55) compared to HCC (0.12, 95% CI 0.05-0.29). For both manual counting and CellProfiler analyses, ten paired HCC and adjacent tissue samples were analyzed (n = 10 pairs). Ten representative images were derived from these paired samples and used for quantitative analysis. Data and error bars represent mean±SD. Corresponding mean values and 95% CI are reported in the text. Statistical significance was assessed using the paired Wilcoxon signed-rank test, with significance denoted by: $^{*}P<0.05$, and $^{**}P<0.01$.

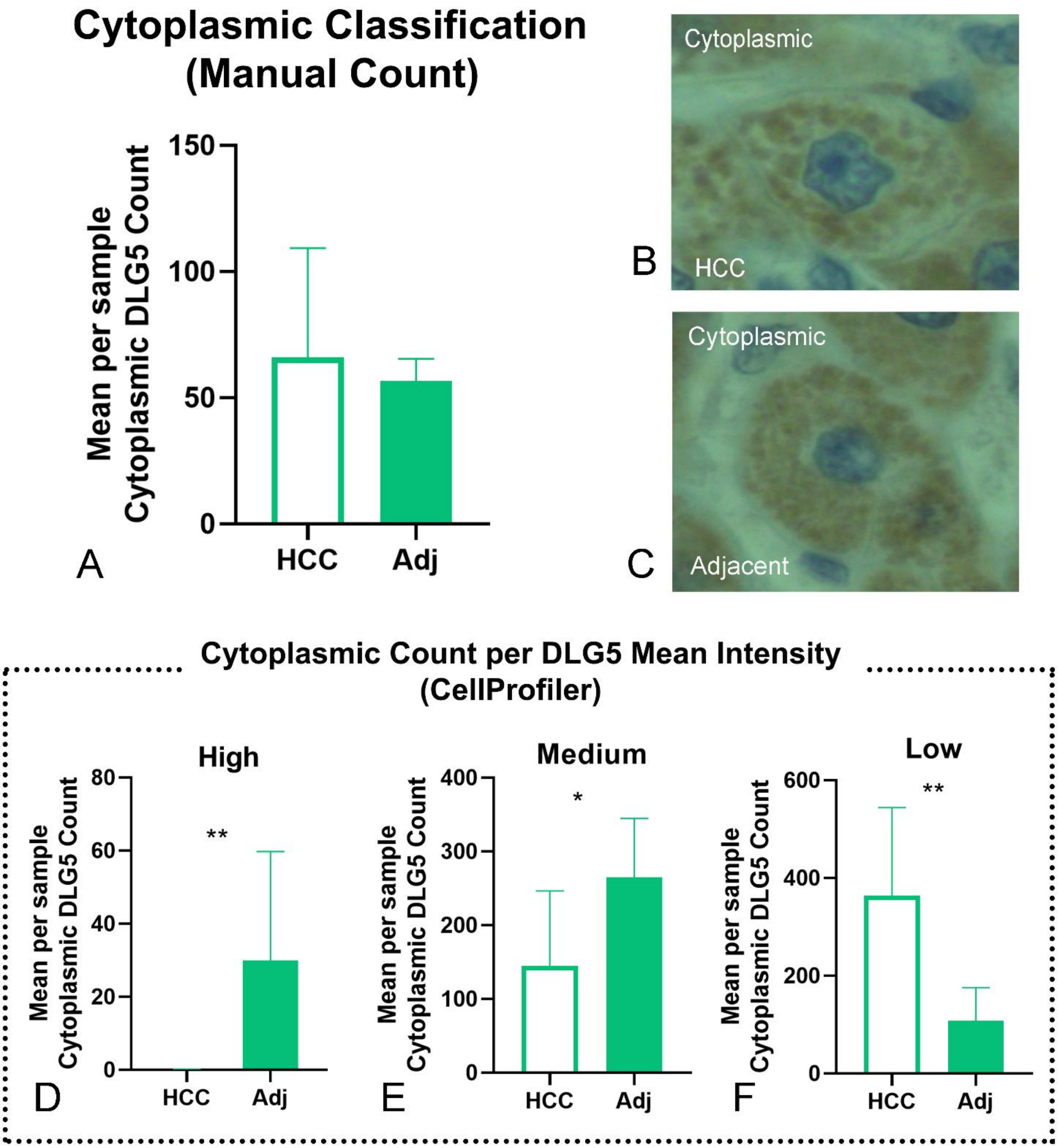
Cytoplasmic Classification (Manual Count)
Mean per sample Cytoplasmic DLG5 Count
150
100
50
0
HCC
Adj
A
Cytoplasmic
B
HCC
Cytoplasmic
C
Adjacent
Cytoplasmic Count per DLG5 Mean Intensity (CellProfiler)
High
Mean per sample Cytoplasmic DLG5 Count
80
60
40
20
0
**
HCC
Adj
D
Medium
Mean per sample Cytoplasmic DLG5 Count
400
300
200
100
0
*
HCC
Adj
E
Low
Mean per sample Cytoplasmic DLG5 Count
600
400
200
0
**
HCC
Adj
F

Figure 21. DLG5 abundance count in cytoplasm of HCC and adjacent tissues. (A) Manual quantification of cytoplasmic DLG5-positive cells per field showing significant difference between HCC (66.12, 95% CI 35.20-97.04) and adjacent tissue (56.67, 95% CI 50.43-62.91). (B–C) Representative images of cytoplasmic DLG5 staining in HCC (B) and adjacent region (C), illustrating dotted to unclear cytoplasmic localization of DLG5 (not to scale). (D-F) High, medium, low mean intensity classified cytoplasmic object counts from CellProfiler. (D) The cytoplasmic count of high mean intensity is significantly higher in adjacent (29.92, 95% CI 8.58-51.26) compared to HCC (0.06, 95% CI 0.03-0.16). For both manual counting and CellProfiler analyses, ten paired HCC and adjacent tissue samples were analyzed (n = 10 pairs). Ten representative images were derived from these paired samples and used for quantitative analysis. Data and error bars represent mean±SD. Corresponding mean values and 95% CI are reported in the text. Statistical significance was assessed using the paired Wilcoxon signed-rank test, with significance denoted by: *$P<0.05$, **$P<0.01$.

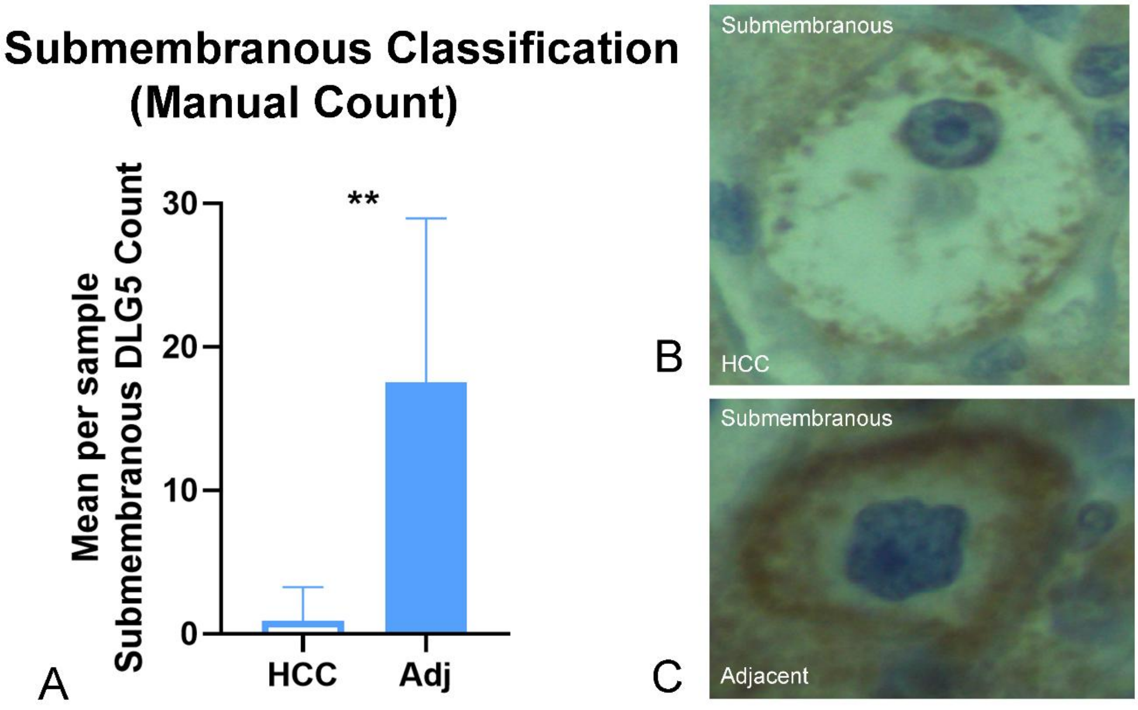
Submembranous Classification
(Manual Count)
Mean per sample
Submembranous DLG5 Count
30
20
10
0
**
HCC
Adj
A
B
Submembranous
HCC
C
Submembranous
Adjacent

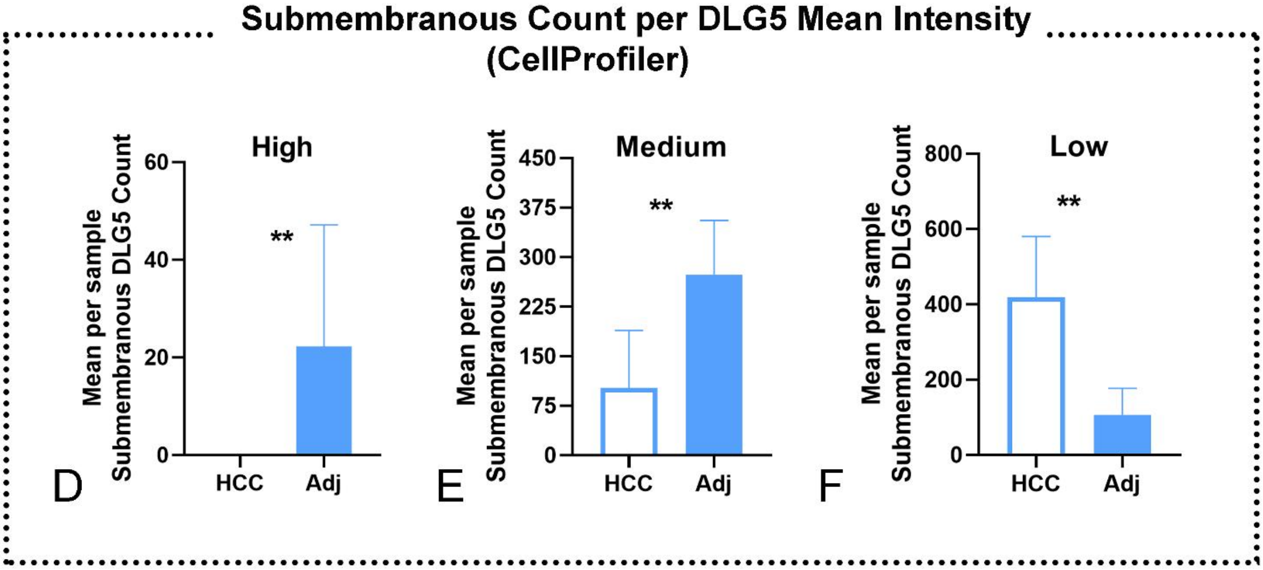
Submembranous Count per DLG5 Mean Intensity
(CellProfiler)
High
Mean per sample
Submembranous DLG5 Count
60
40
20
0
**
HCC
Adj
D
Medium
Mean per sample
Submembranous DLG5 Count
450
375
300
225
150
75
0
**
HCC
Adj
E
Low
Mean per sample
Submembranous DLG5 Count
800
600
400
200
0
**
HCC
Adj
F

Figure 22. DLG5 abundance count in submembranous of HCC and adjacent tissues. (A) Manual quantification of submembranous DLG5-positive cells per field, showing a significantly higher count in adjacent liver compared with HCC. The mean was 17.51, 95% CI of 9.32–25.70 in adjacent liver and 0.92, 95% CI 0.75-2.59 in HCC. (B–C) Representative images of DLG5 staining in the submembranous region of HCC (B) and adjacent region (C) (not to scale). (D–F) High, medium, low mean intensity classified submembranous object counts from CellProfiler. (D) The submembranous count of high mean intensity is significantly higher in adjacent (22.29, 95% CI 4.48-40.10) compared to HCC (0.01, 95% CI 0.01-0.03). For both manual counting and CellProfiler analyses, ten paired HCC and adjacent tissue samples were analyzed (n = 10 pairs). Ten representative images were derived from these paired samples and used for quantitative analysis. Data and error bars represent mean±SD. Corresponding mean values and 95% CI are reported in the text. Statistical significance was assessed using the paired Wilcoxon signed-rank test, with significance denoted by: $^{**}P<0.01$.

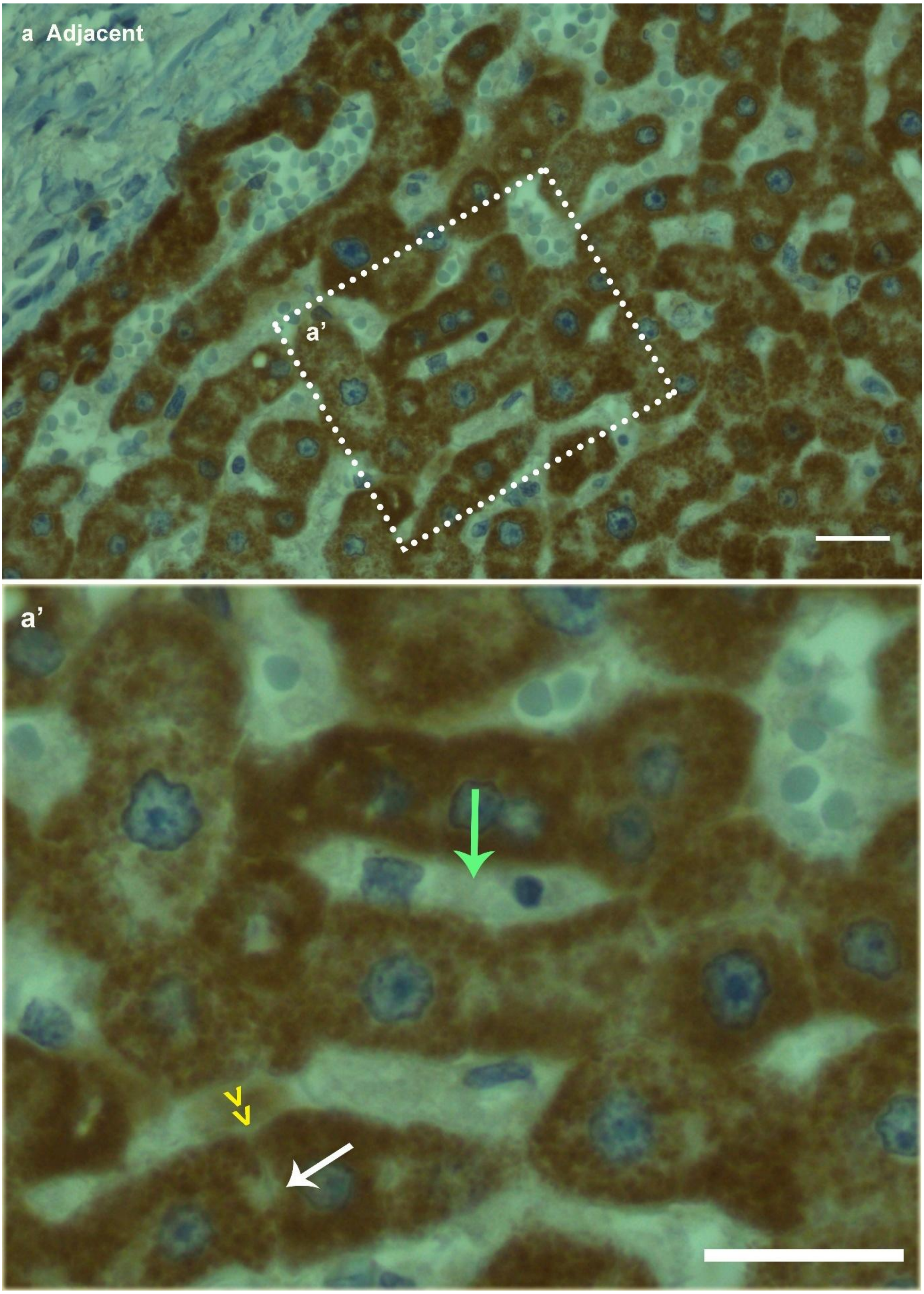
a Adjacent
a’
a’

Figure 23. DLG5 staining in adjacent region. (a) Immunohistochemical staining of DLG5 in adjacent liver tissue showing strong submembranous and cytoplasmic distribution outlining the hepatocyte cords. The bile canalicular architecture remains well preserved, consistent with maintained hepatocyte polarity. (a′) Magnified region from panel (a′) highlighting subcellular features. DLG5 is enriched along the basolateral domain (green arrow), with uniform pericellular staining between neighboring hepatocytes. The white arrow indicates bile canaliculi, while the yellow arrowhead denotes tight junction. Scale bar: 25μm (panels a-a’).

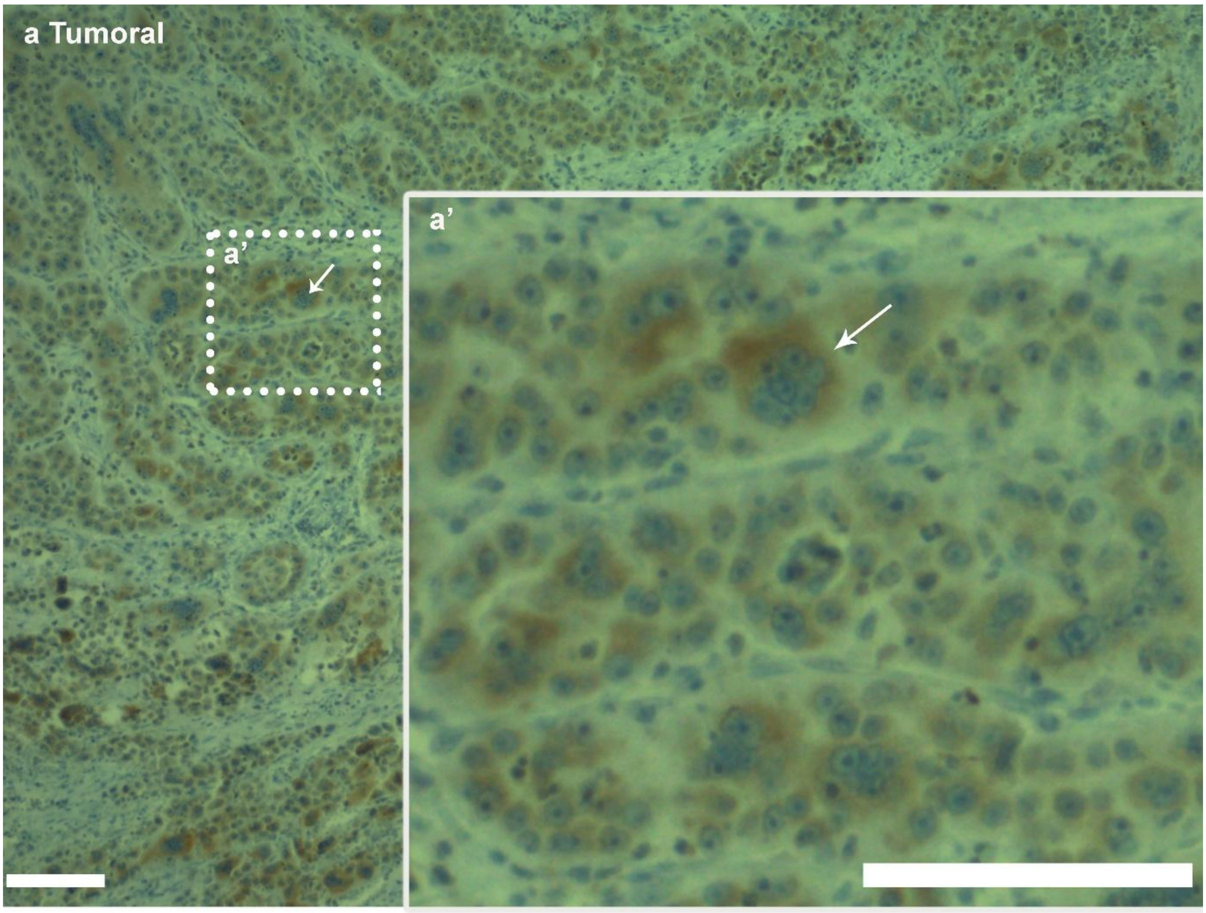

Figure 24. DLG5 staining in HCC region. (a) Immunohistochemical staining of DLG5 in HCC showing weak and diffuse cytoplasmic signal with diminished membranous definition compared to adjacent tissue. Tumor areas display a syncytial pattern of hepatocytes with indistinct cell borders and disrupted trabecular organization. (a′) Higher magnification of the boxed region showing perinuclear DLG5 accumulation (white arrow) within tumor cells. Scale bars: 100µm, (panels a-a’).

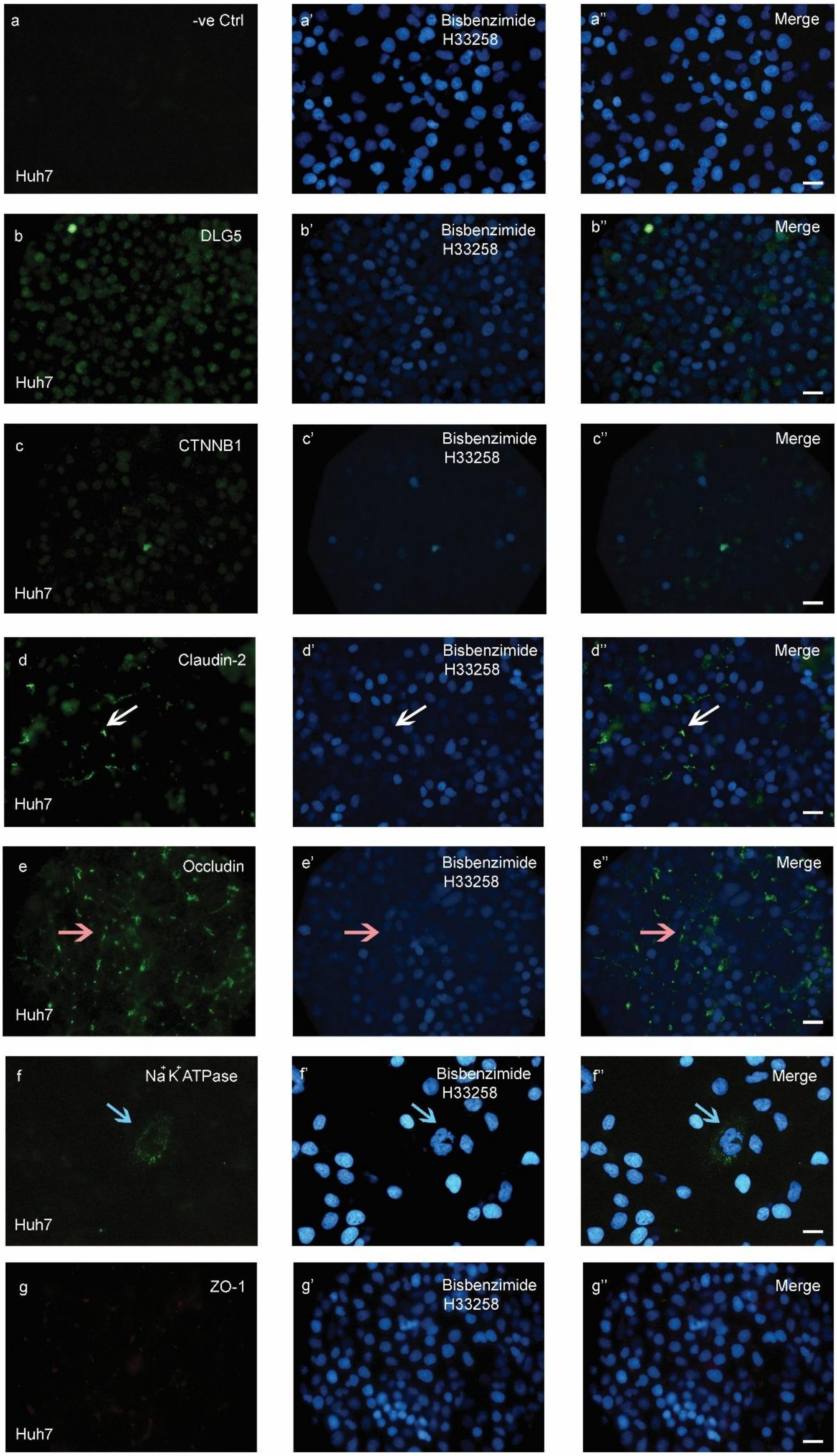
a
-ve Ctrl
Huh7
a’
Bisbenzimide H33258
a’’
Merge
b
DLG5
Huh7
b’
Bisbenzimide H33258
b’’
Merge
c
CTNNB1
Huh7
c’
Bisbenzimide H33258
c’’
Merge
d
Claudin-2
Huh7
d’
Bisbenzimide H33258
d’’
Merge
e
Occludin
Huh7
e’
Bisbenzimide H33258
e’’
Merge
f
Na^+K^+ATPase
Huh7
f’
Bisbenzimide H33258
f’’
Merge
g
ZO-1
Huh7
g’
Bisbenzimide H33258
g’’
Merge

Figure 25. Immunofluorescence staining of DLG5 and polarity proteins in Huh7 cells. (a–a″) Negative control (–ve Ctrl). (b–b″) DLG5 demonstrates punctate staining overlapping the nucleus region. (c–c″) CTNNB1 exhibits scattered cytoplasmic fluorescence with minimal membrane staining. (d–d″) Claudin-2 displays distinct junctional staining (white arrow). (e–e″) Occludin shows peripheral punctate distribution (pink arrow) consistent with junctional membrane presence. (f–f″) Na^+/K^+-ATPase (blue arrow) localizes along the membrane. (g–g″) ZO-1 staining is weak. Nuclei were counterstained with Bisbenzimide H33258 (blue). Scale bars: 25μm applies to all panels. Experiment was done in two biological repeats from different days.

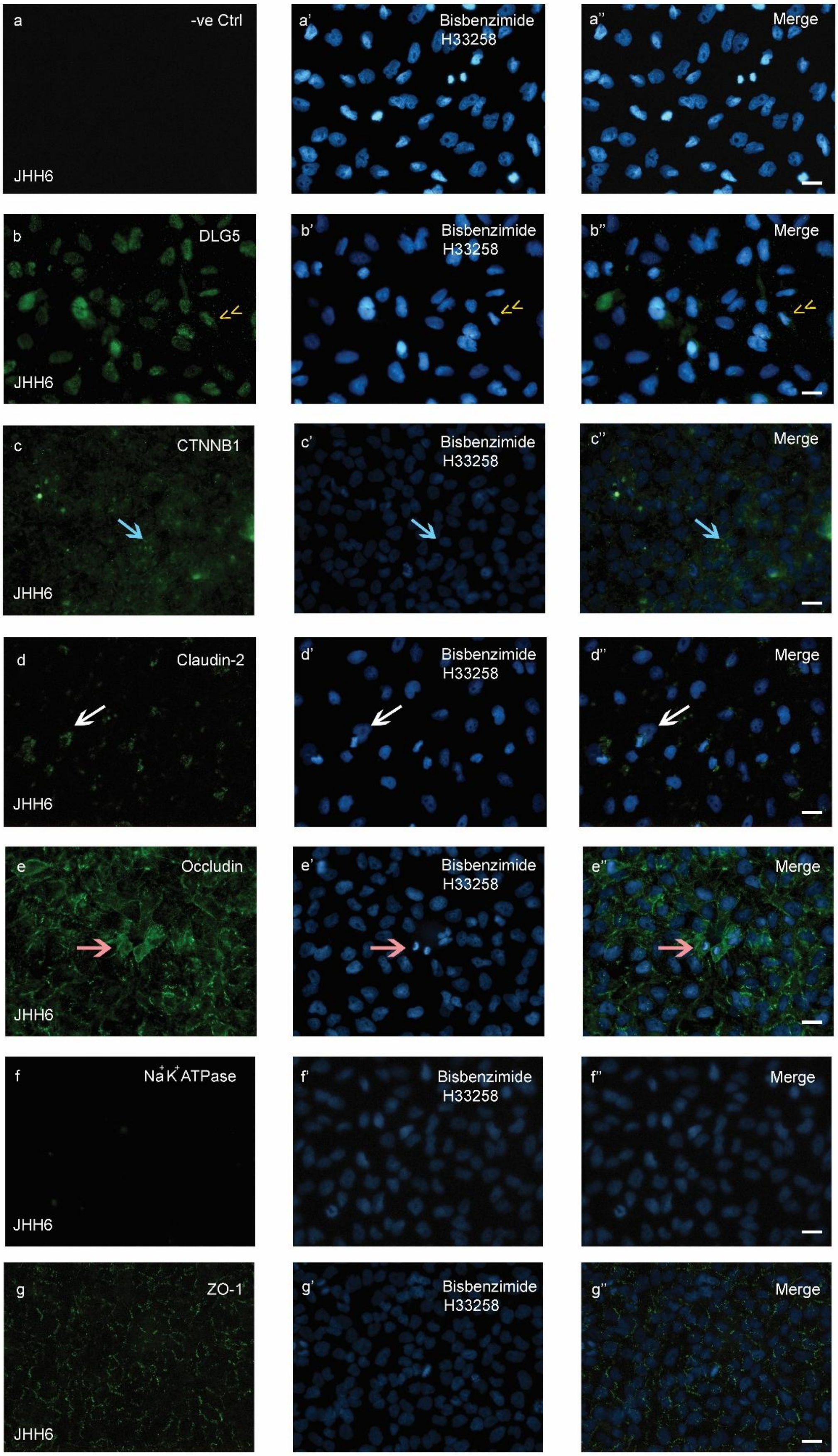
a
-ve Ctrl
JHH6
a'
Bisbenzimide H33258
a''
Merge
b
DLG5
JHH6
b'
Bisbenzimide H33258
b''
Merge
c
CTNNB1
JHH6
c'
Bisbenzimide H33258
c''
Merge
d
Claudin-2
JHH6
d'
Bisbenzimide H33258
d''
Merge
e
Occludin
JHH6
e'
Bisbenzimide H33258
e''
Merge
f
Na^+K^+ATPase
JHH6
f'
Bisbenzimide H33258
f''
Merge
g
ZO-1
JHH6
g'
Bisbenzimide H33258
g''
Merge

Figure 26. Immunofluorescence staining of DLG5 and polarity proteins in JHH6 cells. (a–a″) Negative control (–ve Ctrl). (b–b″) DLG5 shows punctate staining overlapping the nucleus area (yellow double arrowheads). (c–c″) CTNNB1 exhibits (blue arrow) dotted membrane staining (d–d″) Claudin-2 displays sparse punctate expression (white arrow), indicating reduced tight junction formation. (e–e″) Occludin presents diffuse cytoplasmic signal (pink arrow) (f–f″) Na^+/K^+-ATPase staining is absent (g–g″) ZO-1 shows fragmented and discontinuous signal outlining scattered cells. Scale bars: 25 μm applies to all panels. Experiment was done in two biological repeats from different days.

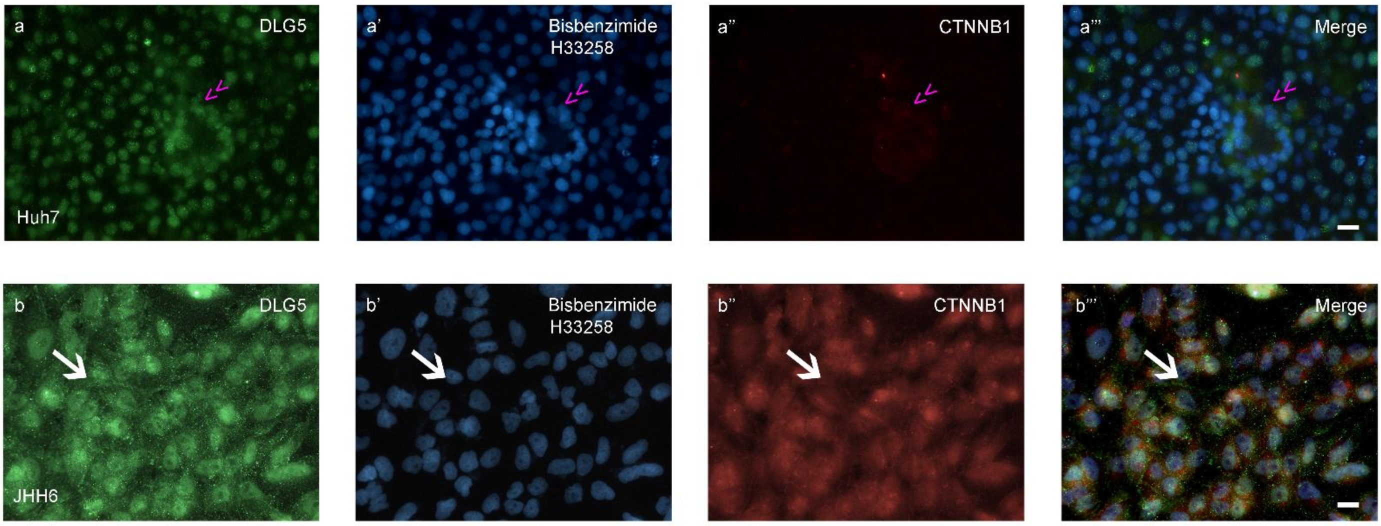

Figure 27. Colocalization of DLG5 and CTNNB1 in Huh7 and JHH6 cells. (a–a‴) In Huh7 cells, DLG5 (green) and CTNNB1 (red) display partial cytoplasmic overlap (magenta arrow), indicating weak signal of colocalization. (b–b‴) JHH6 cells show pronounced colocalization of DLG5 and CTNNB1 (white arrow). Nuclei were counterstained with Bisbenzimide H33258 (blue). Scale bars: 25µm applies to all panels. Experiment was done in two biological repeats from different days.

4.4 Silencing of *DLG5* gene

DLG5 knockdown efficiency was assessed 48 hours after transfection with 5nM *DLG5*-specific siRNA in two hepatocellular carcinoma cell lines, Huh7 and JHH6. Quantitative RT-PCR analysis revealed a marked reduction in *DLG5* mRNA levels in si*DLG5*-treated cells compared with both untreated (U) and scrambled siRNA control (siCtrl) conditions (Figure 28). In both cell lines, *DLG5* transcript levels were reduced by approximately 80–90% following si*DLG5* transfection. Consistent with the mRNA data, DLG5 protein levels were also decreased in si*DLG5*-treated JHH6 cells at 96 hours post-transfection, confirming silencing at the protein level (Figure 29). Differences among groups were assessed using the Kruskal–Wallis test followed by Dunn's multiple comparisons test.

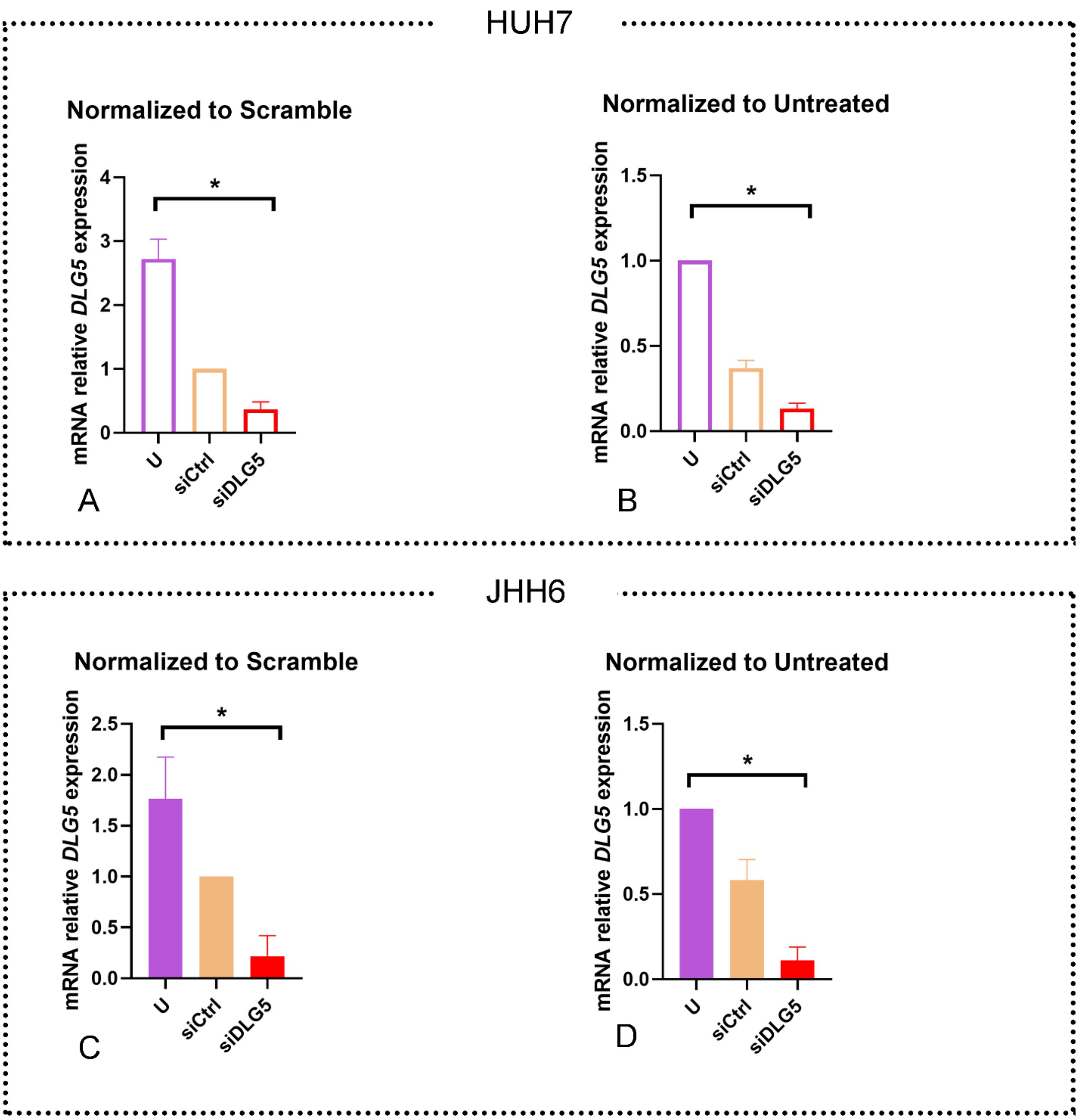

Figure 28. Validation of *DLG5* silencing in Huh7 and JHH6 cells post-48H transfection. (A–B) Relative *DLG5* mRNA expression levels in Huh7 cells following siRNA transfection. (C–D) Relative *DLG5* mRNA expression levels in JHH6 cells under identical transfection conditions. U and siCtrl groups were compared with *DLG5*-specific siRNA (siDLG5) treatment. Quantitative RT-PCR analysis demonstrated downregulation of *DLG5* expression in both Huh7 and JHH6 following siRNA treatment compared with control groups. Data represent mean±SD of three independent biological experiments performed in different days. Statistical significance denoted by: *P<0.05.

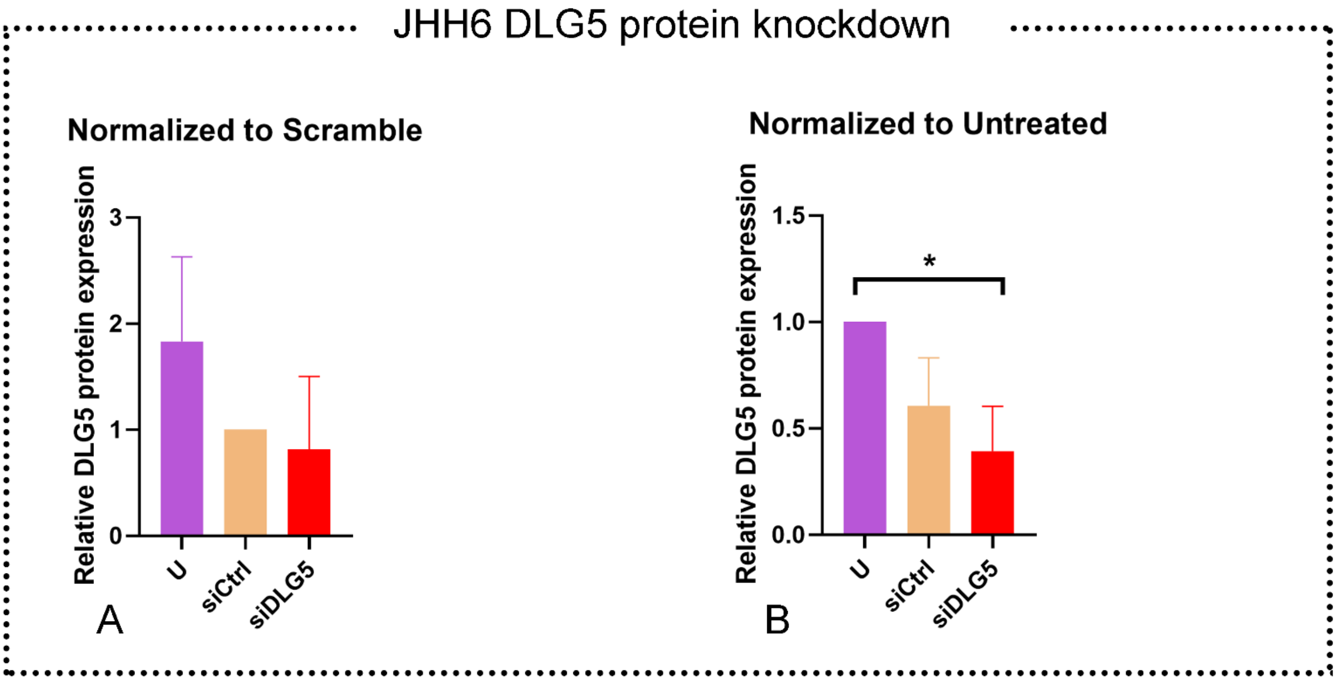

Figure 29. Validation of DLG5 protein silencing in JHH6 cells post-96H transfection. Relative DLG5 protein levels were quantified following transfection with DLG5-specific siRNA and compared with untreated and scrambled siRNA control conditions. Data are shown normalized to siCtrl (A) or to untreated cells (B). Data represent mean ± SD from three independent biological replicates performed in different days. Statistical significance denoted by: **P*<0.05.

CHAPTER 5. DISCUSSION

DLG5 mRNA expression levels were significantly higher in HCC than in adjacent tissue, whereas protein expression levels showed an opposite, non-significant trend. IHC analysis further revealed stronger DLG5 staining in adjacent liver tissue, mainly within cytoplasmic and perinuclear compartments, accompanied by reduced and fragmented submembranous localization. Interestingly, the *in silico* analysis revealed strong positive correlation between DLG5 and β-catenin, which was further confirmed with the colocalization observed in Huh7 and JHH6 cells. Given that DLG5 was abundantly localized along junctional domains in adjacent tissues, these findings support the hypothesis that DLG5 has a role as an anchoring scaffold that stabilizes β-catenin at adherens junctions. Displacement of DLG5 from the membrane may therefore contribute to junctional instability and polarity loss during hepatocarcinogenesis [12].

Like Scribble, DLG5 displacement from the submembranous region toward cytoplasmic and perinuclear compartments confirms polarity disruption as a key mechanism in HCC progression [98]. DLG5 has been proposed as a tumor-suppressive scaffold involved in the maintenance of epithelial polarity, consistent with the reduced submembranous DLG5 signal observed in HCC tissues [105]. Consistent with previous study, DLG5 staining is reduced in HCC compared with adjacent liver tissue [159]. Importantly, the present work extends these findings by systematically classifying both increased and decreased DLG5 intensity in paired samples. This approach revealed not only an overall reduction in DLG5 expression, but also a pronounced loss of submembranous localization accompanied by redistribution toward cytoplasmic and perinuclear compartment.

A limitation of this study is the absence of downstream functional assays following DLG5 silencing. This reflects the substantial methodological effort required to establish and validate DLG5-specific experimental pipelines in HCC models, as no prior protocols were available for investigating DLG5-mediated polarity in hepatocellular carcinoma. Optimization was particularly challenging due to the high molecular weight of DLG5 (~214 kDa) and the intrinsic heterogeneity of human HCC tissues. Considerable time was therefore dedicated to developing robust siRNA knockdown strategies, validating protein detection, and establishing spatial quantification approaches for DLG5 localization. Importantly, the successful validation of DLG5 silencing at both the transcript and protein levels in Huh7 and JHH6 cells provides a solid foundation for future functional analyses.

Future studies should therefore focus on elucidating the molecular mechanisms governing DLG5 regulation, trafficking, and stability in hepatocellular carcinoma, as well as assessing the functional consequences of its mislocalization. In line with a previous study demonstrating that three-dimensional culture systems can unmask polarity-dependent phenotypes not evident in conventional two-dimensional models, the application of 3D hepatocyte models may provide a physiologically relevant platform to investigate how DLG5 depletion or redistribution impacts hepatocyte organization, junctional complexes, and epithelial polarity [109]. Such approaches would allow direct evaluation of whether restoration or stabilization of DLG5 localization is sufficient to rescue polarity defects in a context that more closely recapitulates *in vivo* liver architecture.

CONCLUSION

The findings of this study demonstrated that DLG5 dysregulation in HCC is characterized by the loss of membrane-associated localization and redistribution toward cytoplasmic and perinuclear regions. These results further suggest that DLG5 functions in a localization-dependent manner, where its submembranous positioning is crucial for maintaining epithelial structure, stabilizing β-catenin at adherens junctions, and preserving overall junctional integrity.

APPENDICES

APPENDIX A – Mean Intensity Pipeline (CellProfiler)

The CellProfiler pipeline for quantifying DLG5 mean intensity is illustrated below. Each module represents a sequential step applied to brightfield IHC images. Key modules and outputs are provided.

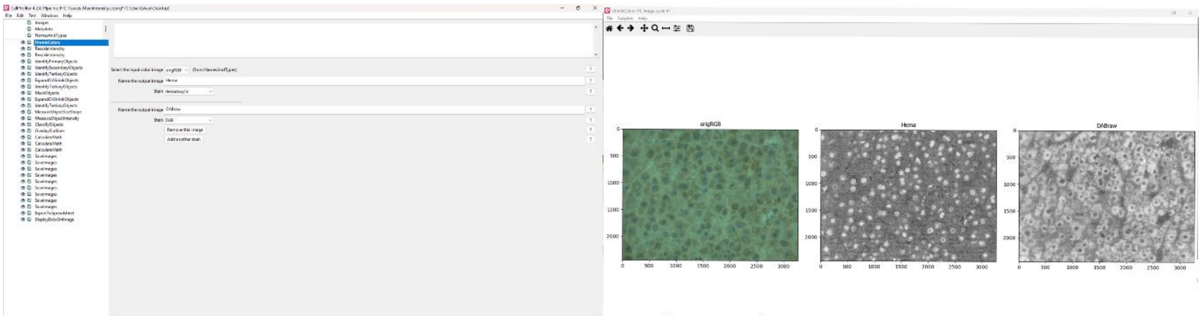

A. Module #5 and output of UnmixColors.

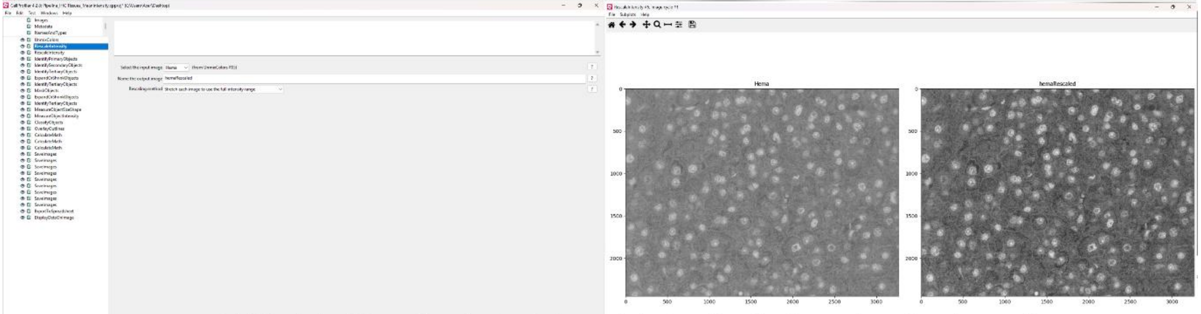

B. Module #6 and output of RescaleIntensity for hematoxylin channel.

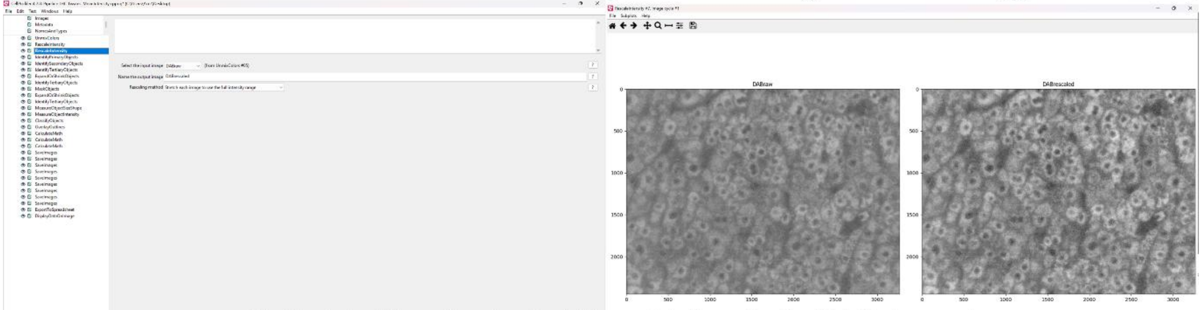

C. Module #7 and output of RescaleIntensity for DAB channel.

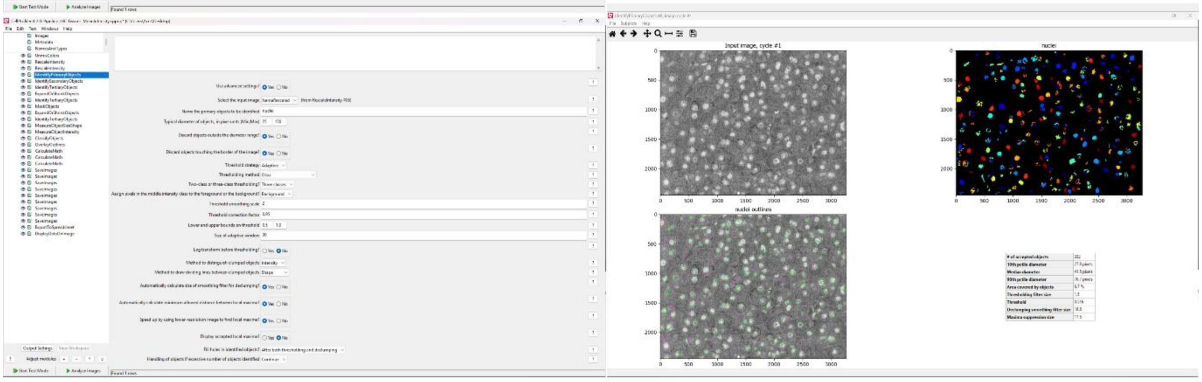

D. Module #8 and output of IdentifyPrimaryObjects.

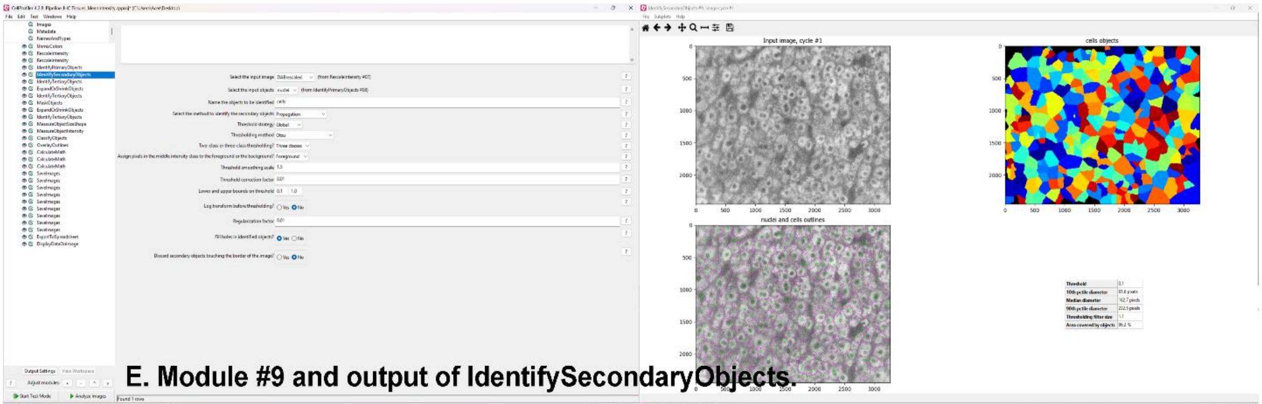

Select the input image: DABrescaled (from RescaleIntensity #07)

Select the input objects: nuclei (from IdentifyPrimaryObjects #08)

Name the objects to be identified: cells

Select the method to identify the secondary objects: Propagation

Threshold strategy: Global

Thresholding method: Otsu

Two-class or three-class thresholding?: Three classes

Assign pixels in the middle intensity class to the foreground or the background?: Foreground

Threshold smoothing scale: 1.5

Threshold correction factor: 0.01

Lower and upper bounds on threshold: 0.1 1.0

Log transform before thresholding?: ○ Yes ● No

Regularization factor: 0.01

Fill holes in identified objects?: ● Yes ○ No

Discard secondary objects touching the border of the image?: ○ Yes ● No

Threshold	0.1
10th pctile diameter	81.8 pixels
Median diameter	162.7 pixels
90th pctile diameter	232.5 pixels
Thresholding filter size	1.1
Area covered by objects	96.2 %

E. Module #9 and output of IdentifySecondaryObjects.

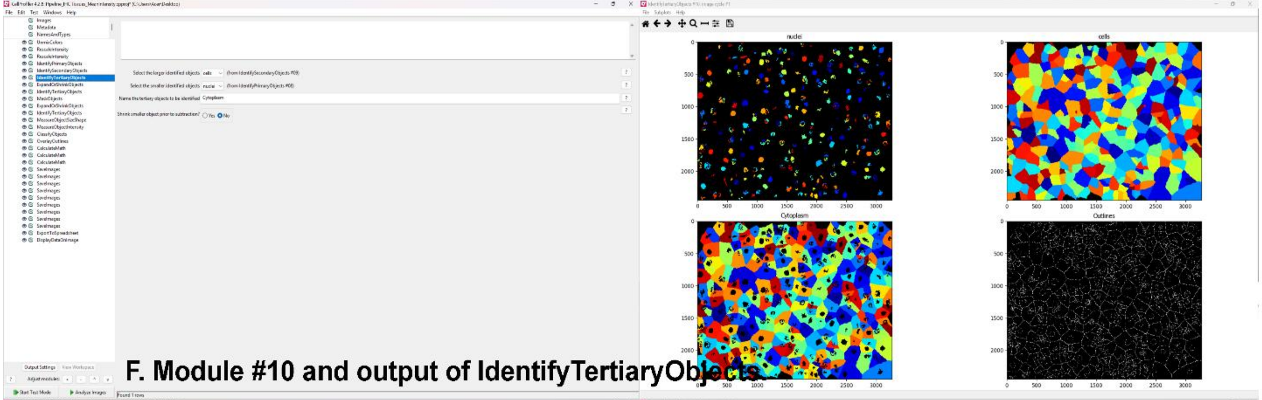

Select the larger identified objects: cells (from IdentifySecondaryObjects #09)

Select the smaller identified objects: nuclei (from IdentifyPrimaryObjects #08)

Name the tertiary objects to be identified: Cytoplasm

Shrink smaller object prior to subtraction?: ○ Yes ● No

F. Module #10 and output of IdentifyTertiaryObjects.

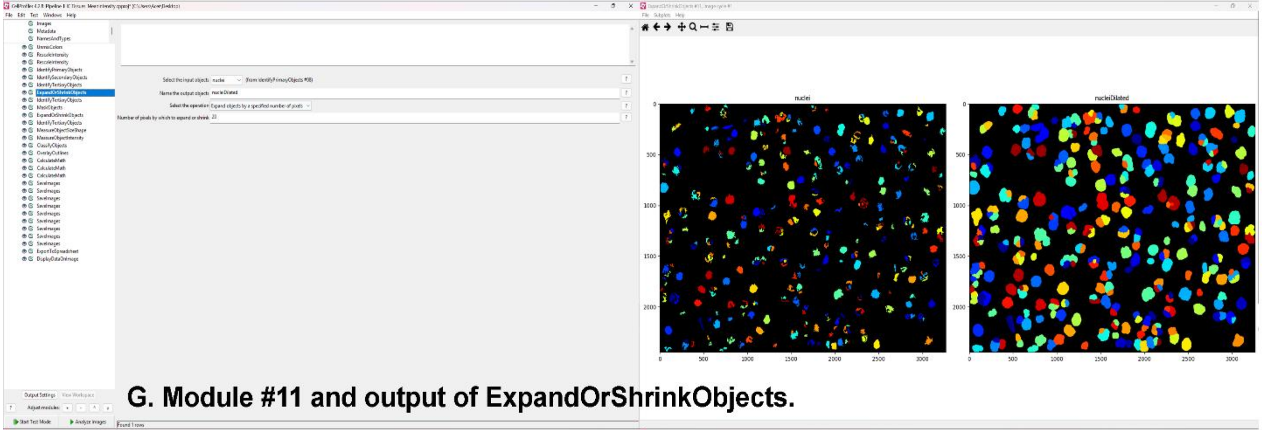

Select the input objects: nuclei (from IdentifyPrimaryObjects #08)

Name the output objects: nucleiDilated

Select the operation: Expand objects by a specified number of pixels

Number of pixels by which to expand or shrink: 20

G. Module #11 and output of ExpandOrShrinkObjects.

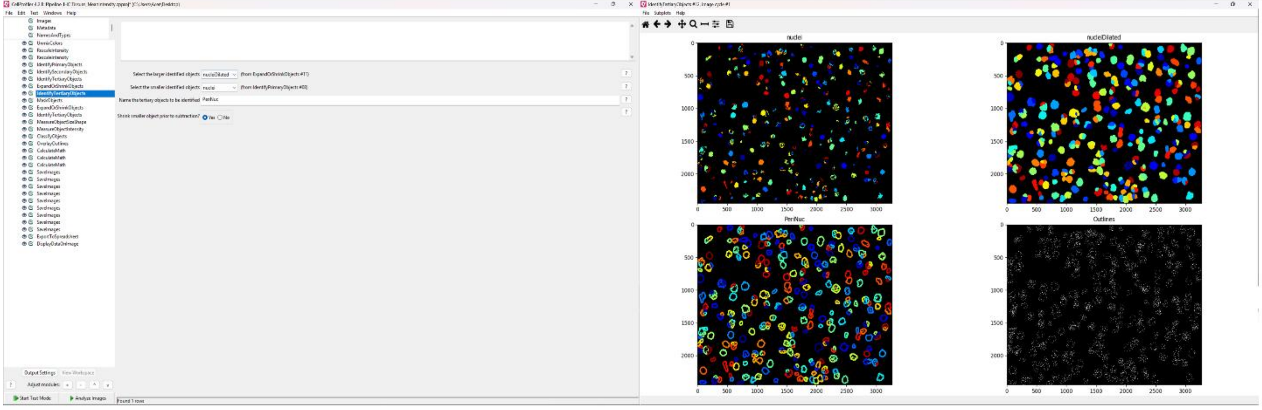

Select the larger identified objects: nucleiDilated (from ExpandOrShrinkObjects #11)

Select the smaller identified objects: nuclei (from IdentifyPrimaryObjects #08)

Name the tertiary objects to be identified: PeriNuc

Shrink smaller object prior to subtraction?: ● Yes ○ No

H. Module #12 and output of IdentifyTertiaryObjects.

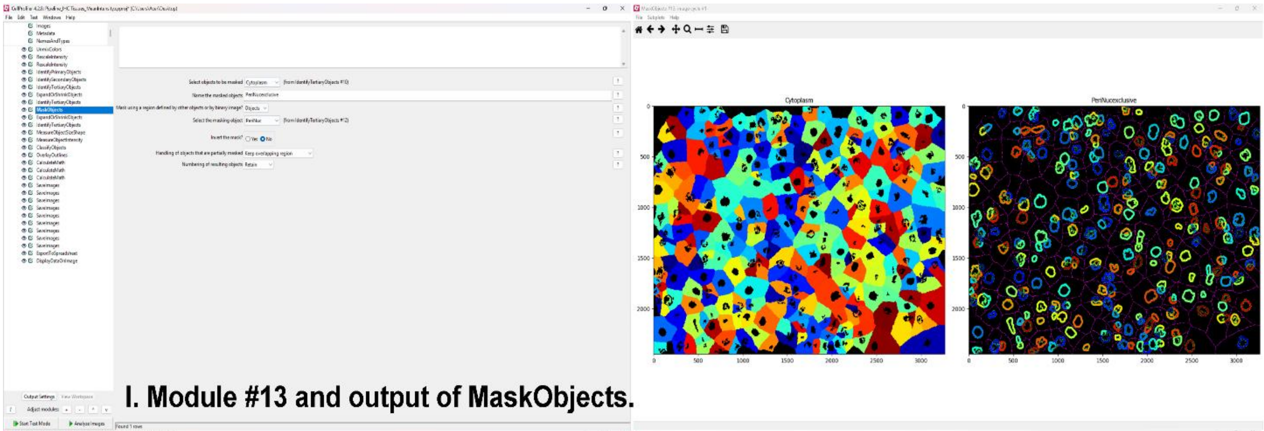

Select objects to be masked: Cytoplasm (from IdentifyTertiaryObjects #10)
Name the masked objects: PeriNucexclusive
Mask using a region defined by other objects or by binary image? Objects
Select the masking object: PeriNuc (from IdentifyTertiaryObjects #12)
Invert the mask? ○ Yes ● No
Handling of objects that are partially masked: Keep overlapping region
Numbering of resulting objects: Retain

I. Module #13 and output of MaskObjects.

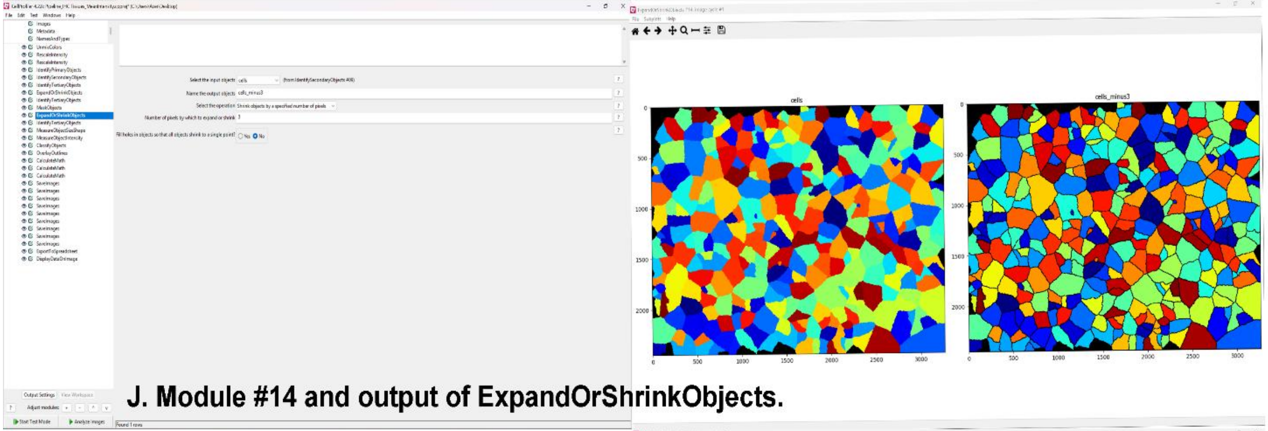

Select the input objects: cells (from IdentifySecondaryObjects #09)
Name the output objects: cells_minus3
Select the operation: Shrink objects by a specified number of pixels
Number of pixels by which to expand or shrink: 3
Fill holes in objects so that all objects shrink to a single point? ○ Yes ● No

J. Module #14 and output of ExpandOrShrinkObjects.

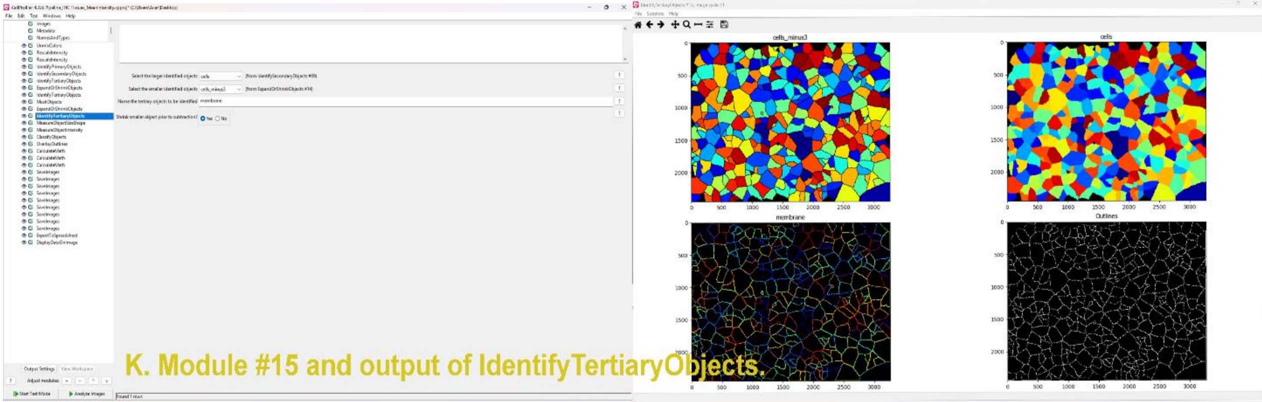

Select the larger identified objects: cells (from IdentifySecondaryObjects #09)
Select the smaller identified objects: cells_minus3 (from ExpandOrShrinkObjects #14)
Name the tertiary objects to be identified: membrane
Shrink smaller object prior to subtraction? ● Yes ○ No

K. Module #15 and output of IdentifyTertiaryObjects.

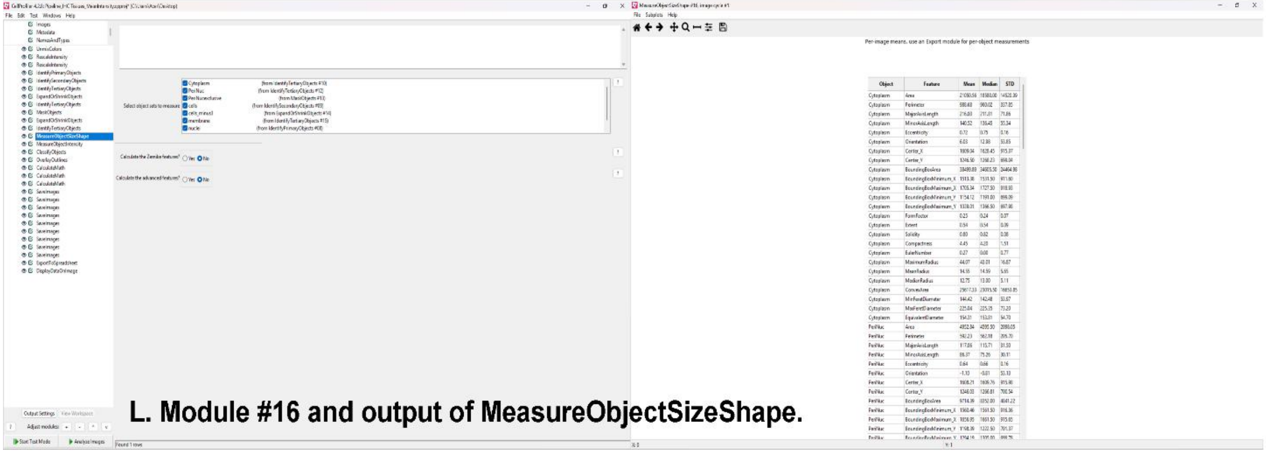

Select object sets to measure:
☑ Cytoplasm (from IdentifyTertiaryObjects #10)
☑ PeriNuc (from IdentifyTertiaryObjects #12)
☑ PeriNucexclusive (from MaskObjects #13)
☑ cells (from IdentifySecondaryObjects #09)
☑ cells_minus3 (from ExpandOrShrinkObjects #14)
☑ membrane (from IdentifyTertiaryObjects #15)
☑ nuclei (from IdentifyPrimaryObjects #08)

Calculate the Zernike features? ○ Yes ● No
Calculate the advanced features? ○ Yes ● No

Per-image means, use an Export module for per-object measurements

Object	Feature	Mean	Median	STD
Cytoplasm	Area	21050.56	18580.00	14520.39
Cytoplasm	Perimeter	986.68	980.02	337.85
Cytoplasm	MajorAxisLength	216.80	211.01	71.86
Cytoplasm	MinorAxisLength	140.52	136.45	55.34
Cytoplasm	Eccentricity	0.72	0.75	0.16
Cytoplasm	Orientation	6.03	12.88	53.85
Cytoplasm	Center_X	1809.04	1828.45	915.37
Cytoplasm	Center_Y	1246.56	1268.23	698.04
Cytoplasm	BoundingBoxArea	38499.89	34605.50	24464.98
Cytoplasm	BoundingBoxMinimum_X	1513.38	1531.50	911.60
Cytoplasm	BoundingBoxMaximum_X	1705.34	1727.50	918.93
Cytoplasm	BoundingBoxMinimum_Y	1154.12	1191.00	699.09
Cytoplasm	BoundingBoxMaximum_Y	1338.01	1366.50	697.98
Cytoplasm	FormFactor	0.25	0.24	0.07
Cytoplasm	Extent	0.54	0.54	0.09
Cytoplasm	Solidity	0.80	0.82	0.08
Cytoplasm	Compactness	4.45	4.20	1.51
Cytoplasm	EulerNumber	0.27	0.00	0.77
Cytoplasm	MaximumRadius	44.07	43.01	16.87
Cytoplasm	MeanRadius	14.55	14.99	5.65
Cytoplasm	MedianRadius	12.75	13.00	5.11
Cytoplasm	ConvexArea	25617.33	23015.50	16853.85
Cytoplasm	MinFeretDiameter	144.42	142.48	53.57
Cytoplasm	MaxFeretDiameter	225.04	225.35	73.20
Cytoplasm	EquivalentDiameter	154.31	153.81	54.70
PeriNuc	Area	4952.84	4595.50	2088.05
PeriNuc	Perimeter	592.23	562.18	205.70
PeriNuc	MajorAxisLength	117.06	115.71	31.50
PeriNuc	MinorAxisLength	88.37	75.26	30.11
PeriNuc	Eccentricity	0.64	0.66	0.16
PeriNuc	Orientation	-1.10	-0.81	53.13
PeriNuc	Center_X	1608.21	1606.76	915.90
PeriNuc	Center_Y	1248.03	1266.81	700.54
PeriNuc	BoundingBoxArea	9714.39	8352.00	4841.22
PeriNuc	BoundingBoxMinimum_X	1560.46	1561.50	916.36
PeriNuc	BoundingBoxMaximum_X	1658.95	1661.50	915.85
PeriNuc	BoundingBoxMinimum_Y	1198.39	1222.50	701.37

L. Module #16 and output of MeasureObjectSizeShape.

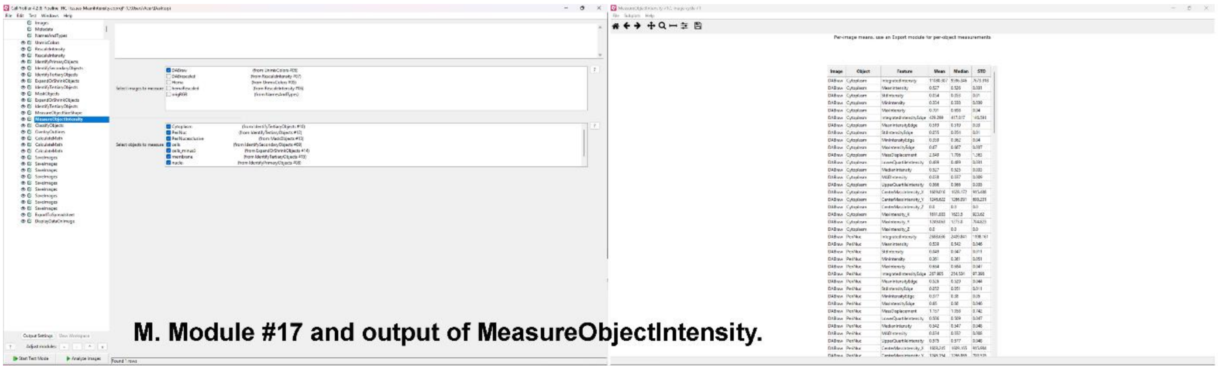

M. Module #17 and output of MeasureObjectIntensity.

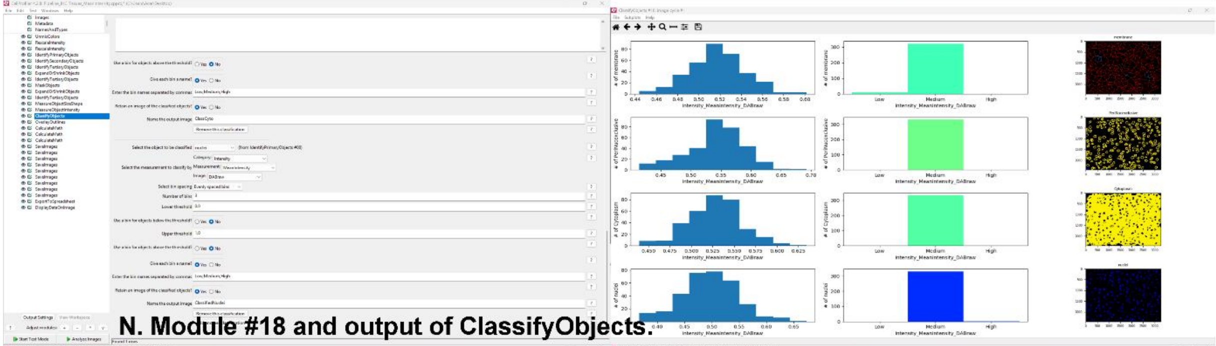

N. Module #18 and output of ClassifyObjects.

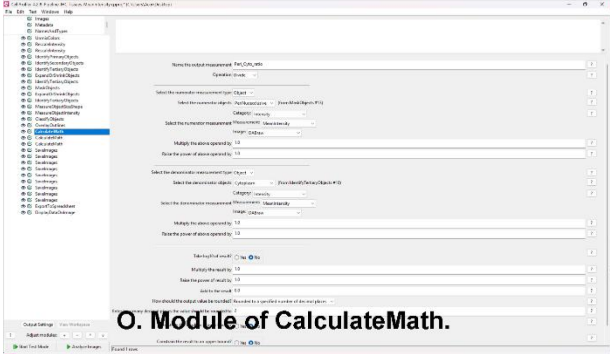

O. Module of CalculateMath.

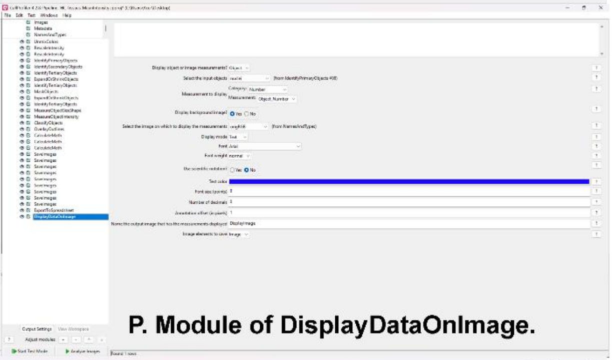

P. Module of DisplayDataOnImage.

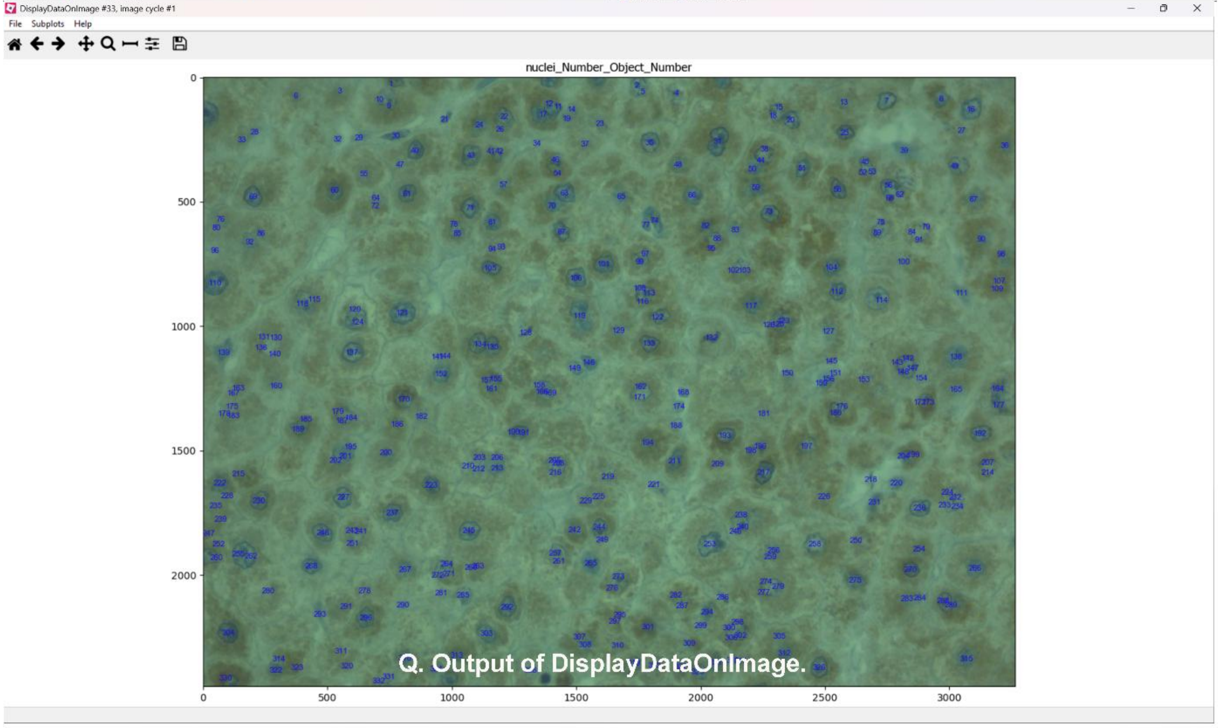

Q. Output of DisplayDataOnImage.

APPENDIX B – Binary Analysis Pipeline (CellProfiler)

The CellProfiler pipeline for quantifying DLG5 binary values is illustrated below. Each module represents a sequential step applied to brightfield IHC images. Key modules and outputs are provided.

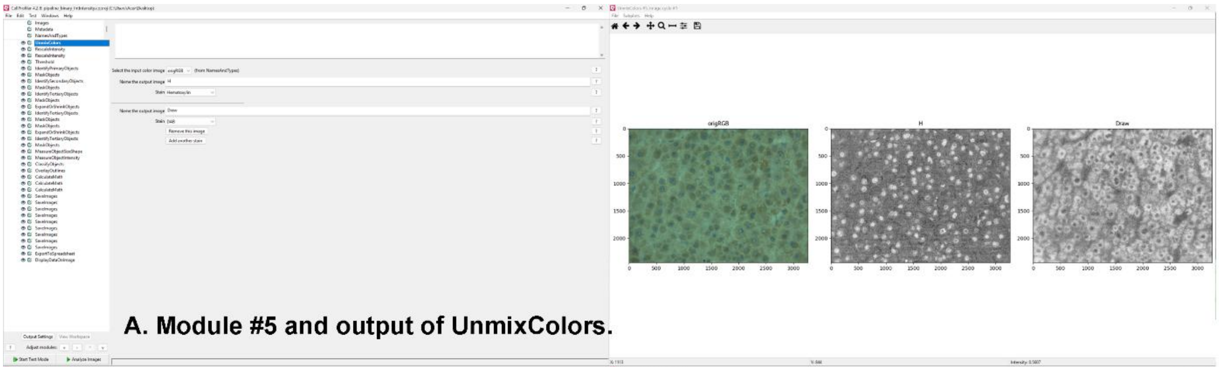

Select the input color image: origRGB (from NamesAndTypes)
Name the output image: H
Stain: Hematoxylin
Name the output image: Draw
Stain: DAB

A. Module #5 and output of UnmixColors.

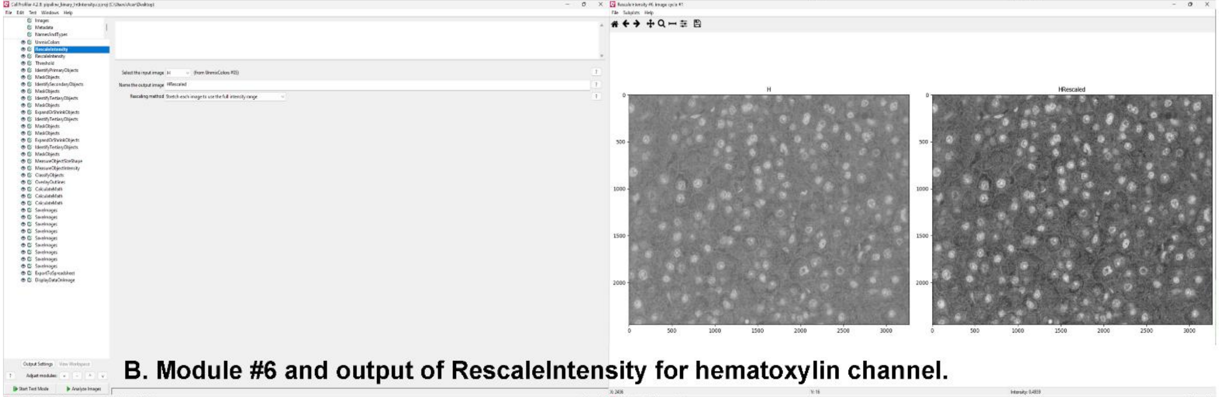

Select the input image: H (from UnmixColors #05)
Name the output image: HRescaled
Rescaling method: Stretch each image to use the full intensity range

B. Module #6 and output of RescaleIntensity for hematoxylin channel.

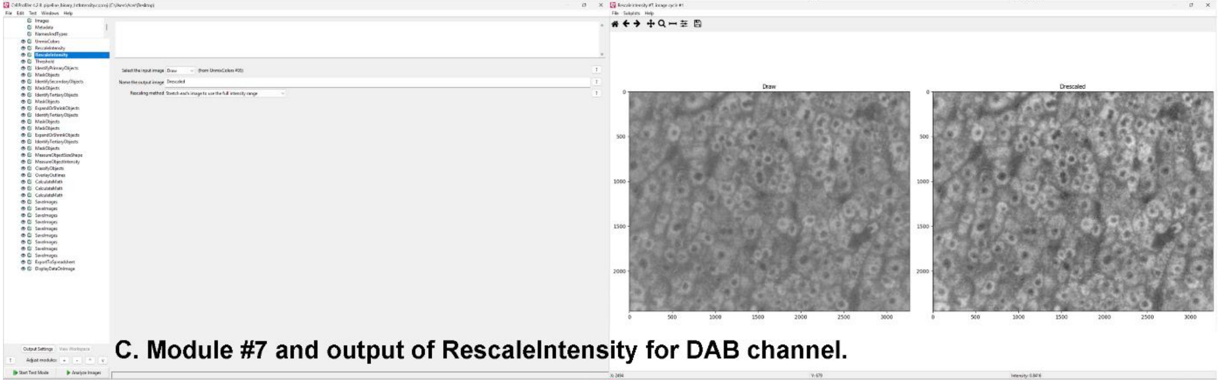

Select the input image: Draw (from UnmixColors #05)
Name the output image: Drescaled
Rescaling method: Stretch each image to use the full intensity range

C. Module #7 and output of RescaleIntensity for DAB channel.

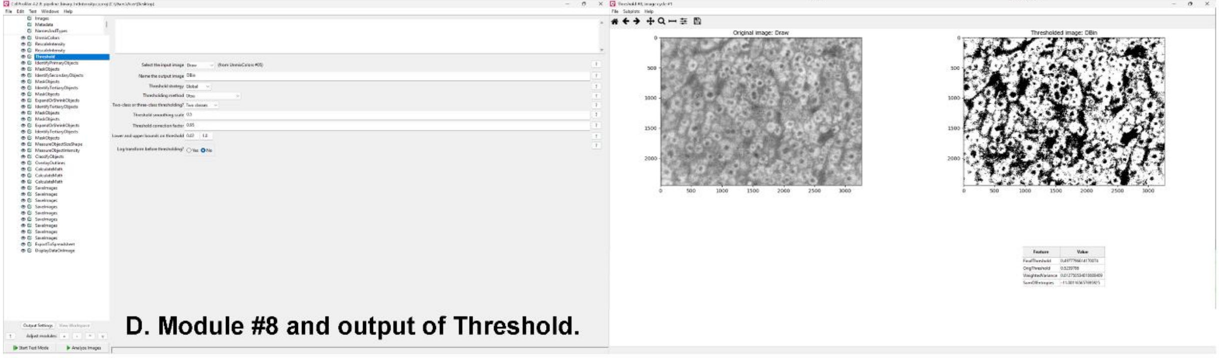

Select the input image: Draw (from UnmixColors #05)
Name the output image: DBin
Threshold strategy: Global
Thresholding method: Otsu
Two-class or three-class thresholding?: Two classes
Threshold smoothing scale: 0.3
Threshold correction factor: 0.95
Lower and upper bounds on threshold: 0.07 1.0
Log transform before thresholding?: ○ Yes ● No

Feature	Value
FinalThreshold	[illegible]
OrigThreshold	[illegible]
WeightedVariance	[illegible]
SumOfEntropies	[illegible]

D. Module #8 and output of Threshold.

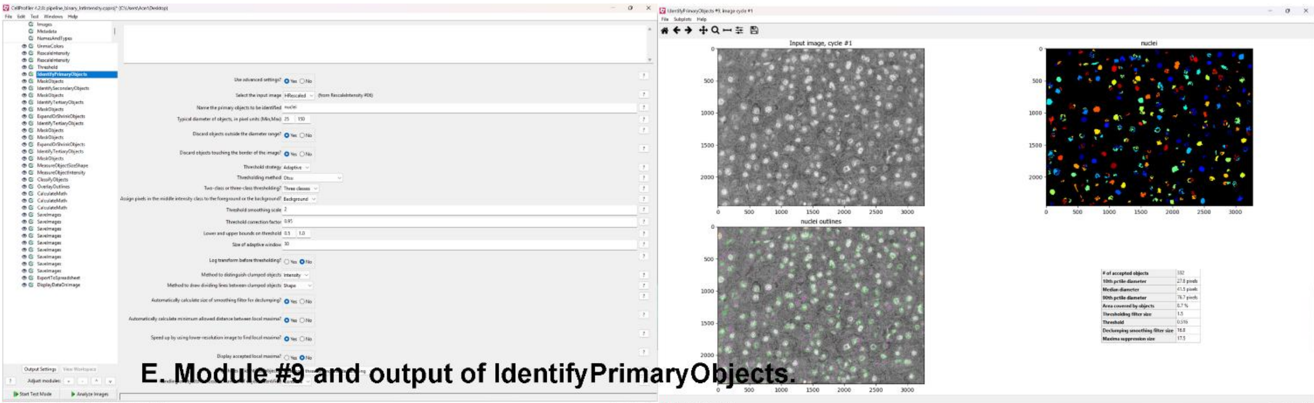

Use advanced settings? ● Yes ○ No
Select the input image: HRescaled (from RescaleIntensity #08)
Name the primary objects to be identified: nuclei
Typical diameter of objects, in pixel units (Min,Max): 25 150
Discard objects outside the diameter range? ● Yes ○ No
Discard objects touching the border of the image? ● Yes ○ No
Threshold strategy: Adaptive
Thresholding method: Otsu
Two-class or three-class thresholding? Three classes
Assign pixels in the middle intensity class to the foreground or the background? Background
Threshold smoothing scale: 2
Threshold correction factor: 0.95
Lower and upper bounds on threshold: 0.5 1.0
Size of adaptive window: 30
Log transform before thresholding? ○ Yes ● No
Method to distinguish clumped objects: Intensity
Method to draw dividing lines between clumped objects: Shape
Automatically calculate size of smoothing filter for declumping? ● Yes ○ No
Automatically calculate minimum allowed distance between local maxima? ● Yes ○ No
Speed up by using lower-resolution image to find local maxima? ● Yes ○ No
Display accepted local maxima? ○ Yes ● No

# of accepted objects	332
10th pctile diameter	27.8 pixels
Median diameter	41.5 pixels
90th pctile diameter	76.7 pixels
Area covered by objects	8.7 %
Thresholding filter size	1.5
Threshold	0.516
Declumping smoothing filter size	18.8
Maxima suppression size	17.5

E. Module #9 and output of IdentifyPrimaryObjects.

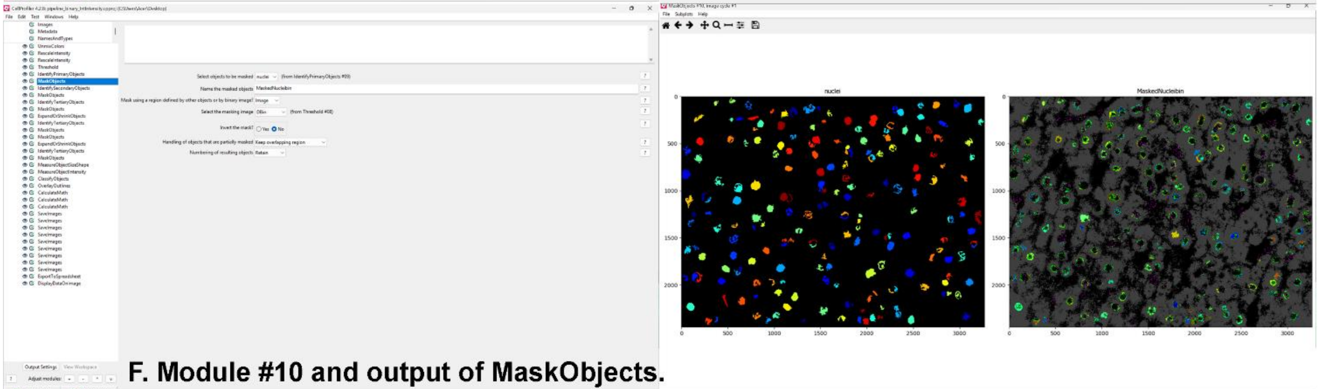

Select objects to be masked: nuclei (from IdentifyPrimaryObjects #09)
Name the masked objects: MaskedNucleibin
Mask using a region defined by other objects or by binary image? Image
Select the masking image: OBin (from Threshold #08)
Invert the mask? ○ Yes ● No
Handling of objects that are partially masked: Keep overlapping region
Numbering of resulting objects: Retain

F. Module #10 and output of MaskObjects.

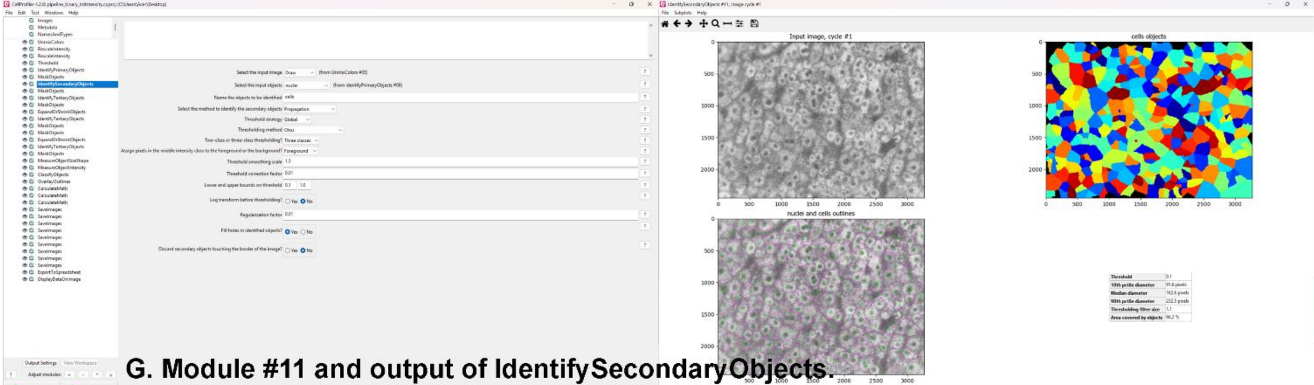

Select the input image: Draw (from UnmixColors #05)
Select the input objects: nuclei (from IdentifyPrimaryObjects #08)
Name the objects to be identified: cells
Select the method to identify the secondary objects: Propagation
Threshold strategy: Global
Thresholding method: Otsu
Two-class or three-class thresholding? Three classes
Assign pixels in the middle intensity class to the foreground or the background? Foreground
Threshold smoothing scale: 1.5
Threshold correction factor: 0.01
Lower and upper bounds on threshold: 0.1 1.0
Log transform before thresholding? ○ Yes ● No
Regularization factor: 0.01
Fill holes in identified objects? ● Yes ○ No
Discard secondary objects touching the border of the image? ○ Yes ● No

Threshold	0.1
10th pctile diameter	91.6 pixels
Median diameter	162.6 pixels
90th pctile diameter	232.5 pixels
Thresholding filter size	1.1
Area covered by objects	96.2 %

G. Module #11 and output of IdentifySecondaryObjects.

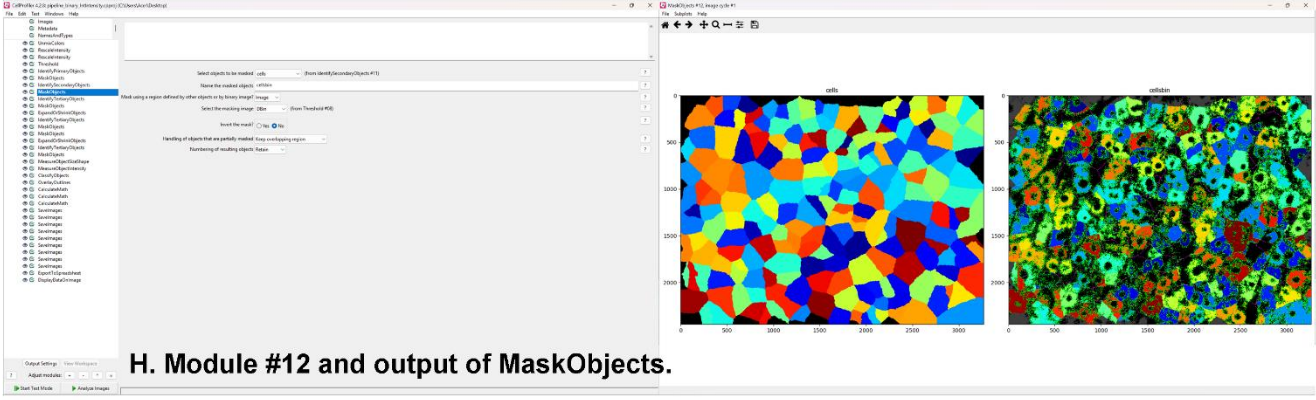

Select objects to be masked: cells (from IdentifySecondaryObjects #11)
Name the masked objects: cellsbin
Mask using a region defined by other objects or by binary image? Image
Select the masking image: DBin (from Threshold #08)
Invert the mask? ○ Yes ● No
Handling of objects that are partially masked: Keep overlapping region
Numbering of resulting objects: Retain

H. Module #12 and output of MaskObjects.

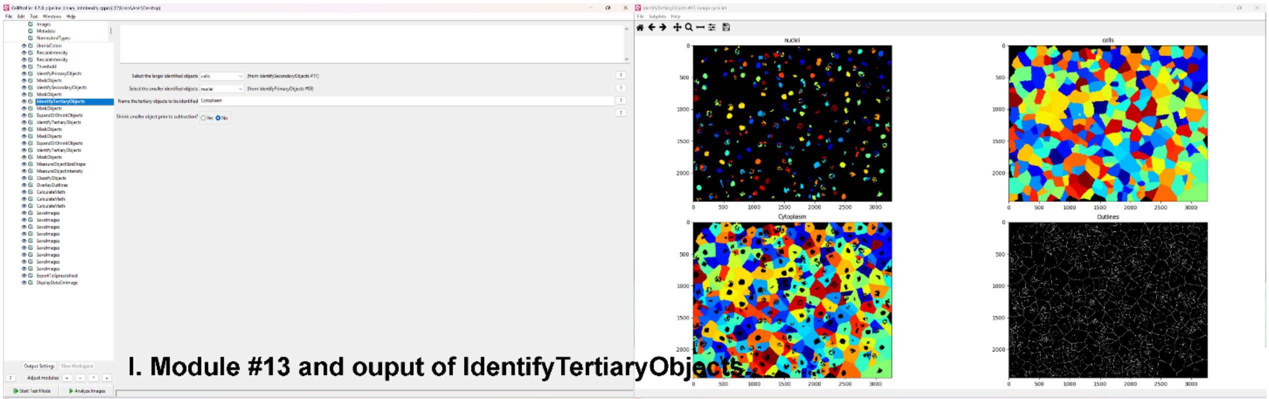

Select the larger identified objects: cells (from IdentifySecondaryObjects #11)

Select the smaller identified objects: nuclei (from IdentifyPrimaryObjects #09)

Name the tertiary objects to be identified: Cytoplasm

Shrink smaller object prior to subtraction? ○ Yes ● No

I. Module #13 and ouput of IdentifyTertiaryObjects.

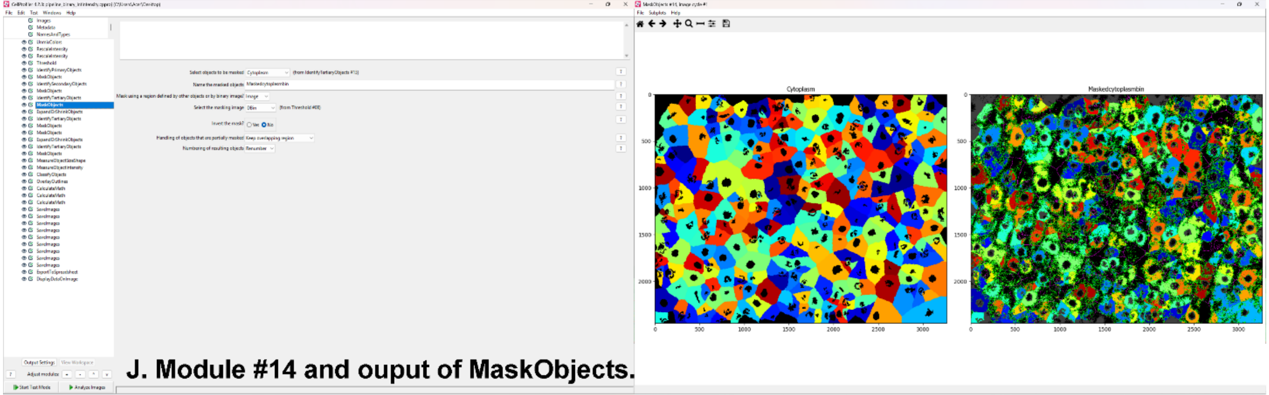

Select objects to be masked: Cytoplasm (from IdentifyTertiaryObjects #13)

Name the masked objects: Maskedcytoplasmbin

Mask using a region defined by other objects or by binary image? Image

Select the masking image: DBin (from Threshold #08)

Invert the mask? ○ Yes ● No

Handling of objects that are partially masked: Keep overlapping region

Numbering of resulting objects: Renumber

J. Module #14 and ouput of MaskObjects.

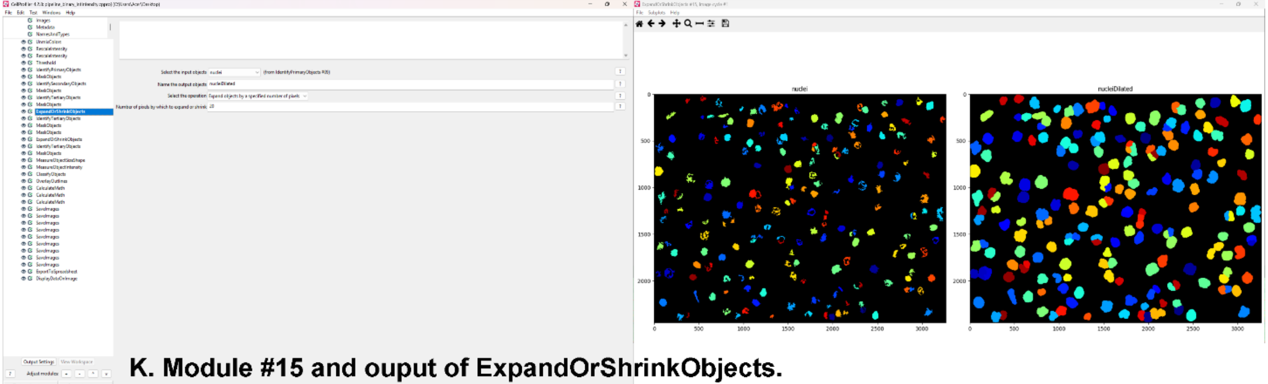

Select the input objects: nuclei (from IdentifyPrimaryObjects #08)

Name the output objects: nucleiDilated

Select the operation: Expand objects by a specified number of pixels

Number of pixels by which to expand or shrink: 20

K. Module #15 and ouput of ExpandOrShrinkObjects.

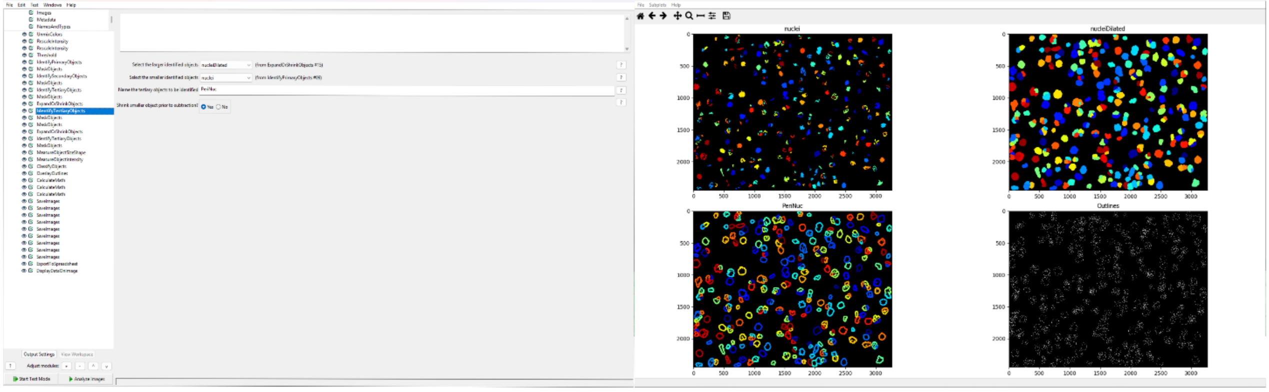

Select the larger identified objects: nucleiDilated (from ExpandOrShrinkObjects #15)

Select the smaller identified objects: nuclei (from IdentifyPrimaryObjects #08)

Name the tertiary objects to be identified: PeriNuc

Shrink smaller object prior to subtraction? ● Yes ○ No

L. Module #16 and ouput of IdentifyTertiaryObjects.

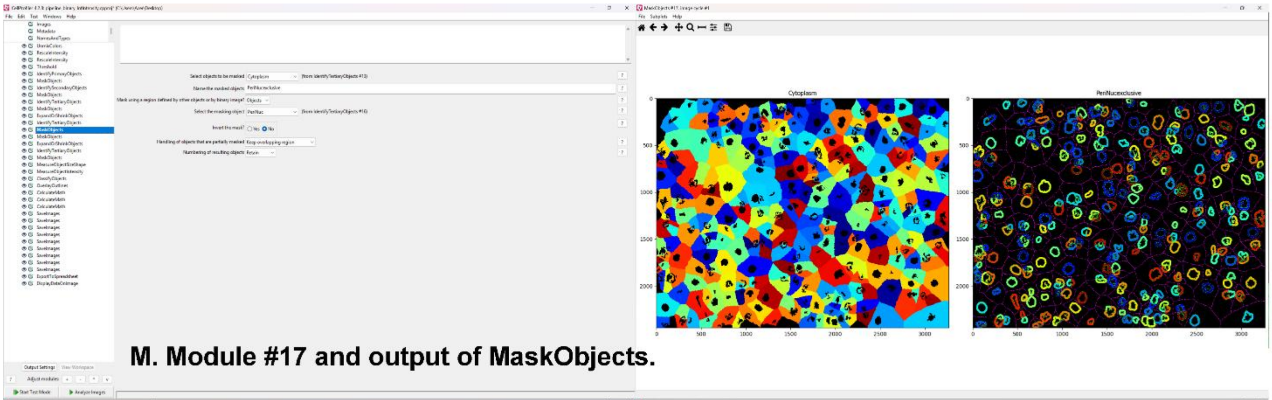

Select objects to be masked: Cytoplasm (from IdentifyTertiaryObjects #13)
Name the masked objects: PeriNucexclusive
Mask using a region defined by other objects or by binary image? Objects
Select the masking object: PeriNuc (from IdentifyTertiaryObjects #16)
Invert the mask? ○ Yes ● No
Handling of objects that are partially masked: Keep overlapping region
Numbering of resulting objects: Retain

M. Module #17 and output of MaskObjects.

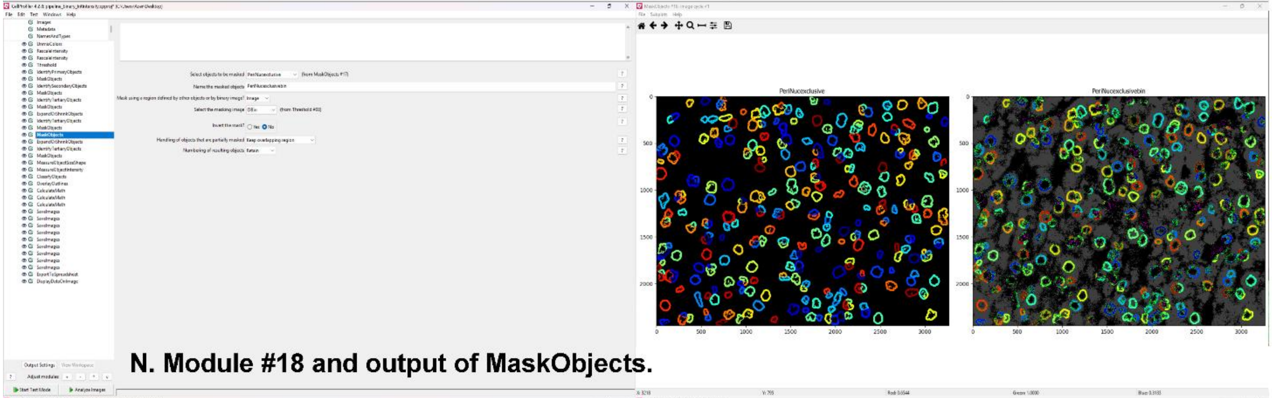

Select objects to be masked: PeriNucexclusive (from MaskObjects #17)
Name the masked objects: PeriNucexclusivebin
Mask using a region defined by other objects or by binary image? Image
Select the masking image: DBin (from Threshold #03)
Invert the mask? ○ Yes ● No
Handling of objects that are partially masked: Keep overlapping region
Numbering of resulting objects: Retain

N. Module #18 and output of MaskObjects.

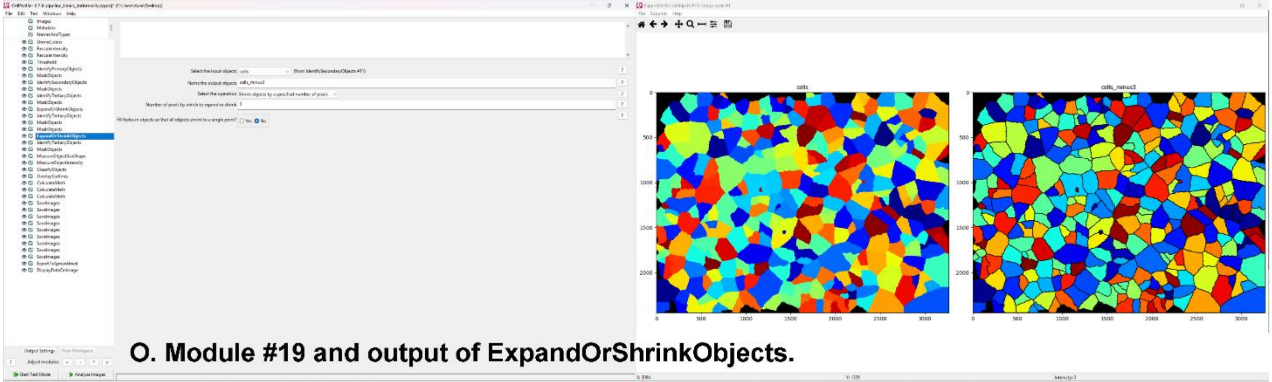

Select the input objects: cells (from IdentifySecondaryObjects #11)
Name the output objects: cells_minus3
Select the operation: Shrink objects by a specified number of pixels
Number of pixels by which to expand or shrink: 3
Fill holes in objects so that all objects shrink to a single point? ○ Yes ● No

O. Module #19 and output of ExpandOrShrinkObjects.

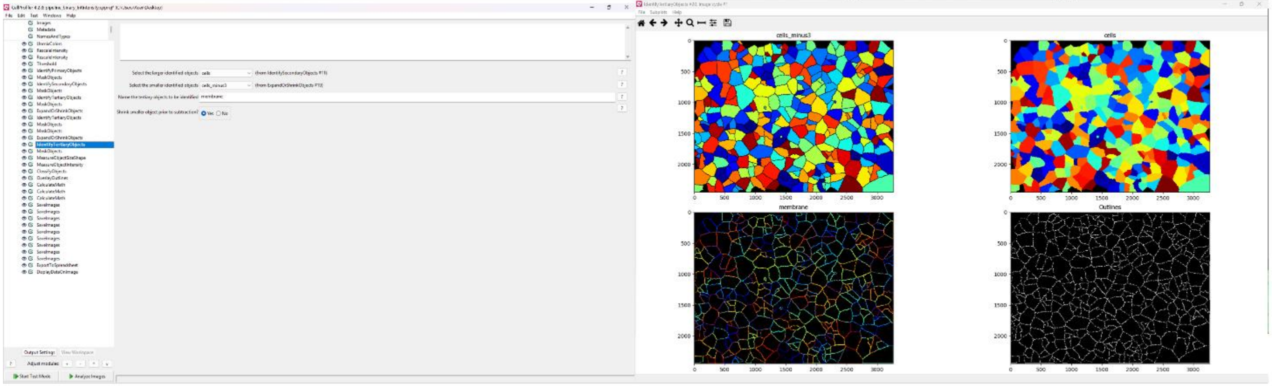

Select the larger identified objects: cells (from IdentifySecondaryObjects #11)
Select the smaller identified objects: cells_minus3 (from ExpandOrShrinkObjects #19)
Name the tertiary objects to be identified: membrane
Shrink smaller object prior to subtraction? ● Yes ○ No

P. Module #20 and output of IdentifyTertiaryObjects.

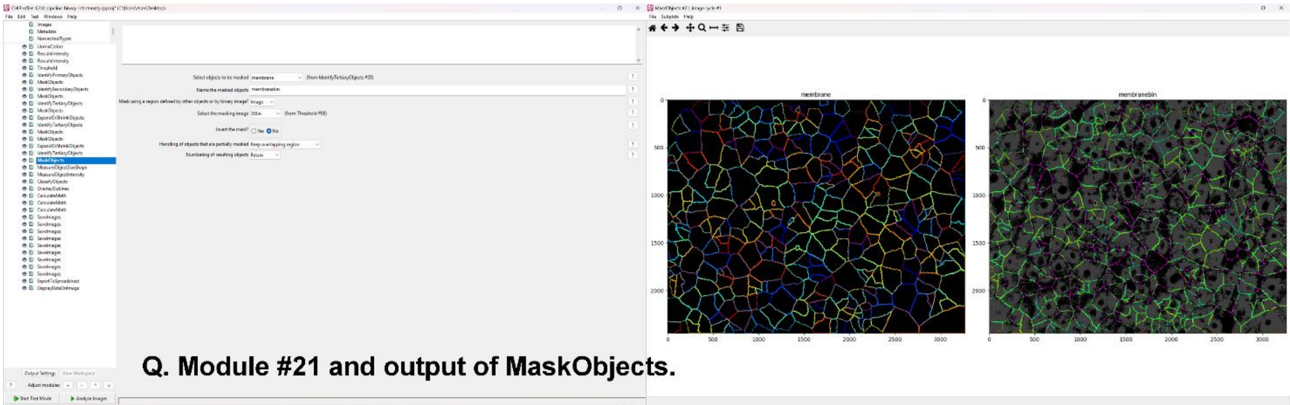

Select objects to be masked: membrane (from IdentifyTertiaryObjects #20)
Name the masked objects: membranebin
Mask using a region defined by other objects or by binary image?: Image
Select the masking image: DBin (from Threshold #08)
Invert the mask? ○ Yes ● No
Handling of objects that are partially masked: Keep overlapping region
Numbering of resulting objects: Retain

Q. Module #21 and output of MaskObjects.

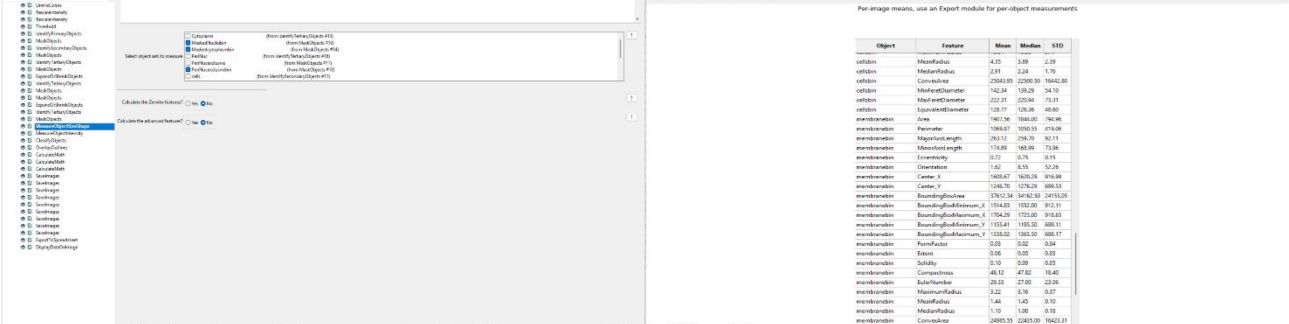

Select object sets to measure:
☐ Cytoplasm (from IdentifyTertiaryObjects #13)
☑ MaskedNucleibin (from MaskObjects #10)
☑ Maskedcytoplasmbin (from MaskObjects #14)
☐ PeriNuc (from IdentifyTertiaryObjects #16)
☐ PeriNucexclusive (from MaskObjects #17)
☑ PeriNucexclusivebin (from MaskObjects #18)
☐ cells (from IdentifySecondaryObjects #11)

Calculate the Zernike features? ○ Yes ● No
Calculate the advanced features? ○ Yes ● No

Per-image means, use an Export module for per-object measurements

Object	Feature	Mean	Median	STD
cellsbin	MeanRadius	4.35	3.89	2.39
cellsbin	MedianRadius	2.91	2.24	1.76
cellsbin	ConvexArea	25043.95	22500.50	16442.80
cellsbin	MinFeretDiameter	142.34	139.29	54.10
cellsbin	MaxFeretDiameter	222.31	220.94	73.31
cellsbin	EquivalentDiameter	128.77	126.36	48.60
membranebin	Area	1907.56	1844.00	794.96
membranebin	Perimeter	1069.87	1050.55	419.06
membranebin	MajorAxisLength	263.12	259.70	92.11
membranebin	MinorAxisLength	174.89	168.99	73.96
membranebin	Eccentricity	0.72	0.75	0.15
membranebin	Orientation	1.62	8.55	52.26
membranebin	Center_X	1608.67	1620.29	916.99
membranebin	Center_Y	1246.70	1276.29	699.53
membranebin	BoundingBoxArea	37612.34	34162.50	24155.05
membranebin	BoundingBoxMinimum_X	1514.83	1532.00	912.11
membranebin	BoundingBoxMaximum_X	1704.29	1723.00	918.63
membranebin	BoundingBoxMinimum_Y	1155.41	1195.50	699.11
membranebin	BoundingBoxMaximum_Y	1338.02	1363.50	698.17
membranebin	FormFactor	0.03	0.02	0.04
membranebin	Extent	0.06	0.05	0.03
membranebin	Solidity	0.10	0.09	0.05
membranebin	Compactness	48.12	47.82	18.40
membranebin	EulerNumber	29.33	27.00	23.06
membranebin	MaximumRadius	3.22	3.16	0.37
membranebin	MeanRadius	1.44	1.45	0.10
membranebin	MedianRadius	1.10	1.00	0.18
membranebin	ConvexArea	24985.55	22435.00	16423.31
membranebin	MinFeretDiameter	142.20	139.21	54.08
membranebin	MaxFeretDiameter	222.27	220.94	73.32
membranebin	EquivalentDiameter	48.12	48.45	10.66

R. Module #22 and output of MeasureObjectSizeShape.

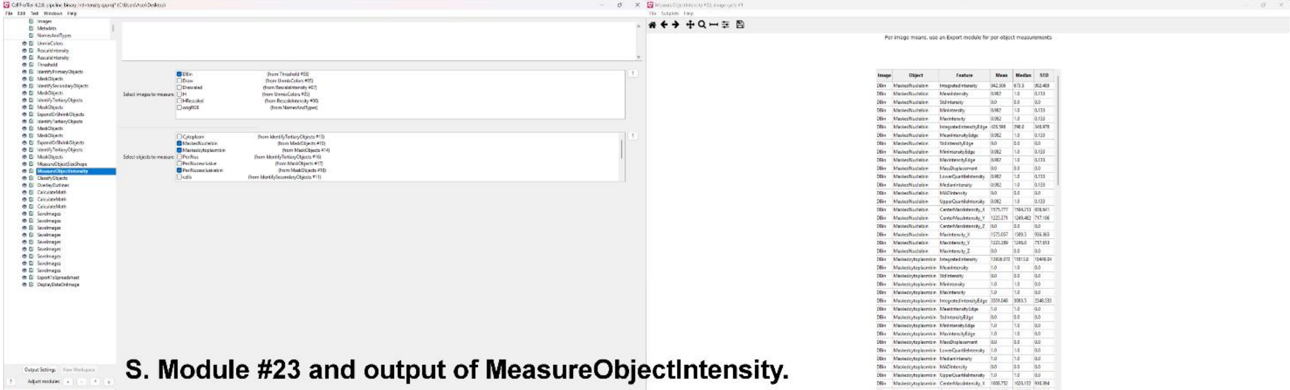

Select images to measure:
☑ DBin (from Threshold #08)
☐ Draw (from UnmixColors #05)
☐ Drescaled (from RescaleIntensity #07)
☐ H (from UnmixColors #05)
☐ HRescaled (from RescaleIntensity #06)
☐ origRGB (from NamesAndTypes)

Select objects to measure:
☐ Cytoplasm (from IdentifyTertiaryObjects #13)
☑ MaskedNucleibin (from MaskObjects #10)
☑ Maskedcytoplasmbin (from MaskObjects #14)
☐ PeriNuc (from IdentifyTertiaryObjects #16)
☐ PeriNucexclusive (from MaskObjects #17)
☑ PeriNucexclusivebin (from MaskObjects #18)
☐ cells (from IdentifySecondaryObjects #11)

Per image means, use an Export module for per-object measurements

Image	Object	Feature	Mean	Median	STD
DBin	MaskedNucleibin	IntegratedIntensity	942.506	673.5	902.488
DBin	MaskedNucleibin	MeanIntensity	0.982	1.0	0.133
DBin	MaskedNucleibin	StdIntensity	0.0	0.0	0.0
DBin	MaskedNucleibin	MinIntensity	0.982	1.0	0.133
DBin	MaskedNucleibin	MaxIntensity	0.982	1.0	0.133
DBin	MaskedNucleibin	IntegratedIntensityEdge	426.596	298.0	346.978
DBin	MaskedNucleibin	MeanIntensityEdge	0.982	1.0	0.133
DBin	MaskedNucleibin	StdIntensityEdge	0.0	0.0	0.0
DBin	MaskedNucleibin	MinIntensityEdge	0.982	1.0	0.133
DBin	MaskedNucleibin	MaxIntensityEdge	0.982	1.0	0.133
DBin	MaskedNucleibin	MassDisplacement	0.0	0.0	0.0
DBin	MaskedNucleibin	LowerQuartileIntensity	0.982	1.0	0.133
DBin	MaskedNucleibin	MedianIntensity	0.982	1.0	0.133
DBin	MaskedNucleibin	MADIntensity	0.0	0.0	0.0
DBin	MaskedNucleibin	UpperQuartileIntensity	0.982	1.0	0.133
DBin	MaskedNucleibin	CenterMassIntensity_X	1575.777	1594.213	938.841
DBin	MaskedNucleibin	CenterMassIntensity_Y	1225.371	1249.482	717.106
DBin	MaskedNucleibin	CenterMassIntensity_Z	0.0	0.0	0.0
DBin	MaskedNucleibin	MaxIntensity_X	1575.057	1589.5	936.365
DBin	MaskedNucleibin	MaxIntensity_Y	1223.389	1248.0	717.813
DBin	MaskedNucleibin	MaxIntensity_Z	0.0	0.0	0.0
DBin	Maskedcytoplasmbin	IntegratedIntensity	13908.072	11813.0	10448.04
DBin	Maskedcytoplasmbin	MeanIntensity	1.0	1.0	0.0
DBin	Maskedcytoplasmbin	StdIntensity	0.0	0.0	0.0
DBin	Maskedcytoplasmbin	MinIntensity	1.0	1.0	0.0
DBin	Maskedcytoplasmbin	MaxIntensity	1.0	1.0	0.0
DBin	Maskedcytoplasmbin	IntegratedIntensityEdge	3501.048	3083.5	2348.533
DBin	Maskedcytoplasmbin	MeanIntensityEdge	1.0	1.0	0.0
DBin	Maskedcytoplasmbin	StdIntensityEdge	0.0	0.0	0.0
DBin	Maskedcytoplasmbin	MinIntensityEdge	1.0	1.0	0.0
DBin	Maskedcytoplasmbin	MaxIntensityEdge	1.0	1.0	0.0
DBin	Maskedcytoplasmbin	MassDisplacement	0.0	0.0	0.0
DBin	Maskedcytoplasmbin	LowerQuartileIntensity	1.0	1.0	0.0
DBin	Maskedcytoplasmbin	MedianIntensity	1.0	1.0	0.0
DBin	Maskedcytoplasmbin	MADIntensity	0.0	0.0	0.0
DBin	Maskedcytoplasmbin	UpperQuartileIntensity	1.0	1.0	0.0
DBin	Maskedcytoplasmbin	CenterMassIntensity_X	1608.752	1626.132	916.394

S. Module #23 and output of MeasureObjectIntensity.

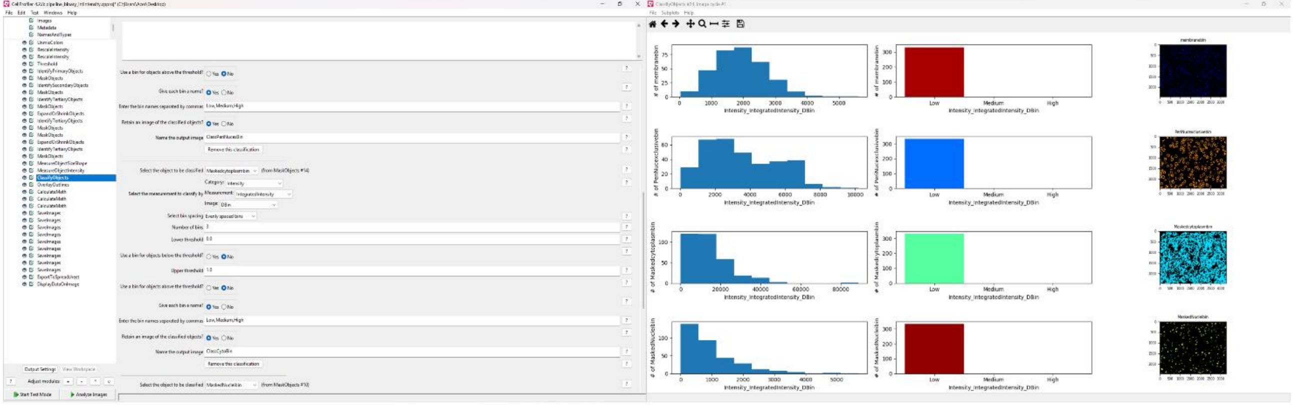

Use a bin for objects above the threshold? ○ Yes ● No
Give each bin a name? ● Yes ○ No
Enter the bin names separated by commas: Low,Medium,High
Retain an image of the classified objects? ● Yes ○ No
Name the output image: ClassPeriNucexBin
Remove this classification

Select the object to be classified: Maskedcytoplasmbin (from MaskObjects #14)
Select the measurement to classify by: Category: Intensity; Measurement: IntegratedIntensity; Image: DBin
Select bin spacing: Evenly spaced bins
Number of bins: 3
Lower threshold: 0.0
Use a bin for objects below the threshold? ○ Yes ● No
Upper threshold: 1.0
Use a bin for objects above the threshold? ○ Yes ● No
Give each bin a name? ● Yes ○ No
Enter the bin names separated by commas: Low,Medium,High
Retain an image of the classified objects? ● Yes ○ No
Name the output image: ClassCytoBin
Remove this classification

Select the object to be classified: MaskedNucleibin (from MaskObjects #10)

T. Module #24 and output of ClassifyObjects.

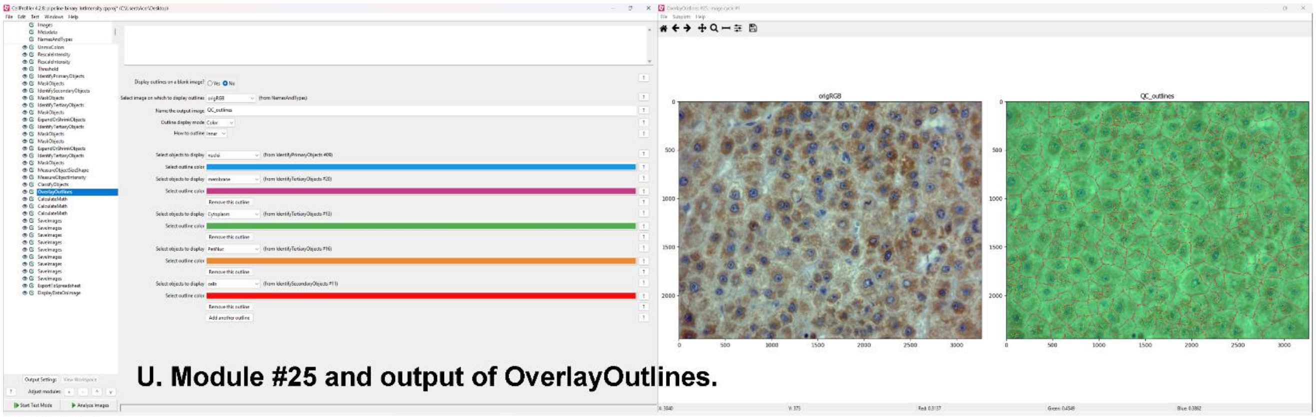

Display outlines on a blank image? ○ Yes ● No

Select image on which to display outlines: origRGB (from NamesAndTypes)

Name the output image: QC_outlines

Outline display mode: Color

How to outline: Inner

Select objects to display: nuclei (from IdentifyPrimaryObjects #09)

Select outline color: 🟦

Select objects to display: membrane (from IdentifyTertiaryObjects #20)

Select outline color: 🟪

Select objects to display: Cytoplasm (from IdentifyTertiaryObjects #13)

Select outline color: 🟩

Select objects to display: PeriNuc (from IdentifyTertiaryObjects #16)

Select outline color: 🟧

Select objects to display: cells (from IdentifySecondaryObjects #11)

Select outline color: 🟥

U. Module #25 and output of OverlayOutlines.

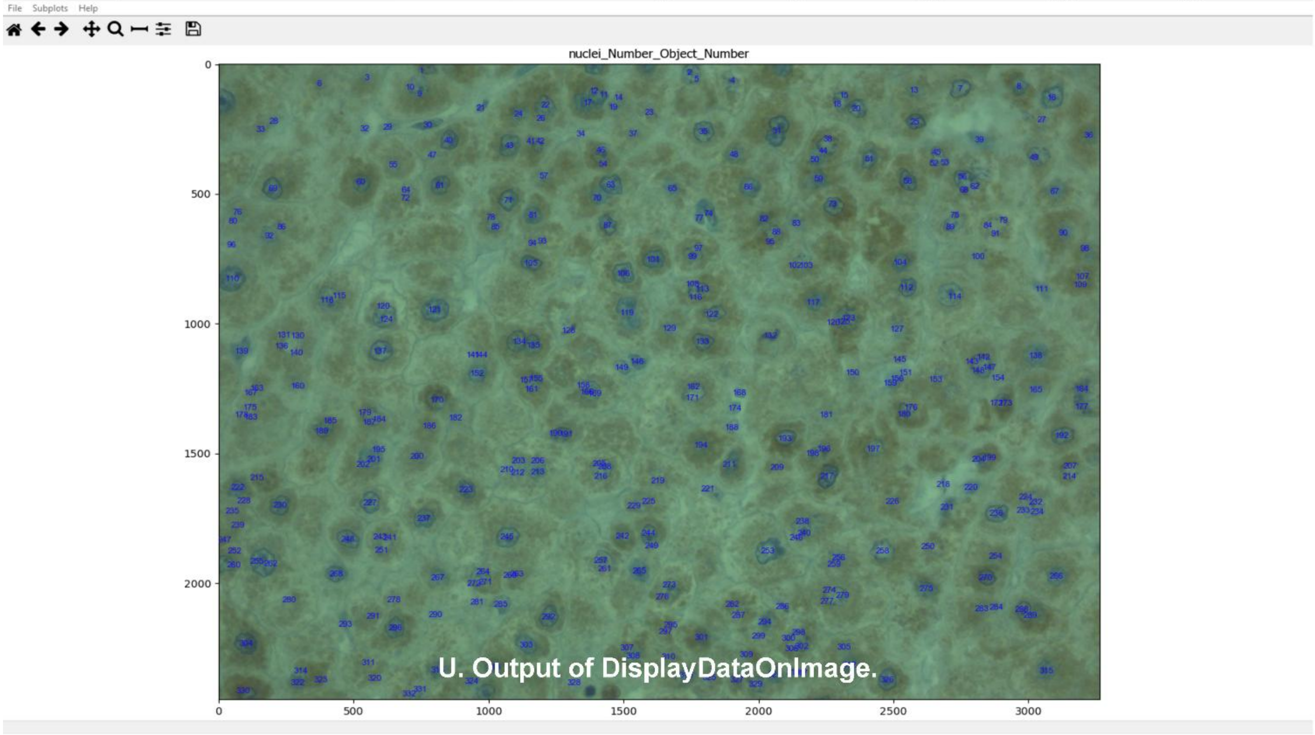

U. Output of DisplayDataOnImage.

APPENDIX C - Full Heatmap of *DLG5* Interactors

Complete transcriptomic heatmap illustrating expression patterns of *DLG5* and its polarity-associated interactors in HCC and adjacent tissues. The heatmap displays normalized $\log_2$ intensity values derived from the TCGA-LIHC dataset (study ID HS-01630) under the mRNA-Seq Gene Level platform.

Experimental	Anatomical Part	Neoplasm	TNM stage (S)
HS-01630 prim_liv hcc_45y_m_7-31	—	liver, hepatocellular carcinoma...	IIIA
HS-01630 prim_liv hcc_66y_m_7-157	—	liver, hepatocellular carcinoma...	I
HS-01630 prim_liv hcc_56y_m_7-85	—	liver, hepatocellular carcinoma...	II
HS-01630 prim_liv hcc_58y_m_7-105	—	liver, hepatocellular carcinoma...	IIIA
HS-01630 prim_liv hcc_59y_m_7-114	—	liver, hepatocellular carcinoma...	IIIA
HS-01630 prim_liv hcc_57y_m_7-89	—	liver, hepatocellular carcinoma...	II
HS-01630 prim_liv hcc_51y_f_7-264	—	liver, hepatocellular carcinoma...	IIIA
HS-01630 prim_liv hcc_24y_m_7-5	—	liver, hepatocellular carcinoma...	II
HS-01630 prim_liv hcc_68y_m_7-176	—	liver, hepatocellular carcinoma...	II
HS-01630 prim_liv hcc_67y_f_7-316	—	liver, hepatocellular carcinoma...	IIIC
HS-01630 prim_liv hcc_55y_m_7-81	—	liver, hepatocellular carcinoma...	II
HS-01630 prim_liv hcc_50y_m_7-49	—	liver, hepatocellular carcinoma...	I
HS-01630 prim_liv hcc_59y_m_7-112	—	liver, hepatocellular carcinoma...	IIIA
HS-01630 prim_liv hcc_66y_f_7-314	—	liver, hepatocellular carcinoma...	IIIC
HS-01630 prim_liv hcc_69y_m_7-184	—	liver, hepatocellular carcinoma...	I
HS-01630 prim_liv hcc_51y_m_7-54	—	liver, hepatocellular carcinoma...	I
HS-01630 prim_liv hcc_70y_m_7-199	—	liver, hepatocellular carcinoma...	IIIB
HS-01630 prim_liv hcc_61y_m_7-126	—	liver, hepatocellular carcinoma...	IIIA
HS-01630 prim_liv hcc_62y_m_7-129	—	liver, hepatocellular carcinoma...	I
HS-01630 prim_liv hcc_73y_m_7-215	—	liver, hepatocellular carcinoma...	IIIA
HS-01630 prim_liv hcc_38y_m_7-19	—	liver, hepatocellular carcinoma...	II
HS-01630 prim_liv hcc_35y_m_7-12	—	liver, hepatocellular carcinoma...	IIIA
HS-01630 prim_liv hcc_61y_f_7-293	—	liver, hepatocellular carcinoma...	IIIC
HS-01630 prim_liv hcc_70y_m_7-197	—	liver, hepatocellular carcinoma...	II
HS-01630 prim_liv hcc_48y_m_7-43	—	liver, hepatocellular carcinoma...	II
HS-01630 prim_liv hcc_57y_f_7-280	—	liver, hepatocellular carcinoma...	I
HS-01630 prim_liv hcc_23y_m_7-3	—	liver, hepatocellular carcinoma...	II
HS-01630 prim_liv hcc_52y_f_7-266	—	liver, hepatocellular carcinoma...	IIIA
HS-01630 prim_liv hcc_60y_f_7-287	—	liver, hepatocellular carcinoma...	I
HS-01630 prim_liv hcc_56y_f_7-277	—	liver, hepatocellular carcinoma...	I
HS-01630 prim_liv hcc_70y_m_7-193	—	liver, hepatocellular carcinoma...	I
HS-01630 prim_liv hcc_51y_m_7-58	—	liver, hepatocellular carcinoma...	I
HS-01630 prim_liv hcc_51y_f_7-261	—	liver, hepatocellular carcinoma...	I
HS-01630 prim_liv hcc_70y_m_7-194	—	liver, hepatocellular carcinoma...	I
HS-01630 prim_liv hcc_48y_m_7-39	—	liver, hepatocellular carcinoma...	I
HS-01630 prim_liv hcc_69y_m_7-189	—	liver, hepatocellular carcinoma...	II
HS-01630 prim_liv hcc_66y_m_7-160	—	liver, hepatocellular carcinoma...	II
HS-01630 prim_liv hcc_48y_m_7-40	—	liver, hepatocellular carcinoma...	I
HS-01630 prim_liv hcc_18y_m_7-2	—	liver, hepatocellular carcinoma...	IIIC
HS-01630 prim_liv hcc_80y_m_7-235	—	liver, hepatocellular carcinoma...	—
HS-01630 prim_liv hcc_81y_f_7-349	—	liver, hepatocellular carcinoma...	II
HS-01630 prim_liv hcc_68y_m_7-180	—	liver, hepatocellular carcinoma...	IIIA
HS-01630 prim_liv hcc_55y_f_7-275	—	liver, hepatocellular carcinoma...	II
HS-01630 prim_liv hcc_64y_m_7-138	—	liver, hepatocellular carcinoma...	I
HS-01630 prim_liv hcc_44y_m_7-27	—	liver, hepatocellular carcinoma...	II
HS-01630 prim_liv hcc_83y_f_7-351	—	liver, hepatocellular carcinoma...	I
HS-01630 prim_liv hcc_59y_f_7-286	—	liver, hepatocellular carcinoma...	IIIA
HS-01630 prim_liv hcc_73y_m_7-214	—	liver, hepatocellular carcinoma...	IIIA
HS-01630 prim_liv hcc_54y_f_7-272	—	liver, hepatocellular carcinoma...	II
HS-01630 prim_liv hcc_60y_f_7-289	—	liver, hepatocellular carcinoma...	IIIA
HS-01630 prim_liv hcc_72y_m_7-205	—	liver, hepatocellular carcinoma...	I
HS-01630 prim_liv hcc_43y_m_7-23	—	liver, hepatocellular carcinoma...	I
HS-01630 prim_liv hcc_51y_m_7-53	—	liver, hepatocellular carcinoma...	—
HS-01630 prim_liv hcc_35y_m_7-13	—	liver, hepatocellular carcinoma...	IIIA
HS-01630 prim_liv hcc_52y_m_7-63	—	liver, hepatocellular carcinoma...	I
HS-01630 prim_liv hcc_51y_f_7-262	—	liver, hepatocellular carcinoma...	II
HS-01630 prim_liv hcc_42y_m_7-22	—	liver, hepatocellular carcinoma...	II
HS-01630 prim_liv hcc_58y_f_7-281	—	liver, hepatocellular carcinoma...	II
HS-01630 prim_liv hcc_46y_m_7-32	—	liver, hepatocellular carcinoma...	I
HS-01630 prim_liv hcc_65y_m_7-149	—	liver, hepatocellular carcinoma...	I
HS-01630 prim_liv hcc_48y_f_7-257	—	liver, hepatocellular carcinoma...	II
HS-01630 prim_liv hcc_71y_f_7-326	—	liver, hepatocellular carcinoma...	IIIC
HS-01630 prim_liv hcc_16y_m_7-1	—	liver, hepatocellular carcinoma...	IIIA
HS-01630 prim_liv hcc_70y_m_7-198	—	liver, hepatocellular carcinoma...	IIIA
HS-01630 prim_liv hcc_72y_m_7-208	—	liver, hepatocellular carcinoma...	I
HS-01630 prim_liv hcc_56y_m_7-86	—	liver, hepatocellular carcinoma...	IIIA
HS-01630 prim_liv hcc_60y_m_7-117	—	liver, hepatocellular carcinoma...	II
HS-01630 prim_liv hcc_74y_f_7-336	—	liver, hepatocellular carcinoma...	IIIA
HS-01630 prim_liv hcc_68y_m_7-172	—	liver, hepatocellular carcinoma...	I
HS-01630 prim_liv hcc_39y_m_7-20	—	liver, hepatocellular carcinoma...	I
HS-01630 prim_liv hcc_68y_m_7-177	—	liver, hepatocellular carcinoma...	IIIA
HS-01630 prim_liv hcc_65y_f_7-307	—	liver, hepatocellular carcinoma...	IIIB
HS-01630 prim_liv hcc_71y_m_7-202	—	liver, hepatocellular carcinoma...	IIIA
HS-01630 prim_liv hcc_62y_m_7-130	—	liver, hepatocellular carcinoma...	I
HS-01630 prim_liv hcc_75y_m_7-223	—	liver, hepatocellular carcinoma...	II
HS-01630 prim_liv hcc_65y_m_7-146	—	liver, hepatocellular carcinoma...	I
HS-01630 prim_liv hcc_70y_m_7-192	—	liver, hepatocellular carcinoma...	I
HS-01630 prim_liv hcc_66y_m_7-159	—	liver, hepatocellular carcinoma...	II
HS-01630 prim_liv hcc_46y_f_7-255	—	liver, hepatocellular carcinoma...	I
HS-01630 prim_liv hcc_56y_m_7-83	—	liver, hepatocellular carcinoma...	I
HS-01630 prim_liv hcc_58y_m_7-92	—	liver, hepatocellular carcinoma...	—
HS-01630 prim_liv hcc_67y_m_7-162	—	liver, hepatocellular carcinoma...	I
HS-01630 prim_liv hcc_51y_m_7-62	—	liver, hepatocellular carcinoma...	IIIC
HS-01630 prim_liv hcc_60y_f_7-288	—	liver, hepatocellular carcinoma...	II
HS-01630 prim_liv hcc_59y_f_7-285	—	liver, hepatocellular carcinoma...	I
HS-01630 prim_liv hcc_59y_m_7-109	—	liver, hepatocellular carcinoma...	I
HS-01630 prim_liv hcc_81y_f_7-348	—	liver, hepatocellular carcinoma...	I
HS-01630 prim_liv hcc_55y_m_7-82	—	liver, hepatocellular carcinoma...	IIIA
HS-01630 prim_liv hcc_74y_f_7-335	—	liver, hepatocellular carcinoma...	IIIA
HS-01630 prim_liv hcc_64y_f_7-298	—	liver, hepatocellular carcinoma...	—
HS-01630 prim_liv hcc_68y_m_7-174	—	liver, hepatocellular carcinoma...	I
HS-01630 prim_liv hcc_69y_m_7-181	—	liver, hepatocellular carcinoma...	—
HS-01630 prim_liv hcc_72y_f_7-327	—	liver, hepatocellular carcinoma...	—
HS-01630 prim_liv hcc_43y_f_7-251	—	liver, hepatocellular carcinoma...	I
HS-01630 prim_liv hcc_65y_m_7-148	—	liver, hepatocellular carcinoma...	I
HS-01630 prim_liv hcc_62y_f_7-294	—	liver, hepatocellular carcinoma...	I
HS-01630 prim_liv hcc_67y_m_7-165	—	liver, hepatocellular carcinoma...	II
HS-01630 prim_liv hcc_77y_m_7-230	—	liver, hepatocellular carcinoma...	—
HS-01630 prim_liv hcc_38y_m_7-16	—	liver, hepatocellular carcinoma...	I
HS-01630 prim_liv hcc_50y_f_7-259	—	liver, hepatocellular carcinoma...	IIIA
HS-01630 prim_liv hcc_45y_f_7-254	—	liver, hepatocellular carcinoma...	IIIA
HS-01630 prim_liv hcc_75y_f_7-340	—	liver, hepatocellular carcinoma...	IIIA
HS-01630 prim_liv hcc_32y_m_7-9	—	liver, hepatocellular carcinoma...	I
HS-01630 prim_liv hcc_56y_f_7-278	—	liver, hepatocellular carcinoma...	I
HS-01630 prim_liv hcc_m_7-240	—	liver, hepatocellular carcinoma...	II
HS-01630 prim_liv hcc_70y_m_7-196	—	liver, hepatocellular carcinoma...	II
HS-01630 prim_liv hcc_75y_m_7-221	—	liver, hepatocellular carcinoma...	I
HS-01630 prim_liv hcc_29y_f_7-246	—	liver, hepatocellular carcinoma...	III
HS-01630 prim_liv hcc_63y_m_7-137	—	liver, hepatocellular carcinoma...	IIIA
HS-01630 prim_liv hcc_69y_m_7-185	—	liver, hepatocellular carcinoma...	I
HS-01630 prim_liv hcc_74y_f_7-334	—	liver, hepatocellular carcinoma...	I
HS-01630 prim_liv hcc_53y_m_7-67	—	liver, hepatocellular carcinoma...	I
HS-01630 prim_liv hcc_52y_f_7-265	—	liver, hepatocellular carcinoma...	I
HS-01630 prim_liv hcc_72y_m_7-204	—	liver, hepatocellular carcinoma...	—
HS-01630 prim_liv hcc_58y_m_7-100	—	liver, hepatocellular carcinoma...	I
HS-01630 prim_liv hcc_50y_m_7-46	—	liver, hepatocellular carcinoma...	—
HS-01630 prim_liv hcc_77y_m_7-232	—	liver, hepatocellular carcinoma...	IIIA
HS-01630 prim_liv hcc_72y_f_7-328	—	liver, hepatocellular carcinoma...	I
HS-01630 prim_liv hcc_61y_f_7-291	—	liver, hepatocellular carcinoma...	I
HS-01630 prim_liv hcc_59y_f_7-283	—	liver, hepatocellular carcinoma...	I
HS-01630 prim_liv hcc_65y_m_7-152	—	liver, hepatocellular carcinoma...	IIIB
HS-01630 prim_liv hcc_39y_f_7-249	—	liver, hepatocellular carcinoma...	IIIA
HS-01630 prim_liv hcc_75y_m_7-224	—	liver, hepatocellular carcinoma...	II
HS-01630 prim_liv hcc_23y_m_7-4	—	liver, hepatocellular carcinoma...	III
HS-01630 prim_liv hcc_57y_m_7-90	—	liver, hepatocellular carcinoma...	IIIA
HS-01630 prim_liv hcc_61y_m_7-127	—	liver, hepatocellular carcinoma...	IIIA
HS-01630 prim_liv hcc_64y_m_7-141	—	liver, hepatocellular carcinoma...	I
HS-01630 prim_liv hcc_61y_m_7-120	—	liver, hepatocellular carcinoma...	I
HS-01630 prim_liv hcc_68y_m_7-178	—	liver, hepatocellular carcinoma...	IIIA
HS-01630 prim_liv hcc_85y_f_7-354	—	liver, hepatocellular carcinoma...	I
HS-01630 prim_liv hcc_66y_f_7-311	—	liver, hepatocellular carcinoma...	I
HS-01630 prim_liv hcc_47y_m_7-35	—	liver, hepatocellular carcinoma...	II
HS-01630 prim_liv hcc_60y_m_7-118	—	liver, hepatocellular carcinoma...	II
HS-01630 prim_liv hcc_20y_f_7-242	—	liver, hepatocellular carcinoma...	I
HS-01630 prim_liv hcc_70y_f_7-324	—	liver, hepatocellular carcinoma...	II
HS-01630 prim_liv hcc_50y_m_7-48	—	liver, hepatocellular carcinoma...	I
HS-01630 prim_liv hcc_64y_f_7-302	—	liver, hepatocellular carcinoma...	II
HS-01630 prim_liv hcc_54y_m_7-77	—	liver, hepatocellular carcinoma...	IIIA
HS-01630 prim_liv hcc_68y_m_7-169	—	liver, hepatocellular carcinoma...	—
HS-01630 prim_liv hcc_51y_m_7-61	—	liver, hepatocellular carcinoma...	II
HS-01630 prim_liv hcc_57y_m_7-91	—	liver, hepatocellular carcinoma...	IIIA
HS-01630 prim_liv hcc_64y_f_7-300	—	liver, hepatocellular carcinoma...	I
HS-01630 prim_liv hcc_45y_f_7-253	—	liver, hepatocellular carcinoma...	IIIA
HS-01630 prim_liv hcc_64y_f_7-301	—	liver, hepatocellular carcinoma...	I
HS-01630 prim_liv hcc_62y_f_7-295	—	liver, hepatocellular carcinoma...	IIIA
HS-01630 prim_liv hcc_71y_f_7-325	—	liver, hepatocellular carcinoma...	—

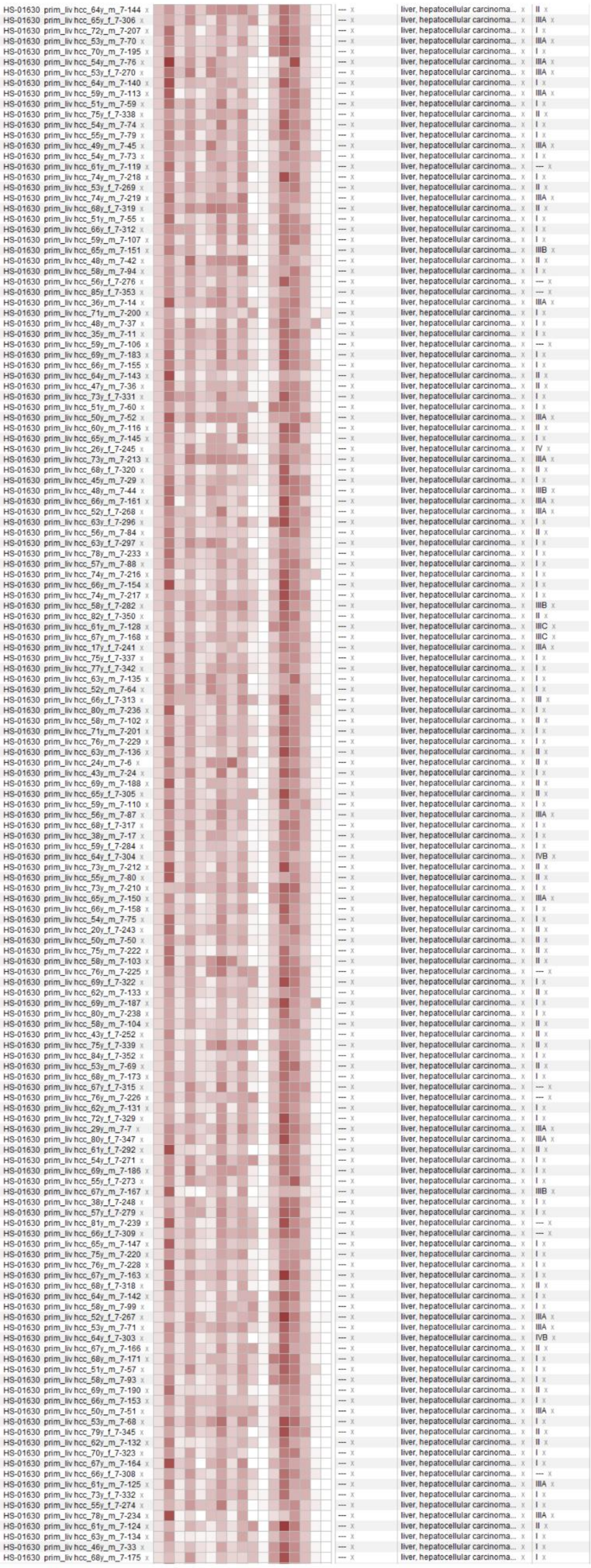

HS-01630 prim_liv hcc_64y_m_7-144	---	liver, hepatocellular carcinoma...	II
HS-01630 prim_liv hcc_65y_f_7-306	---	liver, hepatocellular carcinoma...	IIIA
HS-01630 prim_liv hcc_72y_m_7-207	---	liver, hepatocellular carcinoma...	I
HS-01630 prim_liv hcc_53y_m_7-70	---	liver, hepatocellular carcinoma...	IIIA
HS-01630 prim_liv hcc_70y_m_7-195	---	liver, hepatocellular carcinoma...	I
HS-01630 prim_liv hcc_54y_m_7-76	---	liver, hepatocellular carcinoma...	IIIA
HS-01630 prim_liv hcc_53y_f_7-270	---	liver, hepatocellular carcinoma...	IIIA
HS-01630 prim_liv hcc_64y_m_7-140	---	liver, hepatocellular carcinoma...	I
HS-01630 prim_liv hcc_59y_m_7-113	---	liver, hepatocellular carcinoma...	IIIA
HS-01630 prim_liv hcc_51y_m_7-59	---	liver, hepatocellular carcinoma...	I
HS-01630 prim_liv hcc_75y_f_7-338	---	liver, hepatocellular carcinoma...	II
HS-01630 prim_liv hcc_54y_m_7-74	---	liver, hepatocellular carcinoma...	I
HS-01630 prim_liv hcc_55y_m_7-79	---	liver, hepatocellular carcinoma...	I
HS-01630 prim_liv hcc_49y_m_7-45	---	liver, hepatocellular carcinoma...	IIIA
HS-01630 prim_liv hcc_54y_m_7-73	---	liver, hepatocellular carcinoma...	I
HS-01630 prim_liv hcc_61y_m_7-119	---	liver, hepatocellular carcinoma...	---
HS-01630 prim_liv hcc_74y_m_7-218	---	liver, hepatocellular carcinoma...	I
HS-01630 prim_liv hcc_53y_f_7-269	---	liver, hepatocellular carcinoma...	II
HS-01630 prim_liv hcc_74y_m_7-219	---	liver, hepatocellular carcinoma...	IIIA
HS-01630 prim_liv hcc_68y_f_7-319	---	liver, hepatocellular carcinoma...	II
HS-01630 prim_liv hcc_51y_m_7-55	---	liver, hepatocellular carcinoma...	I
HS-01630 prim_liv hcc_66y_f_7-312	---	liver, hepatocellular carcinoma...	I
HS-01630 prim_liv hcc_59y_m_7-107	---	liver, hepatocellular carcinoma...	I
HS-01630 prim_liv hcc_65y_m_7-151	---	liver, hepatocellular carcinoma...	IIIB
HS-01630 prim_liv hcc_48y_m_7-42	---	liver, hepatocellular carcinoma...	II
HS-01630 prim_liv hcc_58y_m_7-94	---	liver, hepatocellular carcinoma...	I
HS-01630 prim_liv hcc_56y_f_7-276	---	liver, hepatocellular carcinoma...	---
HS-01630 prim_liv hcc_85y_f_7-353	---	liver, hepatocellular carcinoma...	---
HS-01630 prim_liv hcc_36y_m_7-14	---	liver, hepatocellular carcinoma...	IIIA
HS-01630 prim_liv hcc_71y_m_7-200	---	liver, hepatocellular carcinoma...	I
HS-01630 prim_liv hcc_48y_m_7-37	---	liver, hepatocellular carcinoma...	I
HS-01630 prim_liv hcc_35y_m_7-11	---	liver, hepatocellular carcinoma...	I
HS-01630 prim_liv hcc_59y_m_7-106	---	liver, hepatocellular carcinoma...	---
HS-01630 prim_liv hcc_69y_m_7-183	---	liver, hepatocellular carcinoma...	I
HS-01630 prim_liv hcc_66y_m_7-155	---	liver, hepatocellular carcinoma...	I
HS-01630 prim_liv hcc_64y_m_7-143	---	liver, hepatocellular carcinoma...	II
HS-01630 prim_liv hcc_47y_m_7-36	---	liver, hepatocellular carcinoma...	II
HS-01630 prim_liv hcc_73y_f_7-331	---	liver, hepatocellular carcinoma...	I
HS-01630 prim_liv hcc_51y_m_7-60	---	liver, hepatocellular carcinoma...	I
HS-01630 prim_liv hcc_50y_m_7-52	---	liver, hepatocellular carcinoma...	IIIA
HS-01630 prim_liv hcc_60y_m_7-116	---	liver, hepatocellular carcinoma...	II
HS-01630 prim_liv hcc_65y_m_7-145	---	liver, hepatocellular carcinoma...	I
HS-01630 prim_liv hcc_26y_f_7-245	---	liver, hepatocellular carcinoma...	IV
HS-01630 prim_liv hcc_73y_m_7-213	---	liver, hepatocellular carcinoma...	IIIA
HS-01630 prim_liv hcc_68y_f_7-320	---	liver, hepatocellular carcinoma...	II
HS-01630 prim_liv hcc_45y_m_7-29	---	liver, hepatocellular carcinoma...	I
HS-01630 prim_liv hcc_48y_m_7-44	---	liver, hepatocellular carcinoma...	IIIB
HS-01630 prim_liv hcc_66y_m_7-161	---	liver, hepatocellular carcinoma...	IIIA
HS-01630 prim_liv hcc_52y_f_7-268	---	liver, hepatocellular carcinoma...	IIIA
HS-01630 prim_liv hcc_63y_f_7-296	---	liver, hepatocellular carcinoma...	I
HS-01630 prim_liv hcc_56y_m_7-84	---	liver, hepatocellular carcinoma...	II
HS-01630 prim_liv hcc_63y_f_7-297	---	liver, hepatocellular carcinoma...	I
HS-01630 prim_liv hcc_78y_m_7-233	---	liver, hepatocellular carcinoma...	I
HS-01630 prim_liv hcc_57y_m_7-88	---	liver, hepatocellular carcinoma...	I
HS-01630 prim_liv hcc_74y_m_7-216	---	liver, hepatocellular carcinoma...	I
HS-01630 prim_liv hcc_66y_m_7-154	---	liver, hepatocellular carcinoma...	I
HS-01630 prim_liv hcc_74y_m_7-217	---	liver, hepatocellular carcinoma...	I
HS-01630 prim_liv hcc_58y_f_7-282	---	liver, hepatocellular carcinoma...	IIIB
HS-01630 prim_liv hcc_82y_f_7-350	---	liver, hepatocellular carcinoma...	II
HS-01630 prim_liv hcc_61y_m_7-128	---	liver, hepatocellular carcinoma...	IIIC
HS-01630 prim_liv hcc_67y_m_7-168	---	liver, hepatocellular carcinoma...	IIIC
HS-01630 prim_liv hcc_17y_f_7-241	---	liver, hepatocellular carcinoma...	IIIA
HS-01630 prim_liv hcc_75y_f_7-337	---	liver, hepatocellular carcinoma...	I
HS-01630 prim_liv hcc_77y_f_7-342	---	liver, hepatocellular carcinoma...	I
HS-01630 prim_liv hcc_63y_m_7-135	---	liver, hepatocellular carcinoma...	I
HS-01630 prim_liv hcc_52y_m_7-64	---	liver, hepatocellular carcinoma...	I
HS-01630 prim_liv hcc_66y_f_7-313	---	liver, hepatocellular carcinoma...	III
HS-01630 prim_liv hcc_80y_m_7-236	---	liver, hepatocellular carcinoma...	I
HS-01630 prim_liv hcc_58y_m_7-102	---	liver, hepatocellular carcinoma...	II
HS-01630 prim_liv hcc_71y_m_7-201	---	liver, hepatocellular carcinoma...	I
HS-01630 prim_liv hcc_76y_m_7-229	---	liver, hepatocellular carcinoma...	I
HS-01630 prim_liv hcc_63y_m_7-136	---	liver, hepatocellular carcinoma...	II
HS-01630 prim_liv hcc_24y_m_7-6	---	liver, hepatocellular carcinoma...	II
HS-01630 prim_liv hcc_43y_m_7-24	---	liver, hepatocellular carcinoma...	I
HS-01630 prim_liv hcc_69y_m_7-188	---	liver, hepatocellular carcinoma...	II
HS-01630 prim_liv hcc_65y_f_7-305	---	liver, hepatocellular carcinoma...	II
HS-01630 prim_liv hcc_59y_m_7-110	---	liver, hepatocellular carcinoma...	I
HS-01630 prim_liv hcc_56y_m_7-87	---	liver, hepatocellular carcinoma...	IIIA
HS-01630 prim_liv hcc_68y_f_7-317	---	liver, hepatocellular carcinoma...	I
HS-01630 prim_liv hcc_38y_m_7-17	---	liver, hepatocellular carcinoma...	I
HS-01630 prim_liv hcc_59y_f_7-284	---	liver, hepatocellular carcinoma...	I
HS-01630 prim_liv hcc_64y_f_7-304	---	liver, hepatocellular carcinoma...	IVB
HS-01630 prim_liv hcc_73y_m_7-212	---	liver, hepatocellular carcinoma...	II
HS-01630 prim_liv hcc_55y_m_7-80	---	liver, hepatocellular carcinoma...	II
HS-01630 prim_liv hcc_73y_m_7-210	---	liver, hepatocellular carcinoma...	I
HS-01630 prim_liv hcc_65y_m_7-150	---	liver, hepatocellular carcinoma...	IIIA
HS-01630 prim_liv hcc_66y_m_7-158	---	liver, hepatocellular carcinoma...	I
HS-01630 prim_liv hcc_54y_m_7-75	---	liver, hepatocellular carcinoma...	I
HS-01630 prim_liv hcc_20y_f_7-243	---	liver, hepatocellular carcinoma...	II
HS-01630 prim_liv hcc_50y_m_7-50	---	liver, hepatocellular carcinoma...	II
HS-01630 prim_liv hcc_75y_m_7-222	---	liver, hepatocellular carcinoma...	II
HS-01630 prim_liv hcc_58y_m_7-103	---	liver, hepatocellular carcinoma...	II
HS-01630 prim_liv hcc_76y_m_7-225	---	liver, hepatocellular carcinoma...	---
HS-01630 prim_liv hcc_69y_f_7-322	---	liver, hepatocellular carcinoma...	I
HS-01630 prim_liv hcc_62y_m_7-133	---	liver, hepatocellular carcinoma...	II
HS-01630 prim_liv hcc_69y_m_7-187	---	liver, hepatocellular carcinoma...	I
HS-01630 prim_liv hcc_80y_m_7-238	---	liver, hepatocellular carcinoma...	I
HS-01630 prim_liv hcc_58y_m_7-104	---	liver, hepatocellular carcinoma...	II
HS-01630 prim_liv hcc_43y_f_7-252	---	liver, hepatocellular carcinoma...	II
HS-01630 prim_liv hcc_75y_f_7-339	---	liver, hepatocellular carcinoma...	II
HS-01630 prim_liv hcc_84y_f_7-352	---	liver, hepatocellular carcinoma...	I
HS-01630 prim_liv hcc_53y_m_7-69	---	liver, hepatocellular carcinoma...	II
HS-01630 prim_liv hcc_68y_m_7-173	---	liver, hepatocellular carcinoma...	I
HS-01630 prim_liv hcc_67y_f_7-315	---	liver, hepatocellular carcinoma...	---
HS-01630 prim_liv hcc_76y_m_7-226	---	liver, hepatocellular carcinoma...	---
HS-01630 prim_liv hcc_62y_m_7-131	---	liver, hepatocellular carcinoma...	I
HS-01630 prim_liv hcc_72y_f_7-329	---	liver, hepatocellular carcinoma...	I
HS-01630 prim_liv hcc_29y_m_7-7	---	liver, hepatocellular carcinoma...	IIIA
HS-01630 prim_liv hcc_80y_f_7-347	---	liver, hepatocellular carcinoma...	IIIA
HS-01630 prim_liv hcc_61y_f_7-292	---	liver, hepatocellular carcinoma...	II
HS-01630 prim_liv hcc_54y_f_7-271	---	liver, hepatocellular carcinoma...	I
HS-01630 prim_liv hcc_69y_m_7-186	---	liver, hepatocellular carcinoma...	I
HS-01630 prim_liv hcc_55y_f_7-273	---	liver, hepatocellular carcinoma...	I
HS-01630 prim_liv hcc_67y_m_7-167	---	liver, hepatocellular carcinoma...	IIIB
HS-01630 prim_liv hcc_38y_f_7-248	---	liver, hepatocellular carcinoma...	I
HS-01630 prim_liv hcc_57y_f_7-279	---	liver, hepatocellular carcinoma...	I
HS-01630 prim_liv hcc_81y_m_7-239	---	liver, hepatocellular carcinoma...	---
HS-01630 prim_liv hcc_66y_f_7-309	---	liver, hepatocellular carcinoma...	---
HS-01630 prim_liv hcc_65y_m_7-147	---	liver, hepatocellular carcinoma...	I
HS-01630 prim_liv hcc_75y_m_7-220	---	liver, hepatocellular carcinoma...	I
HS-01630 prim_liv hcc_76y_m_7-228	---	liver, hepatocellular carcinoma...	I
HS-01630 prim_liv hcc_67y_m_7-163	---	liver, hepatocellular carcinoma...	I
HS-01630 prim_liv hcc_68y_f_7-318	---	liver, hepatocellular carcinoma...	II
HS-01630 prim_liv hcc_64y_m_7-142	---	liver, hepatocellular carcinoma...	I
HS-01630 prim_liv hcc_58y_m_7-99	---	liver, hepatocellular carcinoma...	I
HS-01630 prim_liv hcc_52y_f_7-267	---	liver, hepatocellular carcinoma...	IIIA
HS-01630 prim_liv hcc_53y_m_7-71	---	liver, hepatocellular carcinoma...	IIIA
HS-01630 prim_liv hcc_64y_f_7-303	---	liver, hepatocellular carcinoma...	IVB
HS-01630 prim_liv hcc_67y_m_7-166	---	liver, hepatocellular carcinoma...	II
HS-01630 prim_liv hcc_68y_m_7-171	---	liver, hepatocellular carcinoma...	I
HS-01630 prim_liv hcc_51y_m_7-57	---	liver, hepatocellular carcinoma...	I
HS-01630 prim_liv hcc_58y_m_7-93	---	liver, hepatocellular carcinoma...	I
HS-01630 prim_liv hcc_69y_m_7-190	---	liver, hepatocellular carcinoma...	II
HS-01630 prim_liv hcc_66y_m_7-153	---	liver, hepatocellular carcinoma...	I
HS-01630 prim_liv hcc_50y_m_7-51	---	liver, hepatocellular carcinoma...	IIIA
HS-01630 prim_liv hcc_53y_m_7-68	---	liver, hepatocellular carcinoma...	I
HS-01630 prim_liv hcc_79y_f_7-345	---	liver, hepatocellular carcinoma...	II
HS-01630 prim_liv hcc_62y_m_7-132	---	liver, hepatocellular carcinoma...	II
HS-01630 prim_liv hcc_70y_f_7-323	---	liver, hepatocellular carcinoma...	I
HS-01630 prim_liv hcc_67y_m_7-164	---	liver, hepatocellular carcinoma...	I
HS-01630 prim_liv hcc_66y_f_7-308	---	liver, hepatocellular carcinoma...	---
HS-01630 prim_liv hcc_61y_m_7-125	---	liver, hepatocellular carcinoma...	IIIA
HS-01630 prim_liv hcc_73y_f_7-332	---	liver, hepatocellular carcinoma...	I
HS-01630 prim_liv hcc_55y_f_7-274	---	liver, hepatocellular carcinoma...	I
HS-01630 prim_liv hcc_78y_m_7-234	---	liver, hepatocellular carcinoma...	IIIA
HS-01630 prim_liv hcc_61y_m_7-124	---	liver, hepatocellular carcinoma...	II
HS-01630 prim_liv hcc_63y_m_7-134	---	liver, hepatocellular carcinoma...	I
HS-01630 prim_liv hcc_46y_m_7-33	---	liver, hepatocellular carcinoma...	I
HS-01630 prim_liv hcc_68y_m_7-175	---	liver, hepatocellular carcinoma...	I

HS-01630 prim_liv hcc_38y_m_7-18 x	--- x	liver, hepatocellular carcinoma... x	II x	
HS-01630 prim_liv hcc_73y_m_7-211 x	--- x	liver, hepatocellular carcinoma... x	II x	
HS-01630 prim_liv hcc_61y_m_7-121 x	--- x	liver, hepatocellular carcinoma... x	I x	
HS-01630 prim_liv hcc_72y_m_7-206 x	--- x	liver, hepatocellular carcinoma... x	I x	
HS-01630 prim_liv hcc_73y_m_7-209 x	--- x	liver, hepatocellular carcinoma... x	I x	
HS-01630 prim_liv hcc_31y_m_7-8 x	--- x	liver, hepatocellular carcinoma... x	I x	
HS-01630 prim_liv hcc_64y_m_7-139 x	--- x	liver, hepatocellular carcinoma... x	I x	
HS-01630 prim_liv hcc_76y_f_7-341 x	--- x	liver, hepatocellular carcinoma... x	I x	
HS-01630 prim_liv hcc_32y_m_7-10 x	--- x	liver, hepatocellular carcinoma... x	I x	
HS-01630 prim_liv hcc_76y_m_7-227 x	--- x	liver, hepatocellular carcinoma... x	I x	
HS-01630 prim_liv hcc_77y_m_7-231 x	--- x	liver, hepatocellular carcinoma... x	II x	
HS-01630 prim_liv hcc_58y_m_7-98 x	--- x	liver, hepatocellular carcinoma... x	I x	
HS-01630 prim_liv hcc_60y_m_7-115 x	--- x	liver, hepatocellular carcinoma... x	I x	
HS-01630 prim_liv hcc_69y_m_7-191 x	--- x	liver, hepatocellular carcinoma... x	IIIA x	
HS-01630 prim_liv hcc_73y_f_7-333 x	--- x	liver, hepatocellular carcinoma... x	I x	
HS-01630 prim_liv hcc_44y_m_7-26 x	--- x	liver, hepatocellular carcinoma... x	II x	
HS-01630 prim_liv hcc_79y_f_7-346 x	--- x	liver, hepatocellular carcinoma... x	II x	
HS-01630 prim_liv hcc_58y_m_7-95 x	--- x	liver, hepatocellular carcinoma... x	I x	
HS-01630 prim_liv hcc_68y_m_7-179 x	--- x	liver, hepatocellular carcinoma... x	IIIA x	
HS-01630 prim_liv hcc_47y_f_7-256 x	--- x	liver, hepatocellular carcinoma... x	I x	
HS-01630 prim_liv hcc_52y_m_7-66 x	--- x	liver, hepatocellular carcinoma... x	II x	
HS-01630 prim_liv hcc_43y_f_7-250 x	--- x	liver, hepatocellular carcinoma... x	I x	
HS-01630 prim_liv hcc_51y_m_7-56 x	--- x	liver, hepatocellular carcinoma... x	I x	
HS-01630 prim_liv hcc_69y_f_7-321 x	--- x	liver, hepatocellular carcinoma... x	I x	
HS-01630 prim_liv hcc_66y_m_7-156 x	--- x	liver, hepatocellular carcinoma... x	I x	
HS-01630 prim_liv hcc_77y_f_7-343 x	--- x	liver, hepatocellular carcinoma... x	II x	
HS-01630 prim_liv hcc_78y_f_7-344 x	--- x	liver, hepatocellular carcinoma... x	I x	
HS-01630 prim_liv hcc_58y_m_7-101 x	--- x	liver, hepatocellular carcinoma... x	II x	
HS-01630 prim_liv hcc_37y_m_7-15 x	--- x	liver, hepatocellular carcinoma... x	IIIA x	
HS-01630 prim_liv hcc_51y_f_7-260 x	--- x	liver, hepatocellular carcinoma... x	--- x	
HS-01630 prim_liv hcc_51y_f_7-263 x	--- x	liver, hepatocellular carcinoma... x	II x	
HS-01630 prim_liv hcc_61y_m_7-122 x	--- x	liver, hepatocellular carcinoma... x	I x	
HS-01630 prim_liv hcc_59y_m_7-111 x	--- x	liver, hepatocellular carcinoma... x	II x	
HS-01630 prim_liv hcc_52y_m_7-65 x	--- x	liver, hepatocellular carcinoma... x	II x	
HS-01630 prim_liv hcc_24y_f_7-244 x	--- x	liver, hepatocellular carcinoma... x	IIIA x	
HS-01630 prim_liv hcc_44y_m_7-25 x	--- x	liver, hepatocellular carcinoma... x	I x	
HS-01630 prim_liv hcc_58y_m_7-97 x	--- x	liver, hepatocellular carcinoma... x	I x	
HS-01630 prim_liv hcc_66y_f_7-310 x	--- x	liver, hepatocellular carcinoma... x	I x	
HS-01630 prim_liv hcc_72y_f_7-330 x	--- x	liver, hepatocellular carcinoma... x	II x	
HS-01630 prim_liv hcc_50y_m_7-47 x	--- x	liver, hepatocellular carcinoma... x	I x	
HS-01630 prim_liv hcc_46y_m_7-34 x	--- x	liver, hepatocellular carcinoma... x	II x	
HS-01630 prim_liv hcc_68y_m_7-170 x	--- x	liver, hepatocellular carcinoma... x	I x	
HS-01630 prim_liv hcc_33y_f_7-247 x	--- x	liver, hepatocellular carcinoma... x	IIIA x	
HS-01630 prim_liv hcc_58y_m_7-96 x	--- x	liver, hepatocellular carcinoma... x	I x	
HS-01630 prim_liv hcc_59y_m_7-108 x	--- x	liver, hepatocellular carcinoma... x	I x	
HS-01630 prim_liv hcc_71y_m_7-203 x	--- x	liver, hepatocellular carcinoma... x	IIIA x	
HS-01630 prim_liv hcc_55y_m_7-78 x	--- x	liver, hepatocellular carcinoma... x	I x	
HS-01630 prim_liv hcc_45y_m_7-30 x	--- x	liver, hepatocellular carcinoma... x	II x	
HS-01630 prim_liv hcc_54y_m_7-72 x	--- x	liver, hepatocellular carcinoma... x	I x	
HS-01630 prim_liv hcc_60y_f_7-290 x	--- x	liver, hepatocellular carcinoma... x	IIIC x	
HS-01630 prim_liv hcc_61y_m_7-123 x	--- x	liver, hepatocellular carcinoma... x	II x	
HS-01630 prim_liv hcc_45y_m_7-28 x	--- x	liver, hepatocellular carcinoma... x	I x	
HS-01630 prim_liv hcc_64y_f_7-299 x	--- x	liver, hepatocellular carcinoma... x	I x	
HS-01630 prim_liv hcc_48y_m_7-38 x	--- x	liver, hepatocellular carcinoma... x	I x	
HS-01630 prim_liv hcc_48y_m_7-41 x	--- x	liver, hepatocellular carcinoma... x	I x	
HS-01630 prim_liv hcc_49y_f_7-258 x	--- x	liver, hepatocellular carcinoma... x	I x	
HS-01630 prim_liv hcc_40y_m_7-21 x	--- x	liver, hepatocellular carcinoma... x	IV x	
HS-01630 prim_liv hcc_80y_m_7-237 x	--- x	liver, hepatocellular carcinoma... x	I x	
HS-01630 prim_liv hcc_69y_m_7-182 x	--- x	liver, hepatocellular carcinoma... x	--- x	
Control				
HS-01630 con_liv_75y_m_1-22 x	liver x	--- x	--- x	
HS-01630 con_liv_70y_f_1-40 x	liver x	--- x	--- x	
HS-01630 con_liv_81y_f_1-49 x	liver x	--- x	--- x	
HS-01630 con_liv_20y_f_1-29 x	liver x	--- x	--- x	
HS-01630 con_liv_42y_m_1-5 x	liver x	--- x	--- x	
HS-01630 con_liv_54y_m_1-10 x	liver x	--- x	--- x	
HS-01630 con_liv_76y_m_1-25 x	liver x	--- x	--- x	
HS-01630 con_liv_66y_f_1-38 x	liver x	--- x	--- x	
HS-01630 con_liv_23y_m_1-1 x	liver x	--- x	--- x	
HS-01630 con_liv_75y_f_1-45 x	liver x	--- x	--- x	
HS-01630 con_liv_69y_m_1-15 x	liver x	--- x	--- x	
HS-01630 con_liv_37y_m_1-3 x	liver x	--- x	--- x	
HS-01630 con_liv_72y_f_1-42 x	liver x	--- x	--- x	
HS-01630 con_liv_72y_f_1-44 x	liver x	--- x	--- x	
HS-01630 con_liv_73y_m_1-21 x	liver x	--- x	--- x	
HS-01630 con_liv_62y_m_1-11 x	liver x	--- x	--- x	
HS-01630 con_liv_73y_m_1-20 x	liver x	--- x	--- x	
HS-01630 con_liv_68y_m_1-14 x	liver x	--- x	--- x	
HS-01630 con_liv_62y_f_1-36 x	liver x	--- x	--- x	
HS-01630 con_liv_46y_m_1-7 x	liver x	--- x	--- x	
HS-01630 con_liv_57y_f_1-35 x	liver x	--- x	--- x	
HS-01630 con_liv_69y_m_1-16 x	liver x	--- x	--- x	
HS-01630 con_liv_55y_f_1-34 x	liver x	--- x	--- x	
HS-01630 con_liv_75y_m_1-23 x	liver x	--- x	--- x	
HS-01630 con_liv_29y_f_1-30 x	liver x	--- x	--- x	
HS-01630 con_liv_71y_f_1-41 x	liver x	--- x	--- x	
HS-01630 con_liv_76y_f_1-46 x	liver x	--- x	--- x	
HS-01630 con_liv_69y_m_1-17 x	liver x	--- x	--- x	
HS-01630 con_liv_52y_f_1-33 x	liver x	--- x	--- x	
HS-01630 con_liv_75y_m_1-24 x	liver x	--- x	--- x	
HS-01630 con_liv_67y_m_1-13 x	liver x	--- x	--- x	
HS-01630 con_liv_76y_m_1-27 x	liver x	--- x	--- x	
HS-01630 con_liv_53y_m_1-9 x	liver x	--- x	--- x	
HS-01630 con_liv_50y_m_1-8 x	liver x	--- x	--- x	
HS-01630 con_liv_73y_m_1-19 x	liver x	--- x	--- x	
HS-01630 con_liv_62y_f_1-37 x	liver x	--- x	--- x	
HS-01630 con_liv_78y_f_1-48 x	liver x	--- x	--- x	
HS-01630 con_liv_40y_m_1-4 x	liver x	--- x	--- x	
HS-01630 con_liv_45y_m_1-6 x	liver x	--- x	--- x	
HS-01630 con_liv_70y_m_1-18 x	liver x	--- x	--- x	adj... x
HS-01630 con_liv_51y_f_1-32 x	liver x	--- x	--- x	adj... x
HS-01630 con_liv_76y_m_1-26 x	liver x	--- x	--- x	adj... x
HS-01630 con_liv_66y_f_1-39 x	liver x	--- x	--- x	adj... x
HS-01630 con_liv_43y_f_1-31 x	liver x	--- x	--- x	adj... x
HS-01630 con_liv_77y_f_1-47 x	liver x	--- x	--- x	adj... x
HS-01630 con_liv_65y_m_1-12 x	liver x	--- x	--- x	adj... x
HS-01630 con_liv_77y_m_1-28 x	liver x	--- x	--- x	adj... x
HS-01630 con_liv_23y_m_1-2 x	liver x	--- x	--- x	adj... x
HS-01630 con_liv_72y_f_1-43 x	liver x	--- x	--- x	adj... x

APPENDIX D - Representative H&E and DLG5 IHC in Human Adjacent Liver Tissues

Adjacent liver sections stained with H&E (A, C, E) and their corresponding DLG5 IHC counterparts (B, D, F). Each pair (A–B, C–D, E–F) illustrates matched tissue fields.

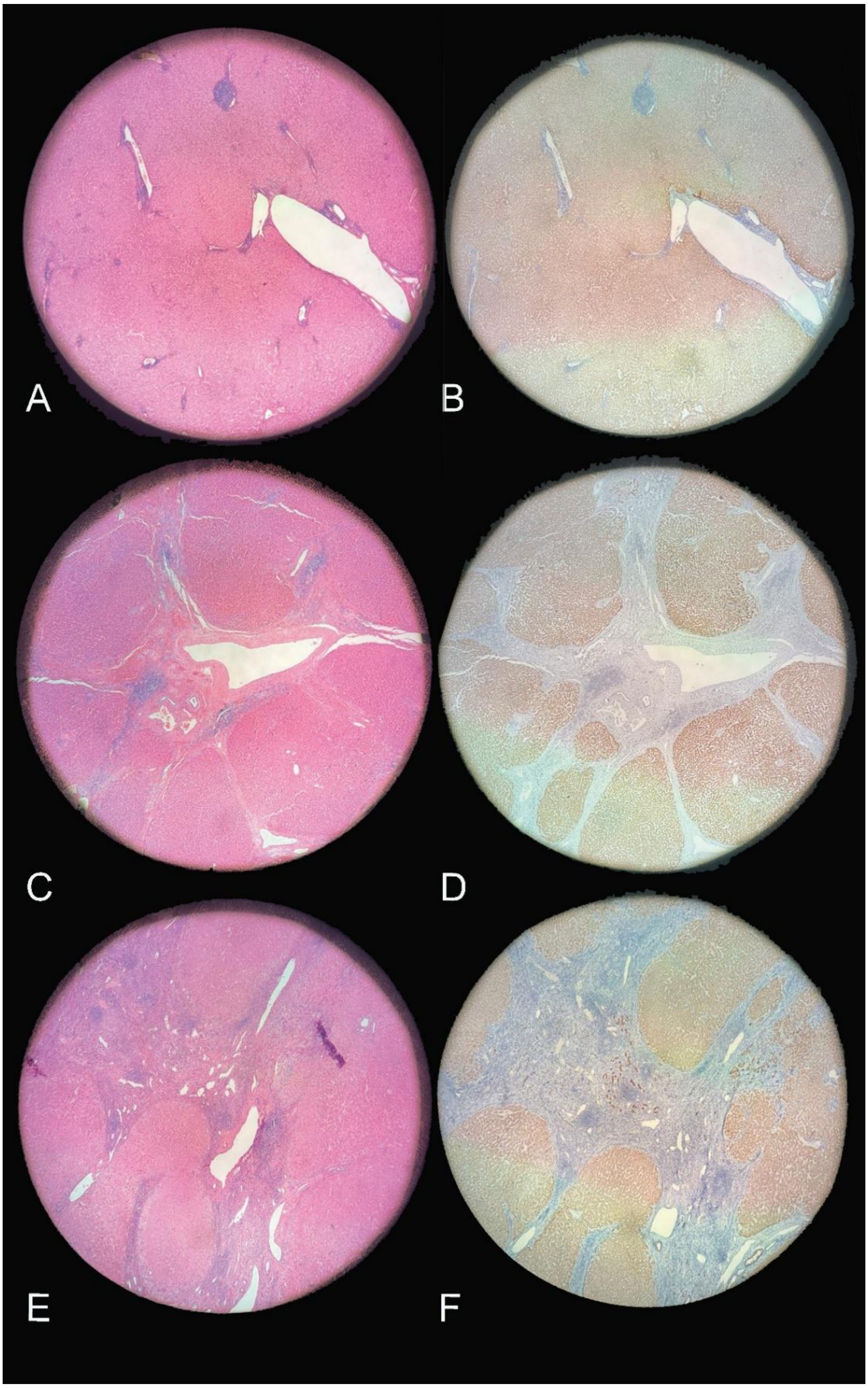

APPENDIX E - Representative H&E and DLG5 IHC in Human HCC Liver Tissues

HCC liver sections stained with H&E (A, C, E) and their corresponding DLG5 IHC counterparts (B, D, F). Each pair (A–B, C–D, E–F) illustrates matched tissue fields.

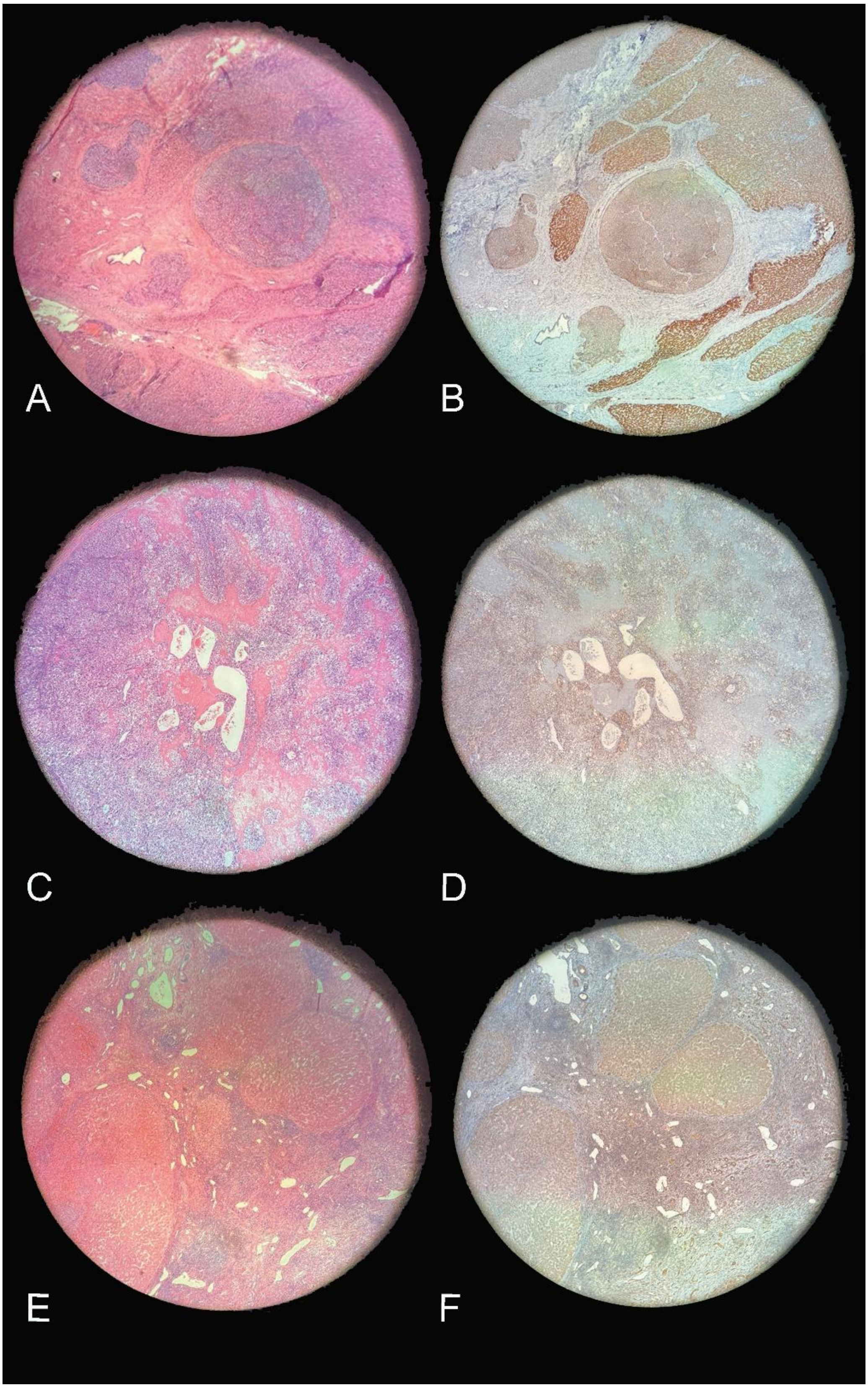

APPENDIX F – DLG5 in Steatotic Liver Tissue

DLG5 IHC image showing hepatic steatosis characterized by macrovesicular lipid accumulation and distortion of hepatic cords. (Top) Low-magnification field displaying widespread lipid vacuoles interspersed with fibrous septa and moderate DLG5 staining along residual hepatocyte trabeculae. (Bottom) High-magnification inset from the boxed region highlighting intense cytoplasmic DLG5 staining adjacent to lipid droplets, consistent with altered polarity and membrane redistribution under steatotic conditions. Images are not set to scale. Intended for morphological description only.

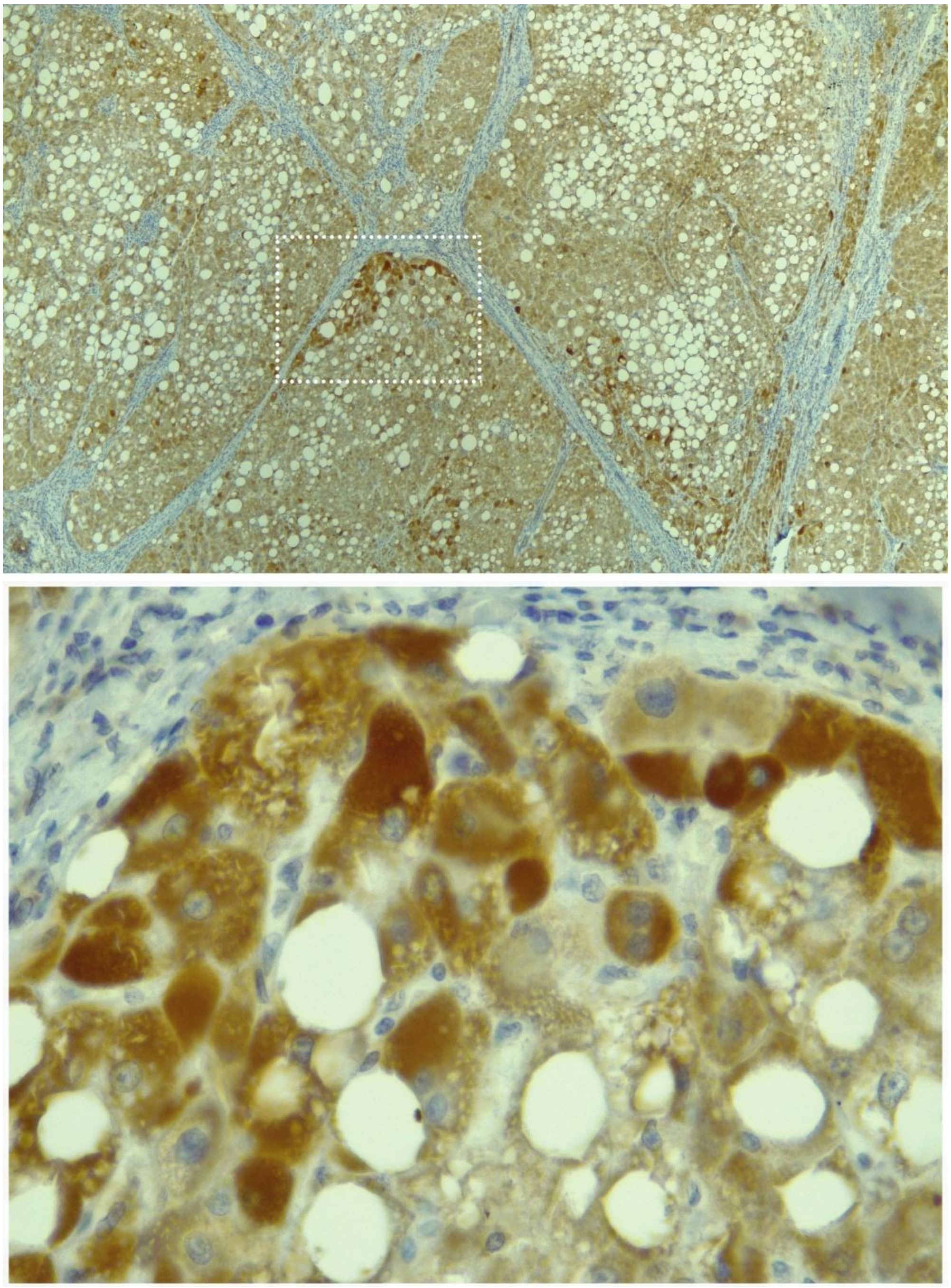

APPENDIX G – Localization indices derived from binary-compartment segmentation of DLG5

Table 12. Localization indices derived from DLG5 binary analysis (CellProfiler)

Parameter	Formula	Purpose	Adjacent	HCC	Interpretation
Perinuclear (P)	-	-	3502.23	3396.70	DLG5 minimally reduced in HCC
Cytoplasmic (C)	-	-	11663.36	8121.10	DLG5 slightly decreased in HCC
Submembranous (SM)	-	-	2786.01	2458.62	DLG5 minimal decrease in HCC
Perinuclear Enrichment Ratio	P/C	Count of DLG5 at the submembranous	0.30	0.42	Indicates relative perinuclear accumulation increased in HCC
Perinuclear/Submembranous Ratio	P/SM	Relative perinuclear accumulation	1.26	1.38	Elevated perinuclear accumulation relative to SM in HCC
Cytoplasmic/ Submembranous Ratio	C/SM	Relative abundance of perinuclear signal over submembranous	4.19	3.30	Reduced cytoplasmic abundance over SM in HCC
DLG5 Submembranous Abundance Index	SM/(P+C)	Cytoplasmic dominance vs SM	0.184	0.213	DLG5 minimal SM staining
DLG5 Internalization Index	(P+C)/SM	Relative abundance of DLG5 at the submembranous	5.44	4.68	Redistribution toward internal compartments persists in HCC
Polarity Retention Score	SM/(P+C+SM)	Overall polarity imbalance	0.155	0.176	Fraction of total DLG5 retained at SM remains low (junctional retention capacity)
Perinuclear Fraction of Total Cell	P/(P+C+SM)	Proportion of total DLG5 at the membrane	0.195	0.243	Increased perinuclear localization in HCC
Cytoplasmic Fraction of Total Cell	C/(P+C+SM)	Share of total DLG5 localized near the nucleus	0.650	0.581	Cytoplasmic fraction decreases in HCC
Total Cell (TC)	-	Proportion of DLG5 within cytoplasm	15165.59	11517.80	Overall intracellular DLG5
Perinuclear DLG5 load (% of total cell)	P/TC	-	0.231 (23.1%)	0.295 (29.5%)	Larger fraction of DLG5 accumulates perinuclearly in HCC
Cytoplasmic DLG5 load (% of total cell)	C/TC	% of DLG5 localized perinuclear	0.769 (76.9%)	0.705 (70.5%)	Cytoplasmic decreases in HCC
Submembranous DLG5 load (% of total cell)	SM/TC	% of DLG5 in cytoplasm	0.184 (18.4%)	0.213 (21.3%)	SM-associated signal remains low

Note: Masks for perinuclear, cytoplasmic, and membrane compartments were defined algorithmically and may slightly overlap; thus, percentages do not necessarily sum to 100%. Values represent compartmental DLG5 loading relative to total cellular intensity rather than exclusive partitioning volumes.

General Interpretation: HCC shows a clear shift toward perinuclear accumulation of DLG5, accompanied by reduced cytoplasmic dominance and persistently low submembranous retention, supporting polarity disruption with internal redistribution rather than membrane anchoring

APPENDIX H – Localization indices derived from manual compartment classification of DLG5

Table 13. Localization indices derived from DLG5 manual classification count

Parameter	Formula	Purpose	Adjacent	HCC	Interpretation
Perinuclear (P)	-	Count of DLG5 perinuclear localization	37.55	94.21	DLG5 strongly enriched in perinuclear in HCC
Cytoplasmic (C)	-	Count of DLG5 cytoplasmic localization	56.67	66.12	Cytoplasmic localization slightly increased in HCC
Submembranous (SM)	-	Count of DLG5 at the submembranous	17.51	0.92	DLG5 nearly lost at the membrane in HCC
Perinuclear Enrichment Ratio	P/C	Relative perinuclear accumulation	0.66	1.43	Redistribution of DLG5 toward the perinuclear in HCC
Perinuclear/Submembranous Ratio	P/SM	Relative abundance of perinuclear signal over submembranous	2.14	102.4	Sharp perinuclear shift and loss of SM polarity in HCC
Cytoplasmic/ Submembranous Ratio	C/SM	Cytoplasmic dominance vs SM	3.24	71.87	Reduced membrane contribution
DLG5 Submembranous Abundance Index	SM/(P+C)	Relative abundance of DLG5 at the submembranous	0.186	0.006	Membrane-associated DLG5 collapses in HCC
DLG5 Internalization Index	(P+C)/SM	Overall polarity imbalance	5.38	173.05	Indicates marked polarity loss in HCC
Polarity Retention Score	SM/(P+C+SM)	Proportion of total DLG5 at the membrane	0.157	0.006	Failure to retain DLG5 at SM in HCC
Perinuclear Fraction of Total Cell	P/(P+C+SM)	Share of total DLG5 localized near the nucleus	0.336	0.584	Strong perinuclear accumulation in HCC
Cytoplasmic Fraction of Total Cell	C/(P+C+SM)	Proportion of DLG5 within cytoplasm	0.507	0.410	Cytoplasmic contribution decreases in HCC
Total Cell (TC)	-	-	111.73	161.25	Total evaluated cells per grid of a field
Perinuclear DLG5 load (% of total cell)	P/TC	% of DLG5 localized perinuclear	0.336 (33.6%)	0.584 (58.4%)	Strong perinuclear accumulation in HCC
Cytoplasmic DLG5 load (% of total cell)	C/TC	% of DLG5 in cytoplasm	0.507 (50.7%)	0.410 (41.0%)	Cytoplasmic share decreases in HCC
Submembranous DLG5 load (% of total cell)	SM/TC	% of DLG5 at submembranous	0.157 (15.7%)	0.006 (0.6%)	Nearly absent membrane signal in HCC

Note: In manual classification, an additional Unclassified category was included to account for cells exhibiting indeterminate DLG5 staining patterns. These unclassified cells were excluded.

General Interpretation: Manual compartment classification reveals a m shift in DLG5 localization in HCC at the cellular phenotype level. HCC samples show a more than two-fold increase in perinuclear DLG5-positive cells, accompanied by an almost complete loss of submembranous localization. All membrane-associated indices collapse in HCC, while the internalization index increases dramatically, indicating that DLG5 is redistributed away from the plasma membrane toward internal compartments. The following indices support polarity disruption characterized by loss of membrane anchoring and perinuclear accumulation rather than cytoplasmic redistribution.

APPENDIX I – DLG5 Top:Huh7 and Bottom:JHH6

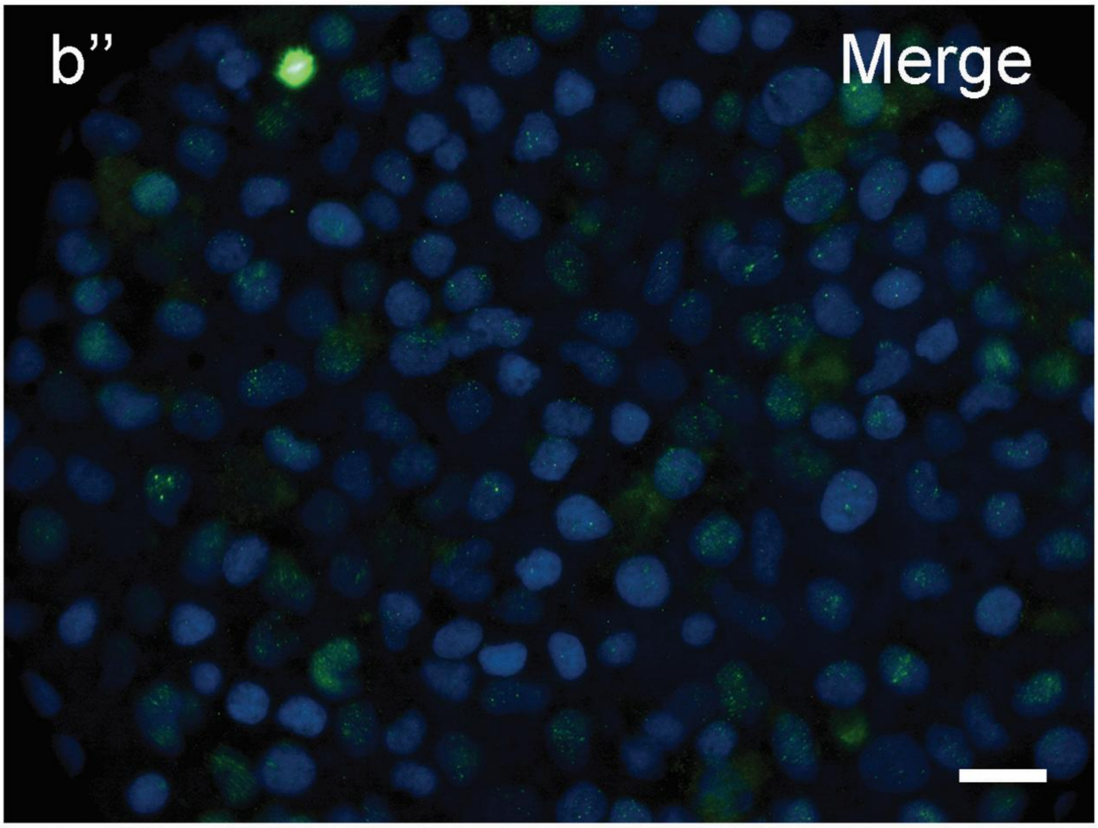

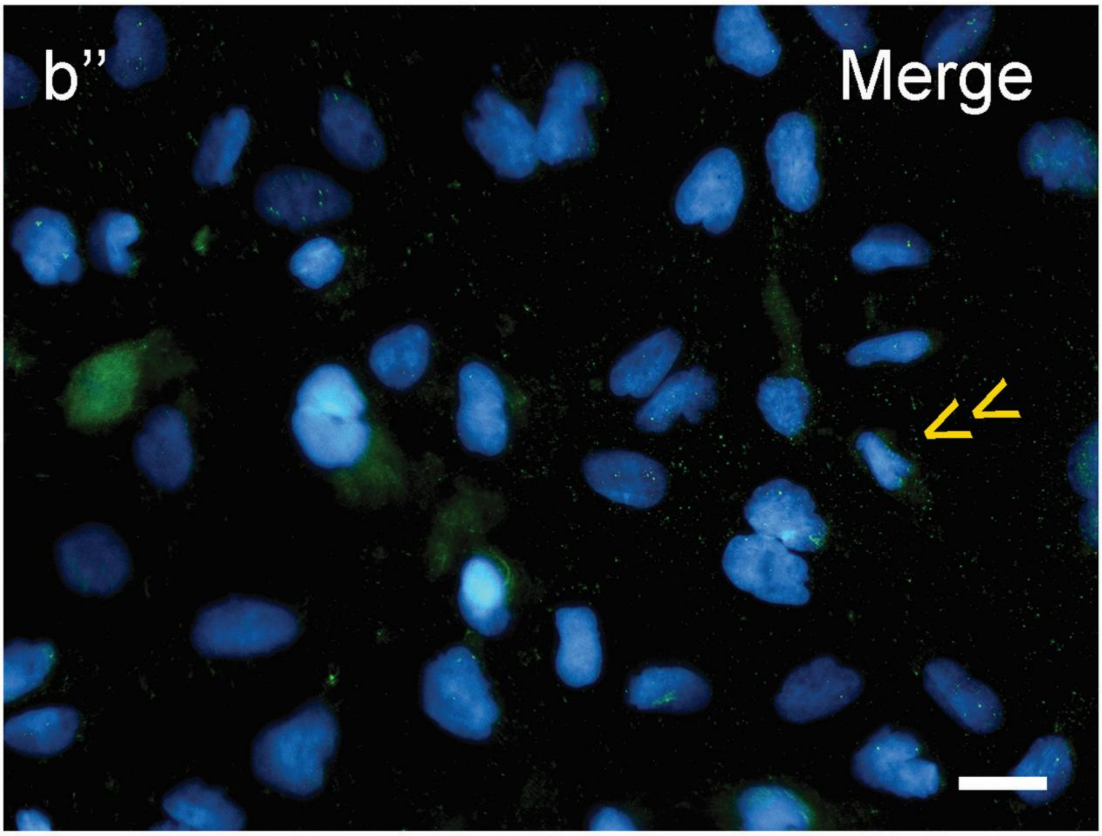

APPENDIX J – Occludin Top:Huh7 and Bottom:JHH6

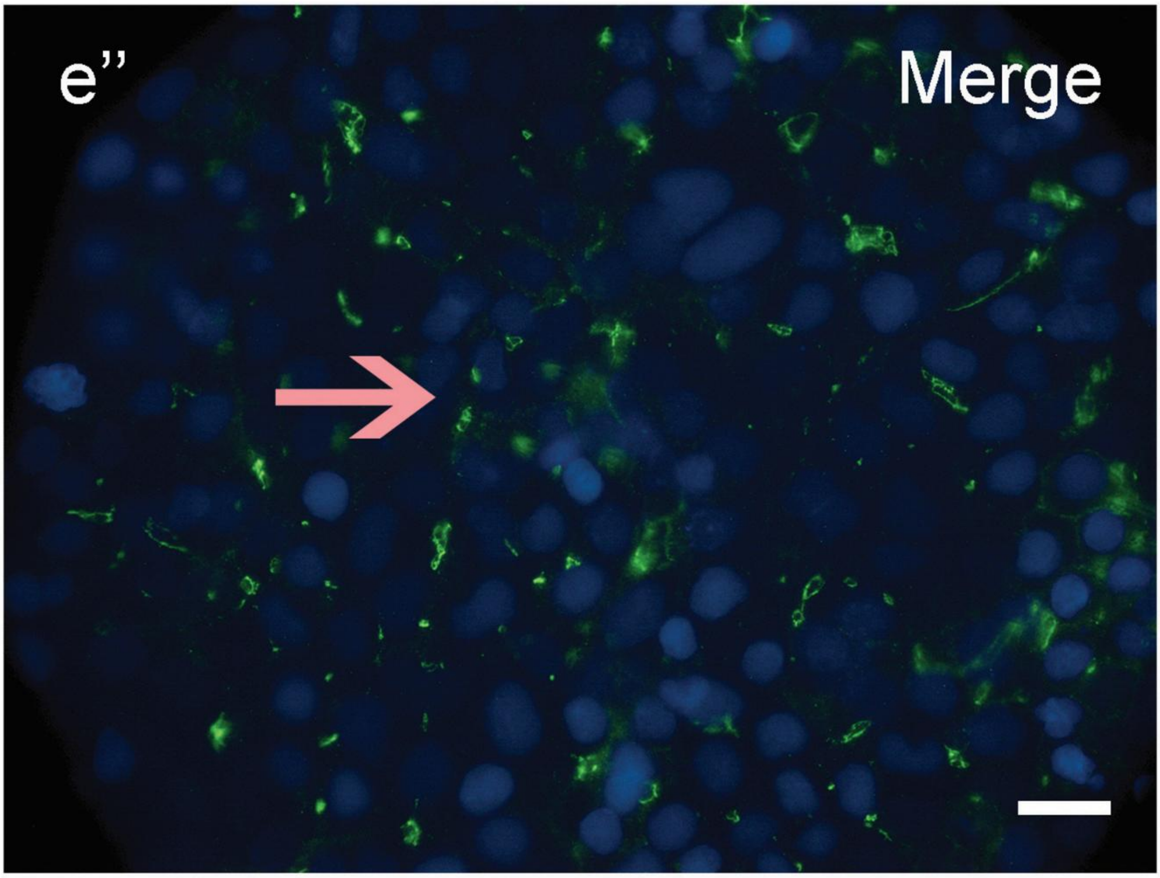

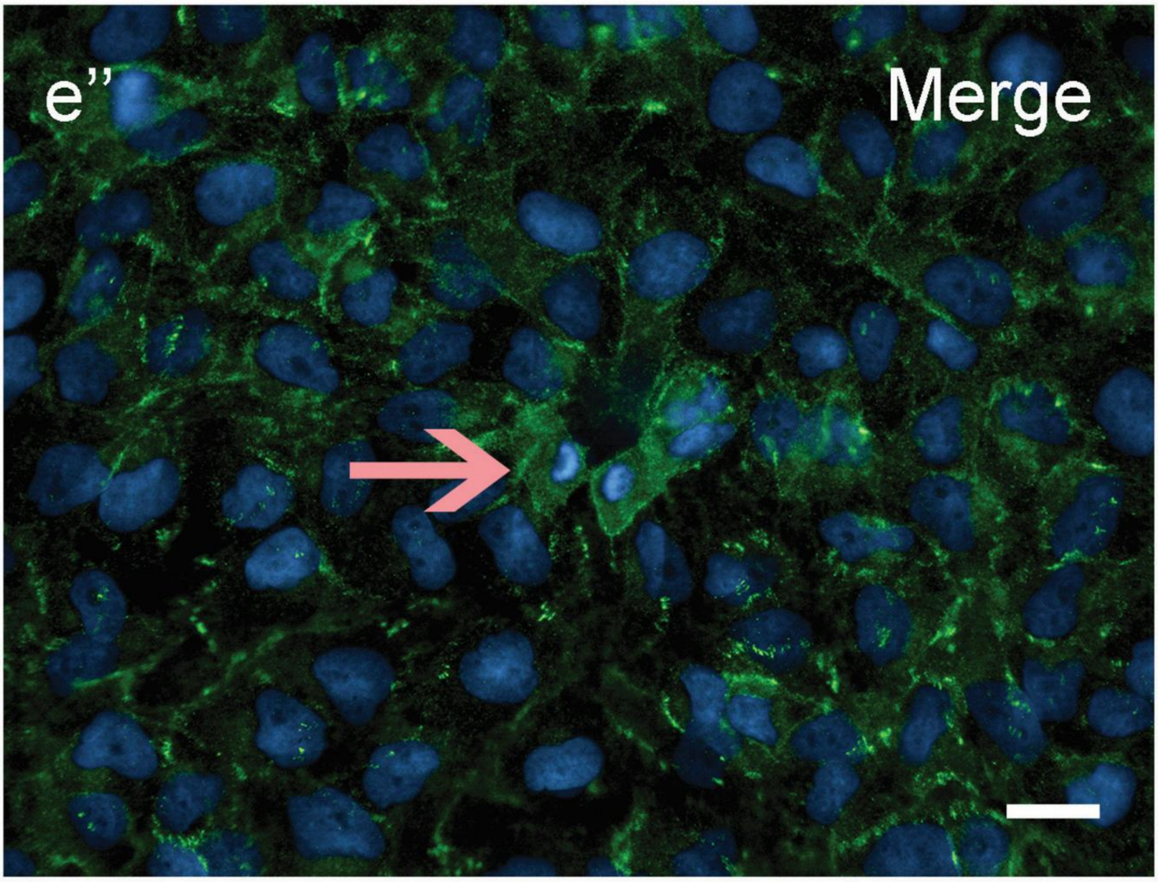

APPENDIX K – ZO-1 Top:Huh7 and Bottom:JHH6

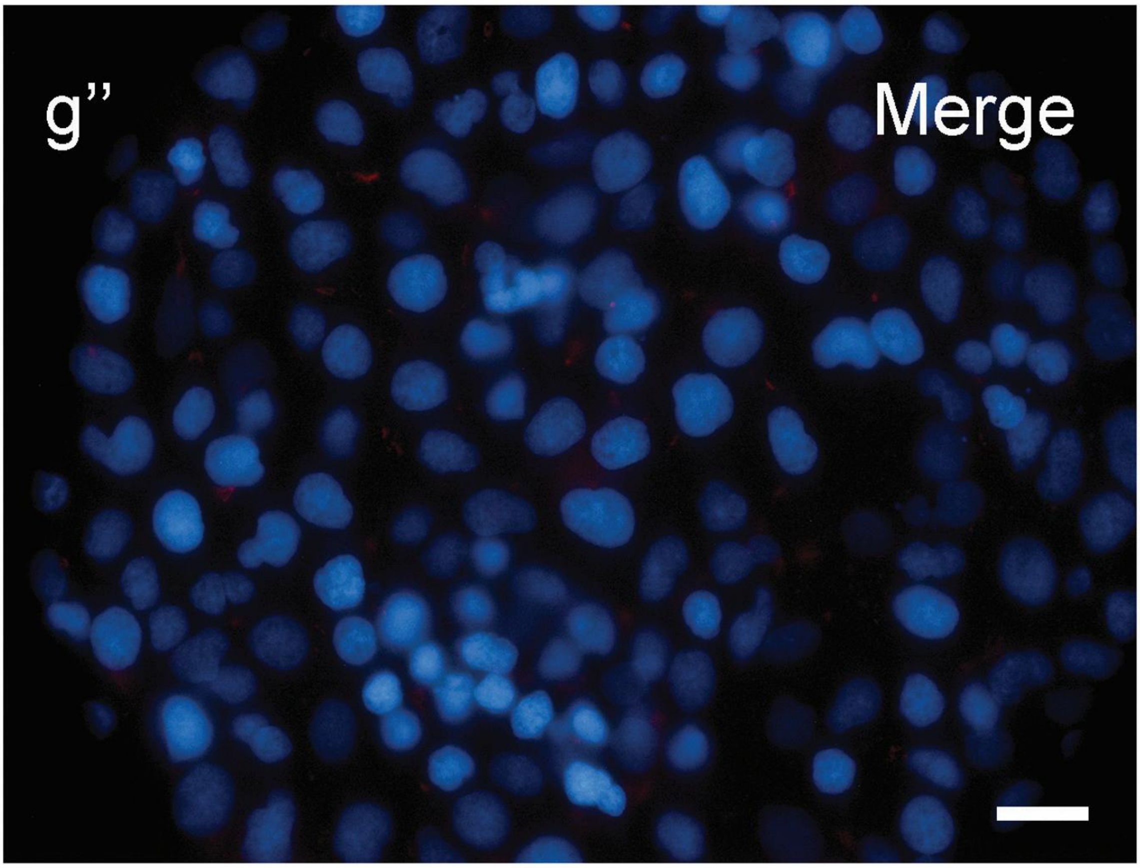

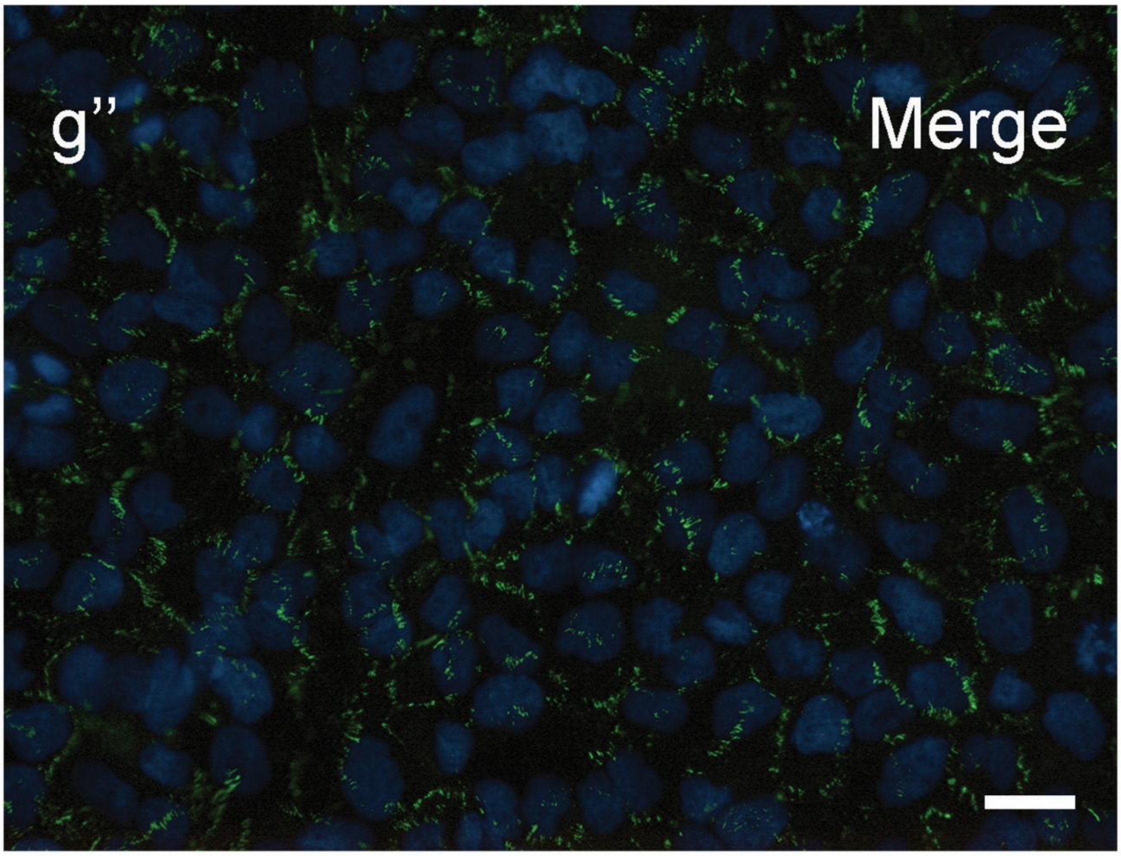

APPENDIX L – DLG5 and CTNNB1 Top:Huh7 and Bottom:JHH6

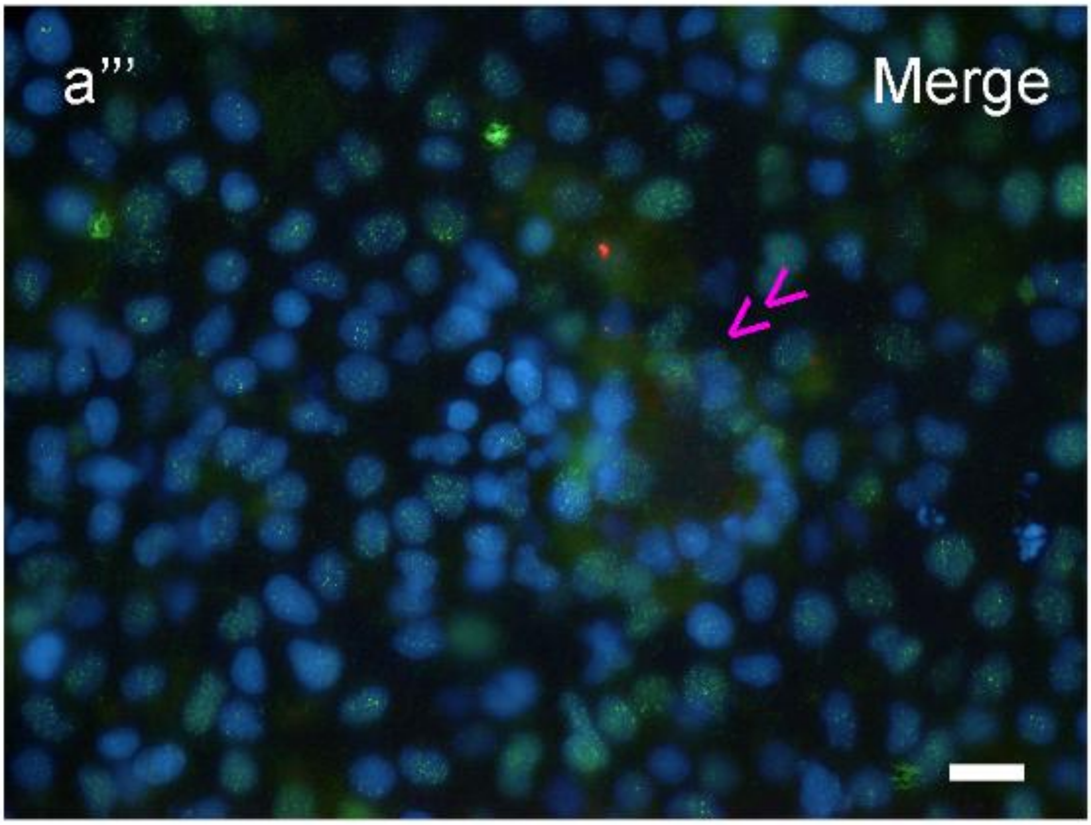

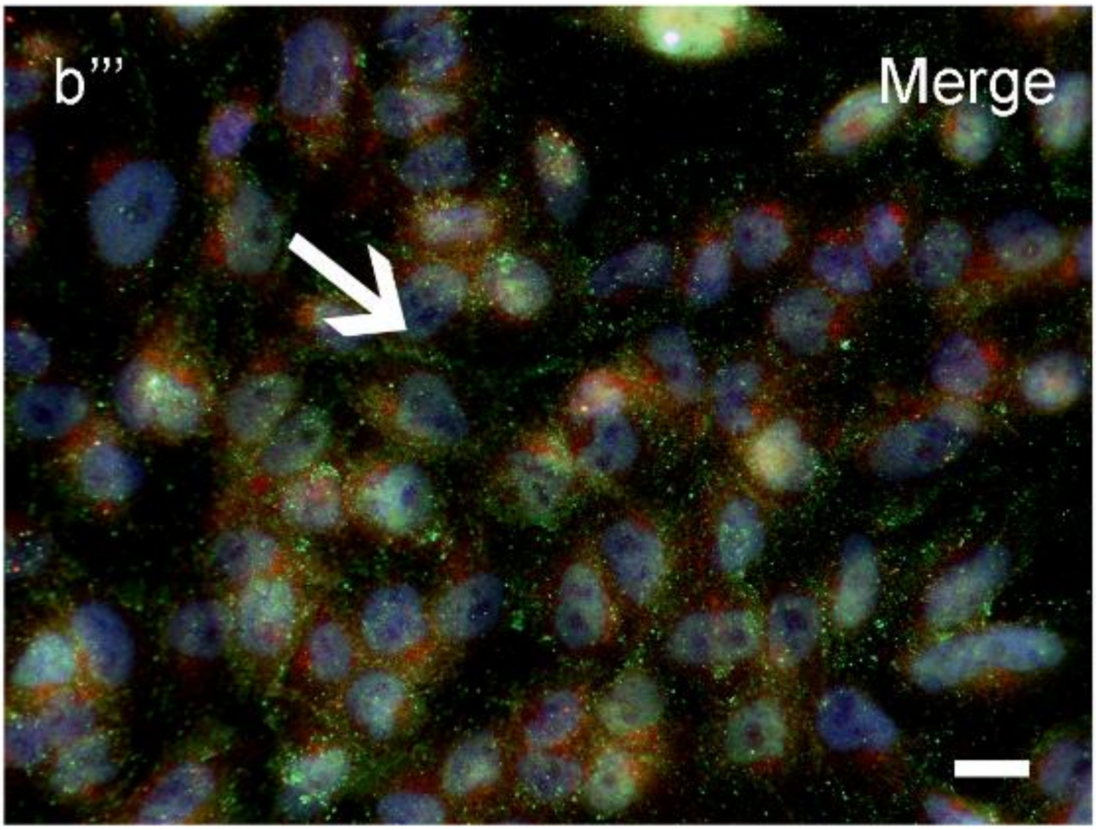

BIBLIOGRAPHY

1. Llovet, J.M., et al., *Hepatocellular carcinoma.* Nat Rev Dis Primers, 2021. **7**(1): p. 6. DOI: https://doi.org/10.1038/s41572-020-00240-3. PMID: 33479224.
2. Martin-Belmonte, F. and M. Perez-Moreno, *Epithelial cell polarity, stem cells and cancer.* Nat Rev Cancer, 2011. **12**(1): p. 23-38. DOI: https://doi.org/10.1038/nrc3169. PMID: 22169974.
3. Pradhan-Sundd, T. and S.P. Monga, *Blood-Bile Barrier: Morphology, Regulation, and Pathophysiology.* Gene Expr, 2019. **19**(2): p. 69-87. DOI: https://doi.org/10.3727/105221619X15469715711907. PMID: 30646969. PMCID: PMC6466181
4. Peglion, F. and S. Etienne-Manneville, *Cell polarity changes in cancer initiation and progression.* J Cell Biol, 2024. **223**(1). DOI: https://doi.org/10.1083/jcb.202308069. PMID: 38091012. PMCID: PMC10720656
5. Mayer, C., et al., *Apical bulkheads accumulate as adaptive response to impaired bile flow in liver disease.* EMBO Rep, 2023. **24**(9): p. e57181. DOI: https://doi.org/10.15252/embr.202357181. PMID: 37522754. PMCID: PMC10481669
6. *International Agency for Research on Cancer*. Cancer Today: Liver Cancer Statistics 2024; Available from: https://gco.iarc.fr/today/en.
7. Tree, C. *Liver Physiology and Energy Metabolism.* 2023; Available from: https://clinicalpub.com/liver-physiology-and-energy-metabolism/.
8. Stokol, T. *Structure of a liver lobule*. March 7, 2016; Available from: https://eclinpath.com/chemistry/liver/liver-structure-and-function/liverlobule/.
9. Szklarczyk, D., Gable, A. L., Lyon, D., Junge, A., Wyder, S., Huerta-Cepas, J., ... & von Mering, C., *STRING-DB: Functional protein association networks [Dataset]*. 2023, Swiss Institute of Bioinformatics: Zurich, Switzerland. DOI: https://doi.org/10.1093/nar/gkac1000. PMCID: PMCID
10. OpenAI, *ChatGPT [Computer software]*. 2025, OpenAI: San Francisco, CA, USA. PMCID: PMCID
11. Cunningham, R.P. and N. Porat-Shliom, *Liver Zonation - Revisiting Old Questions With New Technologies.* Front Physiol, 2021. **12**: p. 732929. DOI: https://doi.org/10.3389/fphys.2021.732929. PMID: 34566696. PMCID: PMC8458816
12. Andolfi, C., C. Tiribelli, and D. Pascut, *Recent Hints on the Dual Role of Discs Large MAGUK Scaffold Protein 5 in Cancers and in Hepatocellular Carcinoma.* Front Biosci (Landmark Ed), 2022. **27**(5): p. 164. DOI: https://doi.org/10.31083/j.fbl2705164. PMID: 35638431.
13. Hall, J.E. and A.C. Guyton, *Guyton and Hall textbook of medical physiology*. 12th ed. xix, 1091 pages. ISBN: 978-1-4160-4574-8
14. Treyer, A. and A. Musch, *Hepatocyte polarity.* Compr Physiol, 2013. **3**(1): p. 243-87. DOI: https://doi.org/10.1002/cphy.c120009. PMID: 23720287. PMCID: PMC3697931
15. Slim, C.L., et al., *The special case of hepatocytes: unique tissue architecture calls for a distinct mode of cell division.* Bioarchitecture, 2014. **4**(2): p. 47-52. DOI: https://doi.org/10.4161/bioa.29012. PMID: 24769852. PMCID: PMC4199811

16. Gissen, P. and I.M. Arias, *Structural and functional hepatocyte polarity and liver disease.* J Hepatol, 2015. **63**(4): p. 1023-37. DOI: https://doi.org/10.1016/j.jhep.2015.06.015. PMID: 26116792. PMCID: PMC4582071
17. Ludwig, J., et al., *Nonalcoholic steatohepatitis: Mayo Clinic experiences with a hitherto unnamed disease.* Mayo Clin Proc, 1980. **55**(7): p. 434-8. PMID: 7382552.
18. Schaffner, F. and H. Thaler, *Nonalcoholic fatty liver disease.* Prog Liver Dis, 1986. **8**: p. 283-98. PMID: 3086934.
19. Sawaki, M., et al., *Chronic liver injury promotes hepatocarcinogenesis of the LEC rat.* Carcinogenesis, 1998. **19**(2): p. 331-5. DOI: https://doi.org/10.1093/carcin/19.2.331. PMID: 9498285.
20. European Association for the Study of the, L., *EASL Clinical Practice Guidelines on the management of hepatocellular carcinoma.* J Hepatol, 2025. **82**(2): p. 315-374. DOI: https://doi.org/10.1016/j.jhep.2024.08.028. PMID: 39690085.
21. European Association for the Study of the, L., *EASL Clinical Practice Guidelines: Management of hepatocellular carcinoma.* J Hepatol, 2018. **69**(1): p. 182-236. DOI: https://doi.org/10.1016/j.jhep.2018.03.019. PMID: 29628281.
22. Sirivatanauksorn, Y. and C. Tovikkai, *Comparison of staging systems of hepatocellular carcinoma.* HPB Surg, 2011. **2011**: p. 818217. DOI: https://doi.org/10.1155/2011/818217. PMID: 21760664. PMCID: PMC3132503
23. Llovet, J.M., C. Bru, and J. Bruix, *Prognosis of hepatocellular carcinoma: the BCLC staging classification.* Semin Liver Dis, 1999. **19**(3): p. 329-38. DOI: https://doi.org/10.1055/s-2007-1007122. PMID: 10518312.
24. Brierley, J., M.K. Gospodarowicz, and C. Wittekind, *TNM classification of malignant tumours*. Eighth edition. ed. 1 online resource (xviii, 253 pages). ISBN: 978-1-119-26356-2
25. *A new prognostic system for hepatocellular carcinoma: a retrospective study of 435 patients: the Cancer of the Liver Italian Program (CLIP) investigators.* Hepatology, 1998. **28**(3): p. 751-5. DOI: https://doi.org/10.1002/hep.510280322. PMID: 9731568.
26. Hoshida, Y., et al., *Integrative transcriptome analysis reveals common molecular subclasses of human hepatocellular carcinoma.* Cancer Res, 2009. **69**(18): p. 7385-92. DOI: https://doi.org/10.1158/0008-5472.CAN-09-1089. PMID: 19723656. PMCID: PMC3549578
27. Zucman-Rossi, J., et al., *Genetic Landscape and Biomarkers of Hepatocellular Carcinoma.* Gastroenterology, 2015. **149**(5): p. 1226-1239 e4. DOI: https://doi.org/10.1053/j.gastro.2015.05.061. PMID: 26099527.
28. Ito, N., et al., *Positive correlation of plasma transforming growth factor-beta 1 levels with tumor vascularity in hepatocellular carcinoma.* Cancer Lett, 1995. **89**(1): p. 45-8. DOI: https://doi.org/10.1016/0304-3835(95)90156-6. PMID: 7882301.
29. Perra, A., et al., *YAP activation is an early event and a potential therapeutic target in liver cancer development.* J Hepatol, 2014. **61**(5): p. 1088-96. DOI: https://doi.org/10.1016/j.jhep.2014.06.033. PMID: 25010260.
30. Fagotto, F., *Looking beyond the Wnt pathway for the deep nature of beta-catenin.* EMBO Rep, 2013. **14**(5): p. 422-33. DOI: https://doi.org/10.1038/embor.2013.45. PMID: 23598517. PMCID: PMC3642384

31. van Zijl, F., et al., *Epithelial-mesenchymal transition in hepatocellular carcinoma.* Future Oncol, 2009. **5**(8): p. 1169-79. DOI: https://doi.org/10.2217/fon.09.91. PMID: 19852728. PMCID: PMC2963061
32. Meng, Z., T. Moroishi, and K.L. Guan, *Mechanisms of Hippo pathway regulation.* Genes Dev, 2016. **30**(1): p. 1-17. DOI: https://doi.org/10.1101/gad.274027.115. PMID: 26728553. PMCID: PMC4701972
33. El-Serag, H.B. and K.L. Rudolph, *Hepatocellular carcinoma: epidemiology and molecular carcinogenesis.* Gastroenterology, 2007. **132**(7): p. 2557-76. DOI: https://doi.org/10.1053/j.gastro.2007.04.061. PMID: 17570226.
34. McGlynn, K.A., J.L. Petrick, and W.T. London, *Global epidemiology of hepatocellular carcinoma: an emphasis on demographic and regional variability.* Clin Liver Dis, 2015. **19**(2): p. 223-38. DOI: https://doi.org/10.1016/j.cld.2015.01.001. PMID: 25921660. PMCID: PMC4712629
35. Sung, H., et al., *Global Cancer Statistics 2020: GLOBOCAN Estimates of Incidence and Mortality Worldwide for 36 Cancers in 185 Countries.* CA Cancer J Clin, 2021. **71**(3): p. 209-249. DOI: https://doi.org/10.3322/caac.21660. PMID: 33538338.
36. Rumgay, H., et al., *Global burden of primary liver cancer in 2020 and predictions to 2040.* J Hepatol, 2022. **77**(6): p. 1598-1606. DOI: https://doi.org/10.1016/j.jhep.2022.08.021. PMID: 36208844. PMCID: PMC9670241
37. Singal, A.G. and H.B. El-Serag, *Hepatocellular Carcinoma From Epidemiology to Prevention: Translating Knowledge into Practice.* Clin Gastroenterol Hepatol, 2015. **13**(12): p. 2140-51. DOI: https://doi.org/10.1016/j.cgh.2015.08.014. PMID: 26284591. PMCID: PMC4618036
38. Calderon-Martinez, E., et al., *Prognostic Scores and Survival Rates by Etiology of Hepatocellular Carcinoma: A Review.* J Clin Med Res, 2023. **15**(4): p. 200-207. DOI: https://doi.org/10.14740/jocmr4902. PMID: 37187717. PMCID: PMC10181349
39. Petruzziello, A., *Epidemiology of Hepatitis B Virus (HBV) and Hepatitis C Virus (HCV) Related Hepatocellular Carcinoma.* Open Virol J, 2018. **12**: p. 26-32. DOI: https://doi.org/10.2174/1874357901812010026. PMID: 29541276. PMCID: PMC5842386
40. Yapali, S. and N. Tozun, *Epidemiology and viral risk factors for hepatocellular carcinoma in the Eastern Mediterranean countries.* Hepatoma Research, 2018. **4**(6). DOI: https://doi.org/10.20517/2394-5079.2018.57.
41. Liu, Y. and L. Liu, *Changes in the Epidemiology of Hepatocellular Carcinoma in Asia.* Cancers (Basel), 2022. **14**(18). DOI: https://doi.org/10.3390/cancers14184473. PMID: 36139633. PMCID: PMC9496757
42. Farrell, A., M. Ryan, and J. Howell, *Epidemiology of non-alcoholic fatty liver disease-related hepatocellular carcinoma: a western perspective.* Hepatoma Research, 2020. **2020**. DOI: https://doi.org/10.20517/2394-5079.2019.019.
43. Noureddin, M. and M.E. Rinella, *Nonalcoholic Fatty liver disease, diabetes, obesity, and hepatocellular carcinoma.* Clin Liver Dis, 2015. **19**(2): p. 361-79. DOI: https://doi.org/10.1016/j.cld.2015.01.012. PMID: 25921668. PMCID: PMC6658171

44. Bellentani, S., et al., *Drinking habits as cofactors of risk for alcohol induced liver damage. The Dionysos Study Group.* Gut, 1997. **41**(6): p. 845-50. DOI: https://doi.org/10.1136/gut.41.6.845. PMID: 9462221. PMCID: PMC1891602
45. Donato, F., et al., *Alcohol and hepatocellular carcinoma: the effect of lifetime intake and hepatitis virus infections in men and women.* Am J Epidemiol, 2002. **155**(4): p. 323-31. DOI: https://doi.org/10.1093/aje/155.4.323. PMID: 11836196.
46. Schilsky, M.L. and S. Fink, *Inherited metabolic liver disease.* Curr Opin Gastroenterol, 2006. **22**(3): p. 215-22. DOI: https://doi.org/10.1097/01.mog.0000218957.63311.0e. PMID: 16550035.
47. Guarino, M. and J.F. Dufour, *Smoking favours hepatocellular carcinoma.* Ann Transl Med, 2019. **7**(Suppl 3): p. S99. DOI: https://doi.org/10.21037/atm.2019.04.90. PMID: 31576306. PMCID: PMC6685865 Fallk, Genfit, Genkyotex, Gilead, Heparegenerix, Intercept, Lilly, Merck, Novartis. M Guarino has no conflicts of interest to declare.
48. Zelber-Sagi, S., M. Noureddin, and O. Shibolet, *Lifestyle and Hepatocellular Carcinoma What Is the Evidence and Prevention Recommendations.* Cancers (Basel), 2021. **14**(1). DOI: https://doi.org/10.3390/cancers14010103. PMID: 35008267. PMCID: PMC8750465
49. Liu, Y. and F. Wu, *Global burden of aflatoxin-induced hepatocellular carcinoma: a risk assessment.* Environ Health Perspect, 2010. **118**(6): p. 818-24. DOI: https://doi.org/10.1289/ehp.0901388. PMID: 20172840. PMCID: PMC2898859
50. Alvarez, C.S., et al., *Analysis of TP53 aflatoxin signature mutation in hepatocellular carcinomas from Guatemala: A cross-sectional study (2016-2017).* Health Sci Rep, 2020. **3**(2): p. e155. DOI: https://doi.org/10.1002/hsr2.155. PMID: 32382660. PMCID: PMC7202218
51. Tzartzeva, K., et al., *Surveillance Imaging and Alpha Fetoprotein for Early Detection of Hepatocellular Carcinoma in Patients With Cirrhosis: A Meta-analysis.* Gastroenterology, 2018. **154**(6): p. 1706-1718 e1. DOI: https://doi.org/10.1053/j.gastro.2018.01.064. PMID: 29425931. PMCID: PMC5927818
52. Lee, J.M., et al., *Recent Advances in CT and MR Imaging for Evaluation of Hepatocellular Carcinoma.* Liver Cancer, 2012. **1**(1): p. 22-40. DOI: https://doi.org/10.1159/000339018. PMID: 24159569. PMCID: PMC3747553
53. Marks, R.M., W.R. Masch, and V. Chernyak, *LI-RADS: Past, Present, and Future, From the AJR Special Series on Radiology Reporting and Data Systems.* AJR Am J Roentgenol, 2021. **216**(2): p. 295-304. DOI: https://doi.org/10.2214/AJR.20.24272. PMID: 33052720.
54. Hansmann, J. and C.E. Ray, Jr., *Overview of Staging Systems for Hepatocellular Carcinoma and Implications for Interventional Radiology.* Semin Intervent Radiol, 2017. **34**(2): p. 213-219. DOI: https://doi.org/10.1055/s-0037-1602757. PMID: 28579689. PMCID: PMC5453774
55. Burkhart, R.A. and T.M. Pawlik, *Staging and Prognostic Models for Hepatocellular Carcinoma and Intrahepatic Cholangiocarcinoma.* Cancer Control, 2017. **24**(3): p. 1073274817729235. DOI: https://doi.org/10.1177/1073274817729235. PMID: 28975828. PMCID: PMC5937249

56. Tsilimigras, D.I., H. Aziz, and T.M. Pawlik, *Critical Analysis of the Updated Barcelona Clinic Liver Cancer (BCLC) Group Guidelines.* Ann Surg Oncol, 2022. **29**(12): p. 7231-7234. DOI: https://doi.org/10.1245/s10434-022-12242-4. PMID: 35854026.
57. Amin, M.B., et al., *The Eighth Edition AJCC Cancer Staging Manual: Continuing to build a bridge from a population-based to a more "personalized" approach to cancer staging.* CA Cancer J Clin, 2017. **67**(2): p. 93-99. DOI: https://doi.org/10.3322/caac.21388. PMID: 28094848.
58. McGlynn, K.A., J.L. Petrick, and H.B. El-Serag, *Epidemiology of Hepatocellular Carcinoma.* Hepatology, 2021. **73 Suppl 1**(Suppl 1): p. 4-13. DOI: https://doi.org/10.1002/hep.31288. PMID: 32319693. PMCID: PMC7577946
59. Llovet, J.M. and J. Bruix, *Prospective validation of the Cancer of the Liver Italian Program (CLIP) score: a new prognostic system for patients with cirrhosis and hepatocellular carcinoma.* Hepatology, 2000. **32**(3): p. 679-80. DOI: https://doi.org/10.1053/jhep.2000.16475. PMID: 10991637.
60. Daniele, B., et al., *Cancer of the Liver Italian Program (CLIP) score for staging hepatocellular carcinoma.* Hepatol Res, 2007. **37 Suppl 2**: p. S206-9. DOI: https://doi.org/10.1111/j.1872-034X.2007.00186.x. PMID: 17877484.
61. Ray, E.M. and H.K. Sanoff, *Optimal therapy for patients with hepatocellular carcinoma and resistance or intolerance to sorafenib: challenges and solutions.* J Hepatocell Carcinoma, 2017. **4**: p. 131-138. DOI: https://doi.org/10.2147/JHC.S124366. PMID: 29184856. PMCID: PMC5687453
62. Pilard, C., et al., *Cancer immunotherapy: it's time to better predict patients' response.* Br J Cancer, 2021. **125**(7): p. 927-938. DOI: https://doi.org/10.1038/s41416-021-01413-x. PMID: 34112949. PMCID: PMC8476530 reports grants, personal fees and/or non-financial support from Novartis, Roche, Pfizer, Lilly, Amgen, Bristol-Myers Squibb, Astra-Zeneca, Daiichi Sankyo, Abbvie, Medimmune and MerckKGaA (not directly related to the submitted work).
63. Reig, M., et al., *BCLC strategy for prognosis prediction and treatment recommendation: The 2022 update.* J Hepatol, 2022. **76**(3): p. 681-693. DOI: https://doi.org/10.1016/j.jhep.2021.11.018. PMID: 34801630. PMCID: PMC8866082
64. Holczbauer, A., K.J. Wangensteen, and S. Shin, *Cellular origins of regenerating liver and hepatocellular carcinoma.* JHEP Rep, 2022. **4**(4): p. 100416. DOI: https://doi.org/10.1016/j.jhepr.2021.100416. PMID: 35243280. PMCID: PMC8873941
65. Roehlen, N., E. Crouchet, and T.F. Baumert, *Liver Fibrosis: Mechanistic Concepts and Therapeutic Perspectives.* Cells, 2020. **9**(4). DOI: https://doi.org/10.3390/cells9040875. PMID: 32260126. PMCID: PMC7226751
66. Bataller, R. and D.A. Brenner, *Liver fibrosis.* Journal of Clinical Investigation, 2005. **115**(2): p. 209-218. DOI: https://doi.org/10.1172/jci200524282.
67. Friedman, S.L., *Hepatic stellate cells: protean, multifunctional, and enigmatic cells of the liver.* Physiol Rev, 2008. **88**(1): p. 125-72. DOI: https://doi.org/10.1152/physrev.00013.2007. PMID: 18195085. PMCID: PMC2888531

68. El-Serag, H.B., *Epidemiology of viral hepatitis and hepatocellular carcinoma.* Gastroenterology, 2012. **142**(6): p. 1264-1273 e1. DOI: https://doi.org/10.1053/j.gastro.2011.12.061. PMID: 22537432. PMCID: PMC3338949
69. Fausto, N., J.S. Campbell, and K.J. Riehle, *Liver regeneration.* Hepatology, 2006. **43**(2 Suppl 1): p. S45-53. DOI: https://doi.org/10.1002/hep.20969. PMID: 16447274.
70. Schrader, J. and J.P. Iredale, *The inflammatory microenvironment of HCC - the plot becomes complex.* J Hepatol, 2011. **54**(5): p. 853-5. DOI: https://doi.org/10.1016/j.jhep.2010.12.014. PMID: 21185341.
71. Schuppan, D. and N.H. Afdhal, *Liver cirrhosis.* Lancet, 2008. **371**(9615): p. 838-51. DOI: https://doi.org/10.1016/S0140-6736(08)60383-9. PMID: 18328931. PMCID: PMC2271178
72. Marra, F. and F. Tacke, *Roles for chemokines in liver disease.* Gastroenterology, 2014. **147**(3): p. 577-594 e1. DOI: https://doi.org/10.1053/j.gastro.2014.06.043. PMID: 25066692.
73. Dooley, S. and P. ten Dijke, *TGF-beta in progression of liver disease.* Cell Tissue Res, 2012. **347**(1): p. 245-56. DOI: https://doi.org/10.1007/s00441-011-1246-y. PMID: 22006249. PMCID: PMC3250614
74. Totoki, Y., et al., *Trans-ancestry mutational landscape of hepatocellular carcinoma genomes.* Nat Genet, 2014. **46**(12): p. 1267-73. DOI: https://doi.org/10.1038/ng.3126. PMID: 25362482.
75. Nault, J.C. and J. Zucman-Rossi, *Genetics of hepatocellular carcinoma: the next generation.* J Hepatol, 2014. **60**(1): p. 224-6. DOI: https://doi.org/10.1016/j.jhep.2013.08.019. PMID: 23994386.
76. Villanueva, A., *Hepatocellular Carcinoma.* N Engl J Med, 2019. **380**(15): p. 1450-1462. DOI: https://doi.org/10.1056/NEJMra1713263. PMID: 30970190.
77. Sia, D., et al., *Liver Cancer Cell of Origin, Molecular Class, and Effects on Patient Prognosis.* Gastroenterology, 2017. **152**(4): p. 745-761. DOI: https://doi.org/10.1053/j.gastro.2016.11.048. PMID: 28043904. PMCID: PMC12160040
78. Anstee, Q.M., et al., *From NASH to HCC: current concepts and future challenges.* Nat Rev Gastroenterol Hepatol, 2019. **16**(7): p. 411-428. DOI: https://doi.org/10.1038/s41575-019-0145-7. PMID: 31028350.
79. Hsu, I.C., et al., *Mutational hotspot in the p53 gene in human hepatocellular carcinomas.* Nature, 1991. **350**(6317): p. 427-8. DOI: https://doi.org/10.1038/350427a0. PMID: 1849234.
80. Olivier, M., M. Hollstein, and P. Hainaut, *TP53 mutations in human cancers: origins, consequences, and clinical use.* Cold Spring Harb Perspect Biol, 2010. **2**(1): p. a001008. DOI: https://doi.org/10.1101/cshperspect.a001008. PMID: 20182602. PMCID: PMC2827900
81. de La Coste, A., et al., *Somatic mutations of the beta-catenin gene are frequent in mouse and human hepatocellular carcinomas.* Proc Natl Acad Sci U S A, 1998. **95**(15): p. 8847-51. DOI: https://doi.org/10.1073/pnas.95.15.8847. PMID: 9671767. PMCID: PMC21165
82. Zucman-Rossi, J., et al., *Differential effects of inactivated Axin1 and activated beta-catenin mutations in human hepatocellular carcinomas.* Oncogene, 2007. **26**(5): p. 774-80. DOI: https://doi.org/10.1038/sj.onc.1209824. PMID: 16964294.

83. Nault, J.C., et al., *High frequency of telomerase reverse-transcriptase promoter somatic mutations in hepatocellular carcinoma and preneoplastic lesions.* Nat Commun, 2013. **4**: p. 2218. DOI: https://doi.org/10.1038/ncomms3218. PMID: 23887712. PMCID: PMC3731665
84. Villanueva, A., et al., *Pivotal role of mTOR signaling in hepatocellular carcinoma.* Gastroenterology, 2008. **135**(6): p. 1972-83, 1983 e1-11. DOI: https://doi.org/10.1053/j.gastro.2008.08.008. PMID: 18929564. PMCID: PMC2678688
85. Talarmin, H., et al., *The mitogen-activated protein kinase kinase/extracellular signal-regulated kinase cascade activation is a key signalling pathway involved in the regulation of G(1) phase progression in proliferating hepatocytes.* Mol Cell Biol, 1999. **19**(9): p. 6003-11. DOI: https://doi.org/10.1128/MCB.19.9.6003. PMID: 10454547. PMCID: PMC84483
86. Fabregat, I., *Exploring liver physiology, pathology, TGF-beta, EMT, stemness and new developments in liver cancer.* Hepat Oncol, 2017. **4**(1): p. 9-13. DOI: https://doi.org/10.2217/hep-2017-0007. PMID: 30191049. PMCID: PMC6095327 affiliations or financial involvement with any organization or entity with a financial interest in or financial conflict with the subject matter or materials discussed in the manuscript. This includes employment, consultancies, honoraria, stock ownership or options, expert testimony, grants or patents received or pending, or royalties. No writing assistance was utilized in the production of this manuscript.
87. Lu, L., M.J. Finegold, and R.L. Johnson, *Hippo pathway coactivators Yap and Taz are required to coordinate mammalian liver regeneration.* Exp Mol Med, 2018. **50**(1): p. e423. DOI: https://doi.org/10.1038/emm.2017.205. PMID: 29303509. PMCID: PMC5992983
88. Giannelli, G., et al., *Role of epithelial to mesenchymal transition in hepatocellular carcinoma.* J Hepatol, 2016. **65**(4): p. 798-808. DOI: https://doi.org/10.1016/j.jhep.2016.05.007. PMID: 27212245.
89. Xu, C., et al., *beta-Catenin signaling in hepatocellular carcinoma.* J Clin Invest, 2022. **132**(4). DOI: https://doi.org/10.1172/JCI154515. PMID: 35166233. PMCID: PMC8843739 exists.
90. Zhou, S.L., et al., *Tumor-Associated Neutrophils Recruit Macrophages and T-Regulatory Cells to Promote Progression of Hepatocellular Carcinoma and Resistance to Sorafenib.* Gastroenterology, 2016. **150**(7): p. 1646-1658 e17. DOI: https://doi.org/10.1053/j.gastro.2016.02.040. PMID: 26924089.
91. Park, E.J., et al., *Dietary and genetic obesity promote liver inflammation and tumorigenesis by enhancing IL-6 and TNF expression.* Cell, 2010. **140**(2): p. 197-208. DOI: https://doi.org/10.1016/j.cell.2009.12.052. PMID: 20141834. PMCID: PMC2836922
92. Luedde, T. and R.F. Schwabe, *NF-kappaB in the liver--linking injury, fibrosis and hepatocellular carcinoma.* Nat Rev Gastroenterol Hepatol, 2011. **8**(2): p. 108-18. DOI: https://doi.org/10.1038/nrgastro.2010.213. PMID: 21293511. PMCID: PMC3295539
93. Ben-Moshe, S. and S. Itzkovitz, *Spatial heterogeneity in the mammalian liver.* Nat Rev Gastroenterol Hepatol, 2019. **16**(7): p. 395-410. DOI: https://doi.org/10.1038/s41575-019-0134-x. PMID: 30936469.
94. Halpern, K.B., et al., *Paired-cell sequencing enables spatial gene expression mapping of liver endothelial cells.* Nat Biotechnol, 2018. **36**(10): p. 962-970.

DOI: https://doi.org/10.1038/nbt.4231. PMID: 30222169. PMCID: PMC6546596

95. Ekberg, K., et al., *Gluconeogenesis and glucuronidation in liver in vivo and the heterogeneity of hepatocyte function.* J Biol Chem, 1995. **270**(37): p. 21715-7. DOI: https://doi.org/10.1074/jbc.270.37.21715. PMID: 7665589.
96. Gebhardt, R. and M. Matz-Soja, *Liver zonation: Novel aspects of its regulation and its impact on homeostasis.* World J Gastroenterol, 2014. **20**(26): p. 8491-504. DOI: https://doi.org/10.3748/wjg.v20.i26.8491. PMID: 25024605. PMCID: PMC4093700
97. Jungermann, K. and N. Katz, *Functional specialization of different hepatocyte populations.* Physiol Rev, 1989. **69**(3): p. 708-64. DOI: https://doi.org/10.1152/physrev.1989.69.3.708. PMID: 2664826.
98. Wan, S., et al., *Cytoplasmic localization of the cell polarity factor scribble supports liver tumor formation and tumor cell invasiveness.* Hepatology, 2018. **67**(5): p. 1842-1856. DOI: https://doi.org/10.1002/hep.29669. PMID: 29152770.
99. McCaffrey, L.M. and I.G. Macara, *Epithelial organization, cell polarity and tumorigenesis.* Trends Cell Biol, 2011. **21**(12): p. 727-35. DOI: https://doi.org/10.1016/j.tcb.2011.06.005. PMID: 21782440.
100. Thiery, J.P., et al., *Epithelial-mesenchymal transitions in development and disease.* Cell, 2009. **139**(5): p. 871-90. DOI: https://doi.org/10.1016/j.cell.2009.11.007. PMID: 19945376.
101. Ellenbroek, S.I., S. Iden, and J.G. Collard, *Cell polarity proteins and cancer.* Semin Cancer Biol, 2012. **22**(3): p. 208-15. DOI: https://doi.org/10.1016/j.semcancer.2012.02.012. PMID: 22465739.
102. Kumar, V., et al., *The Role of Notch, Hedgehog, and Wnt Signaling Pathways in the Resistance of Tumors to Anticancer Therapies.* Front Cell Dev Biol, 2021. **9**: p. 650772. DOI: https://doi.org/10.3389/fcell.2021.650772. PMID: 33968932. PMCID: PMC8100510
103. Wei, K., et al., *Decoding Hepatocellular Carcinoma Metastasis: Molecular Mechanisms, Targeted Therapies, and Potential Biomarkers.* Curr Issues Mol Biol, 2025. **47**(4). DOI: https://doi.org/10.3390/cimb47040263. PMID: 40699663. PMCID: PMC12025613
104. Chaffer, C.L., et al., *EMT, cell plasticity and metastasis.* Cancer Metastasis Rev, 2016. **35**(4): p. 645-654. DOI: https://doi.org/10.1007/s10555-016-9648-7. PMID: 27878502.
105. Song, X.Q., Q. Li, and J. Zhang, *A double-edged sword: DLG5 in diseases.* Biomed Pharmacother, 2023. **162**: p. 114611. DOI: https://doi.org/10.1016/j.biopha.2023.114611. PMID: 37001186.
106. Humbert, P.O., et al., *Control of tumourigenesis by the Scribble/Dlg/Lgl polarity module.* Oncogene, 2008. **27**(55): p. 6888-907. DOI: https://doi.org/10.1038/onc.2008.341. PMID: 19029932.
107. Kudo, M., *Multistep human hepatocarcinogenesis: correlation of imaging with pathology.* J Gastroenterol, 2009. **44 Suppl 19**: p. 112-8. DOI: https://doi.org/10.1007/s00535-008-2274-6. PMID: 19148804.
108. Desmet, V.J., *Ductal plates in hepatic ductular reactions. Hypothesis and implications. I. Types of ductular reaction reconsidered.* Virchows Arch, 2011. **458**(3): p. 251-9. DOI: https://doi.org/10.1007/s00428-011-1048-3. PMID: 21287200.

109. Tocan, V., et al., *Hepatocyte polarity establishment and apical lumen formation are organized by Par3, Cdc42, and aPKC in conjunction with Lgl.* J Biol Chem, 2021. **297**(6): p. 101354. DOI: https://doi.org/10.1016/j.jbc.2021.101354. PMID: 34717957. PMCID: PMC8637150
110. Viloria-Petit, A.M. and J.L. Wrana, *The TGFbeta-Par6 polarity pathway: linking the Par complex to EMT and breast cancer progression.* Cell Cycle, 2010. **9**(4): p. 623-4. DOI: https://doi.org/10.4161/cc.9.4.10779. PMID: 20107326.
111. Margolis, B., *The Crumbs3 Polarity Protein.* Cold Spring Harb Perspect Biol, 2018. **10**(3). DOI: https://doi.org/10.1101/cshperspect.a027961. PMID: 28289060. PMCID: PMC5830892
112. Michgehl, U., H. Pavenstadt, and B. Vollenbroker, *Cross talk between the Crumbs complex and Hippo signaling in renal epithelial cells.* Pflugers Arch, 2017. **469**(7-8): p. 917-926. DOI: https://doi.org/10.1007/s00424-017-2004-0. PMID: 28612137.
113. Elsum, I.A., C. Martin, and P.O. Humbert, *Scribble regulates an EMT polarity pathway through modulation of MAPK-ERK signaling to mediate junction formation.* J Cell Sci, 2013. **126**(Pt 17): p. 3990-9. DOI: https://doi.org/10.1242/jcs.129387. PMID: 23813956.
114. Varelas, X., et al., *The Hippo pathway regulates Wnt/beta-catenin signaling.* Dev Cell, 2010. **18**(4): p. 579-91. DOI: https://doi.org/10.1016/j.devcel.2010.03.007. PMID: 20412773.
115. Umeda, K., et al., *ZO-1 and ZO-2 independently determine where claudins are polymerized in tight-junction strand formation.* Cell, 2006. **126**(4): p. 741-54. DOI: https://doi.org/10.1016/j.cell.2006.06.043. PMID: 16923393.
116. Itoh, M., K. Morita, and S. Tsukita, *Characterization of ZO-2 as a MAGUK family member associated with tight as well as adherens junctions with a binding affinity to occludin and alpha catenin.* J Biol Chem, 1999. **274**(9): p. 5981-6. DOI: https://doi.org/10.1074/jbc.274.9.5981. PMID: 10026224.
117. Fanning, A.S. and J.M. Anderson, *Zonula occludens-1 and -2 are cytosolic scaffolds that regulate the assembly of cellular junctions.* Ann N Y Acad Sci, 2009. **1165**: p. 113-20. DOI: https://doi.org/10.1111/j.1749-6632.2009.04440.x. PMID: 19538295. PMCID: PMC3759978
118. Gonzalez-Mariscal, L., R. Tapia, and D. Chamorro, *Crosstalk of tight junction components with signaling pathways.* Biochim Biophys Acta, 2008. **1778**(3): p. 729-56. DOI: https://doi.org/10.1016/j.bbamem.2007.08.018. PMID: 17950242.
119. Furuse, M., et al., *Occludin: a novel integral membrane protein localizing at tight junctions.* J Cell Biol, 1993. **123**(6 Pt 2): p. 1777-88. DOI: https://doi.org/10.1083/jcb.123.6.1777. PMID: 8276896. PMCID: PMC2290891
120. Balda, M.S., et al., *Functional dissociation of paracellular permeability and transepithelial electrical resistance and disruption of the apical-basolateral intramembrane diffusion barrier by expression of a mutant tight junction membrane protein.* J Cell Biol, 1996. **134**(4): p. 1031-49. DOI: https://doi.org/10.1083/jcb.134.4.1031. PMID: 8769425. PMCID: PMC2120963
121. Matter, K. and M.S. Balda, *Signalling to and from tight junctions.* Nat Rev Mol Cell Biol, 2003. **4**(3): p. 225-36. DOI: https://doi.org/10.1038/nrm1055. PMID: 12612641.

122. Fanning, A.S., et al., *The tight junction protein ZO-1 establishes a link between the transmembrane protein occludin and the actin cytoskeleton.* J Biol Chem, 1998. **273**(45): p. 29745-53. DOI: https://doi.org/10.1074/jbc.273.45.29745. PMID: 9792688.
123. Sakakibara, A., et al., *Possible involvement of phosphorylation of occludin in tight junction formation.* J Cell Biol, 1997. **137**(6): p. 1393-401. DOI: https://doi.org/10.1083/jcb.137.6.1393. PMID: 9182670. PMCID: PMC2132539
124. Furuse, M., et al., *Claudin-1 and -2: novel integral membrane proteins localizing at tight junctions with no sequence similarity to occludin.* J Cell Biol, 1998. **141**(7): p. 1539-50. DOI: https://doi.org/10.1083/jcb.141.7.1539. PMID: 9647647. PMCID: PMC2132999
125. Takasawa, K., et al., *Claudin-18 coupled with EGFR/ERK signaling contributes to the malignant potentials of bile duct cancer.* Cancer Lett, 2017. **403**: p. 66-73. DOI: https://doi.org/10.1016/j.canlet.2017.05.033. PMID: 28624624.
126. van Roy, F. and G. Berx, *The cell-cell adhesion molecule E-cadherin.* Cell Mol Life Sci, 2008. **65**(23): p. 3756-88. DOI: https://doi.org/10.1007/s00018-008-8281-1. PMID: 18726070. PMCID: PMC11131785
127. Peinado, H., F. Portillo, and A. Cano, *Transcriptional regulation of cadherins during development and carcinogenesis.* Int J Dev Biol, 2004. **48**(5-6): p. 365-75. DOI: https://doi.org/10.1387/ijdb.041794hp. PMID: 15349812.
128. Nelson, W.J. and R. Nusse, *Convergence of Wnt, beta-catenin, and cadherin pathways.* Science, 2004. **303**(5663): p. 1483-7. DOI: https://doi.org/10.1126/science.1094291. PMID: 15001769. PMCID: PMC3372896
129. Lamouille, S., J. Xu, and R. Derynck, *Molecular mechanisms of epithelial-mesenchymal transition.* Nat Rev Mol Cell Biol, 2014. **15**(3): p. 178-96. DOI: https://doi.org/10.1038/nrm3758. PMID: 24556840. PMCID: PMC4240281
130. Hirose, T., et al., *Involvement of ASIP/PAR-3 in the promotion of epithelial tight junction formation.* J Cell Sci, 2002. **115**(Pt 12): p. 2485-95. DOI: https://doi.org/10.1242/jcs.115.12.2485. PMID: 12045219.
131. Yang, M.H., et al., *Comprehensive analysis of the independent effect of twist and snail in promoting metastasis of hepatocellular carcinoma.* Hepatology, 2009. **50**(5): p. 1464-74. DOI: https://doi.org/10.1002/hep.23221. PMID: 19821482.
132. Joberty, G., et al., *The cell-polarity protein Par6 links Par3 and atypical protein kinase C to Cdc42.* Nat Cell Biol, 2000. **2**(8): p. 531-9. DOI: https://doi.org/10.1038/35019573. PMID: 10934474.
133. Ozdamar, B., et al., *Regulation of the polarity protein Par6 by TGFbeta receptors controls epithelial cell plasticity.* Science, 2005. **307**(5715): p. 1603-9. DOI: https://doi.org/10.1126/science.1105718. PMID: 15761148.
134. Mu, Y., et al., *TGFbeta-induced phosphorylation of Par6 promotes migration and invasion in prostate cancer cells.* Br J Cancer, 2015. **112**(7): p. 1223-31. DOI: https://doi.org/10.1038/bjc.2015.71. PMID: 25756394. PMCID: PMC4385960
135. Suzuki, A.Y., Tomoyuki; Hirose, Tomonori; Manabe, Naoyuki; Mizuno, Keiko; Shimizu, Miki; Akimoto, Kazunori; Izumi, Yasushi; Ohnishi, Tetsuo; Ohno, Shigeo, *Atypical protein kinase C is involved in the establishment of epithelial*

cell polarity through phosphorylation of Par3 and Lgl. Journal of Cell Biology, 2001. **152**(6): p. 1183–1196. DOI: https://doi.org/10.1083/jcb.152.6.1183.

136. Hurd, T.W., et al., *Phosphorylation-dependent binding of 14-3-3 to the polarity protein Par3 regulates cell polarity in mammalian epithelia.* Curr Biol, 2003. **13**(23): p. 2082-90. DOI: https://doi.org/10.1016/j.cub.2003.11.020. PMID: 14653998.
137. Whiteman, E.L., et al., *Crumbs3 is essential for proper epithelial development and viability.* Mol Cell Biol, 2014. **34**(1): p. 43-56. DOI: https://doi.org/10.1128/MCB.00999-13. PMID: 24164893. PMCID: PMC3911272
138. Martin, T.A. and W.G. Jiang, *Loss of tight junction barrier function and its role in cancer metastasis.* Biochim Biophys Acta, 2009. **1788**(4): p. 872-91. DOI: https://doi.org/10.1016/j.bbamem.2008.11.005. PMID: 19059202.
139. Rosenthal, R., et al., *Claudin-2, a component of the tight junction, forms a paracellular water channel.* J Cell Sci, 2010. **123**(Pt 11): p. 1913-21. DOI: https://doi.org/10.1242/jcs.060665. PMID: 20460438.
140. Wang, W., et al., *Claudins and hepatocellular carcinoma.* Biomed Pharmacother, 2024. **171**: p. 116109. DOI: https://doi.org/10.1016/j.biopha.2023.116109. PMID: 38185042.
141. Santoni, M.J., et al., *The Scribble family in cancer: twentieth anniversary.* Oncogene, 2020. **39**(47): p. 7019-7033. DOI: https://doi.org/10.1038/s41388-020-01478-7. PMID: 32999444. PMCID: PMC7527152
142. Thomas, M., et al., *The hScrib/Dlg apico-basal control complex is differentially targeted by HPV-16 and HPV-18 E6 proteins.* Oncogene, 2005. **24**(41): p. 6222-30. DOI: https://doi.org/10.1038/sj.onc.1208757. PMID: 16103886.
143. Venugopal, P., et al., *Multiple functions of the scaffold protein Discs large 5 in the control of growth, cell polarity and cell adhesion in Drosophila melanogaster.* BMC Dev Biol, 2020. **20**(1): p. 10. DOI: https://doi.org/10.1186/s12861-020-00218-0. PMID: 32552730. PMCID: PMC7301484
144. Chatterjee, S.J. and L. McCaffrey, *Emerging role of cell polarity proteins in breast cancer progression and metastasis.* Breast Cancer (Dove Med Press), 2014. **6**: p. 15-27. DOI: https://doi.org/10.2147/BCTT.S43764. PMID: 24648766. PMCID: PMC3929326
145. Liu, J., et al., *DLG5 in cell polarity maintenance and cancer development.* Int J Biol Sci, 2014. **10**(5): p. 543-9. DOI: https://doi.org/10.7150/ijbs.8888. PMID: 24910533. PMCID: PMC4046881
146. Kwan, J., et al., *DLG5 connects cell polarity and Hippo signaling protein networks by linking PAR-1 with MST1/2.* Genes Dev, 2016. **30**(24): p. 2696-2709. DOI: https://doi.org/10.1101/gad.284539.116. PMID: 28087714. PMCID: PMC5238729
147. Suzuki, A. and S. Ohno, *The PAR-aPKC system: lessons in polarity.* J Cell Sci, 2006. **119**(Pt 6): p. 979-87. DOI: https://doi.org/10.1242/jcs.02898. PMID: 16525119.
148. Funke, L., S. Dakoji, and D.S. Bredt, *Membrane-associated guanylate kinases regulate adhesion and plasticity at cell junctions.* Annu Rev Biochem, 2005. **74**: p. 219-45. DOI: https://doi.org/10.1146/annurev.biochem.74.082803.133339. PMID: 15952887.

149. Yamanaka, T.H., Yosuke; Suzuki, Atsushi; Sugiyama, Yuki; Kitamura, Koichi; Maniwa, Rika; Nagai, Yoko; Yamashita, Akio; Hirose, Tomonori; Ishikawa, Hiroko; Ohno, Shigeo, *PAR-6 regulates aPKC activity in a novel way and mediates cell–cell contact-induced formation of the epithelial junctional complex.* Genes to Cells, 2001. **6**(8): p. 721–731. DOI: https://doi.org/10.1046/j.1365-2443.2001.00456.x.
150. Oughtred, R., Rust, J., Chang, C., Breitkreutz, B. J., Stark, C., Willems, A., ... & Tyers, M., *The BioGRID database: Biological General Repository for Interaction Datasets [Dataset]*, T.B.P.M.S. Hospital, Editor. 2025: Toronto, Canada. PMCID: PMCID
151. Del-Toro, N., Shrivastava, A., Ragueneau, E., Meldal, B., Combe, C., Barrera, E., Perfetto, L., How, K., Ratan, P., Shirodkar, G., Lopez, R., Orchard, S., & Hermjakob, H., *IntAct Molecular Interaction Database [Dataset]*, E.B.I. (EMBL-EBI), Editor. 2024: Hinxton, Cambridgeshire, United Kingdom. PMCID: PMCID
152. Rodchenkov, I., et al., *Pathway Commons 2019 Update: integration, analysis and exploration of pathway data.* Nucleic Acids Res, 2020. **48**(D1): p. D489-D497. DOI: https://doi.org/10.1093/nar/gkz946. PMID: 31647099. PMCID: PMC7145667
153. Caruso, S., et al., *Analysis of Liver Cancer Cell Lines Identifies Agents With Likely Efficacy Against Hepatocellular Carcinoma and Markers of Response.* Gastroenterology, 2019. **157**(3): p. 760-776. DOI: https://doi.org/10.1053/j.gastro.2019.05.001. PMID: 31063779.
154. Pfaffl, M.W., *A new mathematical model for relative quantification in real-time RT-PCR.* Nucleic Acids Res, 2001. **29**(9): p. e45. DOI: https://doi.org/10.1093/nar/29.9.e45. PMID: 11328886. PMCID: PMC55695
155. Bankhead, P., Loughrey, M. B., Fernández, J. A., Dombrowski, Y., McArt, D. G., Dunne, P. D. & Hamilton, P. W., *QuPath: Open source software for digital pathology image analysis [Computer software]*. 2017, University of Edinburgh: Edinburgh, UK. DOI: https://doi.org/10.1038/s41598-017-17204-5. PMCID: PMCID
156. Schneider, C.A., Rasband, W. S., & Eliceiri, K. W., *NIH Image to ImageJ: 25 years of image analysis [Computer software]*. 2012, National Institutes of Health: Bethesda, MD, USA. DOI: https://doi.org/10.1038/nmeth.2089. PMCID: PMCID
157. Carpenter, A.E., Jones, T. R., Lamprecht, M. R., Clarke, C., Kang, I. H., Friman, O., Guertin, D. A., Chang, J. H., Lindquist, R. A., Moffat, J., Golland, P., & Sabatini, D. M., *CellProfiler: Image analysis software for identifying and quantifying cell phenotypes [Computer software]*. 2006, Broad Institute of MIT and Harvard: Cambridge, MA, USA. DOI: https://doi.org/10.1186/gb-2006-7-10-r100. PMCID: PMCID
158. Hruz, T., Laule, O., Szabo, G., Wessendorp, F., Bleuler, S., Oertle, L., Widmayer, P., Gruissem, W., & Zimmermann, P., *Genevestigator: High-performance search engine for gene expression meta-analysis [Computer software]*. 2008, Nebion AG: Zurich, Switzerland. DOI: https://doi.org/10.1186/1471-2164-12-156. PMCID: PMCID
159. Ke, Y., et al., *Discs large homolog 5 decreases formation and function of invadopodia in human hepatocellular carcinoma via Girdin and Tks5.* Int J Cancer, 2017. **141**(2): p. 364-376. DOI: https://doi.org/10.1002/ijc.30730. PMID: 28390157.

RINGRAZIAMENTI

Desidero esprimere la mia più profonda gratitudine al Dott. Devis Pascut e al Professor Claudio Tiribelli, i miei supervisori, per la loro compassione, guida e dedizione durante il mio percorso di dottorato. Grazie di cuore: vi dedico la Figura 26.e", perché i vostri insegnamenti e la vostra visione mi hanno trasformato come una farfalla.

Un sentito ringraziamento al Dott. Luca Grisetti per la sua preziosa guida tecnica durante gli esperimenti e per il supporto morale che mi ha sempre dato.

Si ringrazia la Dott.ssa Paola Tarchi, della Clinica Chirurgica SC (UCO) dell'Azienda Sanitaria Universitaria Giuliano Isontina (ASUGI), per aver raccolto i dati clinici sui pazienti utilizzati in questo studio.

Un sentito ringraziamento alla Dott.ssa Deborah Bonazza, di Anatomia e Istologia Patologica presso l'ASUGI, per la sua competenza e collaborazione.

Desidero ringraziare sinceramente la professoressa Emiliana Giacomello del Dipartimento Clinico Universitario di Scienze Mediche, Chirurgiche e della Salute dell'Università di Trieste per il tempo dedicatomi nell'insegnamento e nella guida dall'ottimizzazione alla quantificazione dell'IHC.

Desidero ringraziare la Dott.ssa Silvia Gazzin per la gentile concessione degli anticorpi contro ZO-1, Occludina e Claudina-2, fondamentali per lo svolgimento di questo studio.

Lubos akong nagpapasalamat sa Kagawaran ng Agham at Teknolohiya – Konseho ng Pilipinas para sa Pananaliksik at Pagpapaunlan sa Kalusugan (DOST-PCHRD). Ang aking pag-aaral sa doktorado ay isinagawa sa ilalim ng Programang Iskolar ng kagawaran at konseho para sa mga Nagtatapos ng Pag-aaral sa Ibang Bansa (Foreign Graduate Scholarship Program).

Fondazione Italiana
Fegato

A Betta, Valentina, Meli, Cami, Gabriela, Gabri, Gio, Giorgia, Georgia, Nicole, Antonio, Matteo e Francesco, grazie per la vostra amicizia. Dicevamo spesso di essere sulla stessa barca e, insieme, abbiamo affrontato ogni difficoltà rimanendo sempre a galla.

Thank you everyone in Fondazione Italiana Fegato, Lucia, Sandra, Sabrina, Sandro, Martina, Cristina, Pablo, Natalia, Cecil, Gianluca, Milos, Naning, Sri, Korri, Yara, Mihaela, Paola, Jessica, Emma and all people I met throughout my PhD journey.

Maraming salamat sa mga kapwa ko iskolar, Ate Kay, Noel, Viv, Nadine, Inah, Cyro, Melvin, Clary, Kuya Allen, JP, Romar at Julia.

Sa pamayanan ng mga Pilipino sa Trieste, Venezia, Milano, Roma, at Torino, maraming salamat.

Ang tesi na ito ay para sa aking ina-Lourdes, kapatid-Luisa, pamilya, kaibigan, bayan at Panginoon. *Ad Majorem Dei Gloriam.*

DEPARTMENT OF SCIENCE AND TECHNOLOGY
PCHRD
PHILIPPINE COUNCIL FOR HEALTH RESEARCH AND DEVELOPMENT